

Spectroscopic Investigations of Doped and Undoped Transition Metal Oxyhalides

Dissertation zur Erlangung des
naturwissenschaftlichen Doktorgrades
der Julius-Maximilians-Universität Würzburg



vorgelegt von
SEBASTIAN GLAWION

AUS GROSS-UMSTADT

Würzburg 2010

Eingereicht am: 13. August 2010

bei der Fakultät für Physik und Astronomie

1. Gutachter:	Prof. Dr. R. Claessen
2. Gutachter:	Prof. Dr. R. Valentí (Uni Frankfurt)
3. Gutachter: der Dissertation	

1. Prüfer:	Prof. Dr. R. Claessen
2. Prüfer:	Prof. Dr. R. Valentí (Uni Frankfurt)
3. Prüfer: im Promotionskolloquium	Prof. Dr. F. Reinert

Tag des Promotionskolloquiums: 10. Dezember 2010

Doktorurkunde ausgehändigt am:

Zusammenfassung

In dieser Doktorarbeit wird die elektronische und magnetische Struktur der Übergangsmetall-Oxyhalogenide TiOCl, TiOBr und VOCl untersucht. Ein Hauptaugenmerk liegt dabei auf spektroskopischen Methoden wie der Photoemissions- (PES) und Röntgenabsorptions- (XAS) Spektroskopie, sowie auf resonanter inelastischer Röntgenstreuung (RIXS). Die Resultate werden mit Dichtefunktionaltheorie, sowie Spektralfunktionen aus dynamischer Molekularfeldtheorie und verschiedenen Modellrechnungen verglichen. Die hauptsächlich zu klärenden Fragestellungen waren die der Dimensionalität magnetischer und elektronischer Wechselwirkungen, die Eignung der Oxyhalogenide als prototypische, stark korrelierte Modellsysteme, sowie die Möglichkeit, einen bandfüllungsinduzierten Isolator-Metall-Übergang zu erreichen. Es zeigt sich, dass TiOCl ein quasi-eindimensionales System mit nicht zu vernachlässigender zweidimensionaler Kopplung darstellt, während der eindimensionale Charakter bei TiOBr bereits stärker unterdrückt ist. In VOCl sind schließlich keine Anzeichen eindimensionalen Verhaltens mehr erkennbar, es handelt sich also um ein zweidimensionales System. In allen Fällen spielen die durch das Gitter verursachten Frustrationen eine Rolle bei der Beschreibung der elektronischen und magnetischen Eigenschaften, und es stellt sich heraus, dass die verwendeten theoretischen Ansätze zwar eine Verbesserung im Vergleich zu früheren Studien bringen, die Unterschiede zu den experimentellen Daten aber weiterhin zumindest teilweise qualitativ und nicht nur quantitativ sind. Bemerkenswert ist, dass mithilfe von RIXS erstmals in TiOCl eine Zwei-Spinon-Anregung identifiziert, und dadurch die bisher angenommene Energieskala magnetischer Anregungen in TiOCl bestätigt werden kann. Durch Interkation von Alkaliatomen (Na, K) können die Oxyhalogenide mit Elektronen dotiert werden, was sich anhand von Röntgen-PES zeigen und sogar quantitativ auswerten lässt. Dabei zeigt sich eine bestimmte vertikale Verteilung der Dotieratome, welche im Rahmen der experimentellen Genauigkeit durch das Modell einer sog. "Polaren Katastrophe" erklärt werden kann. Allerdings kann kein Übergang in eine metallische Phase beobachtet werden, doch dies lässt sich im Rahmen eines Legierungs-Hubbard-Modells, induziert durch das Störpotential der Dotieratome, qualitativ und quantitativ verstehen. Weiterhin zeigt sich in modellhafter Art und Weise ein Transfer von spektralem Gewicht, ein charakteristisches Merkmal stark korrelierter Elektronensysteme. Letztlich kann man den Schluss ziehen, dass die Übergangsmetall-Oxyhalogenide tatsächlich als prototypische Mott-Isolatoren aufgefasst werden können, die jedoch gleichzeitig ein reiches und bei weitem nicht vollständig verstandenes Phasendiagramm aufweisen.

Abstract

In this thesis the electronic and magnetic structure of the transition metal oxyhalides TiOCl, TiOBr and VOCl is investigated. The main experimental methods are photoemission (PES) and x-ray absorption (XAS) spectroscopy as well as resonant inelastic x-ray scattering (RIXS). The results are compared to density-functional theory, and spectral functions from dynamical mean-field theory and different kinds of model calculations. Questions addressed here are those of the dimensionality of the magnetic and electronic interactions, the suitability of the oxyhalides as prototypical strongly correlated model systems, and the possibility to induce a filling-controlled insulator-metal transition. It turns out that TiOCl is a quasi-one-dimensional system with non-negligible two-dimensional coupling, while the one-dimensional character is already quite suppressed in TiOBr. In VOCl no signatures of such one-dimensional behavior remain, and it is two-dimensional. In all cases, frustrations induced by the crystal lattice govern the magnetic and electronic properties. As it turns out, although the applied theoretical approaches display improvements compared to previous studies, the differences to the experimental data still are at least partially of qualitative instead of quantitative nature. Notably, using RIXS, it is possible for the first time in TiOCl to unambiguously identify a two-spinon excitation, and the previously assumed energy scale of magnetic excitations can be confirmed. By intercalation of alkali metal atoms (Na, K) the oxyhalides can be doped with electrons, which can be evidenced and even quantified using x-ray PES. In these experiments, also a particular vertical arrangement of dopants is observed, which can be explained, at least within experimental accuracy, using the model of a so-called “polar catastrophe”. However, no transition into a metallic phase can be observed upon doping, but this can be understood qualitatively and quantitatively within an alloy Hubbard model due to the impurity potential of the dopants. Furthermore, in a canonical way a transfer of spectral weight can be observed, which is a characteristic feature of strongly correlated electron systems. Overall, it can be stated that the transition metal oxyhalides actually can be regarded as prototypical Mott insulators, yet with a rich phase diagram which is far from being fully understood.

Contents

1	Introduction	1
2	Experimental Methods	3
2.1	Photoemission Spectroscopy	3
2.2	X-Ray Absorption Spectroscopy	12
2.3	Resonantly Enhanced Processes	15
2.3.1	Resonant Photoemission Spectroscopy	16
2.3.2	Resonant Inelastic X-Ray Scattering	18
3	Theoretical Concepts	21
3.1	Mott Physics and Hubbard Model	21
3.2	Parametrization of Coulomb Interactions	25
3.3	Computational Methods	32
3.4	Electron-Phonon Coupling	37
3.5	Spin-Peierls Distortion and Spin Wave Theory	39
4	On the Interplay of Different Degrees of Freedom	43
4.1	Crystal and Magnetic Structure	44
4.1.1	Crystal Structure of the Oxyhalides	44
4.1.2	The Spin-Peierls Transition in TiOCl	47
4.1.3	Antiferromagnetic Order in VOCl	49
4.2	Electronic Structure	53
4.2.1	Valence Density of States from Photoemission	53
4.2.2	Electronic Dimensionality	63
4.2.3	Hybridization and Multiplet Effects	73
4.2.4	Two-Spinon and Crystal-Field Excitations	80
4.2.5	Bandwidth-Controlled Closing of the Charge Gap	88
5	Doping a Mott Insulator	97
5.1	Intercalation of Oxyhalides with Alkali Metal Atoms	97
5.1.1	Core Level Studies - Chemical vs. Electronic Doping	99
5.1.2	Low-Energy Electronic Structure - Alloying and Spectral Weight Transfer	107
5.2	Efforts Towards Hole Doping	119

6 Summary and Outlook	123
Bibliography	125
List of Own Publications	141
Acknowledgment	143
Curriculum Vitae	145

List of Figures

2.1	Energetics of PES; schematic drawing of ARPES	4
2.2	ARPES on interacting and non-interacting systems	7
2.3	Universal curve; symmetry considerations for a d orbital	10
2.4	XAS process and possible relaxation channels	13
2.5	Fano lineshape; CIS and CFS measurement mode	17
2.6	dd excitation in RIXS; setup for (de-)polarized RIXS experiments	19
3.1	Hubbard band formation; Mott-Hubbard phase diagram	22
3.2	Bandwidth- and filling-dependent spectral function from DMFT	24
3.3	Energy levels due to crystal-field splitting	29
3.4	Ground state and excited states of a $3d^n$ system including hybridization	31
3.5	Lindhard function; Kohn anomaly; Peierls distortion	38
3.6	Spinon formation; dynamical structure factor $S(\mathbf{q}, \omega)$	41
4.1	Crystal structure of the oxyhalides	45
4.2	Magnetic susceptibility and heat capacity of TiOCl	47
4.3	XRD of TiOCl showing (in-)commensurate peaks	49
4.4	Magnetic susceptibility and heat capacity of VOCl	50
4.5	XRD, neutron diffraction, and magnetic configurations of VOCl	52
4.6	Valence bands of TiOCl and VOCl from XPS and UPS	54
4.7	Ti L edge ResPES on TiOCl	57
4.8	PolPES on TiOCl	58
4.9	DOS of TiOCl and VOCl from GGA and GGA+ U	60
4.10	Cluster-DMFT results	62
4.11	ARPES of the valence band of TiOCl	64
4.12	ARPES of Ti $3d$ structures of TiOCl	65
4.13	Ti $3d$ spectral weight along b from ARPES, DDMRG and VCA	66
4.14	Spectral function from LDA+VCA	67
4.15	Comparison of ARPES from TiOCl and TiOBr	69
4.16	ARPES of the valence band of VOCl	71
4.17	ARPES of V $3d$ structures of VOCl	72
4.18	O K edge absorption spectra of TiOCl	74
4.19	Exemplary Ti L edge simulations within LFM/CTM theory	77
4.20	Ti L edge absorption spectra of TiOCl	79
4.21	Temperature and photon energy dependence of RIXS spectra	82

4.22	Polarization dependence of RIXS spectra	85
4.23	Momentum dependence of RIXS spectra	86
4.24	Pressure-dependent transmittance of TiOCl	89
4.25	Pressure-dependent resistance and lattice parameters of TiOCl	90
4.26	Pressure-dependent XRD and lattice parameters of TiOCl	92
4.27	Optical conductivity of TiOBr under pressure	93
5.1	Ti $2p$, K $2p$ and Na $1s$ core levels of doped TiOCl	99
5.2	Voigt-fits of doped Ti $2p$; time development of x after evaporation	101
5.3	Development of x and x_{stoich} ; Ti $2p$ upon dosing from a Na ampule	102
5.4	Na $1s$ and O $1s$ core levels, and LEED of doped TiOCl	103
5.5	Polar catastrophe model; results from angle-dependent XPS	105
5.6	Valence band of K doped TiOCl	107
5.7	ResPES upon K doping	109
5.8	PolPES upon K doping	111
5.9	Molecular dynamics supercell and CFS upon doping	112
5.10	Site and orbital resolved Ti pDOS from GGA+ U upon doping	113
5.11	Alloy Hubbard model and spectral-weight transfer	115
5.12	EELS of Na doped TiOCl	117
5.13	XPS and UPS of K doped VOCl	118
5.14	XRD, XPS, and UPS results after exposure to acceptors	120

List of Tables

3.1	Relations between Slater-Condon, Racah, and Coulomb parameters . . .	27
3.2	Crystal-field levels in D_{4h} in different notations	30
4.1	Lattice and electronic parameters of TiOCl, TiOBr and VOCl	46
4.2	Ti $3d$ bandwidths and scaling behavior of TiOCl and TiOBr	70
4.3	Configurations and eigenenergies of two d electrons	75
4.4	Best-fit parameters from LFM calculations	78
4.5	Ti $3d$ crystal-field splittings of TiOCl	81

“No hay banda - There is no band!”

Master of Ceremonies at the Club *Silencio*, “Mulholland Drive” (2001)

1 Introduction

Condensed matter research as the driving force for technological development, especially in information technology and related fields, has experienced a shift from semiconductors towards a promising new class of materials and phenomena in the past 20 years. After the discovery of giant and colossal magnetoresistance (GMR/CMR) materials and the copper-oxide-based high- T_C superconductors (“cuprates”) in the late eighties, large efforts have been made in investigating the underlying physics of such strongly correlated electron systems. However, despite enormous research efforts no closed theory with predictive power comparable to that of conventional band theory for, e.g., semiconductors could be developed to date. The challenging point in these materials is the transition from a quantum description towards macroscopic properties. The intimate interplay of many degrees of freedom like spin, charge, lattice, and orbital, would require a quantum-mechanical approach to work in Hilbert spaces with dimensions that easily exceed the number of particles in the known universe. In addition, even if this could be handled, there are so-called “emergent phenomena” which obviously refute a description of the whole as the mere sum of its parts. In order to describe the experimental observations, scientists work on elaborate many-body models and theories, but the sheer complexity of the involved effects and the resulting phase diagrams seems an enormous task. The commonly accepted approach is thus to look for common properties of different materials, hoping to be able to condensate new knowledge from their behavior in one and the same experiment.

Focussing on the high- T_C superconductors such common features include partially filled transition metal $3d$ shells (which provide strong electronic correlations), confinement of the electronic structure to one or at most two dimensions, and the proximity to magnetically ordered and/or frustrated ground states. With this in mind, transition metal oxyhalides of the form TiOX ($X = \text{Cl}, \text{Br}$) and VOCl appear as interesting candidates: they have a $3d^1$ electronic configuration ($3d^2$ for VOCl) and are thus, by virtue of particle-hole symmetry, similar to copper oxides with $3d^9$ (i.e., one hole in that shell); they are built of essentially decoupled double layers which confine electronic interactions to two (and, as we will see, to a considerable degree even to one) dimensions; and they show extraordinary ground states in which frustrations seem to play a significant role.

To the solid state physicists best knowledge, spectroscopic techniques are very suitable to investigate strongly correlated electron systems, as low-energy excitations (i.e., quasiparticles) govern a plethora of a materials properties. Thus, in the course of this thesis, photoemission, x-ray absorption, infrared, and electron energy-loss spectroscopies have been used, complemented by measurements of thermodynamic properties like the

heat capacity and magnetic susceptibility, as well as resonant inelastic x-ray scattering. Combining these methods with theory and model calculations the electronic and magnetic properties of the oxyhalides can to a considerable degree be understood microscopically. It turns out that they can serve as model systems within the highly successful Mott-Hubbard description of strongly correlated system, yet have at the same time some unique and fascinating properties which pose critical tests to dimensionality-related spectroscopic observations as well as state-of-the-art computational methods. This becomes particularly evident when altering their behavior by doping, an important way of inducing metal-insulator transitions, e.g., in the cuprates, tentatively necessary to reach (unconventional) superconductivity.

Outline of the Thesis

This dissertation is structured as follows. In Chap. 2 an overview of the main experimental techniques is given. Chapter 3 introduces theoretical concepts used for the interpretation of the investigated phenomena, in particular the Mott metal-insulator transition upon doping, and discusses different computational methods applied for comparison to experiment. The properties of the oxyhalides inferred from a variety of theoretical and experimental investigations are then presented in Chap. 4, before the results from doping the crystals, which can be interpreted in terms of a so-called alloy Hubbard model, are discussed in Chap. 5. The thesis concludes with a short summary and outlook in Chap. 6.

2 Experimental Methods

2.1 Photoemission Spectroscopy

Besides its general importance for the study of basically all kinds of matter, technical development of light sources and analyzers for photoemission spectroscopy (PES) has profited tremendously from the advent of high-temperature cuprate superconductors in the 1980s [Damascelli03]. It is nowadays maybe the most widely used method to probe the (occupied) electronic structure of, in particular, complex solids, their surfaces and interfaces [Damascelli04, Reinert05]. Depending on the energy of the excitation source one distinguishes roughly between (soft-)x-ray photoemission spectroscopy (XPS; $100 \lesssim E_{ph} \lesssim 1500$ eV) and ultraviolet photoemission spectroscopy (UPS; $E_{ph} \lesssim 100$ eV).

Based on the photoelectric effect discovered by Hertz [Hertz87] due to which an electron is excited from a bound state into a free state in the vacuum, Einstein introduced the fundamental relationship between the energy of the incoming light ($h\nu$) and the kinetic energy of the outgoing electron (E_{kin}) [Einstein05]:

$$E_{kin} = h\nu - |E_{bind}| - \phi \quad . \quad (2.1)$$

Here, ϕ is the energy difference between the chemical potential μ and the vacuum level, known as the work function (typically of the order of 4 – 6 eV), and E_{bind} is the binding energy of the electron in the material under investigation with respect to μ . This formula, which follows from energy conservation, is the basic relationship of electron spectroscopy for chemical analysis (ESCA) [Siegbahn82], the simplest application of PES at least from the theoretical point of view. Using a monochromatic light source, Eq. 2.1 allows one to identify the constituting elements from the binding energies of their respective core-shell electrons. Figure 2.1(a) shows schematically the energy diagrams of a solid in the ground state, and the corresponding spectrum measured by PES. Core levels, which appear as delta peaks with an exact energy in the solid, are broadened in the spectrum due to the finite lifetime of the core hole by a Lorentzian envelope, which together with the Gaussian resolution broadening of the analyzer finally results in a Voigt profile (a convolution of a Gaussian and a Lorentzian). In metals, screening effects can lead to an asymmetry towards higher binding energies, phenomenologically described by the Doniach-Šunjić function [Doniach70], and an exact treatment of the peculiar lineshape in a given material would require even more complex theories [Hüfner99]. For the valence bands in the spectrum no canonical lineshape can be named, although of course both lifetime and resolution broadening apply.

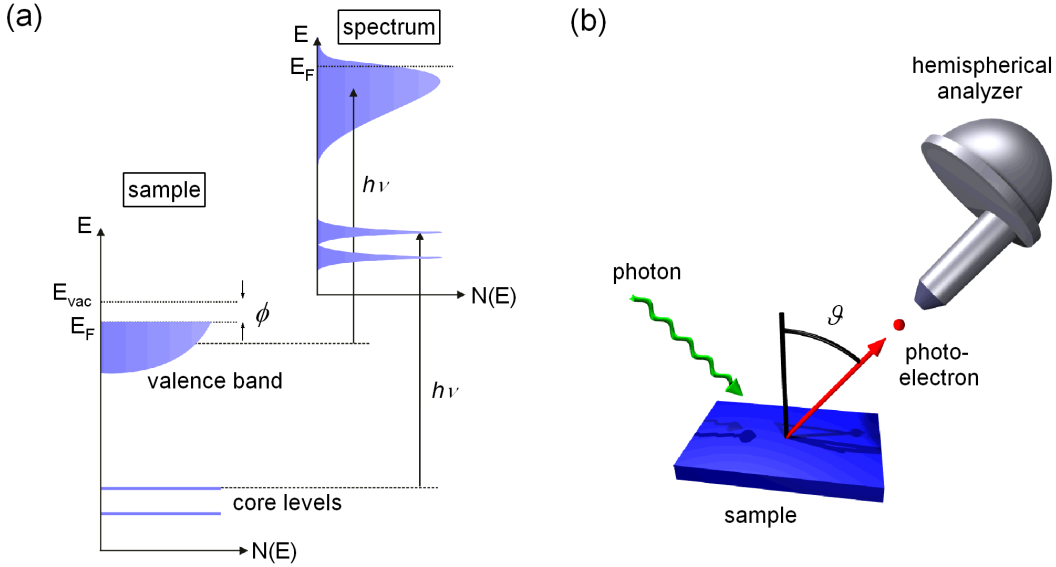


Figure 2.1: (a) Generalized view of the photoemission process in the single-particle picture at fixed $h\nu > E_{bind} + \phi$. On the left, the actual energetics of the sample are shown. The work function ϕ is indicated as the difference between the Fermi energy and the vacuum level. On the right, the resulting spectrum is shown, where all structures are lifetime- and resolution-broadened. At E_F the spectrum follows the Fermi distribution. Neglecting matrix-element effects, the intensity distribution in the spectrum corresponds to the occupied density of electronic states in the sample. (b) Incoming photon, sample, outgoing electron, and hemispherical PES analyzer, visualizing the experimental geometry in an ARPES experiment.

Additionally taking advantage of momentum conservation, the electronic dispersion $E(\mathbf{k})$ of valence-band electrons can be obtained from angle-resolved PES studies, abbreviated as ARPES. Looking at the vacuum momentum \mathbf{K} of the photoelectron parallel and perpendicular to the sample surface one finds the expressions

$$\begin{aligned} \hbar\mathbf{K}_{\parallel} &= \sqrt{2mE_{kin}} \sin \vartheta \\ \hbar\mathbf{K}_{\perp} &= \sqrt{2mE_{kin}} \cos \vartheta \quad . \end{aligned} \quad (2.2)$$

Here, ϑ is the angle between the surface normal and the direction under which the electron is detected [see Fig. 2.1(b)], and m is the electron mass. Neglecting momentum transfer from the photon to the electron (which is a valid approximation for excitation energies below ca. 100 eV, namely in the ARPES measurements presented in this thesis), the excitation corresponds to a vertical transition in a reduced zone scheme ($\mathbf{k}_f - \mathbf{k}_i = 0$; i denotes the initial state, f the final state), or equivalently, in a repeated zone scheme to a transition between points whose momenta differ only by an integer multiple of the reciprocal lattice vector $\mathbf{G} = \mathbf{k}_f - \mathbf{k}_i$. This latter view is most commonly applied

for the interpretation and displaying of ARPES data. In order to obtain $E(\mathbf{k})$ the detection angle ϑ is varied at fixed excitation energy. The connection between vacuum momentum \mathbf{K} and crystal momentum \mathbf{k} can be made by dividing the one-step process which photoemission actually is into three distinct steps, using the so-called three-step model [Berglund64]. It consists of

- (i) excitation of the electron from a bound initial to an unbound final state *within the solid*,
- (ii) transport of the electron to the sample surface, and
- (iii) transition into the vacuum.

The last step in a certain sense marks the point where crystal becomes vacuum momentum. One must note that while translational invariance in the normal direction is broken, this is obviously not the case parallel to the surface. Thus, the parallel momentum component (\mathbf{k}_{\parallel}) is conserved, in contrast to the normal component (\mathbf{k}_{\perp}). With this in mind, one can write

$$\hbar\mathbf{K}_{\parallel} = \hbar\mathbf{k}_{\parallel} = \sqrt{2mE_{\text{kin}}} \sin \vartheta \quad . \quad (2.3)$$

This already indicates that ARPES is particularly well-suited for low-dimensional systems (2D or 1D) where the variation of \mathbf{k}_{\perp} is negligible, e.g., the oxyhalides studied in this thesis. Of course, it is also possible to obtain information on \mathbf{k}_{\perp} , which requires to make further assumptions about the final-state dispersion. Using the free-electron result $E \propto \mathbf{k}^2$ it suffices to introduce a so-called “inner potential” V_0 , which leads to

$$\hbar\mathbf{k}_{\perp} = \sqrt{2m(E_{\text{kin}} \cos^2 \vartheta + V_0)} \quad . \quad (2.4)$$

However, since this was of no relevance for the studies presented here, the discussion of this issue shall not be elaborated on further.

More important is a thorough treatment of the photoemission process within a many-body picture. A central simplification which will be used along the way is the so-called “sudden approximation”. It assumes that the excitation of the electron happens instantaneously, such that the remaining $N - 1$ particle system cannot react to the emission process. The validity of the sudden approximation at low photon energies is currently debated for ARPES using laser sources [Koralek06], but has been accepted for the light sources which were used in the course of this thesis. As a starting point one uses Fermi’s Golden rule, which describes the transition rate between two states and is deduced from first-order perturbation theory:

$$w_{f,i}(h\nu) = \frac{2\pi}{\hbar} |\langle \Psi_f^N | H_{\text{int}} | \Psi_i^N \rangle|^2 \delta(E_f^N - E_i^N - h\nu) \quad . \quad (2.5)$$

Here, $E_i^N = E_i^{N-1} - E_B^{\mathbf{k}}$ and $E_f^N = E_f^{N-1} + E_{\text{kin}}$ are the energies¹ of the N -particle initial and final states Ψ_i^N and Ψ_f^N , respectively. $E_B^{\mathbf{k}}$ is the (negative) binding energy

¹This is the first occasion where the sudden approximation is used.

of an electron with (crystal) momentum \mathbf{k} , $E_{kin} = \hbar^2 \mathbf{k}^2 / 2m$ its final state free-particle kinetic energy, and $\langle \Psi_f^N | H_{int} | \Psi_i^N \rangle$ is the N -particle matrix element of an optical dipole transition. The perturbation operator H_{int} accounts for the interaction of the electrons with the electromagnetic field $\mathbf{A}(\mathbf{r}, t)$. In most relevant cases, photon densities of excitation sources are low enough for terms quadratic in $\mathbf{A}(\mathbf{r}, t)$ to be neglected, which yields with the momentum operator \mathbf{p} , for the interaction Hamiltonian:

$$H_{int} = \frac{e}{2mc} (\mathbf{A} \cdot \mathbf{p} + \mathbf{p} \cdot \mathbf{A}) \approx \frac{e}{mc} \mathbf{A} \cdot \mathbf{p} \quad . \quad (2.6)$$

The last equality implies the dipole approximation, i.e., $\nabla \cdot \mathbf{A} = 0$, which is fulfilled as long as the spatial variation of the light wave is small on the atomic scale (long-wavelength limit) and if one neglects particular surface effects [Miller96]. Equation 2.5 then tells us that (except for matrix element effects in the optical transition) from a measurement of the kinetic energy and momentum of the photoelectron it is possible to obtain the band structure $E(\mathbf{k})$ and, by integration over the Brillouin zone, the density of states (DOS).

To proceed further, note that the use of the sudden approximation allows for a factorization of the total final-state wave function into that of the photoelectron and the remaining $N - 1$ particle system, which is written in second quantization as

$$\Psi_f^N = A \varphi_f^{\mathbf{k}} \Psi_f^{N-1} = A c_{\mathbf{k}}^\dagger \Psi_f^{N-1} \quad , \quad (2.7)$$

where A is an antisymmetric operator to properly account for Pauli's exclusion principle, and $\varphi_f^{\mathbf{k}}$ is the single-particle wave function of the photoelectron, characterized by the quantum number(s) \mathbf{k} . The fermionic operator $c_{\mathbf{k}}^\dagger$ ($c_{\mathbf{k}}$) creates (annihilates) an electron with quantum numbers \mathbf{k} . In this notation, a one-particle interaction Hamiltonian can be written as

$$H_{int} = \sum_{i,j} \langle \varphi_i | H_{int} | \varphi_j \rangle c_i^\dagger c_j = \sum_{i,j} M_{i,j} c_i^\dagger c_j \quad . \quad (2.8)$$

Putting the factorization into Eq. 2.5 and assuming $T = 0$ (i.e., we have the ground state Ψ_0^N as the initial state) the photoemission intensity becomes

$$I(\mathbf{k}, E_{kin}) = \sum_{f,i} w_{f,i} \propto \sum_j |M_{\mathbf{k},j}|^2 \sum_f |\langle \Psi_f^{N-1} | c_i | \Psi_0^N \rangle|^2 \delta(E_{\mathbf{k}} + E_f^{N-1} - E_0^N - h\nu) \quad . \quad (2.9)$$

It is convenient to introduce the chemical potential $\mu = E_0^N - E_0^{N-1}$ and the abbreviation $\varepsilon = E_{\mathbf{k}} - h\nu - \mu$, allowing to rewrite this as

$$\begin{aligned} I(\mathbf{k}, E_{kin}) &= \frac{2\pi}{\hbar} \sum_j |M_{\mathbf{k},j}|^2 \sum_f |\langle \Psi_f^{N-1} | c_i | \Psi_0^N \rangle|^2 \delta(\varepsilon + E_f^{N-1} - E_0^{N-1}) \\ &= \frac{2\pi}{\hbar} \sum_j |M_{k,j}|^2 A^<(\mathbf{k}, \varepsilon). \end{aligned} \quad (2.10)$$

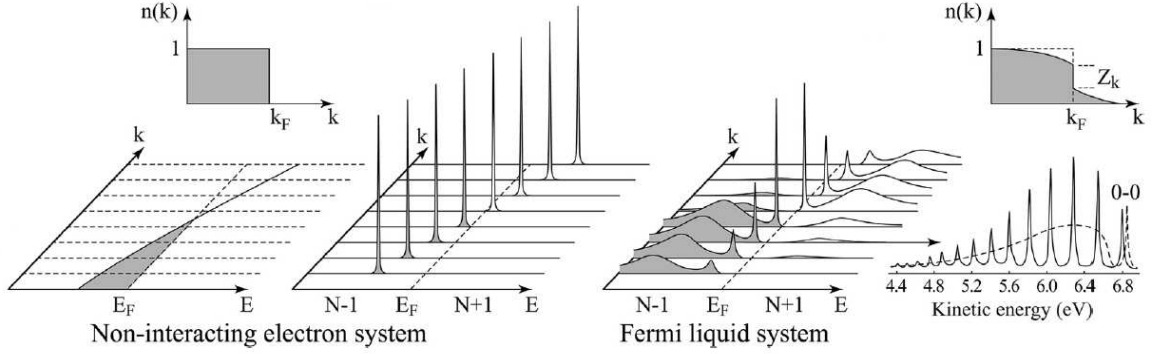


Figure 2.2: Momentum-resolved one-electron removal and addition spectra (from [Damascelli04]). (a) Non-interacting system, having a single band which crosses the Fermi energy at \mathbf{k}_F . (b) Interacting Fermi liquid system. The insets show momentum distribution curves for the two cases.

Here, a central quantity in the description of electron emission (and addition) spectra was introduced, namely the one-particle removal spectral function

$$\begin{aligned} A^<(\mathbf{k}, \varepsilon) &= \sum_f |\langle \Psi_f^{N-1} | c_i | \Psi_0^N \rangle|^2 \delta(\varepsilon + E_f^{N-1} - E_0^{N-1}) \\ &= -\frac{1}{\pi} \text{Im} G(\mathbf{k}, \varepsilon - i0^+) f(\varepsilon, T) \quad , \end{aligned} \quad (2.11)$$

with $f(\varepsilon, T)$ being the Fermi-Dirac distribution function. The simple connection to the imaginary part of the one-particle Green's function $G(\mathbf{k}, E)$ is a great advantage, since there are powerful computational methods to determine $G(\mathbf{k}, \varepsilon)$, which is given by

$$G(\mathbf{k}, \varepsilon) = \frac{1}{\varepsilon - \varepsilon(\mathbf{k}) - \Sigma_{\mathbf{k}}(\varepsilon)} \quad . \quad (2.12)$$

This Green's function contains all contributions from many-body processes in photoemission, like electron-electron or electron-phonon interaction, via the complex self-energy $\Sigma_{\mathbf{k}}(\varepsilon) = \text{Re} \Sigma_{\mathbf{k}}(\varepsilon) + i \text{Im} \Sigma_{\mathbf{k}}(\varepsilon)$. While its real part leads to a renormalization of energetic dispersions, the imaginary part describes the finite lifetime of excitations. Both can be directly obtained from ARPES measurements (or, more precisely, from spectra at constant energy, so-called momentum distribution curves). This shall be illustrated shortly on the example of a Fermi liquid (FL), also introducing the concept and influence of so-called quasiparticles.

Figure 2.2(a) shows the momentum-resolved one-electron removal and addition spectra, which directly reflect $A(\mathbf{k}, \varepsilon)$ for a non-interacting system, i.e., $\Sigma_{\mathbf{k}}(\varepsilon) = 0$. Since the eigenfunction is a single Slater determinant, both adding or removing an electron with momentum \mathbf{k} leads to a single eigenstate. Thus, the Green's function has only one pole and the spectral function corresponds to a single delta peak at the band energy $E_{\mathbf{k}}$,

which crosses the Fermi energy at \mathbf{k}_F . The momentum distribution $n(\mathbf{k})$ in this case gives a sudden drop at \mathbf{k}_F since the occupation numbers $n_{\mathbf{k}\sigma} = c_{\mathbf{k}\sigma}^\dagger c_{\mathbf{k}\sigma}$ are good quantum numbers [cf. inset of Fig. 2.2(a)]. However, switching on the interactions (which should be done adiabatically to ensure equilibrium to result in the FL description) reduces this drop to a finite discontinuity, characterized by the quasiparticle weight $0 < Z_{\mathbf{k}} < 1$ [cf. inset of Fig. 2.2(b)]. This weight is related to the self-energy by

$$Z_{\mathbf{k}} = \left(1 - \frac{\partial \text{Re} \Sigma}{\partial \varepsilon} \Big|_{E_{\mathbf{k},\text{FL}}} \right)^{-1}, \quad (2.13)$$

with $E_{\mathbf{k},\text{FL}} = Z_{\mathbf{k}} E_{\mathbf{k}}$ being the renormalized energy. Due to electron-electron correlations any particle added to the system has a finite probability for scattering with other particles out of the actual Bloch state, thus creating excited states with additional electron-hole pairs. The entity of all these states and the Bloch state are called quasiparticles and constitute the correlated Fermi sea. They can be envisaged as the actual particle (the electron) “dressed” by the excited states. This leads to an energy renormalization of the band(s) to $E_{\mathbf{k},\text{FL}}$ due to the enhanced band mass m^* of the quasiparticle, which is thus connected to the real part of $\Sigma_{\mathbf{k}}(\varepsilon)$. Its imaginary part is related to the intrinsic lifetime via $\Gamma_{\mathbf{k}} = Z_{\mathbf{k}} |\text{Im} \Sigma|$, which only now has become finite.

The resulting spectrum is shown in Fig. 2.2(b). The most obvious difference to the non-interacting case is that the spectral function now is formed by a peak at the lower binding-energy side which continuously sharpens towards \mathbf{k}_F , and a broad hump at higher binding energies. This latter part is called “incoherent” and represents the electron-hole pairs dressing the electron, while the former is called the “coherent” quasiparticle peak. The fact that the coherent peak becomes sharper and gains weight upon approaching \mathbf{k}_F is inherent to the FL picture that was applied.

To conclude, the fundamental sum rules for the spectral function are summarized:

$$\int_{-\infty}^{+\infty} A(\mathbf{k}, \varepsilon) d\varepsilon = \int_{-\infty}^{+\infty} A_{\text{coherent}}(\mathbf{k}, \varepsilon) d\varepsilon + \int_{-\infty}^{+\infty} A_{\text{incoherent}}(\mathbf{k}, \varepsilon) d\varepsilon = 1 \quad (2.14)$$

$$\int_{-\infty}^{+\infty} A_{\text{coherent}}(\mathbf{k}, \varepsilon) d\varepsilon = Z_{\mathbf{k}} \quad (2.15)$$

$$\int_{-\infty}^{+\infty} A_{\text{incoherent}}(\mathbf{k}, \varepsilon) d\varepsilon = 1 - Z_{\mathbf{k}} \quad (2.16)$$

In the case of ARPES, where only the electron-addition part of $A(\mathbf{k}, \varepsilon)$ is measured, the Fermi-Dirac distribution function ensures the correct weight:

$$\int_{-\infty}^{+\infty} A(\mathbf{k}, \varepsilon) f(\varepsilon, T) d\varepsilon = n(\mathbf{k}) \quad (2.17)$$

Some Aspects of Quantitative PES Analysis

An important aspect inherent to PES is that the detected electrons stem only from a very small region close to the sample surface, due to the electrons' short inelastic mean free path (IMFP) λ_e caused by scattering processes with other electrons. Figure 2.3(a) shows λ_e as a function of their kinetic energy, the so-called “universal curve” [Seah79]. By virtue of its connection to the cross-section for inelastic scattering, λ_e depends on the material-specific dielectric function $\epsilon(q, \omega)$. Interestingly, Seah *et al.* find that the functional form

$$\lambda_e(h\nu)[\text{nm}] \approx a(h\nu)^{-2} + b(h\nu)^{0.5} \quad , \quad (2.18)$$

with $a = 143$ and $b = 0.054$ for elements, $a = 641$ and $b = 0.096$ for inorganic solids, is a very good approximation for basically all elements and solids. This is because the dominant inelastic scattering processes are due to plasmon excitations, i.e., collective oscillations of the entire electron gas against the positively charged ion background. The plasmon frequency is proportional to \sqrt{n} (n being the electron density) and thus varies only slightly between different materials, leading to the observed universal behavior. For typical laboratory light sources (He I $_{\alpha}$; Al K $_{\alpha}$), λ_e is of the order of 1–3 nm. This fact (among other influences) necessitates an atomically clean sample surface without, e.g., oxide overlayers, as well as ultra-high vacuum to perform meaningful PES experiments. On the other hand, one can make use of this to do depth profiling of the sample.

Assuming exponential damping due to the scattering processes, the probability for an electron to reach the surface without suffering an energy loss is given by

$$P(z) \propto \exp\left(\frac{-z}{\lambda_e \cos \vartheta}\right) \quad , \quad (2.19)$$

with z being the vertical distance between the ion at which the electron was created and the surface, and ϑ the angle between the surface normal and the direction of detection [cf. Fig. 2.1(b)]. The distance $z = 3\lambda_e \cos \vartheta$ is defined as the *information depth*, since 95% of the detected electrons come from within this depth. For example, varying ϑ from 0° (normal emission, NE) to 70° (grazing emission, GE), $P(z)$ is reduced by 65%, such that one expects significant contributions to the spectrum only from ions close to or at the surface on a scale of at most a few atomic layers. This is used especially in Sec. 5.1.1.

It turns out that especially for large detection angles ϑ the influence of elastic scattering processes on the effective probing depth becomes significant [Cumpson97]. For a detailed analysis it is thus useful to define the attenuation length λ_{AL} which is closely related to the IMFP but encompasses also elastic contributions. Based on Monte-Carlo simulations, Cumpson *et al.* found the following functional form [Cumpson97]:

$$\lambda_{AL}(h\nu)[\text{nm}] \approx 0.316c^{3/2} \left(\frac{h\nu}{Z^{0.45} (\ln \frac{h\nu}{27} + 3)} + 4 \right) \quad , \quad (2.20)$$

where c is the lattice parameter, and Z is the atomic number of the matrix. Thus, this formula can be adapted more flexibly to a specific solid than Eq. 2.18.

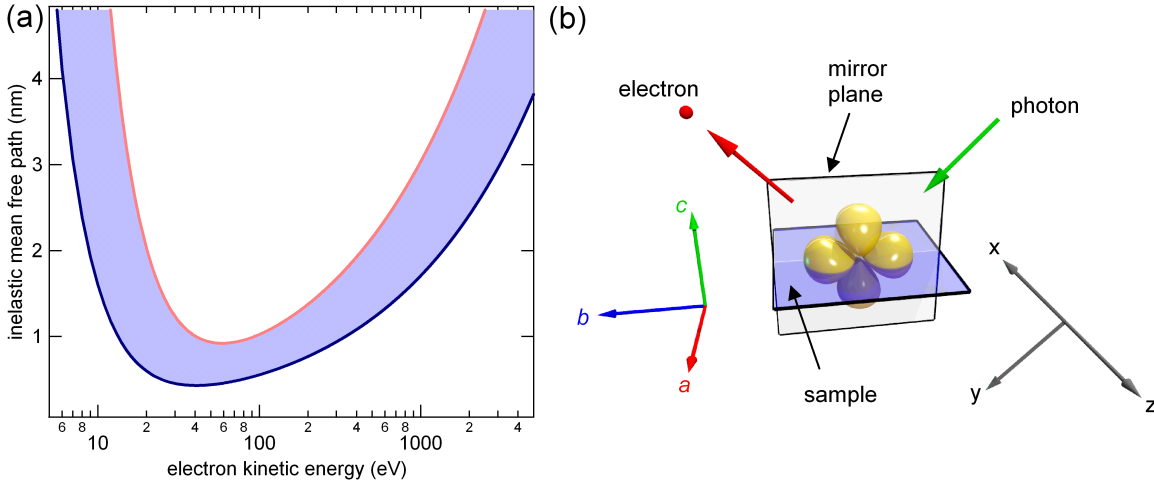


Figure 2.3: (a) “Universal curve” of the inelastic mean free path λ_e vs. electron kinetic energies, represented by the range covered by the empirical function of Eq. 2.18 with parameters for elements (blue curve, lower boundary) and inorganic solids (red curve, upper boundary). (b) $d_{x^2-y^2}$ orbital, lying in the mirror plane spanned by the incoming photon and the ejected photoelectron (in this case corresponding to the bc crystal plane of TiOCl).

Another spurious effect of the processes just described is a secondary background due to the inelastically scattered electrons, which for a quantitative analysis of PES data has to be corrected for. A standard method which will be used in the course of this thesis was introduced by Shirley [Shirley72]. He assumed that the background at given energy E is proportional to the total number of electrons at higher kinetic energies $E' > E$, implying a constant loss function by which the intrinsic core-level spectrum is convoluted. Since the measured spectrum $M(E)$ thus consists of a sum of the intrinsic spectrum $I(E)$ and the inelastically scattered part, $I(E)$ can be obtained by an iterative procedure using $M(E)$ as an initial guess for the intrinsic spectrum, according to:

$$I^{(n+1)}(E) = M(E) - \alpha_n \int_E^{E_2} I^n(E') dE', \quad \text{with} \quad \alpha_n = \frac{M(E_1)}{\int_{E_1}^{E_2} I^n(E') dE'} \quad . \quad (2.21)$$

The only free parameter α_n gives the fraction of background intensity at the low kinetic-energy side. In most practical cases, already a few iteration steps (≤ 5) yield well-converged results.

Once it has been taken care of the background, a (semi-)quantitative stoichiometric analysis of the sample is possible, at least for relative amounts of the constituting elements. However, a considerable number of factors have to be accounted for in such an analysis. First of all, the photoionization cross-section σ_{nl} has to be named as an element-specific quantity. Here, nl are the quantum numbers of the respective subshell. The current of photoelectrons is proportional to the cross-section, which for unpolarized

light is given by the equation [Trzhaskovskaya01]

$$\begin{aligned} \frac{d\sigma_{nl}}{d\Omega} &= \frac{\sigma_{nl}}{4\pi} \left[1 - \frac{\beta_{nl}}{2} P_2(\cos \gamma) + \left(\delta + \frac{\eta}{2} \sin^2 \gamma \right) \cdot \cos \gamma \right] \\ &\approx \frac{\sigma_{nl}}{4\pi} \left[1 - \frac{\beta_{nl}}{2} P_2(\cos \gamma) \right] \quad , \end{aligned} \quad (2.22)$$

with the last equality reflecting the dipole approximation. $P_2(\cos \gamma) = 1/2(3 \cos^2 \gamma - 1)$ is the second-order Legendre polynomial, Ω is a solid angle, β_{nl} is the energy-dependent dipolar and δ, η are higher-order asymmetry parameters. These account for the shape of the absorbing orbital (s, p, d etc.). The parameter γ is the angle between the vectors of photon and electron propagation, which in our laboratory setup for XPS is $\gamma = 54.7^\circ$. For this special angle, $P_2(\cos \gamma) = 0$, which eliminates the β -dependence of the cross-section. For linearly polarized light, Eq. 2.22 changes slightly to

$$\begin{aligned} \frac{d\sigma_{nl}}{d\Omega} &= \frac{\sigma_{nl}}{4\pi} [1 + \beta_{nl} P_2(\cos \theta) + (\delta + \eta \cdot \cos^2 \theta) \cdot \sin \theta \cos \varphi] \\ &\approx \frac{\sigma_{nl}}{4\pi} [1 + \beta_{nl} P_2(\cos \theta)] \quad . \end{aligned} \quad (2.23)$$

In this case, θ is the angle between the photoelectron propagation and the photon polarization, and φ the angle between photoelectron propagation and the plane spanned by the photon direction and its polarization vector. $d\sigma_{nl}/d\Omega$ obtains an energy dependence by virtue of the energy-dependent asymmetry parameters, and it must be noted that large uncertainties are inherent to $\sigma(E)$, for which calculated values are available from tables, but only for single atoms and not the specific situation in a solid [Yeh85, Trzhaskovskaya01].

Apart from this, the hemispherical photoelectron analyzer can contribute with essentially two factors, the detector sensitivity $D(E)$ and the transmission function $T(E)$. While the former dependence can easily be eliminated by measuring with constant pass energy (the energy of electrons that can traverse the analyzer and reach the detector) and varying the retardation potential for the photoelectrons (which was done in all measurements presented in this thesis), one has to know at least the approximated behavior of the transmission function. From phase-space arguments the canonical energy dependence should be such that $T(E) \propto E_{kin}^{-1}$, which was shown to be the case for the analyzer used for the XPS measurements (Omicron EA 125) and the relevant kinetic and pass energy ranges [Ruffieux00]. Should there be deviations from this simple relation, $T(E)$ has to be determined experimentally or by ray-tracing simulations [Wicks09].

Overall, one arrives at the following relation for the relative amounts of two elemental species in a sample:

$$\begin{aligned} x_{stoich} &= \frac{N_A}{N_B} = \frac{A_A \cdot \sigma_B(E_{ph}) \cdot T(E_{kin,B}) \cdot \lambda(E_{kin,B})}{A_B \cdot \sigma_A(E_{ph}) \cdot T(E_{kin,A}) \cdot \lambda(E_{kin,A})} \\ &\approx \frac{A_A \cdot \sigma_B(E_{ph}) \cdot \sqrt{E_{kin,A}}}{A_B \cdot \sigma_A(E_{ph}) \cdot \sqrt{E_{kin,B}}} \quad , \end{aligned} \quad (2.24)$$

where A_i signifies the area covered by a given core-level peak (i.e., the spectral weight). In order to obtain the last equation the canonical energy dependencies $\lambda_e(E) \propto \sqrt{E_{kin}}$ and $T(E) \propto E_{kin}^{-1}$ were used.

Exploiting Matrix Elements Using Polarized Light

Using the form of the interaction Hamiltonian in the dipole approximation (Eq. 2.6) together with the commutator relation between the unperturbed Hamiltonian H_0 and the position operator \mathbf{r} to express the momentum operator \mathbf{p} , one obtains for the matrix element introduced above:

$$M_{f,i}^{\mathbf{k}} = \frac{e}{mc} \langle \varphi_f^{\mathbf{k}} | \mathbf{A} \cdot \mathbf{p} | \varphi_i^{\mathbf{k}} \rangle \propto \langle \varphi_f^{\mathbf{k}} | \varepsilon \cdot \mathbf{r} | \varphi_i^{\mathbf{k}} \rangle \quad , \quad (2.25)$$

where ε is the unit vector along the vector potential \mathbf{A} (polarization vector). If the experimental setup is chosen in such a way that the incoming electron and the outgoing photon span a mirror plane of the sample, the possibility to enhance contributions of certain orbitals follows from simple symmetry considerations. The photoelectron is nothing but a plane wave which has even parity (“+”) with respect to any (mirror) plane. Using linearly polarized light the parity of the dot product $\varepsilon \cdot \mathbf{r}$ can be switched between even ($\varepsilon = \varepsilon_{para}$, i.e., parallel to the mirror plane) and odd ($\varepsilon = \varepsilon_{perp}$, i.e., perpendicular to the mirror plane). Figure 2.3(b) shows a $d_{x^2-y^2}$ orbital which has even parity with respect to the indicated mirror plane, and in this case it follows for the matrix element:

$$\langle \varphi_f^{\mathbf{k}} | \varepsilon \cdot \mathbf{r} | \varphi_i^{\mathbf{k}} \rangle = \begin{cases} \langle + | + | + \rangle \neq 0 & \text{if } \varepsilon = \varepsilon_{para} \quad , \\ \langle + | - | + \rangle = 0 & \text{if } \varepsilon = \varepsilon_{perp} \quad . \end{cases} \quad (2.26)$$

So, if another relevant orbital has odd parity with respect to the same mirror plane, it is possible to distinguish the respective contributions at a given energy in the photoemission spectrum by switching the polarization.

2.2 X-Ray Absorption Spectroscopy

Judging by how widely it is used, the experimental method playing the role of PES for the unoccupied electronic structure is probably x-ray absorption spectroscopy (XAS). Similar to PES, this technique has matured over the last twenty years in terms of instrumentation thanks to major improvements in synchrotron technologies. Again, this was to a considerable degree connected to the interest in cuprate superconductors [Fink94, de Groot08]. The signal one obtains is governed by the energy- and material-dependent variation of the absorption coefficient μ of the sample. In measurements, the excitation energy is varied across an absorption edge (typically K , $L_{2,3}$, or $M_{4,5}$ edges for excitation from $1s$, $2p$, or $3p$ core levels, respectively) in such a way that an electron

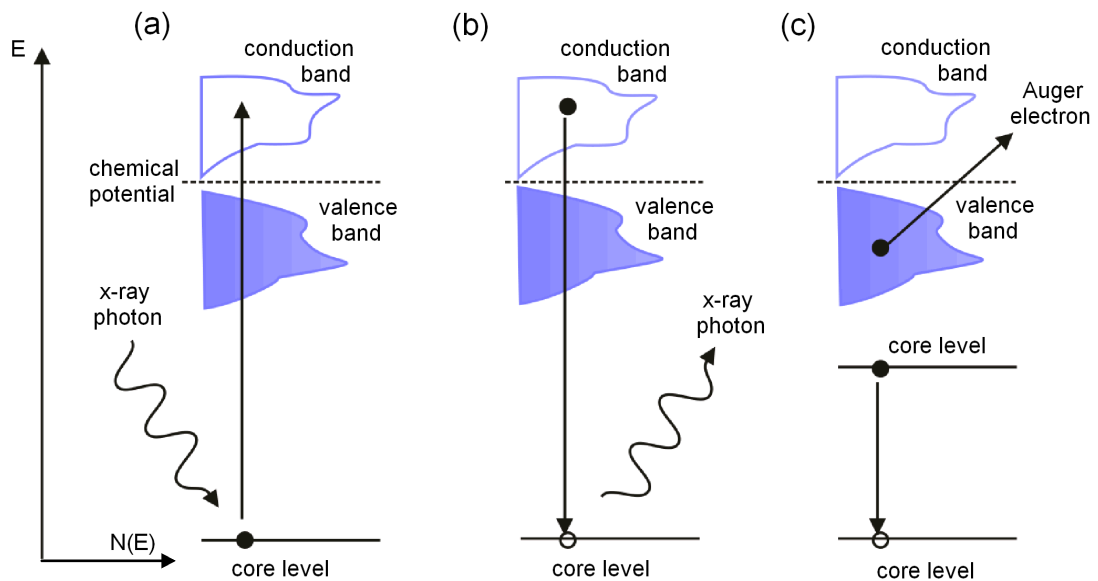


Figure 2.4: Generalized view of the x-ray absorption process in the single-particle picture. Full circles denote an electron, open circles a hole. (a) An electron from a core shell is excited directly into bound unoccupied states just above the chemical potential. (b,c) Examples of possible relaxation channels for the XAS final state: (b) Resonant x-ray fluorescence. (c) Auger electron emission, involving an electron from a second core shell.

is excited from a core level into bound, yet unoccupied states above the chemical potential, resulting in an excited state as shown in Fig. 2.4(a). It is customary to distinguish between two regimes: extended x-ray absorption fine structure (EXAFS), corresponding to energies starting from several 10 eV above the absorption edge, and x-ray absorption near-edge spectroscopy (XANES) for energies closer to the absorption edge. Both are element- and site-specific, but while the former yields mainly information on the geometrical surroundings of a given ion, XANES contains more detailed information on the absorbing ion's chemical state and environment, as well as (with some restrictions hinted at below) on the partial unoccupied electronic DOS [Koningsberger88]. XANES is the method that was applied in the course of this thesis.

Experimentally, there are several ways by which one can record the variation of μ , since there are various decay channels available to refill the core hole after the absorption process, which are visualized in Fig. 2.4(b) and (c). To begin with, it should be noted that the attenuation lengths of x-rays, defined analogously to the mean free path of photoelectrons discussed previously, are of the order of several hundred nanometers [Henke93,cxro10]. Thus, obtaining an absorption signal in transmission geometry is only

possible for very thin samples and/or very high photon energies.¹ Nevertheless, since de-excitation can lead to the emission of x-ray photons it is possible to become truly bulk-sensitive (especially compared to PES) by measuring these photons, which is the so-called fluorescence yield (FY) mode. Unfortunately, analysis of such data can sometimes be hindered by self-absorption, i.e., multiple absorption and emission of photons on their way to the sample surface. Other measurement modes rely on decay processes like, e.g., emission of photoelectrons (direct emission) and Auger electrons (secondary emission), where the latter are created if the relaxation energy of filling the core hole leads to emission of an electron. Its kinetic energy is given by the binding energy difference between the core hole and the de-excited electron which fills it [cf. Fig. 2.4(c)]. This offers the possibility for two kinds of measurements: using a photoelectron analyzer one can record the Auger electrons at fixed analyzer energy, which is called partial electron yield (PEY). Alternatively, by grounding the sample, one can record the current necessary to refill the (total amount of) emitted electrons (typically of the order of nA), which is called total electron yield (TEY) mode. Since the latter is (mostly) governed both by direct photoemission and Auger processes it is of course also possible to use photoelectron analyzers. Both PEY and TEY spectra might be adulterated if the sample is insulating and thus exhibits charging, and information is only available from atoms rather close to the surface.² Since count rates are superior to FY detection, these modes are widely used, especially TEY.

Turning to a theoretical description of XAS, the local nature of the core-electron excitation (absorption happens at a given site) has several implications. Firstly, as the initial-state core level has no overlap with neighboring ions no momentum information is available. Secondly, there is Coulomb attraction between excited electron and induced core hole, leading to excitonic effects which can become significant in some cases. Thus, one has to be aware of such effects when discussing XAS spectra.

In analogy to Eqs. 2.5 and 2.9, and according to Fermi's Golden Rule, the absorption coefficient μ is given by [Fink94]:

$$\mu(h\nu) \propto \sum_{f,i} |\langle \Psi_f^N | H_{int} | \Psi_i^N \rangle|^2 \delta(E_f^N - E_i^N - h\nu) \quad . \quad (2.27)$$

Since the dipole approximation is valid for the rather low photon energies considered here ($400 \lesssim E_{photon} \lesssim 700$ eV) the interaction Hamiltonian H_{int} contains again the (single-particle) matrix element of Eq. 2.25. This implies a polarization dependence comparable to the one described in the previous section, since $\mu \propto \sum_{f,i} \langle \varphi_f^{\mathbf{k}} | \varepsilon \cdot \mathbf{r} | \varphi_i^{\mathbf{k}} \rangle$. Recalling the dipole selection rules $\Delta l = \pm 1, \Delta m_s = 0, \Delta j = 0, \pm 1$ for a single electron, one realizes that the only allowed transitions for the cases of interest here are from occupied s to unoccupied p orbitals (K edge) and from occupied p to unoccupied d (and s) orbitals (L edge). The property one measures is different for the two edges, however, which shall

¹For example within electron energy-loss spectrometer, cf. Sec. 4.2.3.

²Nevertheless, the information depth is about an order of magnitude larger than in PES.

be discussed in the following for the relevant case of XAS on Ti^{3+} as a typical transition metal ion. Both its $1s$ and $2p$ core shells are fully occupied, so K -edge absorption is not possible *per se*. Nevertheless, by virtue of hybridization the O $2p$ DOS reflects the Ti $3d$ DOS, and from comparison to DOS calculations this method has proven to be very successful for many transition metal oxides and related systems [de Groot89, de Groot93].

While one naively could expect that excitations directly at the Ti^{3+} ion (namely at the L edge) give just as direct information on the $3d$ DOS, this turns out not to be the case for a plethora of reasons. Indeed, effects on the spectra are rather prominent. A major example becoming important is that of configuration interaction, as will be seen in Sec. 4.2.3. For the moment, it shall be sufficient to state that the absorption process in the simplest approximation corresponds to an excitation $2p^6 3d^1 \rightarrow 2p^5 3d^2$, i.e., both the $2p$ and the $3d$ shell have finite orbital and spin momenta in the final state. Whenever more than one open shell is present at a given atom there is additional coupling between these shells, governed mostly by the electron-electron repulsion (H_{e-e}) and spin-orbit coupling (H_{ls}) terms in the total Hamiltonian:

$$\begin{aligned} H_{atom} &= H_{kin} + H_{e-p} + H_{e-e} + H_{ls} \\ &= H_{average} + \sum_{pairs} \frac{e^2}{r_{ij}} + \sum_i \zeta(\mathbf{r}_i) l_i \cdot s_i \quad . \end{aligned} \quad (2.28)$$

H_{kin} and H_{e-p} are the one-electron kinetic and electron-proton Coulomb energy, respectively. H_{e-e} can be parametrized with different Coulomb integrals, the so-called Slater integrals (see also Sec. 3.2). $\zeta(\mathbf{r}_i)$ is the spin-orbit coupling constant, and l_i (s_i) is the orbital (spin) angular momentum. Since there are many possible combinations of these quantum numbers (45 in the present example) the absorption spectrum will be composed of these many different so-called multiplets, instead of reflecting the unoccupied DOS. Additionally, the core hole and the excited electron are both localized at the same site, in contrast to O K edge absorption. Thus, their mutual attraction becomes significant, and they can form a (bound) exciton which translates into changes to the observed final-state energies.

2.3 Resonantly Enhanced Processes

Using photon energies which correspond to absorption edges of the sample it is possible to induce resonantly enhanced processes. One advantage is that this usually provides significantly better count rates than off-resonance measurements. Even more important, however, additional information can be extracted, because the fact that the XAS final state now corresponds to an intermediate state makes the measurements element-specific. The two methods used here are resonant photoemission spectroscopy (ResPES) and resonant inelastic x-ray scattering (RIXS), respectively. Due to different final states, ResPES maps occupied electronic states, while RIXS provides access to different kinds of low-energy excitations.

2.3.1 Resonant Photoemission Spectroscopy

In the case of ResPES, the interference which leads to resonance behavior comes from the fact that an Auger decay after (x-ray) absorption renders the system in the same final state as the direct photoemission process. For example, in the case of excitation at the $2p$ edge of a transition metal ion with n electrons ($n \leq 9$) in the $3d$ shell:

$$2p^6 3d^n \rightarrow 2p^6 3d^{n-1} \epsilon \quad (\text{direct PES}) \quad (2.29)$$

$$2p^6 3d^n \rightarrow 2p^5 3d^{n+1} \rightarrow 2p^6 3d^{n-1} \epsilon \quad (\text{Auger decay}) \quad ; \quad (2.30)$$

ϵ is the ejected photoelectron. The generally accepted theoretical approach applicable to describe the resulting energy-dependent photocurrent was introduced by Fano [Fano61]. His derivation of the spectrum for a discrete state (the intermediate state of Eq. 2.30) coupled to a continuum of (final) states is shortly outlined in the following [Allen92].

Denote the discrete state with wave function ϕ (energy E_ϕ), the continuum states with ψ_E (energy E_ψ), and the Auger matrix elements with V_E . One needs to find the matrix element of the transition from the ground state Φ_g to the final state Ψ_E , which is composed of the discrete and the continuum state(s) according to

$$\Psi_E = a_E \phi + \int dE' b_{EE'} \psi_{E'} \quad . \quad (2.31)$$

It turns out that the discrete state imposes a Lorentzian lineshape of half-width $\pi|V_E|^2$ on the transition $\Phi_g \rightarrow \Psi_E$, as the parameter a_E is given by

$$|a_E|^2 = \frac{|V_E|^2}{[E - E_\phi - F(E)]^2 + \pi^2 |V_E|^4} \quad . \quad (2.32)$$

Here, $F(E)$ is a self-energy which shifts the resonance away from the energy of the discrete state, E_ϕ . An expression for the parameter $b_{EE'}$ can be found in [Fano61] but need not be given here. Instead, the relative strength of interference effects can be evaluated from the ratio f of the transition probability for the final state Ψ_E to that for a pure continuum without discrete states, $\tilde{\Psi}_E$:

$$f = \frac{|\langle \Psi_E | T | \Phi_g \rangle|^2}{|\langle \tilde{\Psi}_E | T | \Phi_g \rangle|^2} = \frac{(q + \varepsilon)^2}{1 + \varepsilon^2} = 1 + \frac{q^2 - 1 + 2q\varepsilon}{1 + \varepsilon^2} \quad . \quad (2.33)$$

T is the transition operator, and

$$\varepsilon = \frac{E - E_\phi - F(E)}{\pi |V_E|^2} \quad (2.34)$$

is a reduced energy variable. Finally, the lineshape parameter q is given by

$$q = \frac{\langle \Psi_E | T | \Phi_g \rangle}{\pi V_E^* \langle \tilde{\Psi}_E | T | \Phi_g \rangle} \quad , \quad (2.35)$$

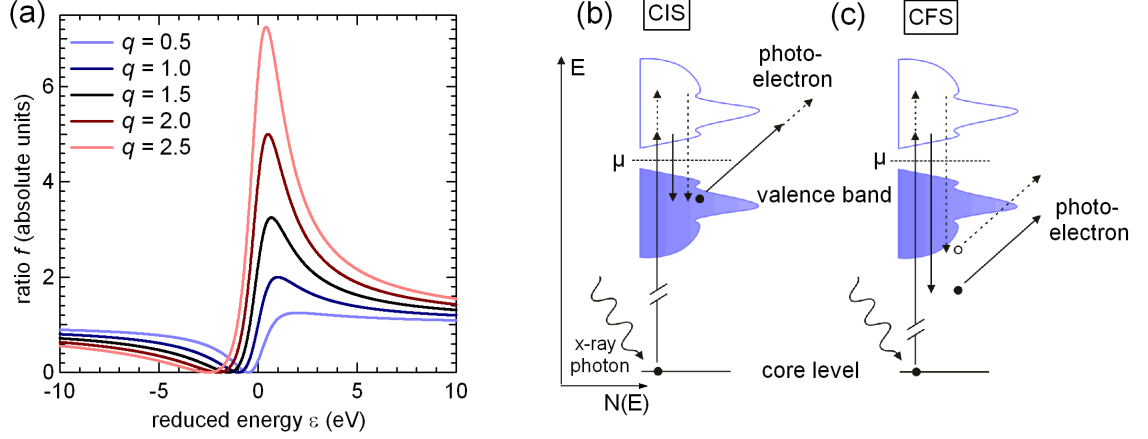


Figure 2.5: (a) Behavior of the ratio f (Eq. 2.33) for different values of q . (b,c) Possible measurement modes in ResPES. Up-arrows denote the excitation energy, down arrows the analyzer (i.e., photoelectron kinetic) energy. Solid and dotted arrows are to visualize two subsequent measurements done to obtain a spectrum. (b) Constant initial state (CIS). $h\nu$ ($\hat{=}$ length of up-arrow) and E_{kin} ($\hat{=}$ length of photoelectron-arrow) are varied parallel such that only electrons from a fixed binding energy are detected. In case of a resonating structure, the intensity modulation corresponds to the Fano behavior shown in panel (a). (c) Constant final state (CFS). $h\nu$ is varied, and E_{kin} is fixed at a value in the inelastic, featureless tail of the spectrum. The photoelectron intensity distribution thus corresponds to the absorption spectrum.

where Ψ_E is any state of the form of Eq. 2.31. The resulting intensity modulation of the resonating excitation is shown in Fig. 2.5(a) for different values of q . Below and above the resonance energy (corresponding to $\varepsilon = 0$) the wave function coefficients a_E and $b_{EE'}$ are such that the components of Eq. 2.31 interfere with opposite phases, which leads to the observed asymmetry. It should be noted that the perfect cancellation before the resonance [$f(\varepsilon \leq 0) = 0$] is found only for the simple case of one discrete state and one continuum considered here.

There are two cases in which resonant enhancement in ResPES does not take place. Firstly, since it is an element-specific probe, a structure in a spectrum only resonates if it is composed of orbitals from the element belonging to the absorption edge at which the measurement is performed. Secondly, if the (constant) direct photoemission amplitude A_{PES} and the intensity-modulated amplitude of the Auger process A_{Auger} are not of the same order of magnitude, resonance effects will also be suppressed. This can be seen from the fact that the total photocurrent is the squared sum of these two contributions, which leads to a phase-dependent crossing term:

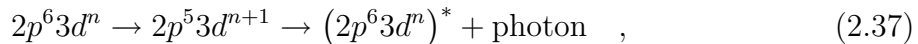
$$j_P = |A_{PES} + A_{Auger}|^2 = A_{PES}^2 + A_{Auger}^2 + A_{PES}A_{Auger} \cos(\varphi_{PES} - \varphi_{Auger}) \quad . \quad (2.36)$$

Since A_{PES}^2 and A_{Auger}^2 are constant, the resonance comes only from the crossing term, which thus must not be small compared to the other two.

A direct way to observe these effects is the so-called constant initial state (CIS) measurement mode, illustrated in Fig. 2.5(b). Here, one varies the photon energy $h\nu$ parallel to the kinetic energy E_{kin} at which the electron analyzer detects the photoelectrons, i.e., one measures the intensity at constant binding energy. If the structure at this binding energy resonates, its intensity follows the Fano behavior shown in Fig. 2.5(a). Another mode often used in ResPES experiments is the so-called constant final state (CFS) mode [see Fig. 2.5(c)]. In this case, one varies $h\nu$ while the detected electron kinetic energy is fixed at low values in the inelastic background. One thus measures essentially the photoabsorption spectrum, i.e., the same distribution as in XAS.

2.3.2 Resonant Inelastic X-Ray Scattering

In analogy to the previous section, the RIXS process at the transition metal L edge corresponds to excitation and de-excitation according to



i.e., it is charge-conserving, but can leave the system in an excited state. Figure 2.6(a) shows a local crystal-field excited state (dd excitation) as an example, but one has access to all kinds of excitations, the most important being phonons, spinons, magnons, and charge-transfer excitations. The foundation for a theoretical description of x-ray scattering processes was laid by Kramers and Heisenberg [Kramers25], which in the dipole approximation results in the Kramers-Heisenberg formula for the RIXS spectrum [Kotani05]:

$$I_i(\omega_1, \omega_2) \propto \sum_f \left| \sum_n \frac{\langle f | T | n \rangle \langle n | T | i \rangle}{E_n - E_i - \omega_1 + i\Gamma_n} \right|^2 \times \frac{\Gamma_f / \pi}{(E_i + \omega_1 - E_f - \omega_2)^2 + \Gamma_f^2} \quad . \quad (2.38)$$

Here, $|i\rangle$, $|n\rangle$ and $|f\rangle$ are the initial, intermediate and final states with energies E_i , E_n and E_f , respectively, T is the dipole operator for the $2p \leftrightarrow 3d$ transition, Γ_n (Γ_f) the core-hole lifetime in the intermediate (final) state, and ω_1 (ω_2) the energy of the incoming (outgoing) photon. In most cases, both Γ_n and Γ_f can be taken to be constant for all possible intermediate and final states, respectively [Kotani01].

In contrast to ResPES, the resonance behavior is governed by interference effects from the two dipole transitions in Eq. 2.38, instead of interference of two different emission processes. Although dipole selection rules still apply and the initial and final state thus have the same parity, the complicated multiplet splitting in the intermediate state of L edge RIXS with initial state configurations $3d^n$, $n \geq 1$, inhibits a straightforward analysis of the polarization dependence as it can be done, e.g., in normal PES. On the other hand, the strong multiplet mixing gives finite weight to transitions which are dipole-forbidden in optical absorption measurements. In particular, the dd excitation in Fig. 2.6(a), having $\Delta l = 0$, can be observed only in special cases in optical absorption,

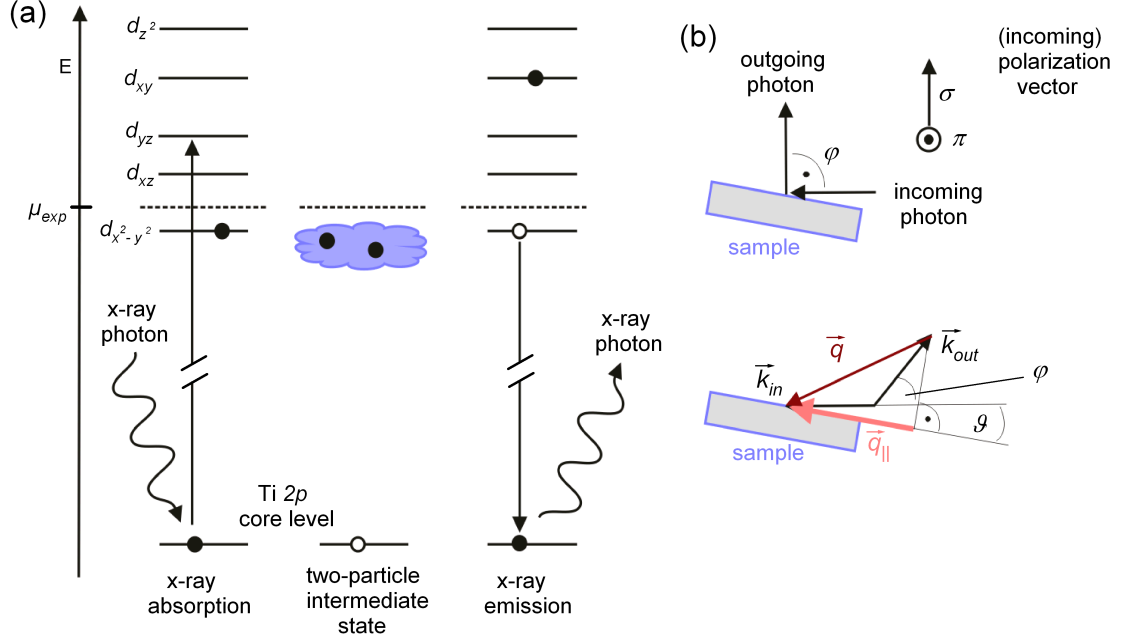


Figure 2.6: (a) One possible dd excitation in RIXS on TiOCl ($3d^1$ initial state). The intermediate state is given by a two-particle wave function, and the one-particle orbitals have no meaning in this case. In the final (excited) state, the d electron occupies a different orbital than in the initial state. (b) Top: Scattering geometry in RIXS allowing for polarized and depolarized measurements. The incident and emitted photons span the scattering plane, the angle between them is $\varphi = 90^\circ$. Bottom: Illustration of the geometry for momentum-dependent RIXS. The momentum transfer \vec{q} is given by the angle (fixed at $\varphi = 50^\circ$) between the momenta of incoming and outgoing photon, \vec{k}_{in} and \vec{k}_{out} , respectively, and the relevant quantity is its projection on the sample surface, $\vec{q}_{||}$, which is varied by changing the angle ϑ between incoming photon and sample surface.

while it will be seen in Sec. 4.2.4 that all possible dd transitions appear in one RIXS spectrum (modulo the polarization dependence).

It is customary to define a polarized (π) and depolarized (σ) configuration in RIXS experiments with linearly polarized light, as is illustrated at the top of Fig. 2.6(b). If the angle between the incident photon and the detection direction (which define the scattering plane) is $\varphi = 90^\circ$ and the polarization of the emitted photon is not detected (which would be cumbersome for x-rays), setting the vector of polarization either parallel or perpendicular to the scattering plane gives two distinct situations. In the former case, the photon polarization must necessarily be different before and after the scattering, which is why this is called the depolarized configuration. No such restriction holds for the perpendicular case, which is thus termed as polarized.

The sketch at the bottom of Fig. 2.6(b) illustrates how momentum-dependent measurements in RIXS can be performed. The momentum vectors of the incoming (\vec{k}_{in}) and

outgoing (\vec{k}_{out}) photons define the available momentum transfer \vec{q} . Mounting the sample such that its projection on the sample surface ($\vec{q}_{||}$) is along a high-symmetry direction of the crystal allows to map the momentum dependence of the observed excitations. From the basic relations

$$E = p \cdot c = \frac{hc}{\lambda}; \quad \mathbf{p} = \hbar\mathbf{k}; \quad k = |\mathbf{k}| = 2\pi/\lambda \quad , \quad (2.39)$$

it follows for our experimental geometry [$\varphi = 50^\circ$, cf. Fig. 2.6(b)] for energies around the Ti *L* edge, that $|\vec{q}(h\nu = 450 \text{ eV})| \approx 0.413 \text{ \AA}^{-1}$. This allows to access significant areas of the first Brillouin zone, which extends to 0.83 \AA^{-1} and 0.94 \AA^{-1} in the *a* and *b* direction of TiOCl, respectively.

3 Theoretical Concepts

3.1 Mott Physics and Hubbard Model

The necessity of considering the mutual repulsion between electrons in order to understand why certain materials with partially filled outer shells remain insulating was realized already in the 1930s [de Boer37, Mott37]. The prime example was NiO, but also other systems with d or f valence electrons (in particular transition metals and lanthanoids, respectively) fall in this category. A few years later, N. F. Mott published seminal works on the aspects of phase transitions [in particular metal-insulator transitions (MIT)] in these cases [Mott49], and his ideas are nowadays used as the standard introduction in textbooks to the field of strongly correlated electron systems. The most successful theoretical approach to such systems is the so-called Hubbard model, which will be discussed in the following.

Although named after Hubbard [Hubbard63], the idea of the model was proposed independently also by Gutzwiller [Gutzwiller63] and Kanamori [Kanamori63]. In the form presented here, the two most severe assumptions made are that (i) all interactions are purely local and (ii) only a single half-filled band (i.e., a single orbital) is involved. Of course, there are cases in which these restrictions have to (or can) be dropped, which, however, does not affect the basic considerations presented in the following. The Hubbard model is very powerful in describing low-energy and low-temperature properties of Mott insulators, since often only one or at most a small number of bands cross the Fermi energy and participate in low-energy excitations. Using second quantization notation, the Hubbard Hamiltonian reads

$$H_{\text{Hubbard}} = \mathcal{T} + \mathcal{U} = -t \sum_{\langle ij \rangle \sigma} \left(c_{i\sigma}^\dagger c_{j\sigma} + c_{j\sigma}^\dagger c_{i\sigma} \right) + U \sum_i n_{i\uparrow} n_{i\downarrow} \quad , \quad (3.1)$$

where i, j are lattice site indices, $\langle ij \rangle$ means a summation over nearest neighbors only, counting each pair only once, and $\sigma = \uparrow, \downarrow$ denotes the spin. In the non-interacting limit ($U = 0$) this operator corresponds to a tight-binding Hamiltonian. Wannier orbitals $\varphi(\mathbf{r} - \mathbf{R}_i)$, which are basically the Fourier transforms of Bloch states and thus represent local (but not atomic) orbitals, have to be used in order to correctly account for the desired locality of interactions. $n_{i\sigma} = c_{i\sigma}^\dagger c_{i\sigma}$ is the number operator, and the product in the second sum effectively counts doubly occupied sites.

The crucial parameters of this Hamiltonian are the hopping integral t , which governs the kinetic energy \mathcal{T} , the band filling n , and the Coulomb repulsion U , commonly

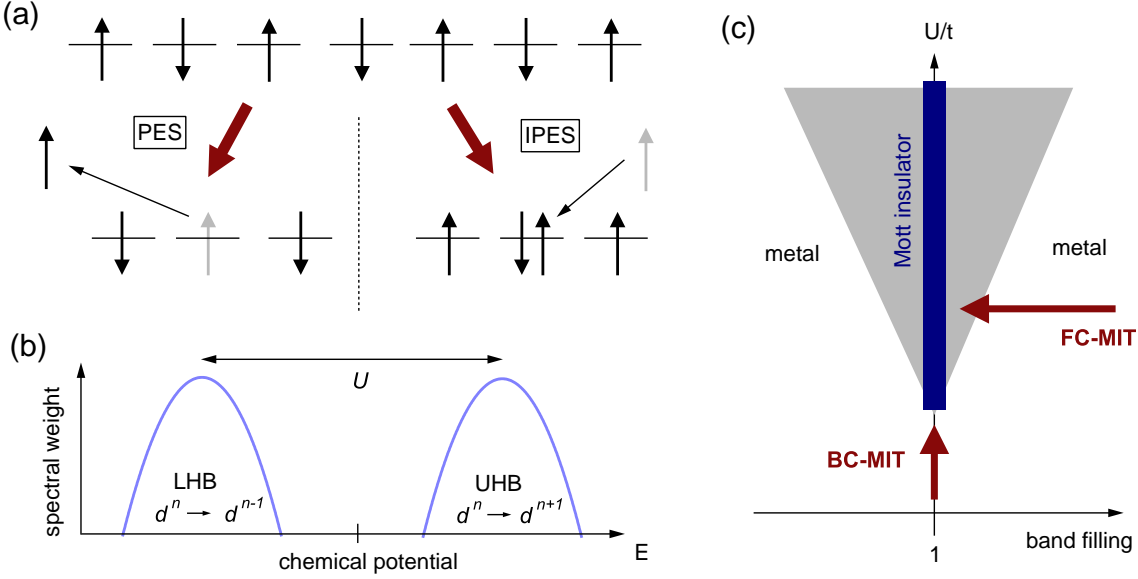


Figure 3.1: (a) One-dimensional chain of singly occupied sites to illustrate the definition of the Hubbard bands from the electron removal ($d^n \rightarrow d^{n-1}$; PES) and addition ($d^n \rightarrow d^{n+1}$; IPES) spectral function. (b) Resulting lower Hubbard band (LHB) and upper Hubbard band (UHB), separated by the on-site Coulomb interaction U (see text for details). (c) Schematic phase diagram of the Hubbard model, illustrating bandwidth-controlled and filling-controlled metal-insulator transitions (BC-MIT and FC-MIT, respectively). The Mott insulator is found at half-filling ($n = 1$; thick line), the shaded area marks the fluctuation regime.

denoted as “Hubbard U ”. The latter is defined in terms of electron addition and removal as the energy difference between removing an electron from a singly occupied site and adding an electron to such a site, namely

$$U(d^n) = E(d^{n-1}) + E(d^{n+1}) - 2E(d^n) \quad , \quad (3.2)$$

with $n \geq 1$. This is illustrated in Fig. 3.1(a) by the processes of photoemission (PES) and inverse photoemission (IPES). When dealing with interacting systems, the density of states (DOS) loses its significance, as it can be defined rigorously only for non-interacting systems. Instead, one has to resort to the spectral function $A(E)$, as has been discussed in Sec. 2.1.¹ Figure 3.1(b) shows that two independent “bands” develop in $A(E)$, related to PES and IPES. These are called lower and upper Hubbard bands (LHB and UHB, respectively), and their maxima are separated by U . They acquire a finite width due to scattering processes not explicitly considered in the current model (e.g., from spins, orbital, or angular momentum). This also motivates why they are called “incoherent” features, as opposed to “coherent” quasiparticle bands. It must be stressed that the LHB

¹Note that, although not fully correct, the DOS is sometimes defined as the \mathbf{k} -integrated spectral function: $\text{DOS}(E) = \sum_{\mathbf{k}} A(\mathbf{k}, E)$ [Imada98].

and UHB are not semiconductor-like bands as in the context of band theory. The very existence of the UHB depends on the presence of electrons in the LHB, i.e., it can only be populated by double occupation of a site. Its appearance is thus a true many-particle effect.

From simple considerations on the Hubbard model it becomes obvious that two kinds of metal-insulator transitions (MIT) should be possible: one can either vary the correlation strength U/t , which is done in practice by changing the bandwidth, or one can change the number of charge carriers away from half-filling. Figure 3.1(c) shows a schematic phase diagram to illustrate the bandwidth-controlled (BC) and filling-controlled (FC) MIT. In this diagram, the Mott insulator is found along the line of half-filling ($n = 1$), indicated in blue. The shaded area is a fluctuation regime which is in principle a metallic phase, but with strong influence of the insulating phase. Other than that, metallic behavior is found. Before discussing the MIT in more detail, an important point shall be named, which is characteristic of the single-band Hubbard model: double occupation is only possible for electrons with opposite spin, i.e., hopping can only happen if neighboring spins are aligned antiferromagnetically. Since this applies for virtual hopping as well, it turns out that antiferromagnetic coupling is favored in Mott-Hubbard systems, although the actual ground state is not a (statically ordered) Néel state, but rather one in which spin fluctuations have lead to a further lowering of the energy [Ashcroft76]. This indicates the close connection between the Heisenberg Hamiltonian introduced in Sec. 3.5 and the Hubbard model.

Before looking at methods to solve the Hubbard model, some general remarks about its symmetries shall be made. First of all, the Hamiltonian in Eq. 3.1 is spin-rotational invariant. This is easy to see for the kinetic term \mathcal{T} , but applies to the seemingly spin-selective interaction term as well. Hence, magnetic ordering of whatever kind spontaneously breaks this symmetry, which has important consequences for the ground state (see Sec. 3.5). Secondly, electron-hole symmetry is not an ubiquitous property of the Hubbard model. Only in the admittedly very important case of a bipartite lattice (one that can be subdivided into sublattices A and B) this symmetry is found, but not, e.g., in triangular lattices or upon doping. However, in the latter case there is a kind of continuous lifting of electron-hole symmetry, meaning that the regimes with and without this symmetry are adiabatically connected. Thirdly, one can realize that the kinetic energy term is not diagonal in the basis of Wannier orbitals, unlike the Coulomb potential interaction term \mathcal{U} . Of course, as \mathcal{T} describes itinerant electrons, a simple Fourier transform back to Bloch waves does the job, yielding

$$\mathcal{T} = \sum_{\mathbf{k}\sigma} \varepsilon_{\mathbf{k}} n_{\mathbf{k}\sigma} \quad . \quad (3.3)$$

\mathbf{k} is now the band index, and for a D -dimensional cubic lattice of lattice constant a the

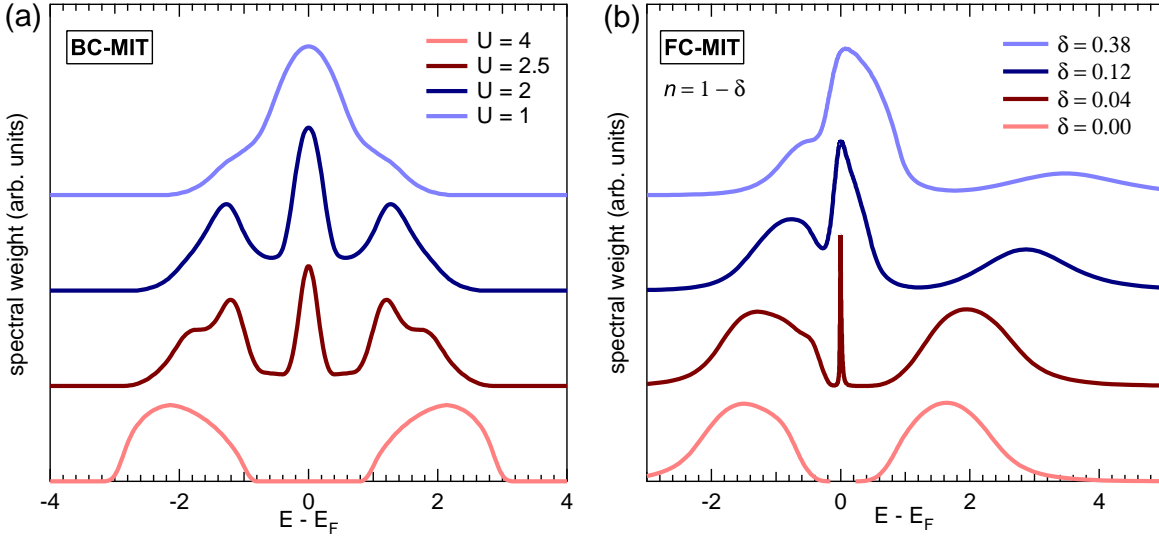


Figure 3.2: Spectral function $A(E)$ obtained from DMFT (data from [Bulla99]). Calculations were performed on a Bethe lattice and solved using iterated perturbation theory and numerical renormalization group, respectively. U is given in units of $W/2$, where W is the bandwidth. (a) Bandwidth-controlled metal-insulator transition at $n = 1$ and with a critical $U_c = 3.3$. (b) Filling-controlled metal-insulator transition at $U = 3.2$ ($U_c = 2.94$).

band energy $\varepsilon_{\mathbf{k}}$ takes on the tight-binding form

$$\varepsilon(\mathbf{k}) = -2t \sum_{j=1}^D \cos k_j a \quad . \quad (3.4)$$

The bandwidth W is proportional to the transfer integral t :

$$W = 4Dt \quad . \quad (3.5)$$

Should $\varepsilon(\mathbf{k})$ be available from a more sophisticated band structure calculation, the form obtained in such a way may of course be used as a more realistic representation of the system under investigation.

In order to grasp the effects of the BC- and FC-MIT it is instructive to anticipate the behavior of the (momentum-independent) spectral function, in the form it results from one of the currently most powerful approaches to strongly correlated electron systems, namely dynamical mean-field theory (DMFT; see Sec. 3.3). This is shown for a BC-MIT at half-filling in Fig. 3.2(a). Starting from the Mott insulating side where the two Hubbard bands (the incoherent features) are well-separated by an excitation gap U ($U > W$), two things happen when the interaction strength, indicated by U/W , is lowered. Firstly, at a critical value¹ U_{c2} , a sharp quasiparticle peak (the coherent weight)

¹ U_c is the interaction strength above which the system is Mott insulating.

develops at the chemical potential and becomes increasingly broad, although this does not (at once) lead to a transition into a metallic state. An important subtlety in this case is the influence of screening. In a simple Hubbard model (Eq. 3.1) non-local Coulomb interactions are completely absent. However, if this absence is only due to screening, the formation of bound (i.e., localized) electron-hole pairs (excitons) is only favorable as long as the exciton radius does not exceed the screening length. Once it does, exciton formation suddenly becomes disadvantageous, and a first-order transition occurs (which would be of second order without the screening).¹ The second effect encountered upon lowering U/W at a value $U_{c1} < U_{c2}$, namely the eventual overlap of LHB and UHB, can lead to a MIT independent of the quasiparticle contribution. In between the two critical values a coexistence region is found, and depending on the starting point ($U < U_{c1}$ or $U_{c2} < U$) the BC-MIT is either governed by the coherent or the incoherent spectral features. Showing that there are different values of the critical interaction strength was one of the major achievements of DMFT [Georges96, Bulla99].

The spectral behavior when traversing a FC-MIT induced by hole-doping is depicted in Fig. 3.2(b). Starting from the insulating state the main effect is a jump of the chemical potential from the middle of the gap to the upper boundary of the LHB. This immediately leads to the formation of a sharp quasiparticle peak at this position, which is composed of spectral weight transferred from *both* the LHB and the UHB, and becomes broader with increasing doping. Also, the energetic positions of LHB and UHB continuously change, but in an unequal manner due to broken electron-hole symmetry. In the case of electron-doping, the behavior of the spectral weight is essentially inverted with respect to the chemical potential (not shown).

3.2 Parametrization of Coulomb Interactions

It is obvious that many aspects of the electronic structure of a solid are not captured by the simple, tight-binding based Hubbard scheme. The intention of the current section is to introduce three effects which are very important in this context: (i) multiplet effects (hinted at already in Sec. 2.2), (ii) crystal-field effects, and (iii) charge transfer or configuration interaction. In addition, parameters which are commonly used in this context will be defined.

Firstly, from the general form of the electron-electron interaction included in the Hamiltonian of an atom (Eq. 2.28), namely

$$H_{el-el} = \sum_{ijkl} V_{ijkl} c_{i,\sigma}^\dagger c_{j,\sigma'}^\dagger c_{k,\sigma'} c_{l,\sigma} \quad , \quad (3.6)$$

with i, j, k and l being orbital indices, and σ and σ' denoting the spin indices, several important Coulomb interactions V_{ijkl} can be (re-)defined. For example, a more mathematical definition than the one in Eq. 3.2 of the intraorbital Hubbard U ($i = j = k = l$,

¹This screening argument was realized early on by Mott, cf. [Mott56].

and $\sigma = -\sigma'$ due to the Pauli principle) would be

$$U = \int d\mathbf{r}_1 \int d\mathbf{r}_2 \varphi_\sigma^*(\mathbf{r}_1) \varphi_\sigma^*(\mathbf{r}_2) \frac{e^2}{|\mathbf{r}_1 - \mathbf{r}_2|} \varphi_{-\sigma}(\mathbf{r}_1) \varphi_{-\sigma}(\mathbf{r}_2) \quad , \quad (3.7)$$

where the φ 's are single-particle-like orbital wave functions (e.g., the 3d orbitals). Similarly, the direct Coulomb interaction between electrons in *different* orbitals ($i = l \neq j = k$) is¹

$$U' = \int d\mathbf{r}_1 \int d\mathbf{r}_2 \varphi_{i,\sigma}^*(\mathbf{r}_1) \varphi_{j,\sigma}^*(\mathbf{r}_2) \frac{e^2}{|\mathbf{r}_1 - \mathbf{r}_2|} \varphi_{j,\sigma'}(\mathbf{r}_2) \varphi_{i,\sigma'}(\mathbf{r}_1) \quad . \quad (3.8)$$

Further combinations of the orbital indices yield for $i = k \neq j = l$ the Heisenberg exchange coupling J_H (also called Hund's rule coupling) appearing in Eq. 3.38, as

$$J = J_H = \int d\mathbf{r}_1 \int d\mathbf{r}_2 \varphi_{i,\sigma}^*(\mathbf{r}_1) \varphi_{j,\sigma}^*(\mathbf{r}_2) \frac{e^2}{|\mathbf{r}_1 - \mathbf{r}_2|} \varphi_{i,\sigma'}(\mathbf{r}_2) \varphi_{j,\sigma'}(\mathbf{r}_1) \quad , \quad (3.9)$$

and finally for $i = j \neq k = l$

$$I = \int d\mathbf{r}_1 \int d\mathbf{r}_2 \varphi_{i,\sigma}^*(\mathbf{r}_1) \varphi_{i,\sigma}^*(\mathbf{r}_2) \frac{e^2}{|\mathbf{r}_1 - \mathbf{r}_2|} \varphi_{k,\sigma'}^*(\mathbf{r}_2) \varphi_{k,\sigma'}(\mathbf{r}_1) \quad , \quad (3.10)$$

the so-called pair-hopping interaction [Maekawa04]. Whenever appropriate, one distinguishes further the cases of interactions between two d electrons from those between one d and one p electron, e.g., by writing U_{dd} and U_{pd} for the Hubbard-like Coulomb parameters, respectively. Within d orbitals, the intra- and interorbital U 's are related by

$$U' = U - 2J_H \quad . \quad (3.11)$$

It is very convenient to separate the total wave functions into a spherical part $Y_l^m(\theta, \phi)$ and a radial part $R_{n,l}(r)$, and to define so-called Slater-Condon parameters or Slater integrals as integrals over the radial part. The direct Slater integrals are given by

$$F^k = \int_0^\infty dr_1 \int_0^\infty dr_2 r_1^2 r_2^2 R_{32}^2(r_1) R_{32}^2(r_2) \frac{r_{<}^k}{r_{>}^{k+1}} \quad , \quad (3.12)$$

where k is a set of quantum numbers related to the orbital momenta $l_{1,2}$ of the two electrons, and

$$(r_{>}, r_{<}) = \begin{cases} (|\mathbf{r}_1|, |\mathbf{r}_2|) & \text{for } |\mathbf{r}_1| > |\mathbf{r}_2| \\ (|\mathbf{r}_2|, |\mathbf{r}_1|) & \text{for } |\mathbf{r}_1| < |\mathbf{r}_2| \end{cases} \quad . \quad (3.13)$$

Exchange Slater integrals are denoted as G^k , with the integral in Eq. 3.12 adjusted accordingly [Cowan81]. Integrals over the angular part (denoted by lower-case letters f_k and g_k , respectively) yield the Clebsch-Gordan coefficients, and accordingly several

¹Here, no restriction due to the Pauli principle applies.

Table 3.1: Cross-relationships between normalized and unnormalized Slater-Condon parameters (SCP), Racah parameters, and parametrization of direct and exchange Coulomb integrals in terms of these parameters. (notation J_i according to [Lee05].)

	SCP	normalized SCP	Racah
SCP	F^0 F^2 F^4	$F_0 = F^0$ $F_2 = \frac{1}{49}F^2$ $F_4 = \frac{1}{441}F^4$	$A = F^0 - \frac{49}{441}F^4$ $B = \frac{1}{49}F^2 - \frac{5}{441}F^4$ $C = \frac{35}{441}F^4$
normalized SCP	$F^0 = F_0$ $F^2 = 49F_2$ $F^4 = 441F_4$	F_0 F_2 F_4	$A = F_0 - 49F_4$ $B = F_2 - 5F_4$ $C = 35F_4$
Racah	$F^0 = A - \frac{7}{5}C$ $F^2 = 49B - 7C$ $F^4 = \frac{441}{35}C$	$F_0 = A - \frac{7}{5}C$ $F_2 = B - \frac{1}{7}C$ $F_4 = \frac{1}{35}C$	A B C
U	$F^0 + \frac{4}{49}F^2 + \frac{36}{441}F^4$	$F_0 + 4F_2 + 36F_4$	$A + 4B + 3C$
U'	$F^0 - \frac{2}{49}F^2 - \frac{4}{441}F^4$	$F_0 - 2F_2 - 4F_4$	$A - 2B + C$
J_1	$\frac{35}{441}F^4$	$35F_4$	C
$J_3(\approx J_H)$	$\frac{3}{49}F^2 + \frac{20}{441}F^4$	$3F_2 + 20F_4$	$3B + C$
J_4	$\frac{4}{49}F^2 + \frac{15}{441}F^4$	$4F_2 + 15F_4$	$4B + C$

selection rules apply. These can be exploited to determine the k values which have to be used for a specific case. It turns out for f_k that k must always be even, and that the maximum value of k equals twice the smallest value of l . For g_k one finds that $k \leq l_1 + l_2$, and k even (odd) if $l_1 + l_2$ even (odd). Thus, for a $2p3d$ configuration ($l_1 = 1, l_2 = 2$) of a transition metal (TM) ion one only has to evaluate direct Slater integrals for $k = 0, 2$ and 4 , and indirect ones for $k = 1$ and 3 .¹ In this case, it is appropriate to distinguish between dd and pd parameters (e.g., $F_{dd}^2 \neq F_{pd}^2$).

The Slater integrals are also often found in their normalized form, denoted by k as a *subscript* instead of a *superscript*. Another famous parametrization is that by G. Racah, who defined the so-called Racah parameters [Racah42]. The matrix in Tab. 3.1 gives the relationships between all these parameters. Furthermore, the table shows how the Coulomb integrals (U, J_H , etc.) can be calculated from Racah and Slater parameters. Although it can often be assumed that these integrals are equal for any combination of the five different d orbitals, the table also contains various values of the exchange integrals, which become significant for non-degenerate d orbitals in a crystal field (see below): J_3 for mixing within t_{2g} electrons only, J_4 between a t_{2g} and a d_{z^2} electron, and J_1 between a t_{2g} and a $d_{x^2-y^2}$ electron, as used in [Lee05] (see also [Oleś05]).²

In the following, the importance of broken symmetry around the TM ion shall be considered, namely, a low-symmetry crystal field imposed by the ligands. Based on group theory, well-defined symbols are assigned to particular point groups and symmetry operations (see, e.g., [Kettle07]). Starting from the spherically symmetric case considered until now, denoted as the SO_3 point group, the first reduction is that to O_h symmetry, where the TM ion is octahedrally coordinated by six equal ligands sitting along the x , y , and z axes [see Fig. 3.3(a)]. This is an important configuration, as it is found to a good approximation in all materials having the Perovskite structure, in particular many transition metal oxides (ligands are oxygen in this case). In this geometry, the orbitals of the so-called t_{2g} triplet (d_{xy} , d_{xz} , and d_{yz}) point in-between two negatively charged ligands, while those of the e_g doublet ($d_{x^2-y^2}$ and d_{z^2}) point exactly towards the ligands. It is thus energetically more favorable for electrons to occupy one of the t_{2g} orbitals, which results in a crystal-field splitting between t_{2g} and e_g , denoted with the parameter $10Dq$. Knowing that the center-of-mass of the d shell remains unchanged and the respective degeneracies, one sees that the t_{2g} orbitals are lowered by $-4Dq$, while the e_g orbitals are lifted up by $6Dq$. Formally, this parametrization results from a perturbation approach to the Coulomb potential at the TM site in which the potential of the ligands is used as a first-order correction to the hydrogen-like (i.e., spherically symmetric) TM ion [Sugano70].³ One then calculates the matrix elements of this symmetry-adapted correction $V_c^0 = V_c - (6Ze^2/a)$ (Z is the number of ligands and a their distance to the

¹It is found in many TM systems that $F^4 \approx 0.62F^2$ [de Groot90b].

²The most important exchange integral for the oxyhalides is that between t_{2g} orbitals, so we set $J_3 = J_H$.

³Note that the validity of a perturbation approach is in many cases not very well justified, since $10Dq$ is often about 1-2 eV, i.e., of the same order of magnitude as other Coulomb interactions.

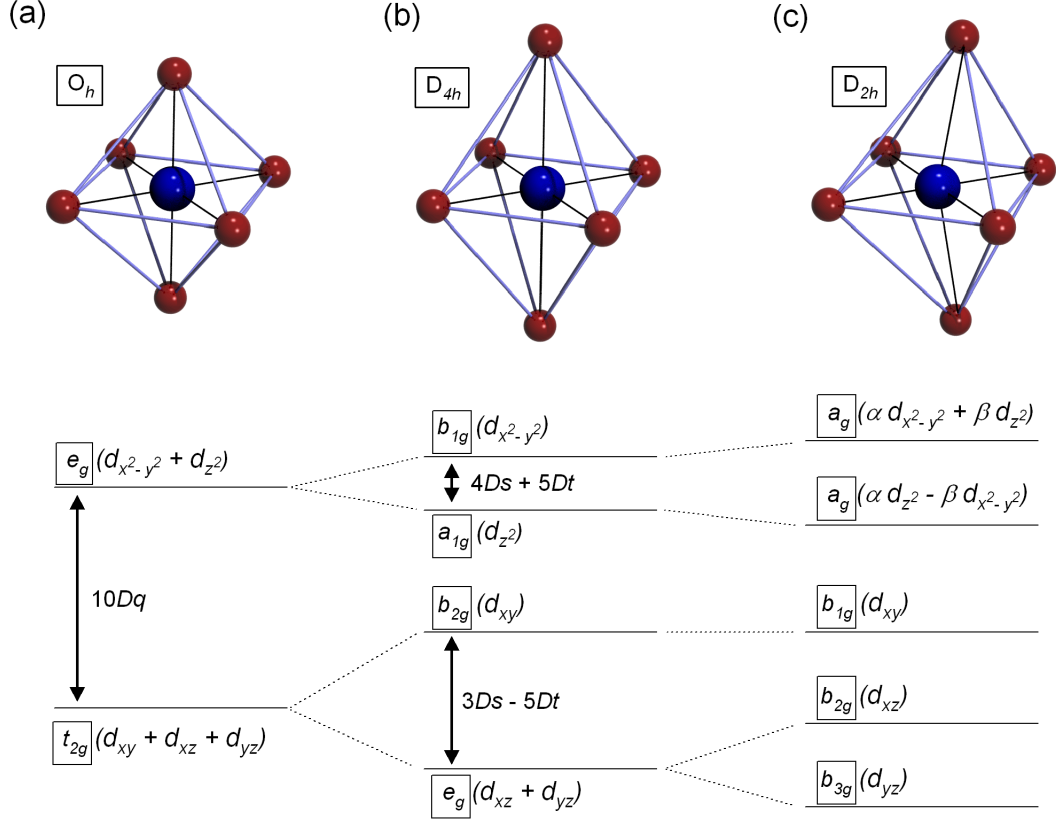


Figure 3.3: Different ligand arrangements around a TM ion (top), and resulting crystal-field-split energy levels (bottom). The latter are denoted by the corresponding symmetry term (e.g., t_{2g}), the constituting single-particle wave functions (e.g., d_{xy}), and crystal-field parameters, where appropriate. α and β are weighting coefficients. (a) Octahedral symmetry; all ligand-TM distances are equal. (b) Tetragonal symmetry, with an elongation along the z axis. (c) Orthorhombic symmetry; the ligands at the top and the bottom are additionally displaced symmetrically in the xy plane.

TM) with the different atomic d wave functions φ_{nlm} , resulting in

$$\begin{aligned}
 \langle \varphi_{nd\pm 2} | V_c^0 | \varphi_{nd\pm 2} \rangle &= Dq, \\
 \langle \varphi_{nd\pm 1} | V_c^0 | \varphi_{nd\pm 1} \rangle &= -4Dq, \\
 \langle \varphi_{nd0} | V_c^0 | \varphi_{nd0} \rangle &= 6Dq, \\
 \langle \varphi_{nd\pm 2} | V_c^0 | \varphi_{nd\mp 2} \rangle &= 5Dq,
 \end{aligned} \tag{3.14}$$

where

$$D = 35Z \frac{e^2}{4a^5} \quad \text{and} \quad q = \frac{2}{105} \langle r^4 \rangle_{nd} \quad , \tag{3.15}$$

Table 3.2: Parametrization of the crystal-field levels in D_{4h} using the crystal-field parameters Dq , Ds and Dt , and those defined by Butler.

orbital	symmetry	energy in D terms	energy in X terms (Butler)
$d_{x^2-y^2}$	b_{1g}	$6Dq + 2Ds - Dt$	$\frac{1}{\sqrt{30}}X_{400} - \frac{1}{\sqrt{42}}X_{420} - \frac{2}{\sqrt{70}}X_{220}$
d_{z^2}	a_{1g}	$6Dq - 2Ds - 6Dt$	$\frac{1}{\sqrt{30}}X_{400} + \frac{1}{\sqrt{42}}X_{420} + \frac{2}{\sqrt{70}}X_{220}$
d_{xy}	b_{2g}	$-4Dq + 2Ds - Dt$	$-\frac{2}{3\sqrt{30}}X_{400} + \frac{4}{3\sqrt{42}}X_{420} - \frac{2}{\sqrt{70}}X_{220}$
d_{xz}, d_{yz}	e_g	$-4Dq - Ds + 4Dt$	$-\frac{2}{3\sqrt{30}}X_{400} - \frac{2}{3\sqrt{42}}X_{420} + \frac{1}{\sqrt{70}}X_{220}$

with the radial integral

$$\langle r^m \rangle_{nd} = \int dr r^{2+m} |R_{nd}(r)|^2 . \quad (3.16)$$

Compressing or stretching the octahedron along one axis (z axis for simplicity) corresponds to a tetragonal distortion and a symmetry group denoted by D_{4h} . As a consequence, the degeneracy of the e_g orbitals is lifted, and also one of the three t_{2g} orbitals is split off, see Fig. 3.3(b). Note here, that the order within t_{2g} - and e_g -derived orbitals is reversed if one is compressing instead of stretching the octahedron. One commonly finds the two additional crystal-field parameters Ds and Dt to parametrize the splitting within D_{4h} . A slightly different way of defining crystal-field parameters is based on Butler's notation [Butler81], which is used for our cluster calculations in Sec. 4.2.3. It is motivated by a nomenclature for symmetry-adapted term symbols used to label the states of a system (which are derived from the atomic orbitals) and to identify symmetry operations. His notation is different from the more often encountered one by Mulliken [de Groot08]. For example, a d orbital might be represented in O_h by the combination of terms $E + T_2$ (Mulliken), or $2 + \hat{1}$ (Butler). Lowering the point symmetry leads to a mixing, or "branching", of different terms using fixed rules. Going from SO_3 to D_{4h} requires three branching series, denoted by Butler as $4 \rightarrow 0 \rightarrow 0$, $4 \rightarrow 2 \rightarrow 0$, and $2 \rightarrow 2 \rightarrow 0$. He thus defines the parameters X_{400} , X_{420} , and X_{220} , which are related to Dq , Ds and Dt as:

$$\begin{aligned} X_{400} &= 6\sqrt{30} Dq - \frac{7}{2}\sqrt{30} Dt, \\ X_{420} &= -\frac{5}{2}\sqrt{42} Dt, \\ X_{220} &= -\sqrt{70} Ds , \end{aligned} \quad (3.17)$$

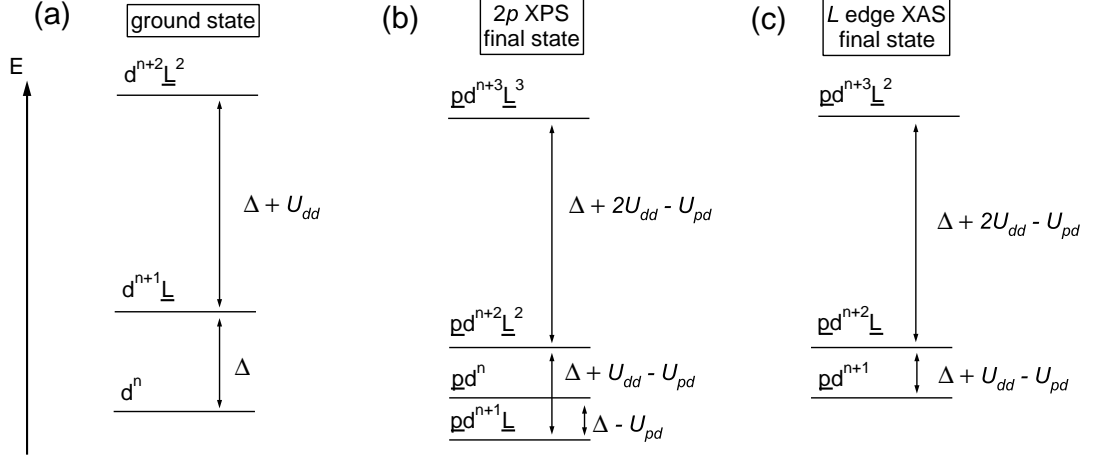


Figure 3.4: Configuration interaction for hybridization between a TM 3d and O 2p states. U_{dd} (U_{pd}) denotes the Coulomb repulsion between two d (a p and a d) electron(s); Δ is the charge-transfer energy, i.e., the energy necessary to transfer an electron from the oxygen p shell to the TM d shell. These terms are all defined relative to the energy of the pure state d^n . (a) Ground state with the two lowest charge-transfer states indicated. (b) Final state in a 2p PES experiment. (c) Final state after L edge XAS. (scheme adopted from [Zaanen85])

and the inverse relationships are

$$\begin{aligned}
 Dq &= \frac{1}{6\sqrt{30}} X_{400} - \frac{7}{30\sqrt{42}} X_{420}, \\
 Ds &= -\frac{1}{\sqrt{70}} X_{220}, \\
 Dt &= -\frac{2}{5\sqrt{42}} X_{420}.
 \end{aligned} \tag{3.18}$$

Using these relations, the resulting energy levels in D_{4h} are summarized in Tab. 3.2.

Going from tetragonal (D_{4h}) to orthorhombic (D_{2h}) symmetry, the degeneracy of the d levels is completely lifted [see Fig. 3.3(c)]. Although it is possible to define additional crystal-field parameters in this case, they cannot be connected with a particular shift directly, and due to this lack of illustrative power no such parameters shall be given. Also, our cluster calculations within D_{2h} symmetry do not require these parameters to be specified (cf. Secs. 4.2.3 and 4.2.4).

Another important contribution to the energetics comes from the interactions of the TM ion with its surrounding ligands by virtue of hybridization between TM 3d and O 2p orbitals. This corresponds to charge transfer from the ligand to the TM, thus leading to several configurations which mix. Figure 3.4 shows a possible ground state, and also revisits the final states of 2p PES and L edge XAS resulting from hybridization. In addition to the pure d^n configuration, states with one, two, or more electrons transferred

from the ligand and denoted as, e.g., $d^{n+2}\underline{L}^2$ (where \underline{L}^2 denotes two holes at the ligand) contribute to the total energy. \underline{p} in the PES and XAS final states denotes a hole in the TM $2p$ core shell. The parameters U_{pd} , U_{dd} , as well as the charge-transfer energy Δ are also indicated in the figure. The latter is an important parameter, e.g., in the cluster calculations for XAS and RIXS, cf. Secs. 4.2.3, 4.2.4, and the following section.

3.3 Computational Methods

There are quite a number of different approaches to calculate the electronic structure of a given material, both based on models like, e.g., the Hubbard model, as well as so-called *ab initio* techniques. In many cases, they complement each other by giving descriptions of different phases and/or properties, while no method is currently available to satisfactorily describe a material by itself. Thus, several computational methods have been applied to study the oxyhalides, and a short introduction and critical comparison shall be given in the following, based mainly on the review by Imada *et al.* [Imada98].

Ab initio or first-principles calculations are defined as methods which do not need empirically adjustable or fitted parameters; instead, eigenfunctions and eigenvalues are obtained directly from the properties of atoms and electrons. One widely used approach is to use an effective single-particle (i.e., mean-field) theory, namely the density-functional theory (DFT) developed by Hohenberg, Kohn and Sham [Hohenberg64, Kohn65]. The basic quantity in this case is the local electronic charge density $\rho(\mathbf{r})$ of the solid, and both the total energy as well as the many-body state are taken as functionals of this density, i.e., $E = E[\rho(\mathbf{r})]$ and $\Psi = \Psi[\rho(\mathbf{r})]$, respectively. The energy can be written as:

$$E[\rho(\mathbf{r})] = E_{kin}[\rho(\mathbf{r})] + \int d\mathbf{r} V_{ext}(\mathbf{r})\rho(\mathbf{r}) + \frac{e^2}{2} \int d\mathbf{r} d\mathbf{r}' \frac{\rho(\mathbf{r})\rho(\mathbf{r}')}{|\mathbf{r} - \mathbf{r}'|} + E_{xc}[\rho(\mathbf{r})] \quad . \quad (3.19)$$

The first term is the kinetic energy of the non-interacting system, the second term represents the external potential provided by the lattice, the third term is the Hartree contribution, and $E_{xc}[\rho(\mathbf{r})]$ gives the exchange and correlation effects not covered by the other terms. In practice, one first assumes that $\Psi[\rho(\mathbf{r})]$ is a Slater determinant and introduces the Kohn-Sham potential V_{KS} such that only Schrödinger equations containing single-particle wave functions ψ_i from this determinant have to be minimized, namely

$$\left[-\frac{\hbar^2}{2m}\nabla^2 + V_{KS}(\mathbf{r})\right]\psi_i = \varepsilon_i\psi_i \quad , \quad (3.20)$$

where V_{KS} represents a *static* mean-field which has to be determined from the self-consistency condition

$$V_{KS} = V_{ext} + \int d\mathbf{r}' \frac{\rho(\mathbf{r}')}{|\mathbf{r} - \mathbf{r}'|} + \frac{\partial E_{xc}[\rho(\mathbf{r})]}{\partial \rho(\mathbf{r})} \quad . \quad (3.21)$$

The ground-state density is given by

$$\rho(\mathbf{r}) = \sum_i f(\varepsilon_i) |\psi_i|^2 \quad , \quad (3.22)$$

with $f(\varepsilon_i)$ being the Fermi distribution function. Calculating the density $\rho(\mathbf{r})$ from the adjusted ψ_i 's, a (most likely) different potential V_{KS} is obtained, allowing to determine new expressions for ψ_i from Eq. 3.20.¹ This procedure is iterated until the charge density $\rho(\mathbf{r})$ has properly converged. The important advantage is that although one only deals with a non-interacting single-particle system, the Kohn-Sham equations yield the correct *ground-state* charge density of the many-body interacting system. It must be kept in mind, though, that the wave functions ψ_i are not electron wave functions; they are simply a mathematical tool to obtain the correct charge density via Eq. 3.22.

The remaining challenge towards practical implementations of the Kohn-Sham DFT is finding an appropriate expression for E_{xc} . The most widely used solution was given directly by Hohenberg, Kohn and Sham, in the form of the local density approximation (LDA). It assumes that the charge density is that of a uniform electron gas, which means that the exchange-correlation term is determined only by $\rho(\mathbf{r}')$ with $\mathbf{r}' = \mathbf{r}$,² and that it can be written as

$$E_{xc}[\rho] = \int d\mathbf{r} \varepsilon_{xc}[\rho(\mathbf{r})] \rho(\mathbf{r}) \quad . \quad (3.23)$$

Although this is admittedly a quite severe approximation since generally there is a non-negligible nonlocal contribution to $\rho(\mathbf{r}')$ coming from $\mathbf{r}' \neq \mathbf{r}$, a spatially not or only slowly varying density of the electron gas yields very good results, in particular for weakly correlated systems (e.g., semiconductors). This can be improved on by adding a correction of first order in the spatial dependence of the charge density, which is typically of the order of 10% [Langreth83]. The resulting method is called generalized gradient approximation (GGA), and throughout this thesis, LDA and GGA (as well as their extensions, see below) are used interchangeably. Even within the GGA approach, however, one major failure of DFT is still present, namely, that the Coulomb and exchange self-interactions of an electron do not exactly cancel out; this is called the self-interaction error [Perdew81]. As a result, the charge gap of correlated systems is severely underestimated, usually such that it vanishes completely and thus gives a metallic solution.

One way to overcome this is the application of the Hartree-Fock (HF) method, where always a single Slater determinant is used to approximate the true many-body wave function, which is not a function of the charge density $\rho(\mathbf{r})$. The ground-state energy is then obtained by self-consistent minimization with respect to the single-particle states constituting the Slater-determinant. However, HF takes into account only correlations

¹Note that these ψ_i are not necessarily atomic single-particle wave functions anymore.

²Note the difference between the local *action* of *any* Kohn-Sham potential, and the local *contributions* to the potential which are restricted in this way only in LDA.

between electrons with equal spin orientation, while that between electrons with opposite spin orientation, which is crucial in strongly correlated systems, is not included. Nevertheless, HF is appropriate for describing Mott insulators due to the absence of a self-interaction error, although this advantage is gained only at the expense of other shortcomings. Firstly, the Coulomb interaction is unscreened, typically yielding values of $U \sim 15 - 20 \text{ eV}$, thus *overestimating* the charge gap by typically a factor of 2 – 3. Secondly, the resulting potentials are nonlocal and orbital-dependent, which makes HF computationally very expensive. If, however, only single free ions are considered, this argument does not hold anymore. Thus, HF can be used as a basis for the very successful methods of ligand field multiplet (LFM) and charge-transfer multiplet (CTM) theory, commonly denoted as configuration interaction (CI) or cluster methods [de Groot08]. Here, the ion of interest (i.e., the TM ion) is embedded into a cluster of ligands, which imposes the correct local symmetry of such a crystal site (cf. Sec. 3.2). Then, the Coulomb parameters of this ion in the ground and in the final state of an excitation process are calculated by HF. The fact that both states are treated on equal footing makes cluster calculations very powerful tools for all kinds of processes where information on the momentum dependence is not needed (in particular x-ray absorption spectroscopy, Sec. 4.2.3, and resonant inelastic x-ray scattering, Sec. 4.2.4), as a single TM site cannot yield this kind of information.

A different route, based again on DFT, is to artificially add a term to the LDA functional which represents strong local Coulomb interactions. This so-called LDA+ U approach can be thought of as follows [Anisimov97]: Take an open-shell d electron system which is decoupled from the other full s and p shells of the solid, and assume that the latter can be approximated well by a one-electron potential (i.e., LDA). Then, the Coulomb interaction energy between the $N = \sum n_i$ electrons in the d shell (n_i is the occupation of the i th orbital) is given by $E = UN(N - 1)/2$. This should be subtracted from the total-energy functional $E_{\text{LDA},\tilde{N}}$ (where $\tilde{N} \neq N$ is the total number of particles in the solid), and then a Hubbard-like term can be added:

$$E = E_{\text{LDA},\tilde{N}} - UN(N - 1)/2 + \frac{1}{2}U \sum_{i \neq j} n_i n_j \quad . \quad (3.24)$$

The energies of specific orbitals are obtained from the derivatives of the above equation with respect to their occupation:

$$\varepsilon_i = \frac{\partial E}{\partial n_i} = \varepsilon_{\text{LDA}} + U\left(\frac{1}{2} - n_i\right) \quad . \quad (3.25)$$

This effectively shifts an occupied orbital ($n_i = 1$) down by an energy of $-U/2$ while an unoccupied orbital is shifted upwards by $+U/2$, i.e., this mimics the formation of a lower and upper Hubbard band. LDA+ U is thus a highly valuable and powerful extension to regular LDA, giving access to ground-state energies and band structures. Nevertheless, care should be taken when applying it to strongly correlated electron

systems, because it is inherently an effective single-particle method. This is particularly true for excitations like, e.g., photoemission spectra. In DFT methods, the LHB/UHB-splitting remains artificial because all quantities obtained represent quasiparticle bands (i.e., coherent features), while the Hubbard bands are incoherent in nature. A suitable way of describing the typical three-peak structure of correlated systems (cf. Fig. 3.2) consisting of both coherent and incoherent spectral features within the same framework is that of dynamical mean-field theory (DMFT) [Metzner89, Kotliar04].

As seen in Sec. 3.5, the Hubbard model at half-filling can be mapped onto a one-dimensional $S = 1/2$ Heisenberg chain, which can be solved analytically using the so-called Bethe-Ansatz [Bethe31]. For higher-dimensional cases there is no exact solution, but when the dimensionality goes to infinity it turns out that the computation is greatly simplified. That is because the coordination number also goes to infinity in this limit,¹ so assuming a continuous bath of non-interacting electrons around the correlated site involves no more approximations. Thus, the Hubbard model (a lattice model) can be mapped onto a quantum impurity model [Georges92], the most famous of which is the Anderson impurity model (AIM), which is expressed by the Hamiltonian

$$H_{\text{AIM}} = H_{\text{atom}} + \sum_{\nu,\sigma} \varepsilon_{\nu}^{\text{bath}} n_{\nu,\sigma}^{\text{bath}} + \sum_{\nu,\sigma} \left(V_{\nu} c_{0,\nu}^{\dagger} a_{\nu,\sigma}^{\text{bath}} + \text{h.c.} \right) \quad . \quad (3.26)$$

The first term represents the impurity site, the second term the energy levels of the bath (given by the kinetic energy alone, as it is non-interacting), and the third term is the hybridization between bath (annihilation operator $a_{\nu,\sigma}^{\text{bath}}$) and impurity site (creation operator $c_{0,\nu}^{\dagger}$); h.c. signifies the Hermitian conjugate. If the potential V_{ν} fulfills a self-consistency condition, the AIM yields the same Green's function as the Hubbard model. The connection between V_{ν} and the bath energies is given by the hybridization function

$$\Delta(\omega) = \sum_{\nu} \frac{|V_{\nu}|^2}{\omega - \varepsilon_{\nu}^{\text{bath}}} \quad , \quad (3.27)$$

which signifies the *dynamical* mean-field due to its frequency dependence. This hybridization can self-consistently be determined from the local Green's function

$$G[\Delta(\omega)] = \sum_{\mathbf{k}} (\omega - \Sigma[\Delta(\omega)] - t_{\mathbf{k}})^{-1} \quad , \quad (3.28)$$

where the self-energy term is defined as $\Sigma[\Delta(\omega)] \equiv \Delta[(\omega)] - 1/G[\Delta(\omega)] + \omega$, and $t_{\mathbf{k}}$ is the Fourier transform of the real-space hopping matrix element t_{ij} . In order to illustrate the analogy to DFT (Eq. 3.19) a functional can be introduced, which in this case is

¹In a two-dimensional hypercubic lattice the coordination number is four, in three dimensions it is six, and so forth.

dependent on the charge density *and* on the local Green's function:

$$\begin{aligned}
E[\rho(\mathbf{r}), G] &= E_{kin}[\rho(\mathbf{r}), G] + \int d\mathbf{r} V_{ext}(\mathbf{r})\rho(\mathbf{r}) \\
&+ \frac{e^2}{2} \int d\mathbf{r} d\mathbf{r}' \frac{\rho(\mathbf{r})\rho(\mathbf{r}')}{|\mathbf{r} - \mathbf{r}'|} + E_{xc}[\rho(\mathbf{r}), G] \quad .
\end{aligned} \tag{3.29}$$

An approximation to the form of E_{xc} is implicit in DMFT, and one should also note that the kinetic energy is not that of free electrons anymore due to the dependence on the Green's function. This direct dependence on G also shows why this approach is more directly related to photoemission spectra, namely by virtue of the connection between the imaginary part of G and the spectral function A , specified in Eq. 2.11.

Some remarks shall be made on subtleties of the DMFT method. Remembering Eq. 3.5, one sees that the average band energy (i.e., the kinetic part of the Hamiltonian) becomes infinite for $D = \infty$ because the band width W proportional to D . As the interaction part stays constant, this would drive the system to its non-interacting limit. This problem can be circumvented, however, by a renormalization of the hopping integral to $t^* = t/\sqrt{2D}$. Another shortcoming is connected to losing the usually observed smooth \mathbf{k} -dependence of the band energies $\varepsilon(\mathbf{k})$, which allows for the concept of a Fermi surface. The latter cannot be defined for $D = \infty$ anymore, as electronic states with nearby momenta possess completely uncorrelated energies. The Fermi *energy*, however, retains its significance.

Introducing a momentum dependence to the calculated spectral function would be an important improvement. This can be achieved by considering clusters of N_c correlated sites which are embedded within n_b bath sites attached to each cluster site. Depending on the number and arrangement of cluster sites, different points in \mathbf{k} -space become accessible. The crucial thing is that one can separate the self-energy into intracluster and intercluster components, and optimize them by a variational procedure. The limit of $n_b = \infty$ is called the cellular DMFT (C-DMFT), which was used by us for $N_c = 2$ (cf. Sec. 4.2.1). Variational parameters in C-DMFT are the bath energies $\varepsilon_v^{\text{bath}}$ and the hopping between the cluster and the bath, t'_{ir} , while the hopping t'_{ij} on the cluster, i.e., between correlated sites, is kept fixed. This latter point is even a necessary condition to satisfy the self-consistency condition of C-DMFT, but of course presents an unwanted restriction [Potthoff03b]. A way to overcome this is the self-energy-functional theory (SFT) which can be cast into the form of the variational cluster approach (VCA) [Potthoff03b, Potthoff03a]. In this case, the number of bath sites is usually kept finite for computational reasons, and this method is in practice often combined with LDA to a two-step procedure. First, an effective Hamiltonian for the noninteracting part is constructed using the input from LDA. Second, VCA is applied to the full Hamiltonian, containing that from LDA as well as Coulomb and Hund interaction terms. The main idea is to approximate the self-energy of the real system with that of the noninteracting reference. The appropriate functional that is minimized is the grand-canonical

potential $\Omega[\Sigma]$ as a function of the self-energy. The latter can be parametrized by the single-particle hopping parameters \mathbf{t}' of the reference system,¹ and is then written as:

$$\Omega(\mathbf{t}') = \Omega' + \text{Tr} \ln[\mathbf{G}_{0,\mathbf{t}'}^{-1} - \Sigma(\mathbf{t}')]^{-1} - \text{Tr} \ln \mathbf{G}_{\mathbf{t}'} \quad . \quad (3.30)$$

Ω' and $\mathbf{G}_{\mathbf{t}'}$ are the grand-canonical potential and the Green's function of the reference system, respectively, and $\mathbf{G}_{0,\mathbf{t}'}$ is the noninteracting Green's function of the physical (lattice) system. The interacting Green's function $\mathbf{G}_{\mathbf{t}'}$ of the reference system is calculated from its ground state, and since its noninteracting Green's function $\mathbf{G}_{0,\mathbf{t}'}$ is also known, the self-energy can be obtained from Dyson's equation:

$$\mathbf{G}_{\mathbf{t}'} = \left(\mathbf{G}_{0,\mathbf{t}'}^{-1} - \Sigma \right)^{-1} \quad . \quad (3.31)$$

This finally allows one to evaluate Eq. 3.30 and minimize it to find the optimal parameter \mathbf{t}' . The power of the LDA+VCA approach is also evidenced by the results from calculations for TiOCl presented in Sec. 4.2.1.

Another method capable of yielding momentum-resolved spectral functions is the dynamical density-matrix renormalization group (dynamical DMRG or DDMRG) [Benthien04]. It is based on the (static) DMRG theory developed by White [White92], which is a variational approach and one of the most powerful methods for one-dimensional systems. Dynamical correlations are then introduced by variationally determining (frequency-dependent) corrections to the eigenstates of the system.² Although valuable insight could be gained from DDMRG (cf. Sec. 4.2.1 and [Benthien04]) the restriction to one dimension makes it much less flexible than, e.g., LDA+VCA, for the application to real systems.

3.4 Electron-Phonon Coupling

By virtue of the coupling between different degrees of freedom, phase transitions of the electronic system can induce changes in the crystal and magnetic structure, and vice versa. In all cases, the system wants to reach its ground state by either minimizing the electronic and/or the magnetic free energy. Depending on which of these is the driving force, one might encounter one of several different ground states, e.g., a charge-density wave (CDW), or a spin-Peierls state. This section is devoted to give a short outline of the underlying processes and the formalism used to describe these states.

First, consider the response of a free electron gas to an external perturbation $\phi(\mathbf{q})$ with wave vector $\mathbf{q} = 2\mathbf{k}_F$. If the perturbation is small, it will be linearly proportional to the induced charge density $\rho_{ind}(\mathbf{q})$,

$$\rho_{ind}(\mathbf{q}) = \chi(\mathbf{q})\phi(\mathbf{q}) \quad , \quad (3.32)$$

¹Primed quantities refer to the reference system.

²The interested reader is referred to [Jeckelmann02] for a more detailed discussion.

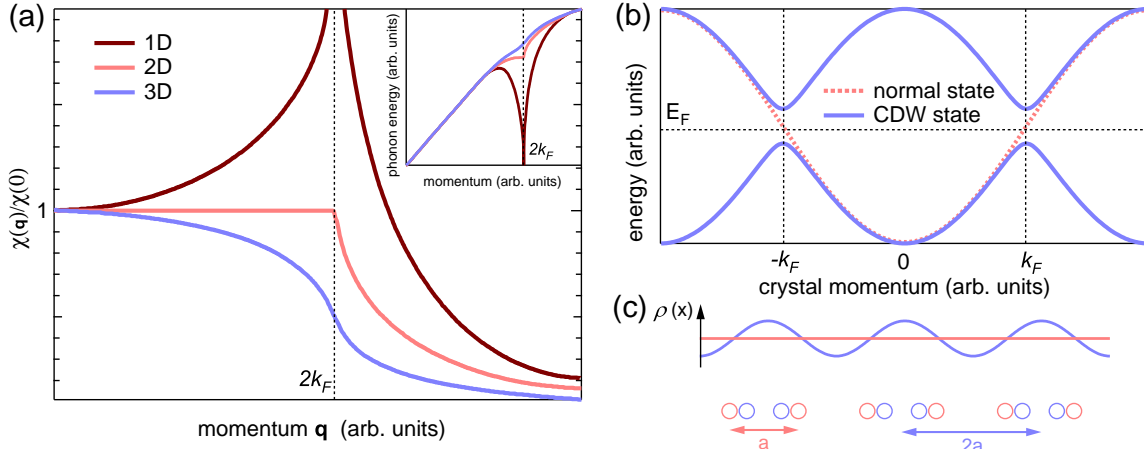


Figure 3.5: (a) \mathbf{q} -dependence of the Lindhard response function χ for a one- (brown), two- (red), and three-dimensional (blue) free electron gas at $T = 0$. The inset shows the corresponding phonon dispersions, which exhibit a Kohn anomaly. (b) Electronic dispersion in the normal (dashed red curve) and in the CDW (solid blue curve) state. (c) Position-dependent charge density (top) and schematic positions of ions (bottom) of a 1D chain with lattice parameter a in the normal (red) and in the CDW (blue) state.

with the susceptibility $\chi(\mathbf{q})$ being the so-called Lindhard response function

$$\chi(\mathbf{q}) = -e^2 \sum_{\mathbf{k}} \frac{f_{\mathbf{k}} - f_{\mathbf{k}+\mathbf{q}}}{\varepsilon(\mathbf{k}) - \varepsilon(\mathbf{k} + \mathbf{q})} . \quad (3.33)$$

$f_{\mathbf{k}} = f(\varepsilon(\mathbf{k}))$ is the Fermi distribution function. Its behavior in one, two, and three dimensions at $T = 0$ is shown in Fig. 3.5(a). In particular, the divergence in one dimension (1D) at $\mathbf{q} = 2\mathbf{k}_F$ shows that the free electron gas is highly susceptible even to the smallest perturbation with such a wave vector. With this in mind, the coupling to lattice vibrations (i.e., phonons) as the source of the perturbation shall be discussed.

The first to introduce a suitable Hamiltonian for this kind of coupling was Fröhlich in 1954, who also lends his name to the operator he described [Fröhlich54]:

$$\begin{aligned} H_{\text{Fröhlich}} &= H_0 + H_{el-ph} \\ &= \sum_{\mathbf{k}} \varepsilon_{\mathbf{k}} c_{\mathbf{k}}^\dagger c_{\mathbf{k}} + \sum_{\mathbf{q}} \hbar\omega_{\mathbf{q}} b_{\mathbf{q}}^\dagger b_{\mathbf{q}} + \sum_{\mathbf{k}, \mathbf{q}} g_{\mathbf{k}, \mathbf{q}} c_{\mathbf{k}}^\dagger c_{\mathbf{k}} \left(b_{-\mathbf{q}}^\dagger + b_{\mathbf{q}} \right) \end{aligned} \quad (3.34)$$

(“Fröhlich-Hamiltonian”) .

The first and second sum in this equation correspond to the unperturbed electron and phonon kinetic energy terms, respectively, while the third describes the electron-phonon interaction, with $g_{\mathbf{k}, \mathbf{q}}$ being the electron-phonon coupling constant. For the sake of simplicity, only one longitudinal mode is considered. The electrons are described using

creation and annihilation operators $c_{\mathbf{k}}^\dagger$ and $c_{\mathbf{k}}$ with wave vector \mathbf{k} , and free-electron band energies $\varepsilon_{\mathbf{k}} = \frac{\hbar^2 \mathbf{k}^2}{2m}$. The phonons are accordingly represented by bosonic operators $b_{\mathbf{q}}^{(\dagger)}$, having energy $\hbar\omega_{\mathbf{q}}$ and wave vector \mathbf{q} . The interaction between the two subsystems can be viewed as two independent processes, namely $b_{-\mathbf{q}}^\dagger c_{\mathbf{k}}^\dagger c_{\mathbf{k}}$ (phonon emission) and $b_{\mathbf{q}} c_{\mathbf{k}}^\dagger c_{\mathbf{k}}$ (phonon absorption).

Applying second-order perturbation theory to Eq. 3.34 the resulting total energy can be written as

$$\varepsilon = \varepsilon_0 + \langle \Psi | H_{el-ph} | \Psi \rangle + \langle \Psi | H_{el-ph} (\varepsilon_0 - H_0)^{-1} H_{el-ph} | \Psi \rangle, \quad (3.35)$$

where ε_0 is the unperturbed energy of Ψ , which has $n_{\mathbf{q}} = b_{\mathbf{q}}^\dagger b_{\mathbf{q}}$ phonons in the longitudinal mode \mathbf{q} and $n_{\mathbf{k}} = c_{\mathbf{k}}^\dagger c_{\mathbf{k}}$ electrons in the state \mathbf{k} . The first-order term vanishes, because it produces only states where one phonon has been added or destroyed, i.e., a state which is orthogonal to the ground state. As for the second-order term, a renormalization of the phonon frequency occurs, which leads to the perturbed phonon frequency

$$\hbar\omega_{\mathbf{q}}^{\text{pert}} = \hbar\omega_{\mathbf{q}} - \sum_{\mathbf{k}} 2|g_{\mathbf{q}}|^2 \frac{\langle n_{\mathbf{k}+\mathbf{q}} (1 - n_{\mathbf{k}}) \rangle}{\varepsilon_{\mathbf{k}} - \varepsilon_{\mathbf{k}+\mathbf{q}}}. \quad (3.36)$$

The resemblance of the sum in Eq. 3.36 to the one in Eq. 3.33 shows that the reaction of the phonon system happens also at $\mathbf{q} = 2\mathbf{k}_F$, and the resulting reduction of the phonon frequency, called ‘‘phonon softening’’, is referred to as the Kohn anomaly. The inset of Fig. 3.5(a) shows the dispersion of an acoustical phonon mode in one, two and three dimensions. As seen for the dielectric response function, the largest effect happens in 1D: Eq. 3.36 shows a singularity, but since a negative phonon frequency would be unphysical, a mere drop to $\hbar\omega_{\mathbf{q}}^{\text{pert}} = 0$ will be observed, i.e., the phonon ‘freezes in’ and causes a static lattice distortion, the so-called Peierls distortion. With increased dimensionality, this behavior is reduced to a kink at $2\mathbf{k}_F$. If one has a half-filled band, \mathbf{k}_F lies halfway between the BZ center and boundary. The static lattice (and, thus, charge-density) distortion due to the softened phonon mode then is commensurate with the lattice, leading to a doubled real-space unit cell [cf. Fig. 3.5(c)], which moves the boundary of the first BZ from π to $\pi/2$. This results in the opening of a gap at the Fermi vector and thus a metal-insulator transition, as can be seen in Fig. 3.5(b), i.e., the CDW state is insulating for half-filling.

3.5 Spin-Peierls Distortion and Spin Wave Theory

Being a general coupling operator, the Fröhlich Hamiltonian can be applied to the spin-phonon coupling as well. A widely used form of the electron hopping term (which is then governed by the spin degree of freedom) is that of the Heisenberg Hamiltonian, which shall be derived in the following. Applying perturbation theory as before, the first-order energy correction term vanishes again due to the orthogonality of spin states with

different occupation. Limiting the interaction to nearest neighbors, the Hamiltonian creating the second-order correction can be written as

$$H_{eff} = -\frac{t^2}{U} \sum_{\langle ij \rangle \sigma \sigma'} \left(c_{i\sigma}^\dagger c_{j\sigma} c_{j\sigma'}^\dagger c_{i\sigma'} + \text{h.c.} \right) . \quad (3.37)$$

σ and σ' label the spin state, and without loss of generality only a one-dimensional spin chain shall be considered. H_{eff} describes hopping processes in which an electron briefly co-occupies a neighboring, initially singly occupied site,¹ and then one of the two electrons at this site hops back. Due to the Pauli exclusion principle, this is only possible if the original electron at the neighboring site has its spin aligned antiparallel to the hopping electron. Thus, this energy gain is not effective for ferromagnetic (FM) arrangement, and as a consequence it is naturally described by an antiferromagnetic (AFM) exchange constant.

Introducing the spin operators $S_i^z = \frac{1}{2}(n_{i\uparrow} - n_{i\downarrow})$, $S_i^+ = c_{i\uparrow}^\dagger c_{i\downarrow}$, and $S_i^- = c_{i\downarrow}^\dagger c_{i\uparrow}$, as well as the Heisenberg exchange constant $J = 4t^2/U$, one can rewrite Eq. 3.37 to yield the Heisenberg Hamiltonian:

$$H_{\text{Heisenberg}} = -J \sum_{\langle ij \rangle} \left(\mathbf{S}_i \cdot \mathbf{S}_j - \frac{1}{4} \right) . \quad (3.38)$$

The constant offset of $J/4$ is due to the Pauli exclusion principle and is usually omitted. Of course, this Hamiltonian is not limited to AFM systems - FM exchange can be described by using a negative exchange constant.² An important point is that the ground state of a quantum-mechanical spin system described by Eq. 3.38 is *not* a statically ordered Néel state, but rather consists of fluctuating spins which can gain energy by forming (singlet) dimers. It can be shown that only for fully decoupled dimers the quantum-mechanical ground-state energy $-S(S+1)NJ$ is reached, which for small spin ($S = 1/2$) is obviously lower than the classical (Ising) value of $-S^2NJ$ [Duffy68, Ashcroft76]. A dimerization at half-filling is exactly what was observed in the CDW/Peierls case, the only difference being that here the magnetic instead of the electronic free energy is minimized. The resulting state is called a spin-Peierls state, which just as the Peierls state is favored in one dimension due to the singularity of the Lindhard function (Eq. 3.33) at $\mathbf{q} = 2\mathbf{k}_F$, but at the same time requires finite coupling to higher dimensions because no long-range order is possible in strictly one dimension.³

¹As before, the half-filled case is considered.

²Lifting the restriction to $n = 1$ (half-filling), the Heisenberg Hamiltonian can be generalized to the so-called t - J -model:

$$H_{t-J} = -t \sum_{\langle ij \rangle} \sum_{\sigma} \left[(1 - n_{i,-\sigma}) c_{i,\sigma}^\dagger c_{j,\sigma} (1 - n_{j,-\sigma}) + \text{h.c.} \right] + \frac{4t^2}{U} .$$

³This is the famous Mermin-Wagner-theorem [Mermin66].

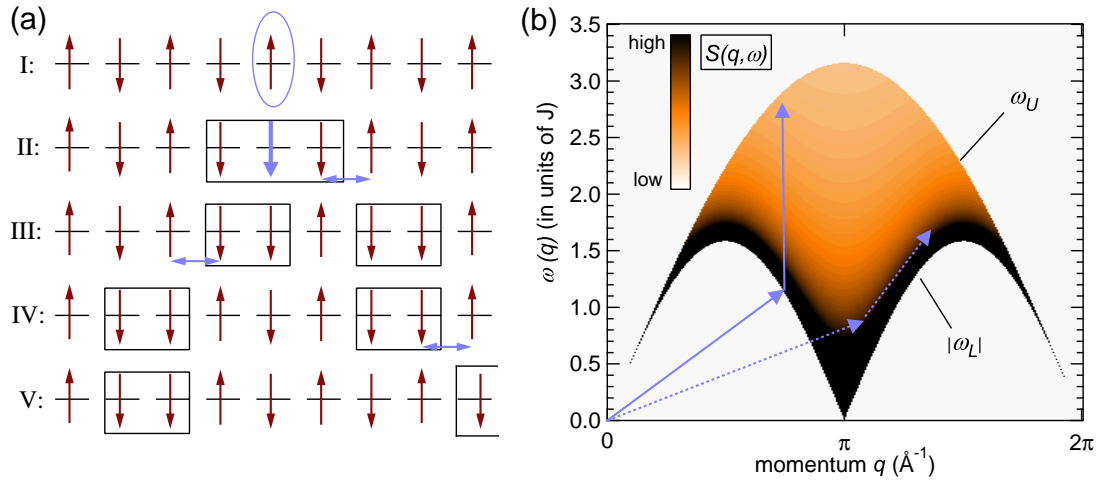


Figure 3.6: (a) One-dimensional $S = 1/2$ Ising model to illustrate the formation of (two-)spinon excitations. First, the spin marked in (I) by the blue ellipse is flipped, creating a $S = 1$ excitation extending over three sites in (II), marked by the rectangle. In (III), the two spins marked by the blue double-arrow have been interchanged (without an energy cost). This separates the excitation into two spinons. They can propagate independently, as illustrated in (IV) and (V). (b) Momentum-dependence of the dynamical structure factor $S(q, \omega)$, Eq. 3.39, and creation of the two-spinon continuum, illustrated by the linear superpositions of two spinon vectors. Highest weight of $S(q, \omega)$ is found along the lower boundary ω_L , and it is suppressed when ω_U goes to zero (e.g., in the zone center at $q = 0$).

Having established the ground state of the one-dimensional Heisenberg model, its excitations shall be discussed. The first thing to note is that the basic excitations are so-called “spinons” (with $S = 1/2$), instead of $S = 1$ spin waves [Lieb62]. In solving the model, the quantity of interest for comparison with experimentally measurable quantities is the dynamical two-spinon correlation function $S(q, \omega)$, also known as the dynamical structure factor (DSF). At $T = 0$ K it is approximately given by [Karbach97]:

$$S(q, \omega) = M(q, \omega)D(q, \omega) = \frac{\Theta(\omega - \omega_L(q)) \Theta(\omega_U(q) - \omega)}{\sqrt{\omega^2 - \omega_L^2(q)}} \quad . \quad (3.39)$$

$\Theta(x)$ is the Heavyside step-function, M is the two-spinon transition rate function, D their density of states, and ω_L (ω_U) the lower (upper) boundary of the two-spinon continuum, given by

$$\omega_L(q) = \frac{\pi J}{2} |\sin q| \quad \text{and} \quad \omega_U(q) = \pi J \left| \sin \frac{q}{2} \right| \quad . \quad (3.40)$$

Note that Eq. 3.39 is only an approximation, because one finds spectral weight also for energies above ω_U , although this weight is smaller by at least one order of magnitude than below ω_U [Müller81]. Figure 3.6(a) tries to illustrate why one always excites two spinons at once, using the example of a $S = 1/2$ Ising chain, where in the ground state all spins are aligned antiferromagnetically (I). Making an excitation, i.e., flipping one spin, requires a change of the spin by a total amount of 1 (II). Now, one spin of this entity with

$S = 1$ can be interchanged with the one next to it (which is oppositely aligned) without an energy penalty, because the total number of up- and down-spins is not changed (III). However, one realizes that the “ $S = 1$ excitation” has been split into two independently moving excitations. As the total spin of the chain remains unchanged, it is natural to assign to each of these a spin $S = 1/2$, i.e., they are spinons. The dispersion resulting for a single spinon is essentially given by $\omega_L(q)$, and that of a two-spinon excitation is a linear combination of the independent single-spinon dispersions, which results in the continuum bounded by ω_L and ω_U [see Fig. 3.6(b)].

The substructure of this continuum is given by the dynamical structure factor $S(q, \omega)$, as shown color-coded also in Fig. 3.6(b). From a closer inspection of Eq. 3.39 it can readily be seen that the DSF (i) diverges at ω_L , (ii) has a tail towards higher energies with a cut-off at ω_U , and (iii) becomes larger for increasing q . As a consequence, most spectral weight is found along the lower boundary (the des Cloizeaux-Pearson triplets [des Cloizeaux62]) and in particular at $q = \pi$, while it is zero at the zone center ($q = 0$).

4 On the Interplay of Different Degrees of Freedom

The interest in the oxyhalides of the form MOX ($M = \text{Ti, V}$; $X = \text{Cl, Br}$) originally developed in the early 1990's due to a work of Beynon and Wilson [Beynon93] who speculated that a resonating-valence-bond (RVB) state [Anderson73] could be realized in TiOCl and TiOBr (in the following, unless indicated otherwise, all arguments named in the context of TiOCl apply in the same manner to TiOBr as well). At that time, the newly discovered high-temperature superconductivity in layered copper oxide materials [Bednorz88] was speculated by notable theoreticians to arise from a RVB ground state of the undoped parent compound [Anderson87, Kivelson87], although this kind of state had not unambiguously been identified in any real system. As for the case of TiOCl , the idea was fueled by the intrinsic low-dimensionality of the crystal structure, its underlying quasi-triangular lattice introducing geometrical frustration of magnetic interactions, and the fact that it is a spin-1/2 system. All these factors promote quantum fluctuations which are essential for different kinds of quantum phases possibly observable at low enough temperatures. Although the magnetic susceptibility measured by Beynon and Wilson might have been interpreted in terms of the RVB picture as it showed Pauli paramagnetic behavior at low temperatures, it was found later on by Seidel *et al.* that the ground state is of the spin-Peierls kind [Seidel03]. However, this finding was hardly less interesting, as TiOCl was only the third inorganic material after CuGeO_3 [Hase93] and NaV_2O_5 [Fujii97] which showed such a state, and the transition temperature was significantly higher than in these other materials.

All oxyhalide samples investigated in the course of this thesis have been grown in our group by a chemical vapor transport (CVT) method, following the description by Schäfer *et al.* [Schäfer58]. In this procedure, the reactants are vacuum sealed at the one end of a quartz ampule, which is placed in a temperature profile. Over a period of typically two to three weeks, the direction of this gradient is switched several times. The temperature gradient is chosen such that one side (where the reactants are placed) is kept slightly above the dissolution temperature of the respective oxyhalide and all reactants (typically in the range of 550-650 °C), while the other is kept below this point. Thus, nucleation of single oxyhalide crystal sets in at the cold end, and a reversal of the profile leads to re-dissolution of the smallest among them. This avoids clustering of small single crystals with random orientation, and after several such steps, single crystals large enough for spectroscopic experiments (typical dimensions $2 \times 4 \times 0.1 \text{ mm}^3$) which do not consist of several twisted domains are obtained. The mixtures typically used to produce oxyhalide

crystals lead to the following reaction equations:



Some remarks shall be given on these reactions. While oxyhalide crystals are sufficiently inert under ambient conditions to handle them conveniently, the fact that highly reactive, liquid TiCl_4 is a product of Eq. 4.1 necessitates a thorough drying of TiOCl in an exsiccator before preparation for actual experiments. Although it is possible to use a reaction as for TiOBr (Eq. 4.2), the thus necessary handling of TiCl_4 as an educt is much more delicate than for TiCl_3 powder. Also, the resulting samples are of equal quality, which is why the method of Eq. 4.1 was employed almost exclusively for TiOCl . Upon growing VOCl , large crystals of up to $5 \times 10 \times 0.5 \text{ mm}^3$ were obtained much more often than for the titanium-based compounds. Nevertheless, smaller crystals were used preferably, because it was assumed that the likelihood of those being grown from twisted single crystals is smaller. A more detailed description of the CVT growth of oxyhalides (temperatures, durations, etc.) can be found in [Hoinkis06].

In the following, the basic properties of TiOCl will be summarized and compared to VOCl , for which several issues have been tackled in the scope of this thesis against the background of results from TiOCl : Is the dimensionality of the system, both electronically and magnetically, 1D or 2D? Which phase transitions occur, and to what ground state do they lead? And how do the electronic and magnetic interactions drive these transitions? In the line of arguments, previously unreported measurements on TiOCl using x-ray absorption spectroscopy, and resonant inelastic x-ray scattering will be presented, shining light on the unoccupied part of its electronic structure and charge-neutral excitations. In the subsequent chapter, further results of the current work, namely the occurrence of so-called electrostatic alloying under electron doping of TiOCl , is discussed extensively based mostly on data from photoemission spectroscopy.

4.1 Crystal and Magnetic Structure

4.1.1 Crystal Structure of the Oxyhalides

Although it is of course the dimensionality of the electronic (and correspondingly, the magnetic) structure which ultimately determines the physical behavior and in particular possible quantum fluctuations of a system, the crystal structure provides to a large extent the framework for a reduced dimensionality. The oxyhalides have an orthorhombic crystal structure of space group $Pmmn(59)$ shown in Fig. 4.1(a), with the lattice parameters from x-ray diffraction (XRD) measurements tabulated in Tab. 4.1. The local

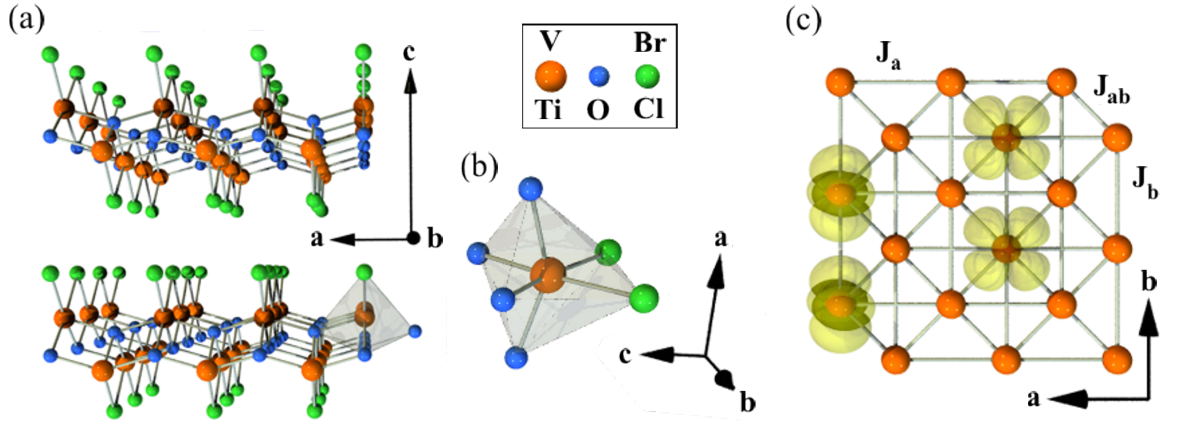


Figure 4.1: Basic structure of the oxyhalides. (a) Layered crystal structure consisting of Ti-O (V-O) double layers sandwiched by halide layers and separated by van-der-Waals gaps. (b) Distorted octahedral coordination of the transition metal (TM) ions by four O and two halide ions. (c) Quasi-triangular TM ion sublattice projected onto the ab plane and viewed along c . Also shown are two $d_{x^2-y^2}$ (left) and two d_{xz} (right) orbitals. In reality, neighboring TM ions along a are shifted along c , cf. panel (a). Exchange couplings J_a , J_b and J_{ab} are also indicated (same nomenclature for hopping integrals t).

symmetry around the Ti ions is C_{2v} ¹. The fundamental building blocks of this structure are Ti-O (V-O) double layers sandwiched by Cl (Br) layers along the crystallographic c axis. Between adjacent blocks along c , only weak van-der-Waals forces exist, thus decoupling them from each other by a gap and confining possible magnetic or electronic interactions to the crystallographic ab plane, i.e., to two dimensions. Looking along the c axis and drawing only the transition metal (TM) ions, a triangular sublattice becomes apparent [see Fig. 4.1(c)]. This is what makes antiferromagnetic (AFM) order potentially frustrated (depending on the magnitudes of the exchange couplings J_a , J_b and J_{ab} ; hopping integrals t defined accordingly) and was a key element in the assumption of possible RVB physics in the oxyhalides [Beynon93].

Locally, each TM ion lies in the center of a $[O_4 Cl_2]$ -octahedron as shown in Fig. 4.1(b). Due to the mixed nature of ligands and the fact that these octahedra are strongly distorted, the orbital degeneracy of the three-fold degenerate t_{2g} and the two-fold degenerate e_g orbitals found in octahedral environments is completely lifted. Choosing $x = c$, $y = b$ and $z = a$ as the basis, density-functional theory (DFT) calculations within the local-density or generalized-gradient approximation (LDA/GGA) result in the order and crystal-field splittings (CFS) shown in Tab. 4.1, with $d_{x^2-y^2}$ being the ground-state orbital. The electron clouds of $d_{x^2-y^2}$ extend along the b and c axis, while for the d_{xz} they lie in the ab plane and are rotated by 45° with respect to the crystal axes [cf. Fig. 4.1(c)]. As it can be seen in Fig. 4.1(a) ions of one kind (in particular the TM ions) form chains along the b axis, and neighboring chains are displaced along the chain direction by half a

¹Associated with the space group is the slightly higher symmetry D_{2h} ; this is just C_{2v} plus one inversion center.

Table 4.1: Properties of TiOCl, TiOBr and VOCl. Room-temperature lattice parameters from XRD, and crystal-field splitting (relative to $d_{x^2-y^2}$) and hopping integrals t from GGA downfolding (related to exchange integrals via $J_i = 4t_i^2/U$). Also given are transition temperatures deduced from magnetic susceptibility.

		TiOCl	TiOBr	VOCl
lattice parameters (Å)	a	3.779 ^a	3.787 ^b	3.770 ^c
	b	3.355 ^a	3.487 ^b	3.290 ^c
	c	8.027 ^a	8.529 ^b	7.930 ^c
crystal-field splitting (eV) (calculated)	d_{xz}	0.241 ^d	0.295 ^e	0.025 ^d
	d_{yz}	0.46 ^d	0.66 ^e	0.33 ^d
	d_{xy}	1.54 ^d	1.45 ^e	1.63 ^d
	d_{z^2}	2.08 ^d	2.25 ^e	1.93 ^d
hopping integrals (eV) (calculated)	t_a	0.04 ^f	0.06 ^f	— ^g
	t_b	-0.21 ^f	-0.17 ^f	— ^g
	t_{ab}	0.03 ^f	0.04 ^f	— ^g
transition temperatures (K)	T_{c1}	67 ^d	28 ^f	($T_{Néel}$) 79 ^d
	T_{c2}	91 ^d	48 ^f	— ^g

^afrom [Schäfer58]

^bfrom [von Schnering72]

^cfrom [Vénien79]

^dfrom present study

^efrom cluster calculations [Fausti07]; corresponding values for TiOCl are consistently larger than those from GGA given here, i.e., the values for TiOBr are possibly overestimated.

^ffrom [Lemmens05]

^gnot available

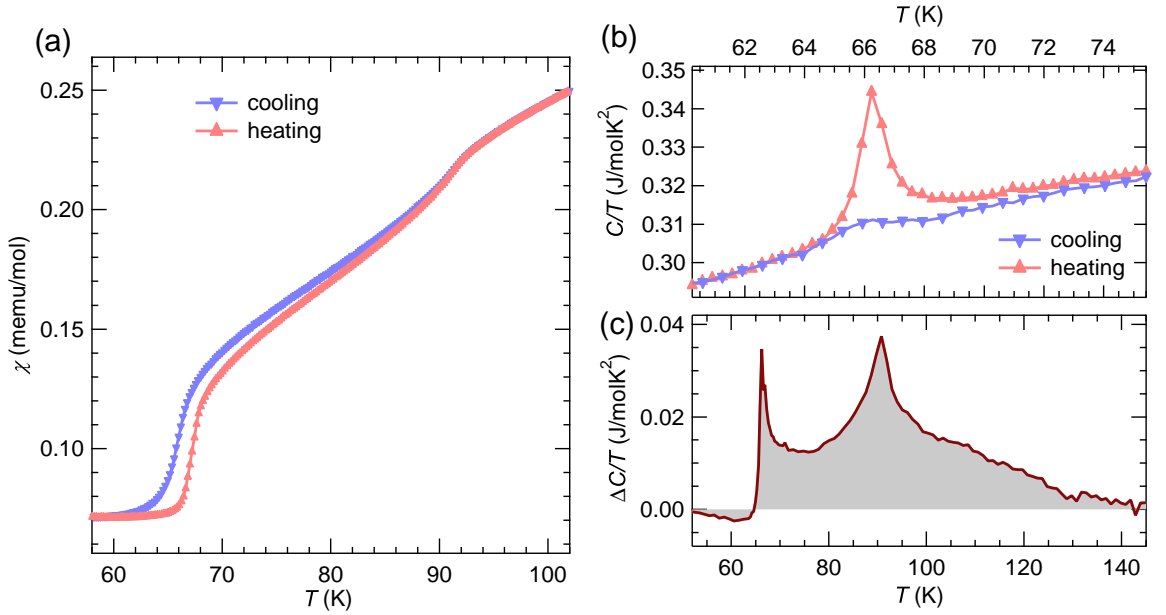


Figure 4.2: (a) Magnetic susceptibility χ from cooling and heating cycles after subtraction of a Curie-like contribution stemming from magnetic impurities. Two successive phase transitions are well discernible at $T_{c1} = 67$ K and $T_{c2} = 91$ K. (b) Heat capacity, plotted as C/T vs. T , in the proximity of the phase transition at T_{c1} . The clear hysteresis between cooling and heating indicates a first-order transition. (c) Difference between modeled and measured heat capacities in the range between the two phase transitions, corresponding to the released entropy.

lattice constant. From ionic considerations, it follows that there is one electron residing at the Ti and two electrons at the V site, creating $3d^1$ and $3d^2$ electronic configurations, respectively, and leaving the TM ions with a formal valency of 3+. Thus, in TiOCl only the $d_{x^2-y^2}$ orbital is expected to be occupied, although d_{xz} is only slightly higher. This creates a preferred one-dimensional (1D) hopping path along the b direction. In VOCl, on the other hand, where the second electron can (and, as it will be shown, actually does) additionally occupy the d_{xz} orbital, a considerably lower in-plane anisotropy is expected. These considerations give strong evidence already from the crystal structure that TiOCl is electronically (quasi-)one-dimensional, while VOCl should behave more like a two-dimensional (2D) system. Later in this chapter, photoemission spectroscopy will be used to experimentally verify and clarify this issue.

4.1.2 The Spin-Peierls Transition in TiOCl

Thermodynamic quantities are powerful tools to observe phase transitions. Figure 4.2 shows the magnetic susceptibility χ and the heat capacity $C(T, H)$ of TiOCl. Measurements of χ using a SQUID magnetometer were performed by M. Klemm, those of C by J. Hemberger [Hoinkis05, Hemberger05].

As the temperature is lowered, a drop of the susceptibility can be seen in Fig. 4.2(a) at $T_{c2} = 91$ K (48 K for TiOBr, cf. [Lemmens05]), followed by a hysteretic behavior at $T_{c1} = 67$ K (28 K for TiOBr). There are obviously two successive phase transitions, the one at lower temperatures being of first order (hysteretic behavior), while the other one appears to be of second order.¹ After subtracting a Curie contribution, which becomes effective at low temperatures and is caused by magnetic impurities, the low- T susceptibility is essentially temperature-independent. Using a Bonner-Fisher curve corresponding to a 1D Heisenberg model with nearest-neighbor interaction to fit the high-temperature part of χ above roughly 130 K (not shown here), an exchange constant of $J = 660$ K can be extracted [Seidel03]. Figure 4.2(b) shows the heat capacity, plotted as C/T , around T_{c1} . Again, a clear hysteresis between cooling and heating indicates the first-order character of this transition. Over a large temperature range (not shown), the heat capacity is that of a three-dimensional (3D) solid dominated by phonons, with a Debye temperature of approximately 200 K, but with a sizable spin-derived component [Hemberger05]. Modeling these two contributions (using one Debye- and two Einstein-like parts, together with a small contribution corresponding to a spin-1/2 chain) one sees that the behavior is not fully captured: from the difference between the experimental and modeled heat capacities a residual entropy release of $S = 0.12R$ can be observed, corresponding to the integral of the curve shown in Fig. 4.2(c). This release is not completed before approx. $T^* \approx 130 - 140$ K, in good agreement with the fluctuation regime and pseudogap observed in NMR [Imai03]. Note also that the value of $0.12R$ is vanishingly small compared to $R \ln 2$ expected for a doubly-degenerate orbital state. Since below T_{c1} a phonon-derived term alone describes the heat capacity satisfactorily it can be concluded that the fluctuations in the relevant temperature range ($T_{c1} < T < T^*$) are simply dominated by the complex spin-Peierls scenario described in the following, instead of possible additional contributions from, e.g., orbital fluctuations. A quenching of the orbital degree of freedom has also been confirmed by various calculations of orbital (crystal-field) splittings [Saha-Dasgupta04, Saha-Dasgupta05, Rückamp05b] and polarization-dependent PES measurements presented later [Hoinkis05].

Figure 4.3(a) shows XRD data along $(2, k, -1)$ around T_{c1} measured by Shaz *et al.* [Shaz05]. Going through the phase transition, a superlattice reflection suddenly appears at $(2, 1.5, -1)$ indicating a unit-cell doubling along b , which can be explained by a dimerization of Ti ions [Seidel03]. As this leads to the formation of $S = 0$ spin singlets the phase below T_{c1} can unambiguously be identified as being of the spin-Peierls kind. However, a canonical spin-Peierls transition would involve only one transition which should be of second order. In order to elaborate on this point, it is worth noting again that the spin-Peierls state is a signature of (predominantly) 1D physics. The Bonner-Fisher behavior of the magnetic susceptibility above T_{c2} indicates 1D character in the high-temperature phase as well, and the question arises what happens in the intermediate phase ($T_{c1} < T < T_{c2}$). From the electronic point of view, band structure calculations

¹Recently, there has been a debate about this interpretation, cf. [Schönleber08].

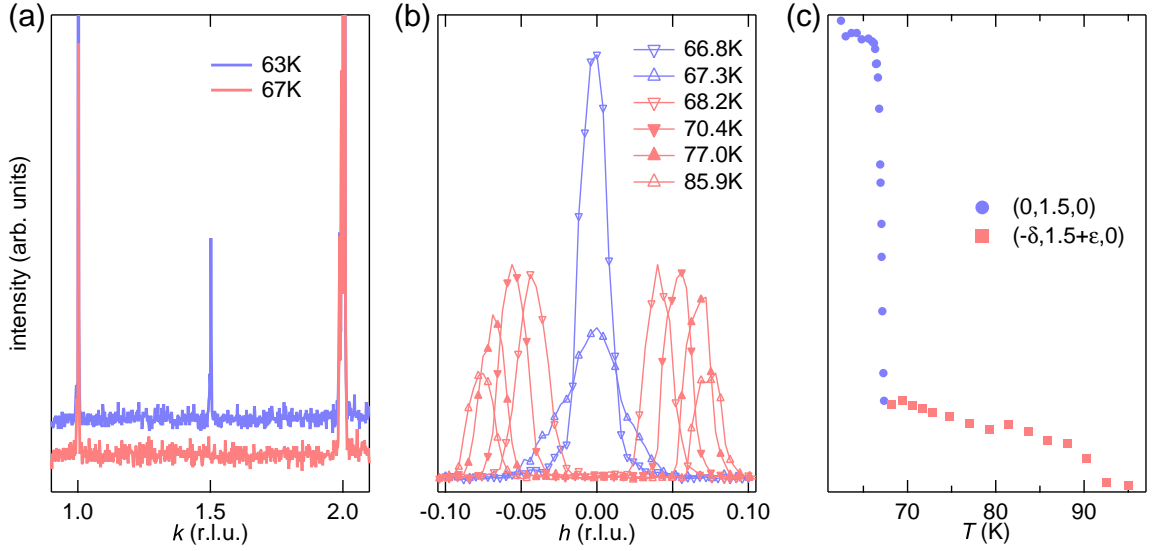


Figure 4.3: Commensurate and incommensurate superstructure reflections observed in x-ray diffraction. (a) Scan along the $(2, k, -1)$ path in reciprocal space slightly below and above T_{c1} . (b) $(h, 1.5, 0)$ scans for temperatures from slightly below T_{c1} well into the intermediate phase. (c) Temperature behavior of the intensities of commensurate (blue) and incommensurate (red) peaks across the two phase transitions.

of the room-temperature crystal structure yield a ratio of the intrachain and interchain hopping matrix elements t_b and t_{ab} of roughly 7:1 (see Tab. 4.1) [Saha-Dasgupta04], which makes the interaction perpendicular to the chains small but finite, and leads to magnetic frustration. At low enough temperatures, this can result in an incommensurate modulation of the lattice due to a competition between frustration and the tendency for spin-Peierls ordering [Rückamp05a, Zhang08a]. Extended XRD studies by several groups have been able to identify the incommensurability [van Smaalen05, Schönleber06, Krimmel06, Clancy07, Schönleber08]. Figure 4.3(b) shows that the $(0, 1.5, 0)$ reflection in the intermediate phase is split into two peaks when scanning along the a^* direction in reciprocal space, evidencing the incommensurate nature of this phase [Krimmel06]. In panel (c) the intensities of the commensurate $[(0, 1.5, 0)]$ and incommensurate $[(-\delta, 1.5 + \epsilon, 0)]$ peaks are plotted versus temperature, and one sees that exactly at T_{c1} the latter merge into the commensurate peak, i.e., the lattice modulation “locks in” at this temperature.

4.1.3 Antiferromagnetic Order in VOCl

As pointed out before, each V site houses two electrons in the $3d$ shell. From band structure calculations presented in Sec. 4.2.1 and the energy considerations summarized in Tab. 4.3 it follows that two orbitals of different character are involved, allowing for and favoring parallel spin alignment at a given V site, which results in $S = 1$. However, the

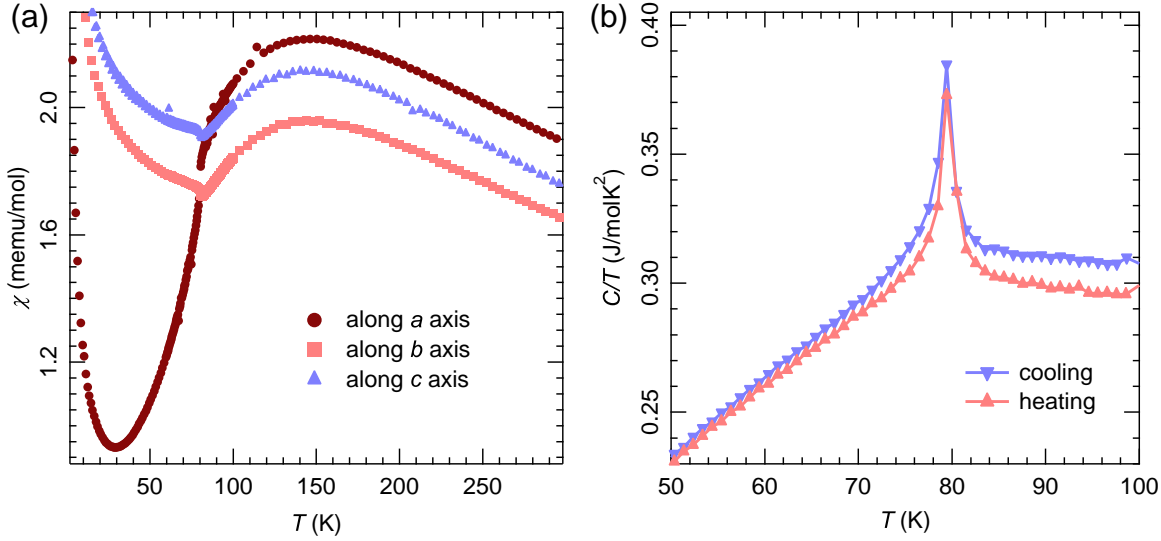


Figure 4.4: (a) Magnetic susceptibility χ of VOCl with the magnetic field applied along the different crystallographic axes. Data points from both cooling and heating are shown, but not discernible on this scale. At $T_{N\acute{e}el} \approx 79$ K a transition from isotropic to in-plane anisotropic behavior is observed by a drop of χ when the field is applied along the a axis. (b) Heat capacity of VOCl in the temperature range close to the phase transition. No hysteresis is observed, i.e., the transition is of second order.

distinctly different behavior of the magnetic susceptibility of VOCl shown in Fig. 4.4(a) from the one of TiOCl has other origins: at $T_{N\acute{e}el} \approx 79$ K a kink is observed, concomitant to an anomaly in the heat capacity shown in panel (b) [Glawion09]. Aligning the samples such that the magnetic field is applied along a certain crystallographic axis, below $T_{N\acute{e}el}$ an anisotropy can be seen by a sharp drop along the a axis, while there is only a slight upturn along b and c . This signifies a transition to an antiferromagnetically ordered Néel state with the spins pointing along a . As there is no hysteresis neither in the heat capacity nor in the susceptibility between heating and cooling cycles (as a matter of fact, the SQUID data shown is a full cooling/heating cycle) this gives strong evidence that the phase transition is of second order.

There is independent experimental and theoretical evidence that supports these findings. In an early neutron diffraction study on powder samples, a complicated two-dimensional magnetic order with moments pointing along the a direction was proposed [Wiedenmann83]. Very recently, two independent, combined neutron diffraction and XRD studies have been performed. While Komarek *et al.* [Komarek09] used only powder samples, Schönleber *et al.* [Schönleber09] applied these methods to both powder and single crystals. Since both draw the same conclusions, only the powder data of Komarek *et al.* will be discussed in the following.

In XRD, the (212) and (-212) [as well as the (121) and (-121)] reflexes of the original orthorhombic $Pm\bar{m}n$ structure split for temperatures below $T_{N\acute{e}el} \approx 79$ K, as can be seen

in Fig. 4.5(a). The low-temperature phase was found by a so-called Rietveld refinement¹ of a wide-range $\theta-2\theta$ -scan to involve a monoclinic distortion along the c axis, compatible with space group $P2/n$. Since this is a subgroup of $Pm\bar{m}n$ the observed change of the lattice parameters ($\delta_{max} < 0.4\%$) and the monoclinic angle γ from 90.0° to 90.2° deduced from the refinement correspond to a symmetry reduction, as opposed to a structural change. The neutron diffraction data acquired by these authors [see Fig. 4.5(b)] can be fitted to the same space group below the transition temperature, but two additional peaks at $(\frac{1}{2} \frac{1}{2} \frac{1}{2})$ and $(\frac{1}{2} \frac{1}{2} \frac{3}{2})$ with respect to the nuclear lattice structure (as opposed to the magnetic structure) appear, marked by the arrows in Fig. 4.5(c). These are clearly connected to the magnetic structure, since XRD would not be sensitive to a corresponding superstructure, in contrast to neutron diffraction. These peaks imply a magnetic propagation wave vector $\mathbf{k} = (\frac{1}{2} \frac{1}{2} \frac{1}{2})$, corresponding to a magnetic supercell enlarged by $2 \times 2 \times 2$. Thus, the subgroup $P112/n$ of $P2/n$ has to be assumed to account for the actual magnetic structure found from neutron diffraction. This group has four possible irreducible representations with different alignment of the spins, which are shown in Fig. 4.5(d) and labeled AFM1–AFM4. In the original space group the configurations AFM1 and AFM2 (and also AFM3 and AFM4) are not distinguishable, because there is only one nearest-neighbor exchange coupling J_{ab} . In the present case, however, this frustration of the lattice is partially lifted due to the monoclinic distortion, which introduces unequal couplings $J_{ab}^<$ and $J_{ab}^>$. Rietveld refinement results using these different configurations are also shown in Fig. 4.5(b). Upon closer inspection one sees that only AFM1, which has its moments aligned along the a direction, can describe both magnetic peaks at once.

The interplay of the magnetic configuration and exchange processes with the observed structural modulation depends on the actual values of J_a , J_b , and $J_{ab}^{>,<}$. In the oxyhalides, nearest-neighboring TM ion chains are displaced along the c axis, thus favoring superexchange between *next*-nearest-neighboring chains via the intermediate O ion. This interaction, scaling with the exchange coupling J_a , is antiferromagnetic, and explains the doubling of the unit cell along a when a static AFM order sets in. It appears tempting to make a connection of the unit-cell doubling within one chain along the b axis in VOCl to the one observed in the spin-Peierls state of TiOCl, as the respective exchange coupling J_b is also antiferromagnetic. However, the structural distortion observed in the latter [cf. Fig. 4.3(a)] is absent in VOCl, and the monoclinic lattice distortion is thus driven solely by the magnetic interactions. As a result, the V–O–V bond angle becomes closer to 180° , which flattens the VO planes and thus favors the superexchange, as the latter would be at its maximum for 180° . Most remarkably, however, the distance between V ions lying in the direction of $J_{ab}^>$ differs from the one along the direction of $J_{ab}^<$ by roughly 0.0073 \AA . This makes $J_{ab}^>$ and $J_{ab}^<$ inequivalent due to different orbital overlap, ultimately stabilizing the configuration AFM1 shown in Fig. 4.5(d).

This interpretation is further justified by calculating the energies of the different con-

¹A standard fitting procedure to identify crystal structures from diffraction patterns.

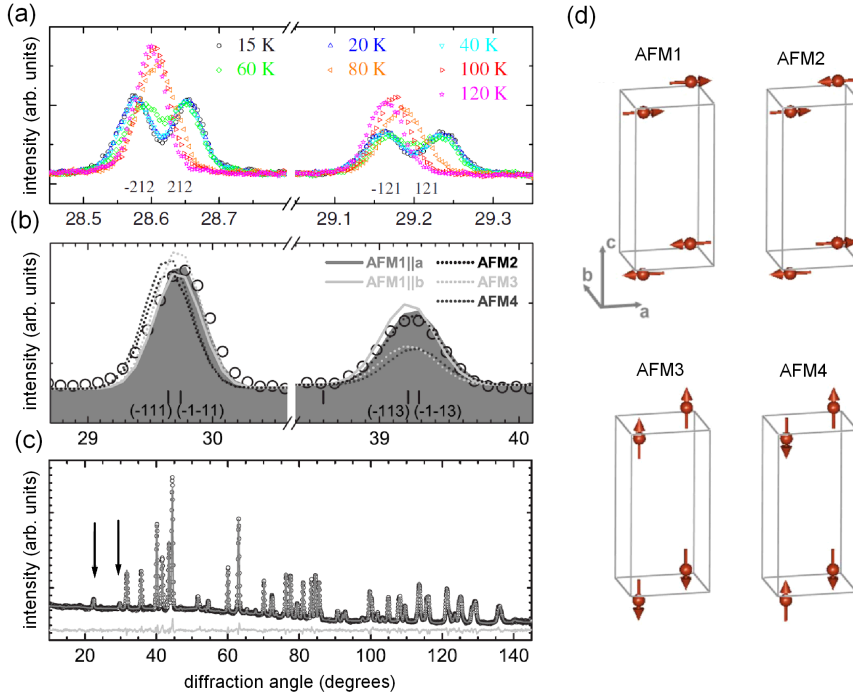


Figure 4.5: X-ray and neutron diffraction data of VOCl (from [Komarek09]). (a) Temperature dependence of the (± 212) and (± 121) reflexes from powder XRD. Below the phase transition at $T_{\text{Néel}} \approx 79$ K, a splitting of the peaks is observed. (b) Blow-up of the magnetic peaks measured in neutron scattering at $T = 2$ K. Also shown are Rietveld fits to the data with the different structures shown in panel (d). (c) Wide-range $\theta - 2\theta$ -scan from powder neutron diffraction at $T = 10$ K. Arrows mark two additional peaks compared to XRD, which are connected to the magnetic structure and shown in panel (b). They correspond to $(\frac{1}{2} \frac{1}{2} \frac{1}{2})$ and $(\frac{1}{2} \frac{1}{2} \frac{3}{2})$ with respect to the nuclear lattice structure [$(\pm 1 \mp 11)$ and $(\pm 1 \pm 13)$ with respect to the magnetic structure]. (d) Possible magnetic configurations of VOCl ions within the $P2/n$ space group. In AFM1 and AFM2, spins lie in the ab plane while they are aligned parallel to the c axis in AFM3 and AFM4.

figurations within GGA+ U and then mapping the results to a 2D Heisenberg model, which was done for the orthorhombic phase [Glawion09]. Although the values depend on the choice of the effective on-site Coulomb interaction $U_{eff} = U' - J$, it turns out that in any case $J_a > J_b > J_{ab}$ (e.g., $J_a/J_b = 1.1$ at $U_{eff} = 1.3$ eV and $J_a/J_b = 1.6$ at $U_{eff} = 3.3$ eV). Both J_a and J_b are always antiferromagnetic, reflecting the 2D magnetic order with spins pointing along the a axis (i.e., lying in the ab plane) already found in the magnetic susceptibility. The nature of J_{ab} , however, depends on the U_{eff} value such that, e.g., $J_{ab}/J_b = 0.31$ at $U_{eff} = 1.3$ eV, while $J_{ab}/J_b = -0.5$ at $U_{eff} = 3.3$ eV. This reflects the frustration present in the high-temperature phase, as obviously both ferro- and antiferromagnetic components can contribute with basically equal magnitudes to J_{ab} . Unfortunately, no calculations have been performed for the structure including the monoclinic distortion, which might have allowed to give further justification for the AFM1 order found by neutron scattering.

4.2 Electronic Structure

In the preceding sections, the issues of dimensionality, fluctuations and correlations in TiOCl and VOCl have been addressed from the viewpoint of the lattice and the magnetic interactions. It was found that in the magnetic sector TiOCl has a more pronounced 1D character than VOCl, and that frustration prevents the system from reaching its (spin-Peierls) ground state over a wide temperature range. At several occasions information about the electronic structure has already been mentioned, which will be discussed and further elaborated on in this section. The key experimental method is photoelectron spectroscopy (PES), which is complemented by several theoretical approaches, namely density-functional and dynamical mean-field theory (abbreviated DFT and DMFT, respectively) solved by various methods. From these, first the insulating nature of the oxyhalides as being due to correlations will be explained. Afterwards, the question of dimensionality will be tackled by angle-resolved photoemission spectroscopy (ARPES), with additional comparison to specific model calculations. As in the previous section, the line of arguments will be driven by a close comparison of the respective aspects of TiOCl and VOCl as well as TiOBr. This section closes with an extensive discussion of spectroscopic data on the unoccupied electronic structure of TiOCl obtained using x-ray absorption spectroscopy (XAS), as well as excitations observed by resonant inelastic x-ray scattering (RIXS). This data is compared to spectra simulated within configuration interaction, multiplet and spinon theory.

4.2.1 Valence Density of States from Photoemission

The most important aspect that must be reproduced by any calculation of the electronic structure is the insulating nature of the oxyhalides. For the $3d^1$ system TiOCl it is clear that this will not be possible in a single-particle picture where many-body effects are not

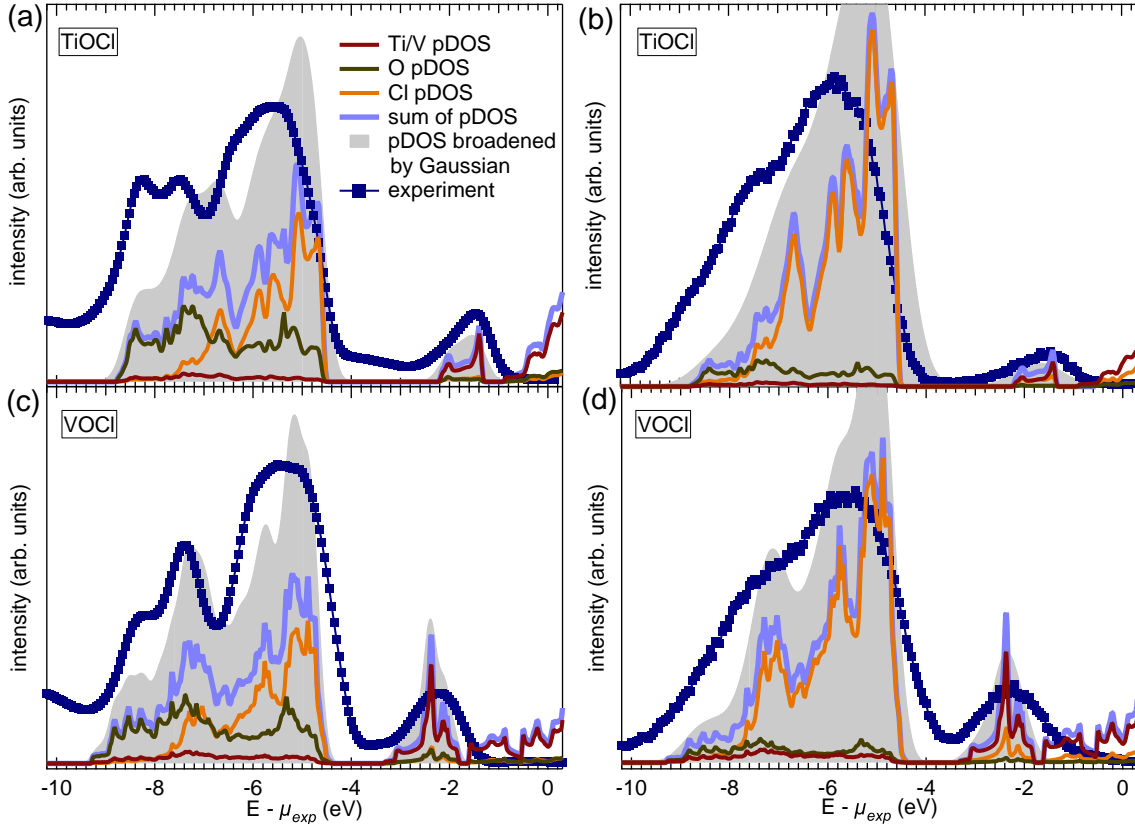


Figure 4.6: Angle-integrated valence electronic structure of TiOCl (a,b) and VOCl (c,d). Spectra have been measured with UPS (left) and XPS (right). Also shown is the pDOS from GGA+ U calculations weighted by the photoionization cross-sections at the corresponding excitation energies, the total DOS obtained by summing the pDOS, and the total DOS broadened by a Gaussian with FWHM 70 meV [panels (a),(c)] and 150 meV [panels (b),(d)], respectively. All spectra have been normalized to equal spectral weight over the range from -10 eV to μ_{exp} .

properly accounted for, as fully occupied bands are a necessary condition for solids to be insulators in this limit. Since VOCl has two d electrons, it might well be that it has band insulating character if these electrons were to occupy the same d subband, which would thus be full. However, should single-particle calculations yield a metallic state, this would identify VOCl as a Mott insulator.

UPS and ARPES experiments have been conducted in our home lab using the He I_α radiation ($h\nu = 21.2\text{ eV}$) from a helium discharge lamp, as well as core level spectroscopy (XPS) using a monochromatized excitation source yielding Al K_α radiation ($h\nu = 1486.6\text{ eV}$). The total energy resolution of the OMICRON EA125 analyzer used for the results presented here was set to 70 meV for UPS/ARPES, and 700 meV for XPS, respectively. The pressure in the vacuum chamber was in the low 10^{-10} mbar regime during the measurements. Unless noted otherwise, all PES measurements were performed

at slightly elevated temperatures ($T = 360 - 370$ K). Due to the strongly insulating nature of the oxyhalides, photoemission leads to charging, which manifests itself most prominently in a rigid energetic shift of the spectrum. Tracking the energy of a suitable spectral structure (we used the maximum of the Ti $3d$ spectral weight, see below) upon temperature variation a saturation of the shift above $T \approx 360$ K is observed, such that the maximum of the Ti $3d$ peak comes to rest at 1.45 eV below the chemical potential μ_{exp} . The latter was determined from the Fermi edge of sputtered polycrystalline silver foil [Hoinkis06]. This dependence is due to thermally activated charge carriers which partially compensate the missing photoelectrons, and the position determined from the temperature series was used as an absolute reference point to which all spectra (even those acquired at lower temperatures) were shifted. The value obtained for VOCl by the same method is 2.3 eV.

The DFT calculations were performed using the Full Potential Linearized Augmented Plane Wave basis as implemented in the WIEN2k code [Blaha01], with a k mesh of $(15 \times 17 \times 7)$ in the irreducible Brillouin zone.

The experimentally observed angle-integrated valence spectra together with the densities of states (DOS) calculated using the generalized gradient approximation including local correlations (GGA+ U) of TiOCl and VOCl are shown in Fig. 4.6. Two basic observations from experiment are consistently reproduced in the total DOS from GGA+ U for both compounds. Firstly and most importantly, the oxyhalides are insulators with a finite gap between the highest occupied states and the chemical potential of approx. 0.7 eV and 1.1 eV for TiOCl and VOCl, respectively. Below it will be shown that a gap only appears upon inclusion of strong correlation effects in a phenomenological manner using a Hubbard U . It is thus a correlation-induced gap, and in a simple Mott-Hubbard scenario the values just given correspond to half the gap between the lower and upper Hubbard bands (LHB and UHB), respectively. The second characteristic feature is a separation of the spectra into a low-energy part close to the chemical potential ($E - \mu_{exp} > -4$ eV) and a high-energy part ($E - \mu_{exp} \approx -9$ to -5 eV). The figure contains also the calculated contributions from the different atomic species (Ti/V, O, Cl) separately. The total DOS is the sum of these individual contributions, which however have to be weighted with the photoionization cross-sections at the excitation energy used (21.2 eV or 1486.6 eV, respectively) to compare them with experimental spectra. For single atoms, the cross-sections are tabulated [Yeh85] and have as such been used here, although this is expected to introduce a significant uncertainty when applied to the actual situation of ions in a solid. They are strongly dependent on the energy of the incoming photon, which leads to the pronounced differences especially in the high-energy part between the two excitation energies. For the UPS valence spectrum, this part can roughly be further subdivided into a peak of mostly Cl character in the range $-6.5 < E - \mu_{exp} < -4$ eV, and a structure of mixed O and Cl character below -6.5 eV, while in the XPS case it is completely dominated by Cl character. The changes of shape in the O/Cl bands for different excitation energies are nicely accounted for by the appropriate cross-sections, despite the uncertainty just mentioned. Even more important,

however, is the low-energy part: in all cases, this structure barely changes its shape due to the fact that it is almost completely derived from TM d orbital character. This is not a resolution effect, but instead shows that there is only small hybridization with the ligand O and Cl orbitals, which is especially important when interpreting this feature in terms of Hubbard bands.

Further experimental evidence on hybridization can be gained from resonant photoemission spectroscopy (ResPES). Since the absorption edge at which this is performed is element-specific, only contributions from the respective element are expected to be resonantly enhanced, according to what was described in Sec. 2.3. We performed measurements around the Ti L_3 edge at beamline UE56-2/PGM-2 of the synchrotron BESSY II in Berlin, Germany, using the MUSTANG endstation at which a SPECS PHOIBOS 150 electron analyzer was installed. The polarization-dependent photoemission spectroscopy (PolPES) discussed later, as well as XAS and ResPES measurements shown in Secs. 4.2.3 and 5.1.2, respectively, were also taken with this setup.¹ The pressure in the vacuum chamber was below $1 \cdot 10^{-9}$ mbar during the measurements. The energy resolution as well as the position of the chemical potential were determined from the Fermi edge of a sputtered polycrystalline silver foil, the former being 350 meV at $h\nu = 500$ eV.

Results for TiOCl are compiled in Fig. 4.7. From the ResPES spectra in panels (a) and (b) it can be seen that the Ti $3d$ peak shows a clear resonant enhancement by a factor of ~ 8 [cf. Fig. 4.7(d)] when adjusting the excitation energy across the main peak of the absorption edge [see points marked in Fig. 4.7(c)]. Effects on the high-energy bands are much less pronounced, in line with the observation that they are dominated by O and Cl character. Their seemingly stronger enhancement along a is a misconception, however, because actually the low-energy part is *less* enhanced than along b . This becomes clear from comparing spectra labeled 'b' (first on-resonance spectrum) and 'f' (resonance-maximum spectrum) in the two cases. Since a more detailed discussion of these bands based on the available data is destined to remain inconclusive, however, we will turn our attention back to the low-energy Ti $3d$ spectral weight.

Figure 4.7(d) shows the development of the Ti $3d$ peak maximum for beam energies across the L_3 absorption edge. Ideally, it should follow a Fano-like behavior given by Eq. 2.33, as shown in Fig. 2.5(a). However, one realizes from a comparison to a curve of this form that the experimentally determined resonance is significantly narrower. It must be noted here that even the fair agreement concerning the height of the resonance between the experimental values and the curve with lineshape parameter $q = 2.5$ (chosen for its comparatively good agreement with experimental data points) depends strongly on the relative normalization of the measured PES spectrum, for which no canonical guideline is available.² Also, during the limited amount of beamtime, spectra could only be measured at a rather small number of photon energies, which inhibits an unambigu-

¹In all these cases linearly polarized synchrotron light was used. For the remainder of this thesis, the term “light polarization along the a/b axis” will be replaced by “along the a/b axis” or “along a/b ”.

²Thus, normalization to equal effective acquisition time was performed.

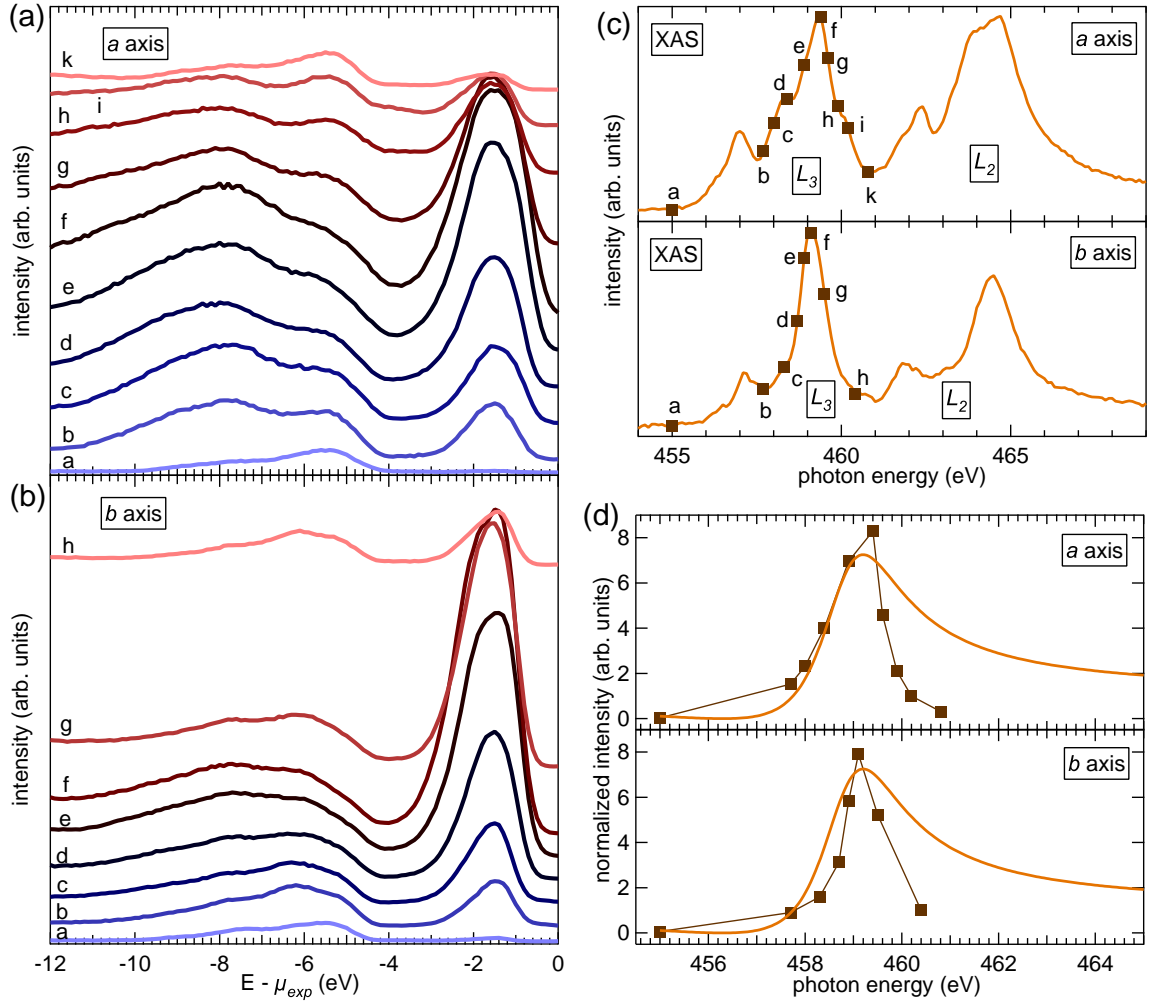


Figure 4.7: Angle-integrated Ti *L* edge ResPES of the TiOCl valence band with light polarization along the (a) *a* and (b) *b* axis, respectively. Different photon energies are marked by letters according to those assigned in the corresponding absorption spectra shown in panel (c) along the *a* (top) and *b* (bottom) axis, respectively. To account for increased sample charging for high resonant enhancement all spectra have been shifted in energy such that the Ti 3*d* peak is centered at 1.5 eV below μ_{exp} . The observable broadening of this peak is another charging effect. All spectra were normalized to equal effective acquisition times. (d) Resonant enhancement of the Ti 3*d* peak for the different photon energies along *a* (top) and *b* (bottom), determined from the peak height after background subtraction. These values were normalized so that the height at $h\nu = 460.2$ eV ($h\nu = 460.4$ eV) along *a* (*b*) is equal to one. The solid lines show Fano curves (Eq. 2.33) for $q = 2.5$.

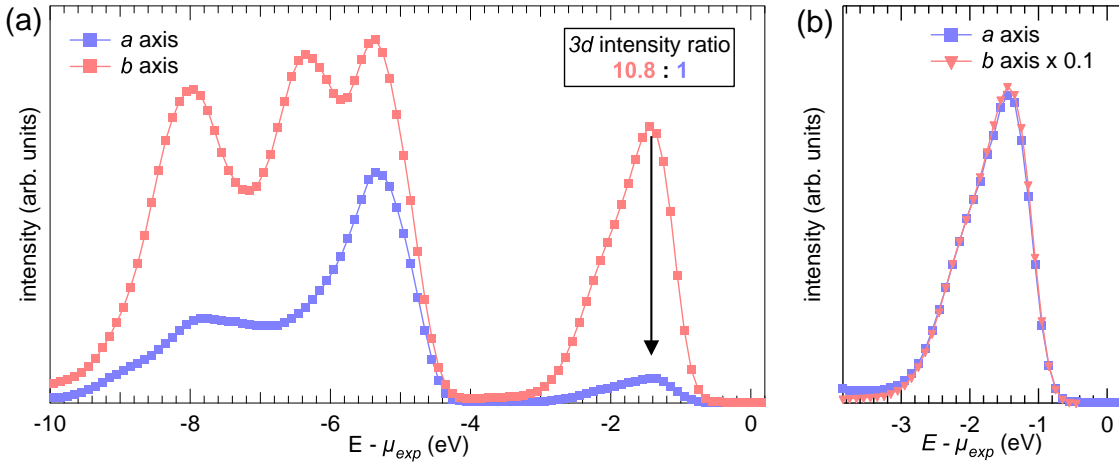


Figure 4.8: Polarization-dependent angle-integrated PES on TiOCl taken in normal emission at an excitation energy of $h\nu = 150$ eV. (a) Full valence band. Spectra have been normalized using the photocurrent induced in the mirror of the beamline optics (“mirror current”). The spectral weight of the Ti 3d derived peak reduces by a factor of 10 when switching from horizontal (along b ; red curve) to vertical (along a ; blue curve) polarization. (b) Same data in the range around the Ti 3d peak, with the spectrum along b divided by 10 to evidence the absence of a change in peak shape.

ous identification of the interference effects leading to the characteristic photocurrent suppression *before* the resonance [cf. Fig. 2.5(a)]. Finally, the interpenetration of the L_2 and L_3 absorption edges in TiOCl visible in Fig. 4.7(c) exacerbates a determination of the individual resonances of these two edges, because the L_2 resonance already sets in before the L_3 resonance is completely traversed. On the other hand, this should lead to an *overestimation* of the L_3 weight instead of the observed *underestimation* especially on the high-photon-energy side where the agreement with the Fano lineshape is particularly poor.

Having shown the Ti character of the low-energy structure in various ways, its orbital character can be investigated using PolPES. The beam energy in this case was set to $h\nu = 150$ eV unless noted otherwise, as the flux of the beamline is maximal at this energy, and the energy resolution determined as before is 230 meV. While early LDA+ U calculations predicted a high orbital polarization, with $d_{x^2-y^2}$ orbitals as the ground state of TiOCl [Saha-Dasgupta04], conflicting results came from a dynamical mean-field theory (DMFT) study using iterated perturbation theory (IPT) as an impurity solver [Craco06]. The latter found an equal mixture of $d_{x^2-y^2}$ and d_{xz} orbitals in the ground state. This result should be reflected in our PolPES data displayed in Fig. 4.8. Here, the sample was aligned such that the polarization vector was in the bc plane for horizontal and along the a axis for vertical polarization, where the uncertainty in this alignment is estimated to be below $\pm 3^\circ$. Measurements were performed in normal emission, i.e., around the Γ point. Since the $d_{x^2-y^2}$ orbitals have even symmetry with respect to the bc crystal mirror plane, and the $d_{xz,yz}$ orbitals are odd, in this geometry the

dipole matrix element (Eq. 2.25) of $d_{x^2-y^2}$ is switched between zero along a and non-zero along b , while the opposite is true for $d_{xz,yz}$ orbitals. The strong suppression of the Ti $3d$ peak in vertical polarization by a factor of ~ 10 identifies $d_{x^2-y^2}$ as the true ground-state orbital in TiOCl, since the remaining spectral weight in vertical polarization can be attributed to a finite degree of polarization of the incident photons, small misalignment of the sample, and symmetry-breaking phonons due to which the arguments concerning vanishing dipole matrix elements would be relaxed. Additionally, Fig. 4.8(b) shows that the shape of this peak does not change between the two polarizations, i.e., that the orbital character probed is exactly the same. These results are strong evidence that the orbital degree of freedom is not active at room temperature, from which it follows that orbital fluctuations do not play a role for the low-temperature physics of TiOCl, either.

The importance of correlations can be seen in Figs. 4.9(a) and (b), where the Ti and V partial DOS from GGA and GGA+ U calculations is compared [Saha-Dasgupta04, Glawion09]. In GGA, all t_{2g} bands are crossing the chemical potential, and both TiOCl and VOCl should be metals, in contrast to experimental observation. Introducing local Coulomb repulsion phenomenologically via the Hubbard parameter U using GGA+ U , the situation changes dramatically: now, there is a finite gap at the Fermi energy, rendering both materials insulators, and since this behavior is obviously driven by correlations they can be identified as Mott insulators. Furthermore, the orbitally resolved DOS now has only $d_{x^2-y^2}$ character below μ_{exp} for TiOCl, in line with the results from PolPES, and shows that in VOCl both $d_{x^2-y^2}$ and d_{xz} are equally occupied with one electron each.

An issue concerning the choice of U in the calculations shall be addressed for the example of VOCl. First of all, because of the two electrons in the $3d$ shell, the effective local interaction energy in this case is given by $U_{eff} = U' - J$, where U' is the interorbital Coulomb repulsion and J the magnetic exchange integral, as introduced in Sec. 3.2. As the O/Cl bands are rather delocalized due to their p character (compared to the strongly localized $3d$ orbitals of the TM), they are not affected by correlation effects in the same way, and U_{eff} in the calculations need only be used in treating the V $3d$ orbitals. Thus, in addition to the charge gap between occupied V $3d$ states and unoccupied ones, also the gap between the O/Cl p bands and the V $3d$ bands closer to the Fermi edge will depend on the value of U_{eff} . On the other hand, the widths of the different bands are essentially unaffected, remaining constant upon variation of U_{eff} . Figure 4.9(c) shows the GGA+ U pDOS for four values of U_{eff} . For $U_{eff} = 1.3$ eV (bottom) the observed PES separation between O/Cl and V occupied bands is reproduced by the calculations (see also Fig. 4.6). However, for this value the gap between the highest occupied and the lowest unoccupied states is underestimated compared to twice¹ the gap observed in photoemission, as well as to optical absorption experiments, which reported a charge gap of ≈ 2 eV for VOCl and TiOCl [Vénien79, Maule88, Rückamp05b]. For $U_{eff} = 4.3$ eV (top) the charge gap

¹Assuming the chemical potential lies in the center between LHB and UHB results in this additional factor of two.

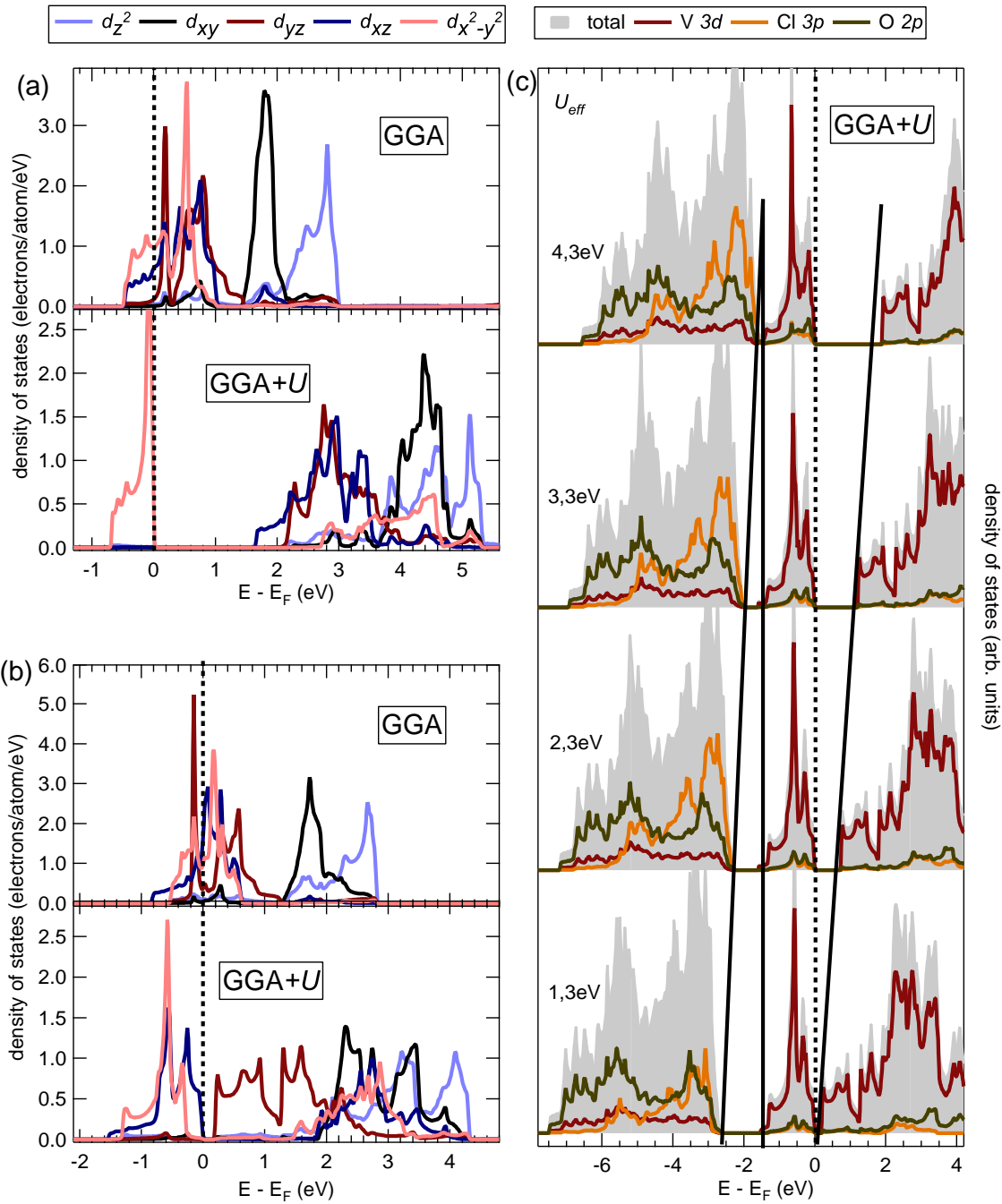


Figure 4.9: Comparison of GGA and GGA+ U calculations for TiOCl and VOCl. Dotted lines mark the Fermi energy. (a) TiOCl ($U_{eff} = 4.3$ eV in the bottom panel). (b) VOCl ($U_{eff} = 1.3$ eV in the bottom panel). An insulating state with a finite gap at the chemical potential is observed only upon inclusion of U . (c) Comparison of calculations for VOCl with $U_{eff} = 1.3$ eV, 2.3 eV, 3.3 eV, and 4.3 eV from bottom to top. Straight lines serve as guides to the eye, indicating the development of the gap between occupied O/Cl and V derived weight as well as between occupied and unoccupied states.

is basically reproduced, but the O/Cl–V gap is strongly underestimated. The latter is fundamentally determined by the hybridization pattern in VOCl. It has thus to be captured in the calculations, especially when comparing with PES results, while a correct description of the charge (i.e., correlation) gap cannot be expected, because even upon inclusion of U all DFT methods remain inherently single-particle approaches. The parameter value $U_{eff} = 1.3$ eV appears thus as the most sensible choice for describing VOCl.

Although it was stated previously that the shape of the valence band structures measured in UPS is not resolution-limited one easily realizes that GGA+ U does not reproduce these spectra even if they are artificially broadened (cf. Fig. 4.6). As was just shown, the influence of the more or less phenomenological parameters U and J is limited to rigid band shifts and leaves the shape of the DOS essentially unchanged. The remaining flexibility in choosing their values is another hint that DFT omits further important aspects of the electronic structure. Thus, different theoretical approaches were made by various groups. First of all, the influence of dynamical fluctuations absent within LDA+ U and GGA+ U was tested by performing calculations within dynamical mean-field theory (DMFT) [Saha-Dasgupta05, Craco06]. While the width of the computed spectral functions obtained in these studies gives better agreement with PES results, the magnitude of the correlation gap remains highly underestimated, and also the peak shape is not yet satisfactorily reproduced [Hoinkis05]. The dimerization in the spin-Peierls ground state of TiOCl suggests that correlation-driven intersite fluctuations may be important for the proper description of the oxyhalides. This motivated a further study where nonlocal correlation effects were included by considering Ti-Ti pairs/dimers as basic units instead of single Ti sites, and performing cluster-DMFT calculations [Saha-Dasgupta07].

The inset of Fig. 4.10(a) shows the four-site Ti cluster used, which corresponds to a supercell doubled along the a and b axes compared to the above DFT studies. Since the effective intradimer interactions (t_b) are about an order of magnitude larger than those between dimers (t_{ab}), the interdimer self-energy was neglected and the resulting impurity problem solved by a numerically exact quantum Monte Carlo (QMC) scheme. Exploiting the large energy of e_g orbitals due to CFS it is possible to simplify this task by a N th order muffin-tin orbital-based downfolding method to construct a Hubbard Hamiltonian containing only t_{2g} orbitals [Andersen00]. In accordance with most previous DFT and single-site DMFT studies [Saha-Dasgupta04, Saha-Dasgupta05], but at variance with the results of Craco *et al.* [Craco06], a 99% occupancy of the $d_{x^2-y^2}$ orbital is found. Also, the calculation correctly describes the insulating behavior of TiOCl with a charge gap of about 1.1 eV, as can be seen in Fig. 4.10(a). Although this gives only moderate agreement with the value from optical absorption, the gap appears 0.3 eV larger than the one obtained from the single-site DMFT using the same values of $U = 4$ eV and $J = 0.7$ eV [Saha-Dasgupta05], giving evidence of the importance of intersite correlations. Also shown is the lower Hubbard band measured by UPS, as well as oxygen K edge absorption data, the t_{2g} part of which in principle corresponds to the

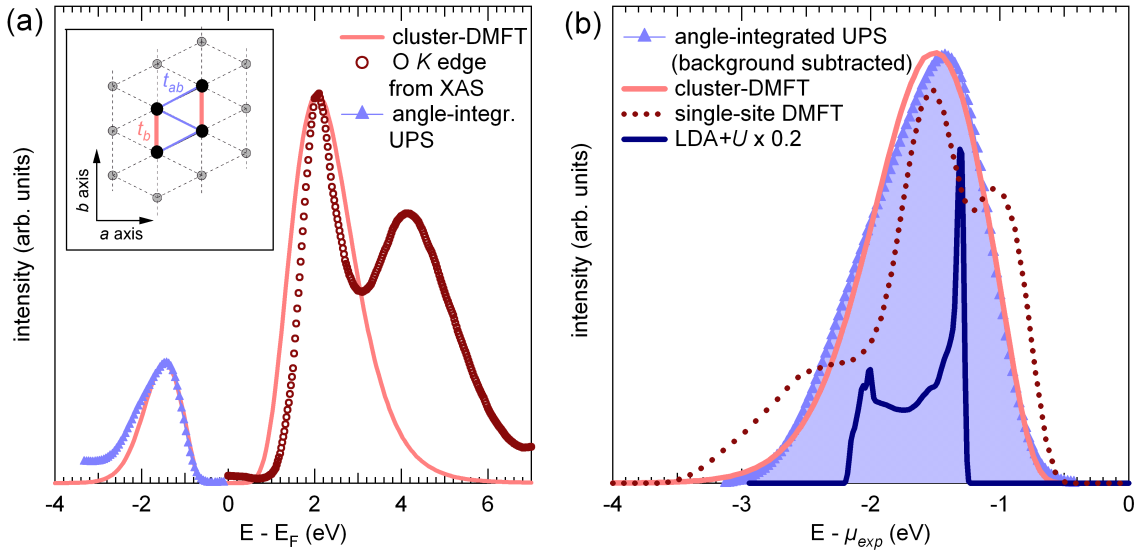


Figure 4.10: (a) Comparison of the spectral function from cluster-DMFT with angle-integrated UPS data (no background subtracted) and an O K edge absorption spectrum. Experimental spectra have been shifted in energy and adjusted in intensity to match the theoretical spectrum. Inset: Four-site Ti cluster used for the cluster-DMFT calculations. (b) LDA+U DOS, cluster-DMFT, and single-site DMFT spectral functions compared to UPS data (background subtracted). All spectra are aligned to the first-order moment of the experimental spectrum and scaled to the same integrated spectral weight.

upper Hubbard band (an extensive discussion of XAS data is given in Sec. 4.2.3). In this graph, both experimental spectra have been aligned in energy such that their maxima are at the same positions as those of the cluster-DMFT peaks. The e_g feature of the absorption spectrum is not present in the calculations because of the downfolding procedure, although the tail on the high-energy side of the calculated XAS t_{2g} peak as well as the slightly larger width compared to experimental spectra are partially due to remaining e_g admixtures. More importantly, however, the temperature in the calculations is much higher than in the experiments (1400 K vs. 360 K) which also leads to broadening. In Fig. 4.10(b), which compares the results from LDA+U, single-site DMFT, and cluster-DMFT, with an angle-integrated UPS spectrum of the lower Hubbard band, the peak shape from cluster-DMFT has the best agreement with the experimental one, but one could argue that it is due to enhanced temperature broadening. Thus, the most notable improvement compared to previous approaches is that the gap appears larger (1.1 eV compared to 0.3 eV in single-site DMFT, cf. [Saha-Dasgupta05]) despite the elevated temperatures. To see this, note that the absolute energy scale in Fig. 4.10(a) was fixed by the experimental position of the LHB. The calculated spectrum has been shifted accordingly, and the maximum of the experimental x-ray absorption spectrum was afterwards aligned with the maximum of the theoretical electron-addition spectral function. A short-coming of the present approach is that it does not allow for an in-

vestigation of the \mathbf{k} -resolved spectral function (except for the points $\mathbf{k} = 0$ and $\mathbf{k} = \pi$ because of the two-site character of the cluster). However, the LDA+VCA approach discussed in the next section can be used to fill this gap.

4.2.2 Electronic Dimensionality

The issue of dimensionality has been tackled previously from the viewpoint of magnetic interactions. The next step is to check how this translates into the dimensionality of the electronic structure. This is best done by looking at the ARPES dispersions of TiOCl, which can be compared quantitatively to those of TiOBr. Accordingly, this section will be structured as follows: first, the properties of TiOCl will be discussed in detail, followed by a comparison with TiOBr. Finally, the focus is shifted to the situation in VOCl.

The $3d^1$ System TiOCl

Figure 4.11 shows intensity plots $I(\mathbf{k}, E)$ of the \mathbf{k} -resolved valence band region of TiOCl from the chemical potential down to energies including the high-binding-energy O/Cl hybridized bands. The path ΓX (ΓY) in reciprocal space corresponds to a measurement along the real-space a (b) axis, with X (Y) being the Brillouin zone (BZ) boundary. Of course, as discussed in Sec. 2.1, this is only true if the perpendicular component of the momentum, \mathbf{k}_\perp , vanishes. Luckily, the layered structure of the oxyhalides makes the orbital overlap along the c axis and thus the \mathbf{k}_\perp dispersion negligible.

Since there is always an uncertainty in the experimental setup for measuring at normal emission, i.e., at the Γ point in the center of the BZ, spectra were taken in both directions until the region of the zone boundary, and the Γ point was determined afterwards from the symmetry of the dispersions. This can be seen in Fig. 4.11(b) and (c), where the full data sets from panel (a) are shown as waterfall plots of the energy distribution curves (EDCs) in which the development of the peak shape(s) can be seen better than in the intensity plots. In any case, very pronounced dispersions are observed for the O/Cl bands between roughly -9 eV and -4 eV, which also differ significantly along the two perpendicular directions. The fact that they are well pronounced and also symmetric about the Γ point indicates the good quality of our single crystals.

The Ti $3d$ -derived LHB spectral-weight dispersions are shown more clearly in the blow-ups of Fig. 4.12. As before, there are well pronounced differences observable between the ΓX and ΓY directions: while in the former case the peak shape remains basically the same and essentially no dispersion is observed, the situation is quite different along ΓY , i.e. along the chain direction. First of all, the peak shape evolves from a broad, slightly asymmetric “peak” at the Γ point into an even broader “hump” at the zone boundary. This is due to an additional shoulder at higher binding energies, appearing in the outer third of the BZ. Secondly, the LHB starts out with its maximum roughly at 1.5 eV below the chemical potential at Γ , then moves closer towards μ_{exp} , and reaches

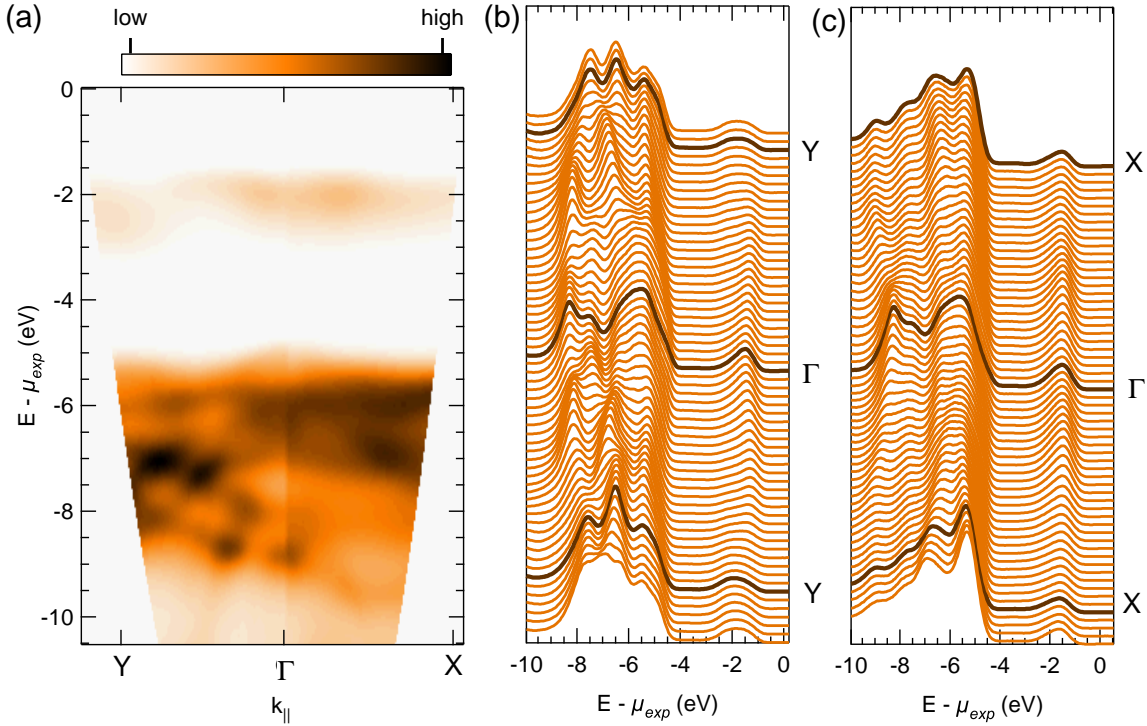


Figure 4.11: ARPES of the valence band of TiOCl. (a) Intensity plot $I(\mathbf{k}, E)$ along the b (TY) and a (ΓX) axis. (b) Waterfall plot of spectra along YTY. (c) Waterfall plot of spectra along X Γ X.

its minimum binding energy about halfway between Γ and Y. From there, its maximum is not well-defined anymore because of the overlap with the additional shoulder just mentioned. The intensity appears somehow redistributed amongst the two, making the LHB broad and shifting its first-order moment towards higher binding energies.

Overlaid in Fig. 4.12(a) is the band dispersion resulting from LDA+ U calculations (LDA+ U^{FM} ; blue solid lines).¹ Note that the energy scale of the experimental data was used as a reference, and that the calculated spectra have been shifted in energy to give a good match at the Γ point. It is easily seen that the LDA+ U band structures can by no means account for the behavior observed in ARPES, especially along the b axis, i.e., the 1D chain direction along which significant overlap of Ti 3d wave functions is expected. Thus, Fig. 4.13 shows several approaches made in order to achieve a better agreement in this manner. In panel (b) results from a 1D single-band Hubbard model solved using dynamical density-matrix renormalization group (DDMRG) are shown [Benthien04, Hoinkis05]. Using this method it is possible to calculate the spectral function, in contrast to the LDA band structure methods which yield only the

¹Obtained assuming ferromagnetic spin alignment; antiferromagnetic alignment (not shown) leads to a doubling of the unit cell and thus a “symmetric” dispersion between Γ and Y, but not to a qualitatively better agreement [Hoinkis05].

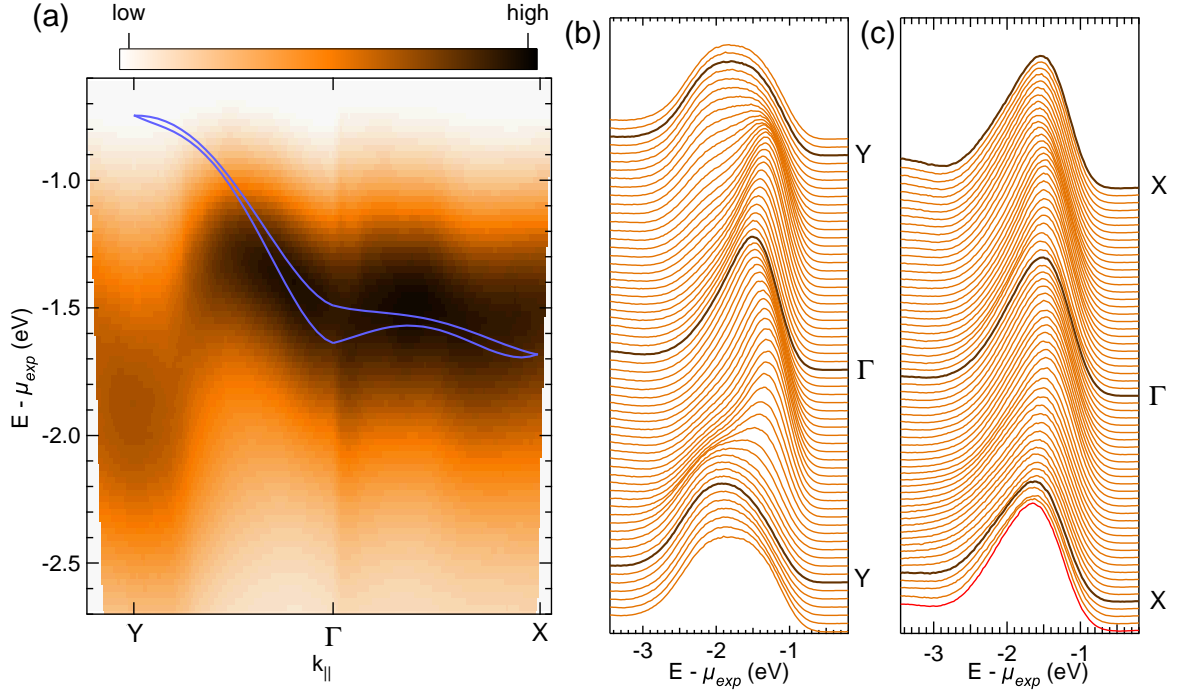


Figure 4.12: ARPES of the Ti 3d part of the TiOCl valence band. (a) Intensity plot $I(\mathbf{k}, E)$ along the b (ΓY) and a (ΓX) axis. Blue solid lines are Ti 3d band dispersions obtained using $LDA+U^{FM}$ (see text). (b) Waterfall plot of spectra along YTY . (c) Waterfall plot of spectra along XTX .

single-particle dispersions. As the DDMRG has dealt with a truly 1D system, several generic features can be seen here: at the Γ point, two well-separated branches are observed, reflecting the phenomenon of spin-charge separation. The one with lower binding energy is called the spinon branch, whose bandwidth scales with the exchange integral J , while the other one is the so-called holon branch, expected to scale with the transfer integral t . Additionally, an inverted replica of these branches is observed dispersing away from the Y point, which is the so-called shadow band. Obviously, this feature is completely absent in the experimental spectra, and also the spinon-holon splitting at Γ is not observable, which has to be noted is not due to, e.g., a limited experimental resolution. Nevertheless, the asymmetry of the spectral weight distribution between zone center and zone boundary [evidenced by different energies of the first-order moment of the spectral function $A(\mathbf{k} = \Gamma, \omega)$ compared to $A(\mathbf{k} = Y, \omega)$] is in a certain sense reproduced by DDMRG, although from the viewpoint of the electronic structure TiOCl cannot be characterized as a truly 1D system.

The \mathbf{k} -resolved spectral function shown in Fig. 4.13(c) has been calculated by M. Aichhorn via a two-step process of using LDA with both linearized and N th order muffin-tin orbitals (LMTO/NMTO) to construct the non-interacting part of the many-body Hamiltonian, followed by adding interaction terms and using a variational cluster approach

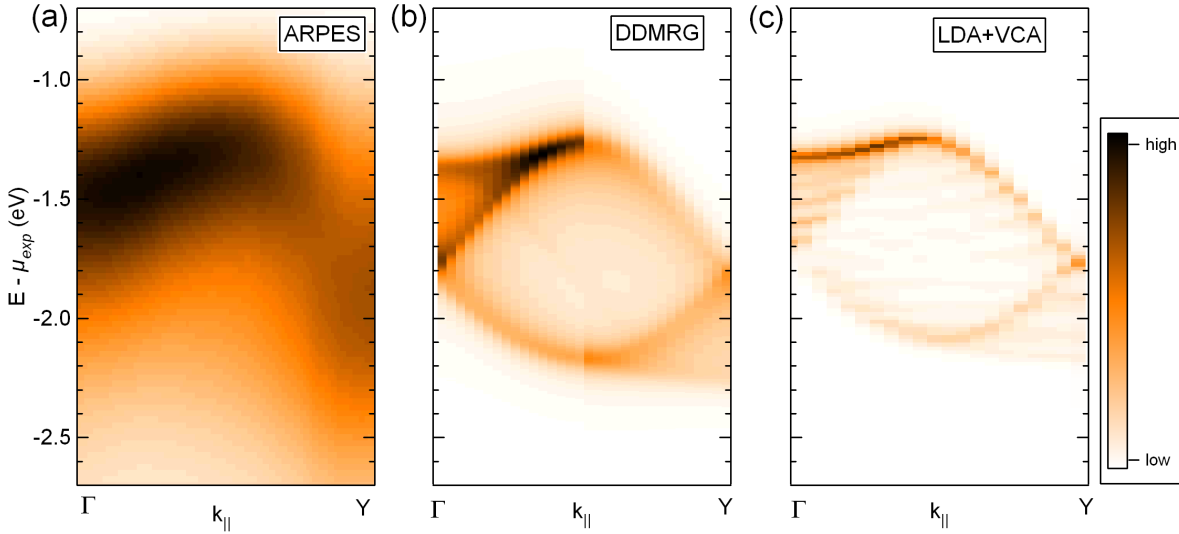


Figure 4.13: Comparison of the experimental and calculated Ti 3d spectral-weight distribution along the chain direction (b axis). (a) ARPES data from Figs. 4.11 and 4.12. (b) Calculated spectral function $A(\mathbf{k}, \omega)$ of a 1D Hubbard chain using DDMRG. (c) $A(\mathbf{k}, \omega)$ from a combination of LDA and VCA using a single-band Hamiltonian (for details see text). Calculated spectra have been shifted such that their first-order moments coincide with the one of the experimental data.

(VCA) to solve the full low-energy model, including local interaction effects and Hund’s rule coupling [Aichhorn09, Chioncel07]. This method was only recently developed [Pothoff03b] and has been applied to a plethora of strongly correlated and low-dimensional systems like, e.g., high- T_C cuprate [Sénéchal04, Aichhorn06] and iron-based superconductors [Daghofer08], in very good agreement with state-of-the-art DMFT calculations. Also for the case of TiOCl there is significant improvement compared to, e.g., the DDMRG approach. The spectral weight of the shadow band is significantly suppressed, as is the case for the holon branch. This makes the spectrum even more asymmetric in the sense explained above, thus giving better agreement with the ARPES data.

Different variants of clusters as well as different degrees of downfolding have been tested to investigate their influence on the observed spectral distribution in LDA+VCA. First of all, looking at the sizes of intra- and interchain self-energies of TiOCl, it was mentioned earlier that those perpendicular to the chains are almost an order of magnitude weaker [Saha-Dasgupta04]. Thus, it was possible to use 1D clusters of the kind shown at the bottom of Fig. 4.14(a) instead of 2D clusters like the ones at the top of the panel. In contrast to the DDMRG calculations presented above, however, within VCA these 1×12 clusters are only the building blocks of the solid and repeated “infinitely”.¹ Thus, although the self-energies are effective only on single clusters it is possible to include also finite interchain hoppings t_{ab} and t_a .

¹Here, infinity is of the order of 50.

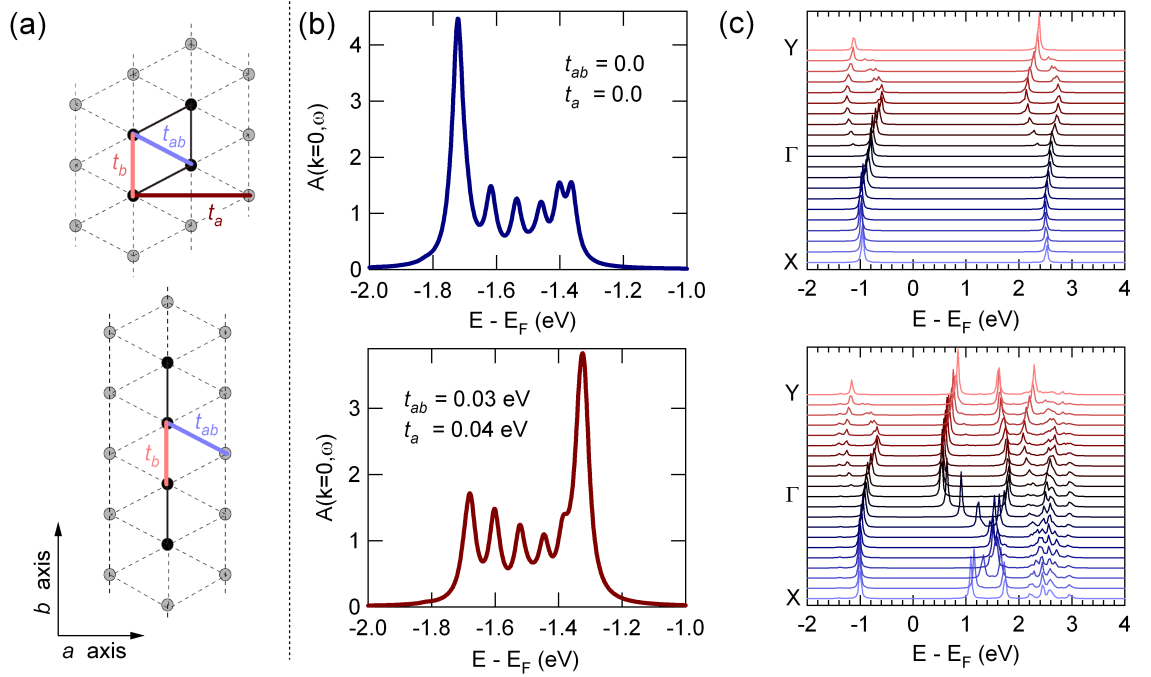


Figure 4.14: (a) Triangular lattice structure with interchain (top) and intrachain (bottom) clusters used for LDA+VCA calculations. Interchain self-energies are only included in the former, which does not mean that interchain hopping integrals need to be zero. The integrals are termed in analogy to the exchange couplings, cf. Fig. 4.1. Full circles mark the actual clusters. (b) Influence of interchain hopping integrals t_{ab} and t_a on the single-particle spectral function at the Γ point ($k=0$). A 1×12 reference system with $t_b = -0.21$ eV was used. (c) Comparison of the spectral function of single-band (top) and multi-band model (bottom), both calculated with a 2×2 reference system. Parameters are $U = 3.3$ eV and $J = 0.5$ eV, and a Lorentzian broadening of 0.02 eV was used.

The most prominent changes upon inclusion of interchain terms are illustrated by the spectral function at the Γ point, as shown in Fig. 4.14(b): giving finite values to the interchain hopping integrals, the high peak at around -1.7 eV (for a truly one-dimensional system corresponding to the holon branch) loses weight, while at the same time at the low-binding-energy side around -1.3 eV a peak (the spinon branch) gains intensity, enhancing the overall asymmetry. On the other hand, including only next-nearest-neighbor hopping along the chain direction without interchain coupling leaves the spectrum in the upper panel of Fig. 4.14(b) essentially unchanged (not shown). One might thus conclude that TiOCl is a 2D compound, since the influence of the interchain hopping t_{ab} is dominant over that of next-nearest-neighbor hopping, albeit with strong anisotropy. However, it can be carefully addressed as more or less quasi-one-dimensional in comparison to TiOBr and VOCl, as will be elaborated on in the following subsections.

Another important result from the VCA analysis is that it confirms the quenching of the orbital degree of freedom and thus the effective single-band nature of TiOCl. While

it is clear that the e_g orbitals can be projected out altogether because of the significant octahedral CFS, a proper check of the situation for higher-lying t_{2g} orbitals is necessary. Thus, two different model Hamiltonians have been considered in our VCA study. Taking all three t_{2g} orbitals, the Hamiltonian reads

$$\begin{aligned}
 H &= \sum_{ij,\sigma} \sum_{\alpha,\beta} t_{ij}^{\alpha,\beta} c_{i\alpha,\sigma}^\dagger c_{i\beta,\sigma} - \mu \sum_{i\alpha} n_{i\alpha} \\
 &+ \frac{U}{2} \sum_{i\alpha\sigma} n_{i\alpha\sigma} n_{i\alpha\sigma'} + \frac{U'}{2} \sum_{i,\alpha\neq\beta} n_{i\alpha} n_{i\beta} - J \sum_{i,\alpha\neq\beta} S_{i\alpha}^z S_{i\beta}^z \\
 &- \frac{J}{2} \sum_{i,\alpha\neq\beta} (S_{i\alpha}^+ S_{i\beta}^- + S_{i\alpha}^- S_{i\beta}^+) \quad , \quad (4.4)
 \end{aligned}$$

with i, j site, α, β orbital, and σ spin indices, respectively. The interaction parameters are related as $U' = U - 2J$, and S^z, S^+ , and S^- are the components of the spin- $\frac{1}{2}$ operator. In this Hamiltonian, the first line corresponds to the non-interacting (LDA) part together with an adjustable chemical potential μ . The second line has the diagonal interaction components, and the last line contains the non-diagonal (spin-flip) term. From Eq. 4.4, a single-orbital Hamiltonian can be obtained by downfolding, leading to

$$H = \sum_{ij,\sigma} t_{ij} c_{i\sigma}^\dagger c_{j\sigma} + U \sum_i n_{i\uparrow} n_{i\downarrow} - \mu \sum_i n_i \quad , \quad (4.5)$$

where only the $d_{x^2-y^2}$ channel is kept active and interorbital terms ($\propto U'$) as well as exchange interactions drop out. A comparison of the momentum-resolved single-particle spectral functions obtained from the single- and multi-orbital Hamiltonian is shown in Fig. 4.14(c) (top and bottom panel, respectively). Here, a 2×2 cluster as an additional check of possible size effects on the spectral function was used. As the results agree well with those from the 1×12 cluster [shown partially in Fig. 4.13(c)] the validity of this latter *ansatz* is confirmed. It is seen that the occupied part of the spectrum (the $d_{x^2-y^2}$ orbital) which is observable by PES barely changes between the single- and multi-orbital cases. This shows that an effective single-band Hubbard model is appropriate for a description of the low-energy physics in TiOCl.

As a final remark, it shall be noted that the size of the charge gap in the LDA+VCA approach also depends on U and J , in a fashion comparable to what was discussed previously for VOCl. However, focus of this work was on the importance of multi-orbital and dimensionality-induced effects on the spectral-weight distribution seen in ARPES, and the results turn out to be basically independent from the gap size. Also, the value of roughly 1.2 eV obtained for the parameters used for the results shown above is in reasonable agreement with the gap extracted from optical absorption experiments (approx. 2 eV, cf. [Rückamp05b]).

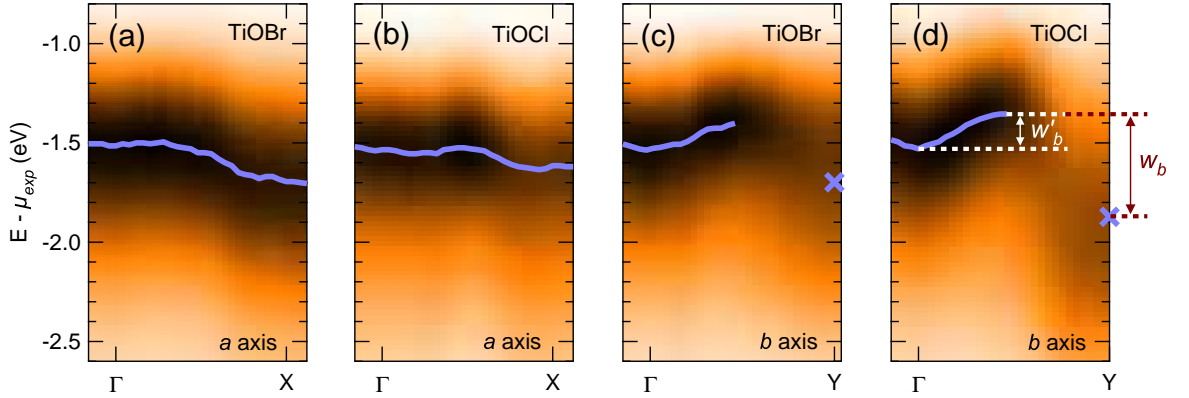


Figure 4.15: ARPES intensity plot $I(\mathbf{k}, E)$ of the Ti 3d part of the TiOBr [panels (a), (c)] and TiOCl [panels (b), (d)] valence bands along the a (ΓX ; left panels) and b (ΓY ; right panels) axes. Solid lines indicate the peak positions of the EDCs. Crosses mark the first-order moment of the EDCs at the Y point. Also indicated are the phenomenological bandwidths w'_b and w_b (w_a is defined in analogy to w_b).

Origin of the Dispersions in TiOCl and TiOBr

From the results presented up to this point comes clear evidence that the interchain coupling in TiOCl plays a major role for the electronic structure. Additionally, the LDA+VCA findings could be interpreted such that the electronic dispersions are driven by magnetic exchange, as the enhancement of the spinon-like branch leads to better agreement with experiment. However, the quantitative comparison between TiOCl and TiOBr presented in the following shows that this interpretation is not as straight-forward as it may seem [Hoinkis07].

Figure 4.15 displays the Ti 3d spectral weight distribution from ARPES of TiOBr and TiOCl both along the a and b axes as intensity plots. Although qualitatively very similar, there are subtle quantitative differences between the two compounds, especially along the b direction. The dispersion of TiOBr appears less asymmetric between Γ and Y , and the widths of EDC spectra do not become as large as in TiOCl. Included are lines as guides to the eye to indicate the spectral dispersion. Except for the region from roughly $\frac{1}{2}\Gamma Y$ to Y these were determined by the maximum position obtained from a fitting procedure. At the Y point, the first-order moment of the EDCs was used as the reference point. Several phenomenological bandwidths are defined by extracting the energy differences between the maxima at Γ and the point of lowest binding energy (roughly at $\frac{1}{2}\Gamma Y$) which is termed w'_b , as well as the overall bandwidth between the lowest and highest binding energy points (the latter being at the zone boundary), termed $w_{a,b}$.

It can be seen from Fig. 4.15 and Tab. 4.2 that the bandwidths thus obtained are significantly smaller in TiOBr along the b axis, while w_a is larger than in TiOCl and comparable to w_b , in contrast to the chloride system. This indicates that TiOBr has

Table 4.2: Bandwidths w_a , w_b , and w'_b of the Ti 3d band in TiOBr and TiOCl as defined in Fig. 4.15, as well as various parameters possibly relevant for the observed dispersions: Width of the central part of the Ti 3d band dispersion along b (w'_b), exchange constant J obtained from the magnetic susceptibility [Rückamp05a], transfer integral t derived from experimental J values, and t from downfolding LDA+ U studies [Lemmens05]. The numbers given in parenthesis indicate the scatter from different samples. The last column corresponds to 1 minus the ratio of, e.g., $J(\text{TiOBr})$ and $J(\text{TiOCl})$ (other quantities accordingly), given in percent.

	TiOBr	TiOCl	$\Delta x/x$
w_a	0.27(3) eV	0.12(3) eV	
w_b	0.26(5) eV	0.47(5) eV	
w'_b	0.13(1) eV	0.17(1) eV	23 %
J from magnetic susceptibility	32 meV	58 meV	45 %
$t = \sqrt{JU}/2$	0.16 eV	0.22 eV	26 %
t from LDA+ U	0.17 eV	0.21 eV	19 %

smaller anisotropies and thus a less pronounced 1D character, a view supported by the fact that its high-temperature magnetic susceptibility cannot be fitted well by a Bonner-Fisher curve of a 1D Heisenberg chain, as it was possible for TiOCl [Lemmens05]. As mentioned earlier, there are basically two quantities which could govern the dispersion, namely the hopping or transfer integral t and the magnetic exchange coupling J . The latter can be extracted from measurements of the susceptibility, while transfer integrals can be obtained from LDA+ U or related calculations using appropriate downfolding methods. In a Hubbard model description the two are related via $J = 4t^2/U$, i.e., $t = \sqrt{JU}/2$, allowing for a cross-check of the different approaches. The last column of Tab. 4.2 shows how much smaller the quantities of interest are in TiOBr compared to TiOCl. It is seen that the experimental value for the ratio of w'_b bandwidths is in good agreement with that of hopping integrals t both from direct calculations and from using experimental J values to extract t . It can thus be stated that the inner part of the dispersions where generic 1D features like, e.g., spin-charge separation might be observable (cf. the discussion of Fig. 4.13), has charge (i.e., holon) character, and that a spinon branch is absent. Although this is in seeming contrast to the tentative conclusions drawn from LDA+VCA, it should not be over-interpreted as a direct contradiction, as the latter underestimates w'_b by almost a factor of two. Instead, the common finding is that a proper description of the normal-state electronic structure has to take into account the anisotropic frustrated interchain interactions of the underlying triangular lattice.

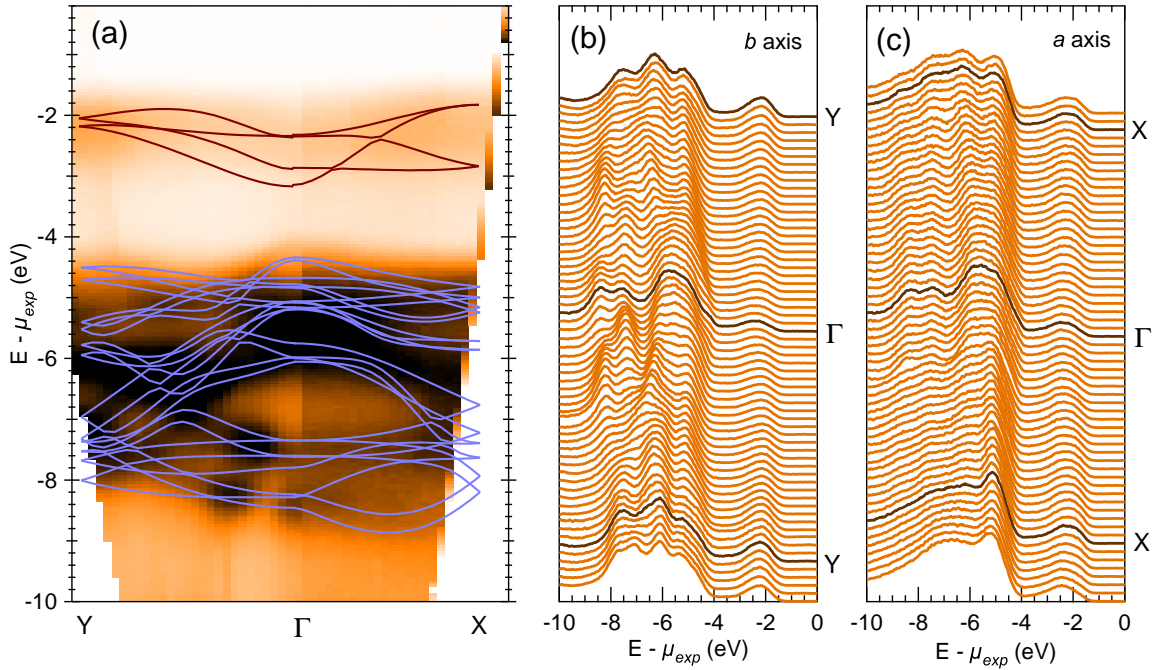


Figure 4.16: ARPES of the valence band of VOCl. (a) Intensity plot $I(\mathbf{k}, E)$ along the b (ΓY) and a (ΓX) axis. Band structures calculated by GGA+ U are shown as an overlay. The V 3d derived bands are marked in brown color, those of mainly O and Cl character in blue. (b) EDCs along YTY. (c) EDCs along XTX.

The $3d^2$ System VOCl

At a first glance, the ARPES data from VOCl shown in Fig. 4.16 look very similar to those of TiOCl [Glawion09]. As in the latter case, there are rich dispersive features which differ between the two crystallographic directions in the O/Cl bands. Obviously, there is quite good agreement between their experimental dispersion and the one obtained from GGA+ U , which are shown as blue solid curves. This is due to the uncorrelated nature of these bands. In the low-binding-energy region, GGA+ U shows a total of four V 3d bands (brown solid curves) since there are two electrons per V site and two V sites per unit cell. The V 3d weight appears as a rather broad and weakly dispersing hump without any sharp features, even more than the Ti 3d weight did in TiOCl, as can be seen in the blow-up shown in Fig. 4.17. Since these experimental features do not have quasi-particle character, but must be interpreted as incoherent weight in the spirit of a Mott-Hubbard scenario, a proper description can only be expected from calculating the spectral function, similar to what was done for TiOCl. With this in mind, the dispersions from GGA+ U appear already quite reasonable in the present case. One reason could be that fluctuations are probably less effective here because VOCl is less one-dimensional, which could be checked, e.g., by application of DMFT methods.

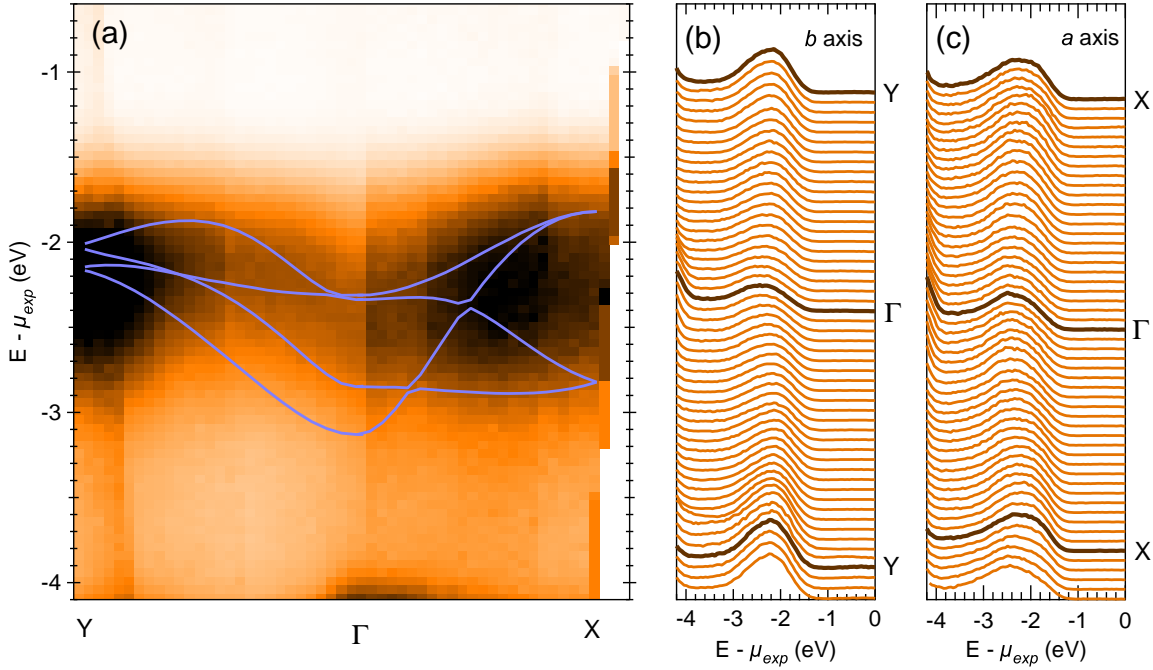


Figure 4.17: ARPES of the V 3d part of the VOCl valence band. (a) Intensity plot $I(\mathbf{k}, E)$ along the b (TY) and a (ΓX) axis. The V 3d derived bands calculated by GGA+ U are shown as an overlayer (blue solid lines). (b) EDCs of spectra along YTY. (c) EDCs of spectra along XT X.

In contrast to TiOCl, the weak dispersions in the ARPES spectra of the V 3d weight show no pronounced difference between a and b axis, yet in both cases the peak maximum appears at highest binding energies at the Γ point and shifts to slightly lower energies towards the zone boundary. A comparison shows that the trend towards lower binding energies as well as the evolution of the spectral weight distribution are qualitatively in line with the presented calculations: large weight is found along a half way between Γ and X , along b right at the Y point, i.e., where bands cross in both cases (cf. solid lines in Fig. 4.17). The shape of the peak, which can be seen in the waterfall plots of Figs. 4.17(b) and (c), reflects these trends as well: along b it develops from a flat hump to a more distinct, symmetric peak towards the zone boundary, while along a the slight asymmetry towards the high-binding-energy side at Γ shifts towards the low-binding-energy side at X . However, a detailed interpretation of this behavior needs further analysis which is beyond the scope of the present work.

Overall, the agreement between GGA+ U and ARPES for VOCl is better than in the case of TiOCl. This is probably due to the fact that the influence of dynamical and/or spatial fluctuation effects in VOCl is smaller than in TiOCl.

4.2.3 Hybridization and Multiplet Effects

Two major aspects of the oxyhalide electronic structure cannot be investigated by PES: (i) the unoccupied electronic states above the Fermi energy, offering valuable clues to the lowest-energy states which could provide conducting channels upon doping, and (ii) the low-temperature phases. XAS is an appropriate technique to tackle these issues. As explained in Sec. 2.2, although it is an element-specific method, different approaches can be made to obtain information on the relevant Ti $3d$ electronic structure, namely measurements with excitation energies close to the Ti $2p$ binding energy (the Ti L edge) or the O $1s$ core levels (the O K edge).

The experiments were conducted both at beamline PM-3 at BESSY II using the MUSTANG endstation, and at the ADRESS beamline at the Swiss Light Source (SLS) in Villigen, Switzerland. Fluorescence yield (FY) and total electron yield (TEY) signals were measured simultaneously, the latter by mounting the sample in an isolated fashion and recording the drain current necessary to compensate the photoemitted electrons, using a KEITHLEY Nanoampere-meter. The energy resolution in this case is given by the beamline optics and amounts to 100 meV and 50 meV for BESSY and SLS data, respectively. Due to the broadness of spectroscopic features no differences are observed between these two data sets. Unless noted otherwise, measurements were performed in normal incidence geometry, i.e., the incoming beam aligned along the crystallographic c axis. The effective polarization along the different crystallographic axes could be changed either by rotating the sample stage around the beam axis (BESSY) or by setting the undulator such that the incoming photon polarization is switched by 90° (SLS). The angle between the incoming beam and the FY detection direction was 45° in the horizontal plane. The sample could be cooled down to $T = 80$ K, i.e., well below the higher transition temperature of TiOCl ($T_{c2} = 92$ K). In all spectra, the influences of variations in the ring current and of absorbance in the monochromator have been divided out, and different spectra have been normalized to each other by subtraction of a constant background determined at the low photon-energy side just before the absorption edge, and subsequent multiplication to equal intensity at the high photon-energy side several eV above the relevant spectral features.

Figure 4.18 shows a complete set of O K edge FY and TEY spectra taken at room temperature and at 80 K for linear polarization both along the a and b axis. From the FY data one sees that no significant changes in the electronic structure take place between the high-temperature phase and the incommensurate intermediate phase ($T_{c1} < 80$ K $< T_{c2}$). Since this observation is resolution-limited, changes in the electronic structure occur obviously only on the energy scale of some meV or less. This supports the assumption that the electronic degrees of freedom are barely involved in the spin-Peierls transition(s) in the oxyhalides. From the very good correspondence between FY and TEY spectra [cf. panel (b)] we conclude that, despite a reduced probing depth, TEY spectra reflect bulk properties of TiOCl and can be used for a detailed analysis. Thus, one circumvents possible problems from self-absorption which appear, e.g., in the FY spectrum with po-

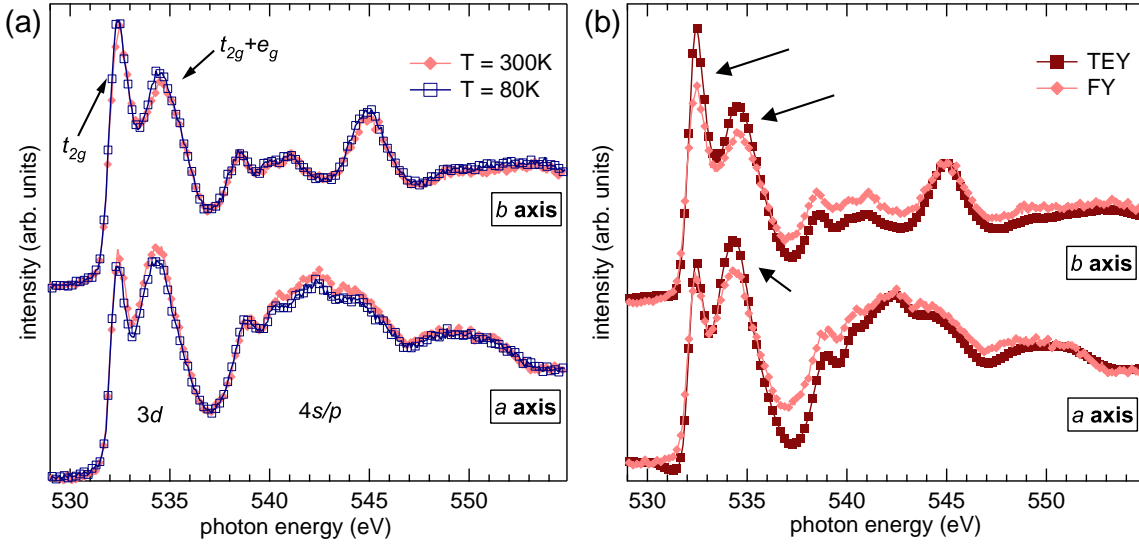


Figure 4.18: O K edge absorption spectra of TiOCl. Spectra with polarization along b are vertically offset for clarity. (a) FY spectra at room temperature (full red markers) and 80 K (open blue markers). The ranges representing predominantly Ti 3d ($h\nu \lesssim 537$ eV) and Ti 4s/p ($h\nu \gtrsim 537$ eV) bands, hybridized with O/Cl bands, are indicated at the bottom. For the former, the peaks of mainly t_{2g} and mixed t_{2g} and e_g character are marked at the top. (b) Comparison between FY (light red) and TEY (dark brown) spectra at $T = 300$ K. FY spectra obviously suffer from self-absorption; arrows mark prominent examples.

larization along b , where the intensity of the first peak appears suppressed. As in many transition metal oxides, the observed absorption features can roughly be assigned to O $2p$ states mixed with TM 3d ($E_{ph} \approx 531 - 537$ eV) or 4s/4p ($E_{ph} \approx 537 - 548$ eV) orbitals, respectively, and the double peak structure in the low-energy part comes mostly from the (quasi-) octahedral coordination of the TM ion. In an ideal O_h symmetry this peak separation would directly reflect the $t_{2g}-e_g$ crystal-field splitting $10Dq$. Although the oxyhalides belong to the point group C_{2v} with considerably lower symmetry, qualitative arguments can be made on the assignment of different spin configurations to these peaks using terms of O_h symmetry.

The final state of the XAS process in TiOCl involves two electrons in the d shell, which basically allows for triplet and singlet configurations with both electrons in t_{2g} orbitals (t_{2g}^2 ; 3T_1 for $S = 1$; 1T_2 , 1E , and 1A_1 for $S = 0$), one in a t_{2g} and one in an e_g orbital ($t_{2g}^1e_g^1$; triplet states are 3T_2 and 3T_1), as well as $t_{2g}^0e_g^2$ configurations. The latter as well as $t_{2g}^1e_g^1$ singlet configurations can be neglected, since they lie in energy well above all others and thus certainly do not contribute to the first two peaks. Table 4.3 gives the basic energetics of these configurations in terms of U , J and $10Dq$, as well as values calculated by applying an embedded cluster approach to O K edge spectra of TiOBr [Lee05, Macovez07]. The energetic order found by the authors of [Macovez07] is such that the triplet configuration 3T_1 is at lowest energy, followed by the singlet

Table 4.3: Possible configurations, term symbols and energy eigenvalues of a d^2 system in O_h symmetry (t_{2g} threefold degenerate). The definitions of U and J in terms of Racah parameters can be found in Sec. 3.2. In the second-to-last column energy ranges (in eV) relative to the ground state (3T_1) from an embedded cluster approach to $O K$ edge spectra of TiOBr are given (as available from [Macovez07]). The last column gives energies (in eV) relative to the ground state, calculated using the best-fit parameters to the Ti L edge spectra from LFM theory in D_{4h} symmetry (see below for details).

configuration	term(s)	eigenenergy ^a	range in TiOBr	best-fit energy
t_{2g}^2 triplet	3T_1	$U - 3J_3$	0	0 ^b
t_{2g}^2 singlet	${}^1T_2; {}^1E$	$U - J_3$	– ^c	1.44
t_{2g}^2 singlet	1A_1	$U + 2J_3$	0.78-1.28	3.40
$t_{2g}^1 e_g^1$ triplet	3T_2	$U - 3J_4 + 10Dq$	1.32-1.61	1.61 - 2.52
$t_{2g}^1 e_g^1$ triplet	3T_1	$U - 3J_1 + 10Dq$	– ^c	1.90 - 2.82
$t_{2g}^1 e_g^1$ singlet	1T_2	$U - J_4 + 10Dq$	– ^c	1.65 - 3.25
$t_{2g}^1 e_g^1$ singlet	1T_1	$U - J_1 + 10Dq$	– ^c	3.34 - 3.65

^aNotation adopted from [Lee05].

^bThe absolute value using U and J is 3.04 eV.

^cNot given in [Macovez07].

1A_1 , and finally the 3T_2 and 3T_1 $t_{2g}^1 e_g^1$ triplet configurations. Due to symmetrically inequivalent O sites in the applied supercell, only an energy range for the different configurations could be given from this calculation, depending on the position of the induced core hole on a specific O site. It is well justified to assume that these results and assignments also apply to TiOCl. We thus identify the peak at $E_{ph} \approx 532$ eV as the $t_{2g}^2 e_g^0$ triplet configuration, while the one centered at $E_{ph} \approx 534$ eV is a superposition of 1A_1 singlet and 3T_2 triplet configurations. Calculating the eigenenergies from the relations given in the third column of Tab. 4.3 either with $U = 4.5$ eV, $J = J_3 = 0.7$ eV from GGA or $U = 5.2$ eV, $J = 0.72$ eV from best fits within LFM theory calculations (last column in the table; see below for details) shows how important the attractive force between core hole and excited electrons is in x-ray absorption: in neither case can the results from the embedded cluster approach (which takes this Coulomb interaction correctly into account) be reproduced by the simple d^2 energetic scheme. If no core hole is present, however, this simple picture gives a remarkably good description of the electronic structure. This will be seen later when dealing with a d^2 ground-state system, namely electron-doped TiOCl.

Upon switching the light polarization between a and b , two major changes are observed. Firstly, the s/p hybridized bands change their shape significantly. However, due to large number of bands involved here, a simple interpretation of this behavior is not possible, but these features serve well as a cross-check of the sample orientation. Secondly, the intensity ratio of the two $3d$ peaks is changed, making the first peak at

$E_{ph} \approx 532$ eV higher than the one at $E_{ph} \approx 534$ eV for polarization along b . Again, simple dipole matrix arguments as used for example for PolPES are not applicable, and a calculation of the Ti partial DOS would be required to possibly explain this observation.

Interpretation of L edge absorption spectra is more intricate, as was explained already in Sec. 2.2. A very powerful and well-established many-body approach to x-ray absorption and emission processes, especially in strongly correlated systems, is the ligand-field multiplet (LFM) theory, and its extension to the charge-transfer multiplet (CTM) [de Groot08]. LFM calculations were performed using program codes originally developed by R. D. Cowan [Cowan81], P. H. Butler [Butler81], and B. T. Thole and F. M. F. de Groot [de Groot90a]. As the desired symmetry is reached by successive symmetry reduction via different point groups it becomes increasingly difficult to define the correct (and meaningful) crystal-field parameters and operators for given polarizations. Thus, comparatively high tetrahedral symmetry (D_{4h}) with a distortion along the crystallographic a axis was used to simulate XAS spectra of TiOCl. Additionally, CTM calculations in D_{2h} symmetry were performed by M. W. Haverkort.

The programs start from calculating ground-state properties of free ions within Hartree-Fock, based on which additional interactions are included. Before specifically discussing TiOCl spectra and corresponding simulations, the effects of the different ingredients to the calculations shall be illustrated by starting from the simplest possible case of XAS at the Ti $2p$ absorption edge, and successively turning on the different interactions, however, without attention to the specific magnitude of the involved parameters.

Consider a Ti^{4+} ion ($3d^0$ configuration) in spherical (SO_3) symmetry, with all Slater-Condon parameters set to zero (i.e., in the single-particle limit without multiplet effects), and finite $2p$ spin-orbit coupling (SOC). The underlying process is $2p^6 3d^0 \rightarrow 2p^5 3d^1$, and the initial state has only completely filled shells. The SOC is thus only active in the final state, and the resulting spectrum consists of exactly two peaks with an intensity ratio of 2:1 (for SOC only between $2p$ electrons), corresponding to absorption resulting in $2p_{3/2}$ (L_3 edge) and $2p_{1/2}$ (L_2 edge) states, respectively. Including spin-orbit coupling also between $3d$ electrons (which is two orders of magnitude smaller than the $2p$ SOC in transition metals) has only a minute effect of a very slight redistribution of spectral weight due to new terms becoming allowed, and also leads to a different ground state [Fig. 4.19(a)]. However, the spectrum is essentially indistinguishable from that with $2p$ SOC alone (which is thus not shown). Embedding the ion in an octahedral crystal field of six equivalent ligands lowers the symmetry to O_h and introduces CFS of the two peaks into a t_{2g} and a e_g peak each, reflecting the crystal-field parameter $10Dq$ [Fig. 4.19(b)]. As a next step, the Slater-Condon parameters are given finite values, which introduces many-body interactions, i.e., multiplet effects [Fig. 4.19(c)]. Working out the new multiplets one realizes that the t_{2g} and e_g peaks of the L_3 edge are split further into five non-degenerate levels, resulting in two additional small pre-peaks. A detailed calculation shows that spectral weight is shifted from the t_{2g} into the e_g peaks in this case. Since in O_h symmetry no changes occur if the exciting photons are linearly polarized along the different octahedral axes, the symmetry has to be lowered, e.g., by either elongating

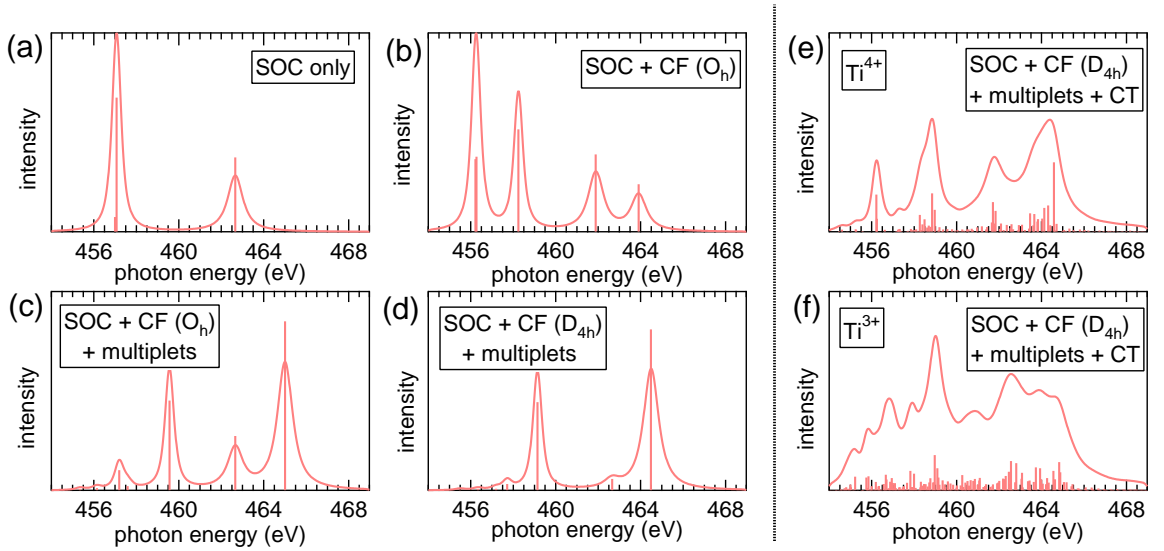


Figure 4.19: (a-e) Ti^{4+} L edge absorption spectra, simulated within LFM and CTM theory. Eigenenergies are indicated by sticks, while the spectra have been broadened by Gaussian and Lorentzian curves of varying widths (0.1 - 0.4 eV). (a) Only spin-orbit coupling ($2p + 3d$). (b) Crystal field (CF) of O_h symmetry included. (c) Finite values to Slater-Condon parameters (i.e. multiplet effects included). (d) Symmetry reduction to tetrahedral D_{4h} . (e) Inclusion of charge-transfer (CT) states. (f) Same as in (e), but for a Ti^{3+} ion ($3d^1$ initial state).

or compressing the octahedron along, say, the z axis (a tetrahedral distortion, corresponding to D_{4h} symmetry), leading to differences between polarization parallel and perpendicular to this direction. The changed crystal field leads to a further splitting of all peaks: the t_{2g} level is split into a doubly-degenerate e_g and a non-degenerate b_{2g} level, while e_g is split into non-degenerate a_{1g} and b_{1g} levels, respectively.¹ This can be described by the additional crystal-field parameters Ds and Dt , which also renormalize $10Dq$ (cf. Sec. 3.2).

Up to now, the discussion was done within LFM theory. This can be expanded by making the transition to CTM, i.e., including charge transfer or hybridization [Fig. 4.19(e)]. In this case, the initial state is a linear combination of $2p^63d^0$ with states in which one (or more) electrons have been transferred from the ligands to the TM ion, e.g., $2p^63d^0 + 2p^63d^1\underline{L}$, where \underline{L} denotes the ligand hole. The two main consequences are additional satellites and new substructures to the peaks because even more terms become allowed, as well as a contraction of the multiplet structure due to Coulomb attraction between the ligand hole(s) and the valence electron(s). Considering a $3d^1$ instead of a $3d^0$ (initial state) system, the number of multiplet states (and thus the complexity of the spectral shape) is even higher, and thus x-ray absorption spectra at the L edge can by no means be interpreted using simple analogies to DOS calculations which are single-particle-like by definition [cf. Fig. 4.19(f)].

¹Here, this results in a mere shift of spectral weight, and is not resolved in Fig. 4.19(d).

Table 4.4: Best-fit input parameters from LFM calculations in D_{4h} symmetry to simulate Ti L edge TEY spectra, and resulting crystal-field, Racah and Hubbard parameters. The first four rows are the input parameters to the programs, and the last four rows have been calculated from these according to the relations given in Sec. 3.2. The values given for the Slater integrals are the atomic parameters from Hartree-Fock, which were reduced to 80% of that value to give the best fit.^a Crystal-field splitting is given relative to the ground-state orbital. All values are given in eV.

spin-orbit coupling	$2p$	$3d$	
	3.8 ± 0.4	0.0272 ± 0.01	
direct Slater integrals	F_{pd}^2	F_{dd}^2	F_{pd}^4
	5.581	10.343	6.499
exchange Slater integrals	G_{pd}^1	G_{pd}^3	
	3.991	2.268	
crystal-field integrals ^b	X_{400}	X_{420}	X_{220}
	4.9	-0.05557	1.29
crystal-field parameters ^b	$10Dq$	Dt	Ds
	1.5	0.00343	-0.1543
crystal-field splitting ^c	$d_{xz,yz}$	$d_{x^2-y^2}$	d_{z^2}
	0.48^d	1.48	2.08
Racah parameters	A	B	C
	3.559	0.101	0.413
Hubbard parameters	U	$J(= J_3)$	
	5.6	0.74	

^aIt is well-known that this reduction mimics the Slater integrals in actual solids [de Groot08].

^bApply only to LFM calculations.

^cThese resemble the values observed in RIXS, cf. Sec. 4.2.4. The latter were used as initial guesses for the crystal-field parameters in LFM calculations. In CTM calculations, they were not used as fit parameters but kept fix to reproduce RIXS spectra in the subsequent modeling step.

^dThis corresponds to the average value of the d_{xz} and d_{yz} crystal-field splitting seen in RIXS.

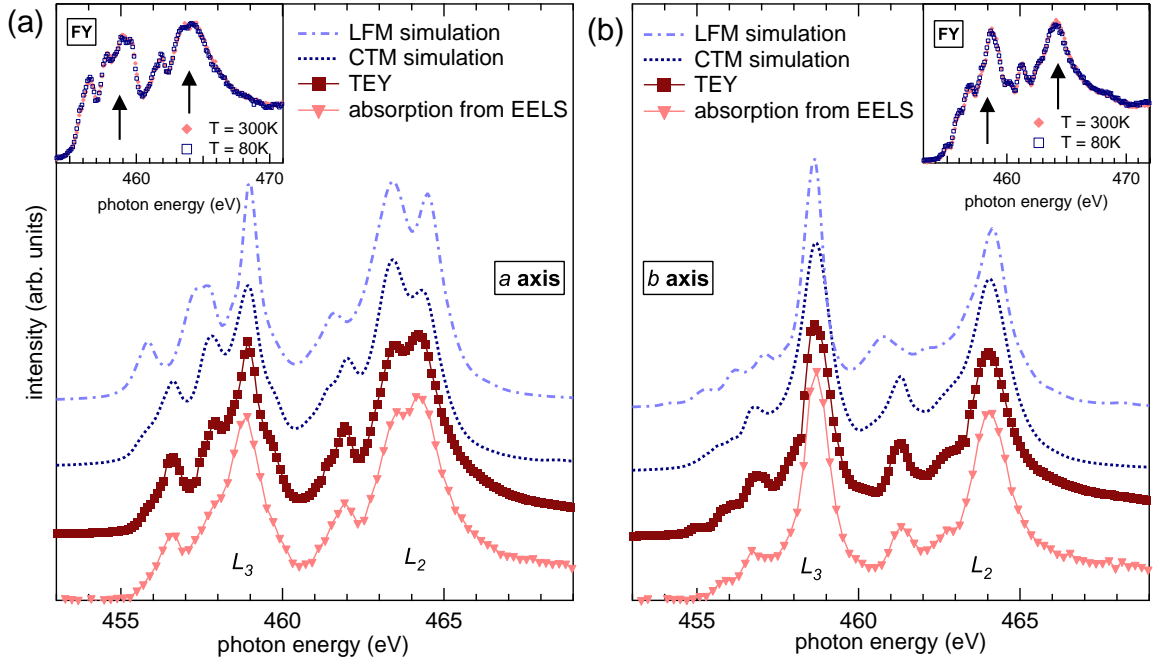


Figure 4.20: Ti L edge absorption spectra of TiOCl at $T = 300\text{ K}$ along the (a) a and (b) b axis. Absorption spectra from EELS (red triangles) provide the correct (photon) energy scale. Also shown are TEY measurements (brown square markers) and results from LFM (dash-dotted curve) and CTM (dotted curve) calculations (for details see text). The insets show corresponding FY spectra at room temperature (red) and 80 K (blue). Self-absorption effects appear even stronger than in O K edge spectra, cf. structures marked by arrows.

Figure 4.20 presents measurements of the Ti L edge using a EELS spectrometer,¹ and TEY spectra from BESSY, taken at room temperature both along the a and b axis. Ti L edge spectra from FY, which appear to suffer even more from self-absorption than the O K edge spectra in Fig. 4.18, are shown as insets both at $T = 300\text{ K}$ and $T = 80\text{ K}$. No differences can be observed between the high- T and low- T phases, similar to the O K edge. As discussed before, we used TEY data to compare with our simulations, as they show finer structures and need not be corrected for self-absorption. Results from calculations within LFM theory in D_{4h} symmetry and from CTM theory in D_{2h} symmetry are also shown in Fig. 4.20. All theoretical spectra have been broadened by a Gaussian with FWHM of 0.1 eV to account for the experimental resolution, and Lorentzians with FWHM of 0.4 eV and 0.2 eV for the L_2 and L_3 edges, respectively, to account for lifetime broadening. Different values for the two edges are justified by the fact that there is an additional Auger decay channel available at the L_2 edge, leading to enhanced broadening [de Groot90b]. The best-fit parameters corresponding to the spectra are given in Tab. 4.4.

¹Primary beam energy 172 keV , energy resolution $\Delta E \sim 80\text{ meV}$.

Comparing first the LFM calculations (dash-dotted curve) with the experimental spectra one realizes that although the basic shape in terms of number of peaks, relative intensity and polarization dependence can be reproduced, they appear stretched energetically compared to experiment. This can be straightforwardly attributed to the omission of charge-transfer effects when one looks at the spectra calculated within CTM (dotted curve). It is well known that these effects lead to a contraction of multiplet structures if the charge-transfer energy Δ ($= 5.0$ eV for the shown spectra) is positive, and produce additional small satellite structures [Okada93]. As stated previously, also the degeneracy between d_{xz} and d_{yz} is lifted only in these calculations due to the lower symmetry used.¹ Nevertheless, transmuting the fit parameters from the different methods into the on-site Coulomb repulsion U and exchange interaction J ($= J_3$ for the cases relevant to TiOCl) one finds good agreement with typical values needed for reasonable results from density functional calculations.

4.2.4 Two-Spinon and Crystal-Field Excitations

In the previous section it was shown that although x-ray absorption spectra give valuable information on the unoccupied electronic structure, no straight-forward interpretation is possible because one has to deal with many-body final states leading to complicated multiplet structures, or needs to take the detour via ligand orbitals. Resonant inelastic x-ray scattering (RIXS), on the other hand, allows to directly map orbital, spin and phonon excitations. As the XAS final state is the intermediate state of RIXS, the selection rules and polarization dependencies valid in the former apply in RIXS as well. Nevertheless, these can fully be implemented into calculations of spectra, and in the $3d^1$ final state of TiOCl even allow for a direct interpretation of the observed structures.

We performed RIXS experiments at the ADDRESS beamline at SLS, using the SAXES spectrometer [Ghiringhelli06]. The beamline allows for sample cooling down to lowest temperatures (4 K) and switching of the linear polarization from horizontal to vertical. The measurement geometry has already been shown in Fig. 2.6(b). Except for the \mathbf{q} -dependent measurements discussed at the end of this section, the setup was such that the angle between incident beam and emitted photons was kept constant at $\varphi = 90^\circ$, and we used light incidence 20° off from grazing. The energy resolution, which was determined from the full width at half maximum (FWHM) of the elastic line of carbon tape at the used energies (around the Ti L edge at ≈ 460 eV), was set to 100 meV or better in all measurements. The pressure in the experimental chamber was in the low 10^{-9} mbar regime. Since RIXS is a bulk-sensitive technique, this pressure was sufficient to allow for experiments on the same sample for several days without noticeable contamination effects. Additionally, samples could be cleaved already in air and then transferred into the vacuum chamber, still allowing for measurements of intrinsic (bulk) properties of the

¹In D_{2h} one can define two additional crystal-field parameters [Haverkort05]. While Du directly describes the splitting between d_{xz} and d_{yz} , the parameter Dv gives a mixing (and thus additional splitting) of d_{z^2} and d_{xy} orbitals.

Table 4.5: $3d$ crystal-field splittings (in eV) obtained from different theoretical and experimental methods (at room temperature unless noted otherwise), relative to the lowest $3d$ orbital ($d_{x^2-y^2}$). GGA results taken from [Glawion09], optical spectroscopy and cluster model taken from [Rückamp05b].

	d_{xz}	d_{yz}	d_{xy}	d_{z^2}
RIXS	0.36	0.58	1.45	2.05
RIXS @ 36 K	0.35	0.62	1.48	2.08
opt. spectroscopy	– ^a	0.65 ^b	1.5 ^c	– ^a
cluster model	0.25	0.69	1.24	2.11
cluster @ 4 K	0.25	0.77	1.47	2.18
GGA	0.24	0.46	1.54	2.08

^anot observable

^bonly for $E||a$

^conly for $E||b$

sample. Due to the comparatively¹ low absolute count rates and thus bad statistics of RIXS experiments, all shown spectra are summed up from many single measurements, which had to be calibrated in energy using the maximum of their respective elastic line at zero energy loss. Typical acquisition times were between 5 and 10 min, and 2 – 20 such spectra were summed up for each spectrum shown in the figures.

Figure 4.21(a) shows typical RIXS spectra at room temperature and at $T = 36$ K, i.e., in the spin-Peierls phase, taken at a photon energy $h\nu = 454.2$ eV in σ polarization and with ac being the scattering plane (“ ac scattering geometry”). In both cases, five peak-like features are observable. Besides the elastic line there are four well distinguished peaks at approx. 0.35, 0.62, 1.48, and 2.08 eV, as determined from fitting Gaussian peaks to the low- T data. Looking at results from previous experimental and theoretical investigations summarized in Tab. 4.5 these features can be attributed to on-site dd excitations whose energies in a $3d^1$ system directly correspond to the crystal-field splitting. RIXS is the first experimental probe by which the lowest (inelastic) dd excitation (d_{xz}) can be observed at all, and also the first to display all dd excitations in one spectrum. This is because the Kramers-Heisenberg formula (Eq. 3.38) involves two dipole transitions, and thus excitations which are dipole-forbidden in regular optical spectroscopy become allowed. The order of d orbitals is $d_{x^2-y^2}$, d_{xz} , d_{yz} , d_{xy} , and d_{z^2} from zero to 2.1 eV energy loss, as indicated in the figure. Charge-transfer excitations of the type $2p^63d^1 \rightarrow 2p^53d^2 \rightarrow 2p^63d^2\bar{L}$ lie at higher energy losses (not shown). Cooling from room temperature down to the spin-Peierls phase, the peaks become narrower and show slight shifts towards smaller energy losses, which were also predicted by cluster model calculations [Rückamp05b]. This is due to a temperature-dependent change in

¹As opposed to, e.g., PES and XAS.

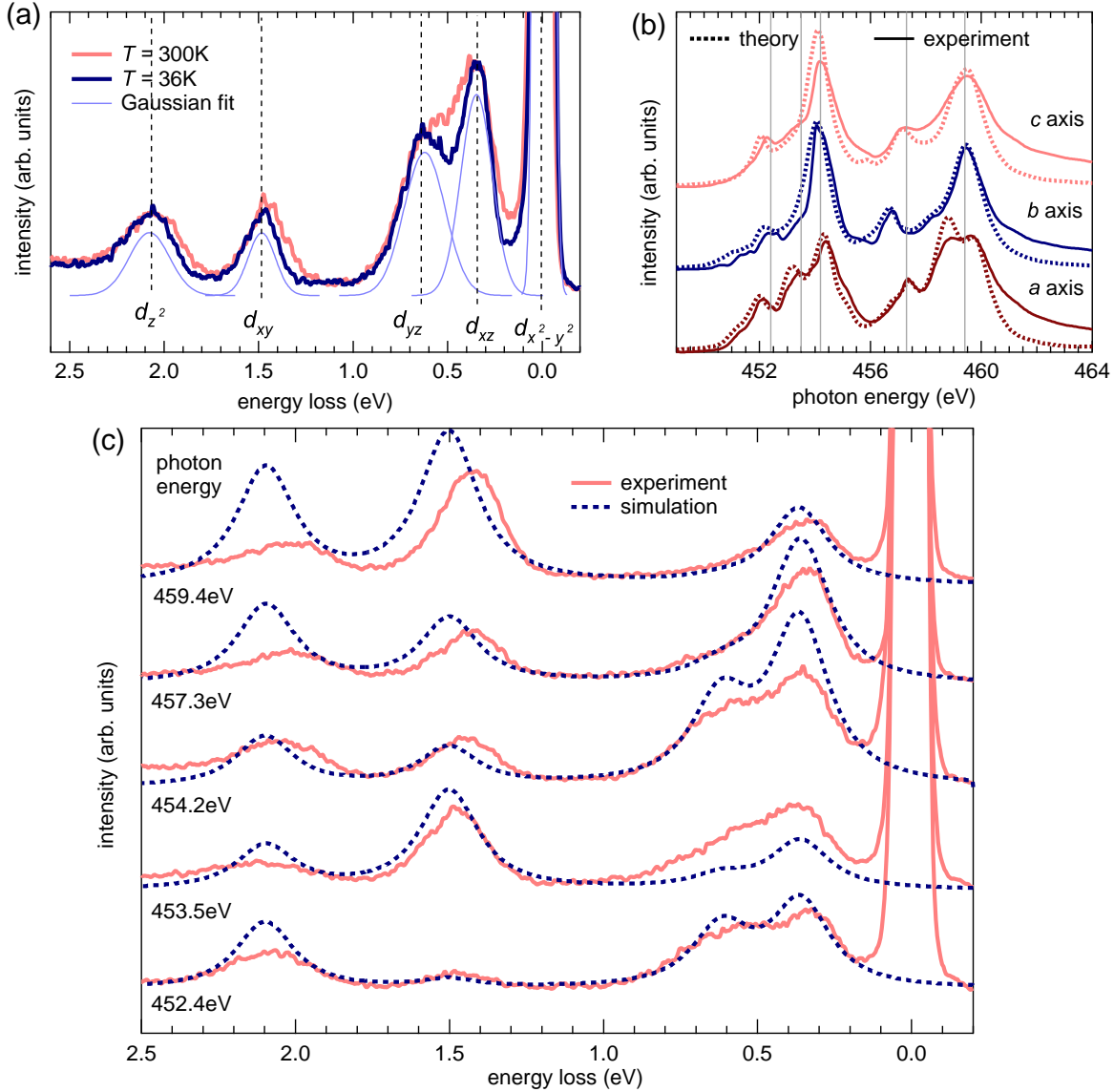


Figure 4.21: (a) RIXS spectra at $T = 36\text{ K}$ (blue) and $T = 300\text{ K}$ (red) measured with $h\nu = 454.2\text{ eV}$ in σ polarization and ac scattering geometry. Results from fitting Gaussian lineshapes to obtain the peak positions are shown as light blue solid curves. Also, the orbital character of the crystal-field excitations is indicated. (b) Measured (solid curves) and calculated (broken curves) Ti L edge XAS spectra for different polarizations. The different photon energies used in panel (c) are indicated by gray lines. (c) Photon-energy dependence of RIXS spectra at $T = 300\text{ K}$ (solid curves; σ polarization; ac scattering geometry). Results from CTM calculations are shown as broken curves.

the distortion of the TiO_4Cl_2 octahedra.

Figure 4.21(c) shows the photon-energy dependence of room-temperature RIXS spectra, in the same geometry and polarization as in panel (a), but at a number of different photon energies $h\nu$ across the Ti L edge. Panel (b) shows the Ti L edge absorption spectrum acquired in TEY for different polarizations along the three crystal axes,¹ and the used photon energies are indicated. From a closer inspection it can be realized that certain spectral features can be at slightly different energies when comparing experiment with theory; this will be revisited below. In Fig. 4.21(c) also results from CTM calculations on a single TiO_4Cl_2 cluster are displayed, which were also performed by M. W. Haverkort. In order to obtain such calculated spectra one constructs a suitable basis by downfolding the band structure calculated with LDA [Andersen00] such that the basis wave functions correspond essentially to atomic d orbitals, centered on the Ti site in the center of the cluster. Then, the Kramers-Heisenberg formula is evaluated to get the particular intensities of dd excitations. In this step, appropriate lifetime broadening in the intermediate state (the x-ray absorption spectrum) is applied to account for the observed peak widths. Finally, the elastic line (reflecting the contribution from $d_{x^2-y^2}$ orbitals) can be added as a Gaussian having the experimentally observed FWHM. However, this has to be done artificially, since for an ideal crystal surface implied by the neglect of surface effects in our calculations, its weight is fully transferred to Bragg reflections (at $\mathbf{q} = 0$), leaving it with zero intensity for other values of \mathbf{q} . The fact that it is observed in experiment is due to the roughness of the sample surface.

The orbital excitations contained in this theory are in principle dispersive, because one can make them at each site with equal energy cost, given that the ratio of the hopping matrix element t and the on-site Coulomb repulsion U is large enough to make them non-local.² However, even if this was the case, due to coupling to bosonic modes like phonons, their weight could become incoherent, i.e., the momentum dependence would be smeared out. This is related to the Franck-Condon principle and well-known from photoemission experiments on hydrogen molecules [Asbrink70], but can also be observed, e.g., in cuprates [Damascelli03], other transition metal oxides [Schrupp05], and quasi-one-dimensional conductors [Perfetti01]. From the \mathbf{q} -dependent measurements shown below, no dispersion of the orbital excitations in TiOCl can be identified, and as a result they should be termed on-site dd excitations, as opposed to orbitons, which are dispersive orbital excitations. Also, these observations justify the usage of single clusters for our calculations, which cannot produce a momentum dependence. Using a lifetime broadening of 200 meV the photon-energy dependence of the dd excitations is very well captured in our simulations, cf. Fig. 4.21(c). Also for different polarizations there is very good agreement between theory and experiment, as can be seen in Fig. 4.22 for selected photon energies. The fact that this holds for many different photon energies and

¹Polarization along the c axis means grazing incidence at an angle of 20° in our experiments, i.e., we are never fully polarized along this direction.

²Such dispersions have been observed recently with RIXS on LSCO [Schlappa10].

polarizations evidences the great suitability of our cluster approach to simulate RIXS spectra.

Although they are quite minute, some discrepancies remain, and possible explanations shall be discussed in the following. Firstly, there seems to be an energetic contraction of the experimental RIXS spectrum at higher photon energies, manifested in shifts of (especially) the e_g -derived excitations towards lower energy losses. Secondly, not all weights are correctly reproduced for different polarizations, again most notably in the case of e_g orbitals π polarization at higher photon energies [cf. Figs. 4.22(a) and (b)]. Since there is a large number of possible multiplet states, already a slight photon energy shift could lead to involvement of different intermediate states with largely different selection rules. This is illustrated by the comparison between experimental and calculated x-ray absorption spectra in Fig. 4.21(b). It is intuitively clear that a simulated RIXS spectrum can never have better agreement with experimental data than the according intermediate state (i.e., XAS) spectrum. Though not very well resolved in the figure, given spectral features can be off by as much as 200 meV between experiment and theory. This happens although the calculated spectra have been shifted towards the absolute photon energy scale of the measurements, i.e., it is not possible to match all spectral features at once. Such a shift could be due to an unintendedly nonlinear energy scaling of the beamline crystal mirror, which might also developed spontaneously during measurements. Analogous effects might come from fluctuations on the meV scale of the photon energy during data acquisition.

One of the reasons why high-resolution RIXS has become a widely used tool in the past five years is that it is sensitive not only to orbital (local dd or orbiton) but also to magnetic excitations (spinons and magnons). Investigation of the latter has previously been a domain of inelastic neutron scattering (INS), which however has several short-comings compared to RIXS: due to small cross-sections, one needs large sample volumes of the order of several cm^3 and has to measure for several days or even weeks, while the resonant enhancement in RIXS provides reasonable statistics for sample volumes $\lesssim 0.1 \text{ mm}^3$ within minutes or hours. Furthermore, in the investigation of spinon excitations, INS is limited to the Brillouin zone (BZ) boundary, as the two-spinon dynamical structure factor, which for neutrons is smaller than for RIXS *per se*, goes to zero for small \mathbf{q} in a quasi-linear fashion [Karbach97]. RIXS in the soft-x-ray regime, on the other hand, while it gives access only to rather small \mathbf{q} values due to the small photon momenta available, can provide sufficient signal-to-noise ratios in the zone center due to large cross-sections. This becomes important when noticing a low-energy feature at roughly 0.1 eV, barely visible in the experimental spectra shown up to now, which can be seen in Fig. 4.23. Since this feature also is not present in the CTM calculations which neglect magnetic excitations, the considerations just made give reason to test by comparison to suitable models, if this peak is of magnetic origin. An obvious choice for TiOCl is a one-dimensional $S = 1/2$ Heisenberg chain for which various solutions exist. It has an analytic solution called the Bethe-Ansatz [Bethe31], but can also be tackled more flexibly (e.g., including finite interchain coupling) using linear spin-wave theory [Müller81].

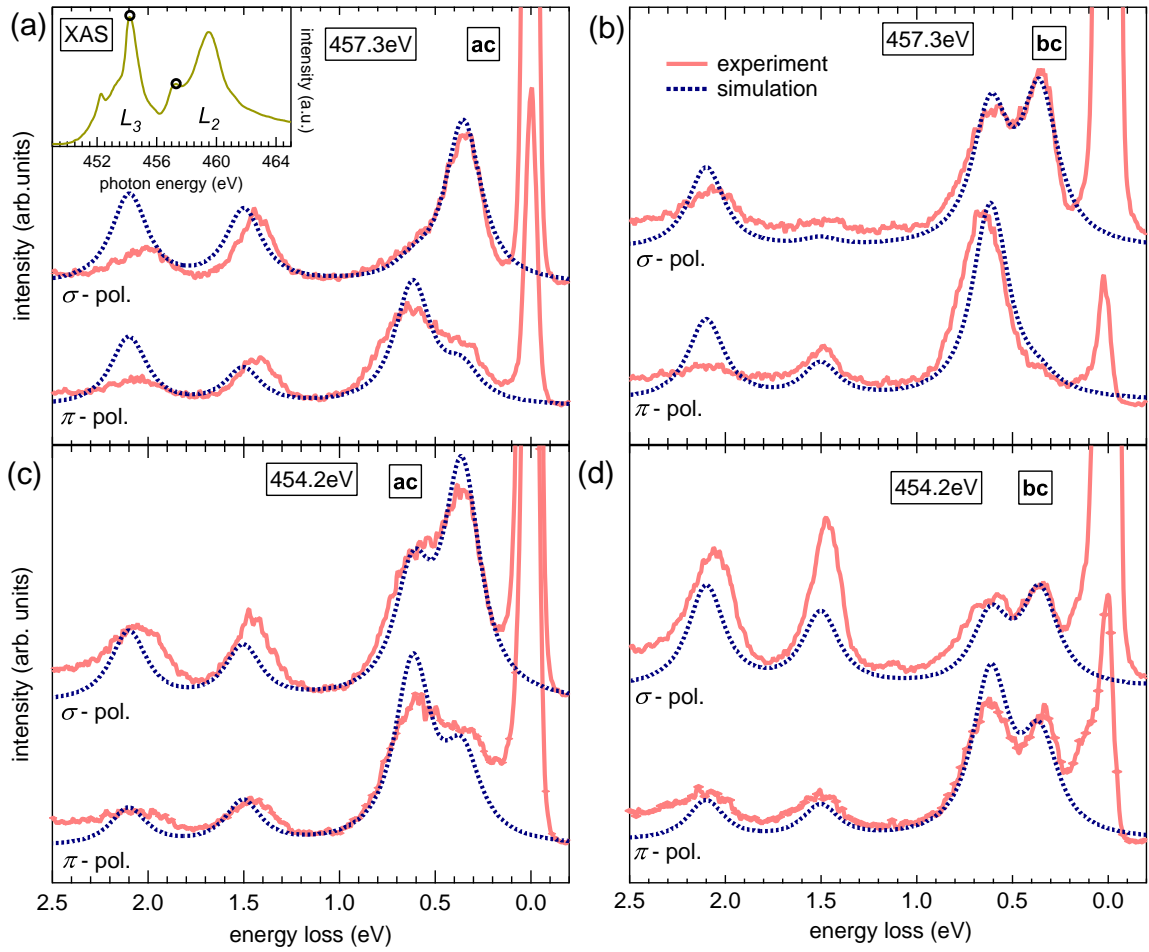


Figure 4.22: π - and σ -polarized RIXS spectra for $h\nu = 457.3\text{ eV}$ (a,b) and $h\nu = 454.2\text{ eV}$ (c,d), with scattering geometries *ac* (a,c) and *bc* (b,d) from experiments (solid curves) and multiplet calculations (broken curves). The inset in panel (a) shows the corresponding Ti L edge XAS spectrum (polarization along *c*). The used photon energies are indicated by markers.

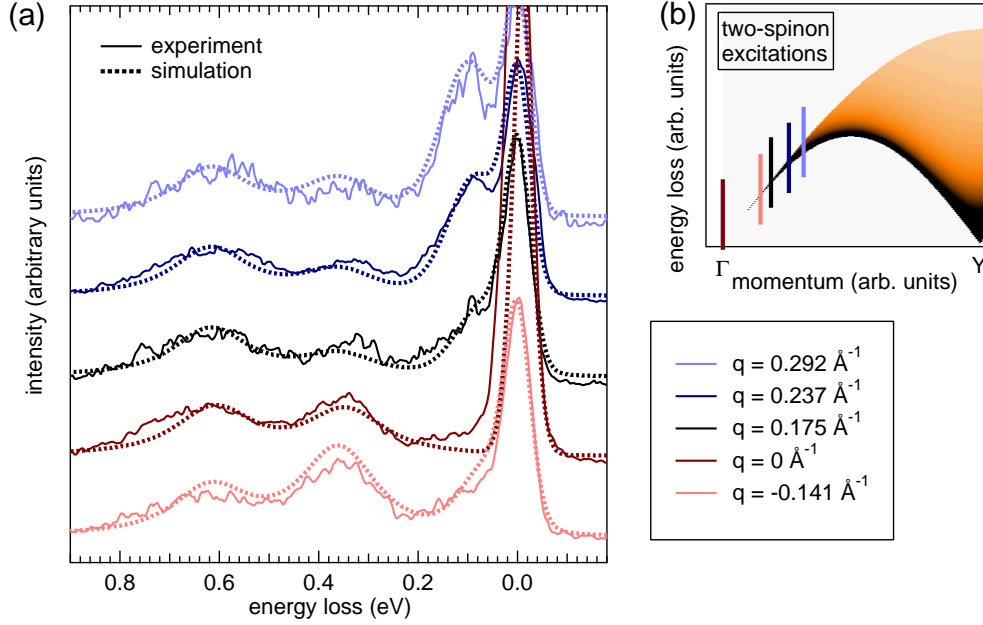


Figure 4.23: (a) RIXS spectra taken at $h\nu = 458.1$ eV in π polarization and bc scattering geometry ($T = 36$ K), for q_{\parallel} -values corresponding to (from top to bottom) 31%, 25%, 18%, 0%, and -15% of the ΓY path in the BZ. (b) Two-spinon dynamical structure factor $S(\mathbf{q}, \omega)$ (cf. Fig. 3.6) for the path ΓY . The momentum positions at which the spectra in panel (a) were taken are indicated in the corresponding color.

As an important side-effect, these approaches introduce a momentum dependence which was not included in the previous CTM calculations (see the above discussion of orbital excitations). Recently, the intimate connection also of magnetic excitations to the intermediate state has been highlighted from the theoretical point of view [Haverkort10]. In the case of RIXS, the appropriate scattering operator is proportional to

$$\sigma^{(1)}(\omega_{in}) \epsilon_{in} \times \epsilon_{out} \cdot \hat{S} \quad , \quad (4.6)$$

where ϵ_{in} (ϵ_{out}) is the incoming (outgoing) photon polarization vector, ω_{in} the energy of the incoming photon, and \hat{S} the spin operator. $\sigma^{(1)}(\omega_{in})$ is the direction-dependent fundamental x-ray magnetic circular dichroism (XMCD) spectral function, i.e., the XMCD signal one would obtain if one could *fully* magnetize the sample and then calculate the difference between spectra measured using left and right polarized light.

Figure 4.23 shows spectra at different points in the BZ. Simulated spectra come from a combination of CTM (for orbital excitations) and spin wave (for magnetic excitations) theory, with an additional elastic line (a Gaussian with FWHM of 60 meV) added for better comparison with experiment. Although only a limited number of points in the BZ was available experimentally due to limitations concerning photon momentum and geometry, one can clearly see a \mathbf{q} -dependence of both peak position and intensity of

the feature at approx. 0.1 eV. Data was acquired in the spin-Peierls phase for different \mathbf{q}_{\parallel} values along b [π polarization, bc scattering geometry; $\varphi = 50^\circ$, cf. Fig. 2.6(b)]. All spectra consist of at most eight single shots of 5 minutes acquisition time each, because otherwise the low-energy peak of interest was observed to blur and drown in the background (see discussion below). As discussed in Sec. 2.3 the available photon momentum is $\mathbf{q}(460 \text{ eV}) \approx 0.422 \text{ \AA}^{-1}$, and the BZ boundary along the 1D direction (the Y point) lies at 0.94 \AA^{-1} , allowing to cover approx. 30% of the path $\overline{\Gamma Y}$ with \mathbf{q}_{\parallel} .

As noted previously, within experimental accuracy and with the rather poor signal-to-noise ratio no sizable dispersion is observed for the dd excitations, from which it is concluded that they are essentially localized. The fact that their intensity is \mathbf{q} -dependent is due to the geometrical realization of different momentum transfer: \mathbf{q}_{\parallel} is changed by rotating the sample, which also changes the polarization and thus the observed intensity. This is captured by the orbital peaks generated by CTM calculations.

The 100 meV peak has highest intensity at the highest measured $\mathbf{q}_{\parallel} = 0.292 \text{ \AA}^{-1}$, corresponding to $0.31\overline{\Gamma Y}$ (top), while it is suppressed towards the Γ point. Figure 4.23(b) shows the \mathbf{q} -dependent dynamical structure factor of two-spinon excitations, where also the \mathbf{q} points are marked in the color corresponding to the momentum-dependent RIXS spectra in panel (a). Unfortunately, we have only access to the inner branch where the two-spinon scattering continuum is still indistinguishable energetically from the one-spinon dispersion lying along its low-energy boundary. Nevertheless, while the latter would have its maximum intensity at Γ the opposite is true for two spinons, in line with our experimental observation. Note again that this poses no problem, since flipping one spin in an antiferromagnetically ordered chain¹ creates two spinons which move with different velocities through the lattice (cf. Fig. 3.6). Similar observations were made in a RIXS study on La_2CuO_4 [Ament09], but TiOCl is the first non-copper-based compound to display such clear evidence for spin excitations in RIXS.

Being sure about the magnetic origin of the 100 meV peak, some further comments shall be made concerning the spectra in Fig. 4.23. Firstly, the huge intensity of the elastic line at $\mathbf{q} = 0$ (or, similarly, its suppression at other \mathbf{q} values) nicely reflects the arguments named previously for the transfer of elastic intensity to Bragg reflections. Secondly, the remaining intensity of the magnetic peak at $\mathbf{q} = 0$ in the experiment might be an indication for finite interchain coupling and/or dispersion in the c direction, as we actually only have $\mathbf{q}_{\parallel} = 0$, while \mathbf{q}_c is finite. Thirdly, in nuclear magnetic resonance (NMR) experiments a spin gap in TiOCl has been observed, the value of which was extracted to be approx. 430 K (37 meV) [Imai03]. Thus, the (two-)spinon branch should display a gap at $\mathbf{q} = 0$, which probably is not observable in the available data due to the vanishing of the dynamical structure factor in this region of the BZ.

This last argument is intimately connected to a fourth comment, namely, the limited lifetime of the spinon peak in RIXS experiments, which made it very hard to observe.

¹This also holds if there is no long-range, *static* antiferromagnetic order, as expected in TiOCl due to the frustrated lattice.

It turned out that the peak decays on time scales of less than 10 minutes of exposure to synchrotron radiation, but can be restored by changing the position of the light spot on the sample. Had we not been able to verify the intrinsic nature of this feature (e.g., by the \mathbf{q} -dependence of the cross-section unique to magnetic excitations), adsorbate or impurity vibrations could have come to ones mind as a possible origin of such fast-decaying structures. Although no studies of adsorbates on TiOCl are available at present, there are strong arguments against this possibility. The only “impurity element” found by XPS in sizable amounts to be connected to the rather strong signal observed here is carbon. Vibrations of common carbon compounds like CO or CO₂ [NIST10] are off too far from the observed peak as to possibly explain it. Water as another candidate, which is basically impossible to detect by PES on an oxide sample, has vibrations only in an energy range well above 200 meV [Max09]. TiOCl lattice phonons can also be excluded because they have energies of roughly 18 – 53 meV, as measured by Raman spectroscopy [Lemmens04] and calculated by LDA+ U [Pisani05]. Multi-phonon excitations which could reach the observed energy range, on the other hand, have too low cross-sections to produce significant contributions to the RIXS spectrum. Also, it can be assumed that a loss of phonon signatures would go along with a *de facto* destruction of the crystal lattice. It appears unlikely that this could happen (i) locally and/or reversibly, thus allowing to find the peak again at a different sample spot, and (ii) without destroying the electronic structure (i.e., the orbital excitations) first.

4.2.5 Bandwidth-Controlled Closing of the Charge Gap

Having investigated the insulating phases of the oxyhalides in detail, the possibility of driving them into a metallic state can be tackled based on a solid footing. The first route which was investigated is that of a bandwidth-controlled metal-insulator transition (MIT). Since isovalent ions with different radii (which would apply “chemical pressure”) are hard to be incorporated into oxyhalide crystals without losing their characteristic features like the spin-Peierls (SP) phase [Clancy08], the only way to achieve changes in the bandwidth is the exertion of external pressure. This can be done in controlled ways using, e.g., diamond anvil cells (DAC), which make it possible to perform both spectroscopic and transport measurements under pressure. First results came from studying the transmittance and reflectance of TiOCl and TiOBr in the infrared and visible frequency range at room temperature, in collaboration with the group of C. Kuntscher [Kuntscher06, Kuntscher07]. For these experiments, DACs and various pressure-transmitting media [CsI, argon, methanol:ethanol (4:1)-mixture] were used, and the signal was recorded by a Bruker IFS 66v/S FT-IR spectrometer. Although the results agree qualitatively, there are quantitative differences when using different pressure media: Pressure-induced effects set in at approx. 4 GPa higher pressures for CsI, which is not unexpected, however, because it does not provide good hydrostatic conditions [Loa99]. Nevertheless, for the reflectance measurements finely ground CsI powder had to be used to ensure direct contact of the sample with the diamond window.

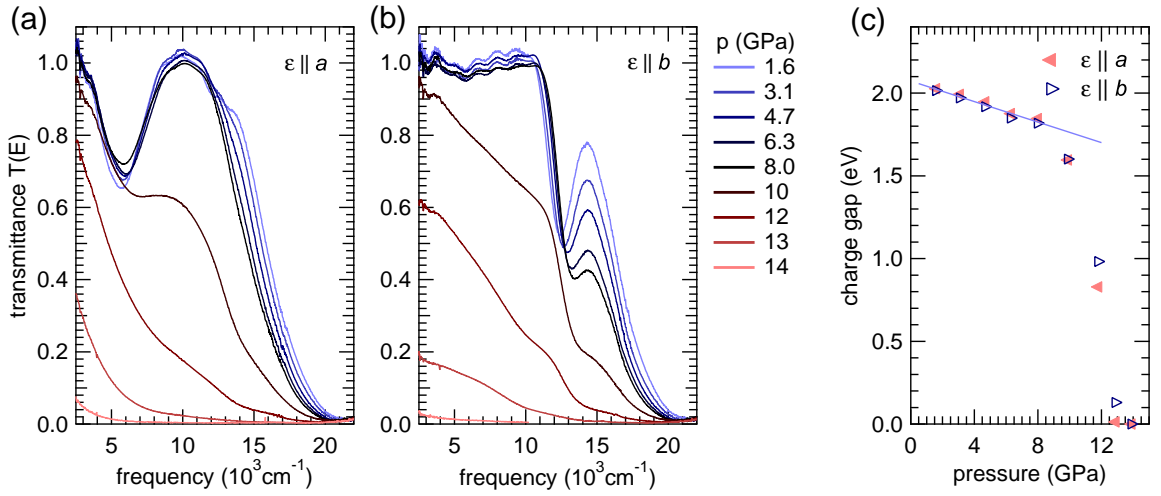


Figure 4.24: (a,b) Pressure dependence of the transmittance $T(E)$ of TiOCl for polarizations parallel to the (a) a and (b) b axis, respectively. (c) Charge gap, estimated from a linear extrapolation of the absorption edge, as a function of pressure. The full line corresponds to a linear fit to the data for pressures below 8 GPa.

Due to the small gasket dimensions of the pressure cell, small single-crystalline samples ($\leq 80 \times 80 \times 5 \mu\text{m}^3$) were used. The actual pressure was determined from the well-known luminescence behavior of a small ruby crystal placed next to the sample in the pressure cell [Mao86].

Figure 4.24 shows two panels with the pressure-dependent transmittance $T(E)$ of TiOCl in an energy range up to 2.5 eV ($1 \text{ eV} \approx 8075 \text{ cm}^{-1}$) with light polarization along the a and b axis, respectively. $T(E)$ is the ratio of the intensity transmitted through the sample and the one transmitted through the empty pressure cell. At low pressures, dd excitations to the d_{yz} ($E = 0.66 \text{ eV}$) and d_{xy} ($E = 1.53 \text{ eV}$) orbitals are observed as Gaussian-shaped dips in the transmittance, in accordance with other optical absorption experiments [Rückamp05b] and our RIXS results (cf. previous section). Up to pressures around 8 GPa the energetic positions of these excitations shift to slightly higher energies, which is due to a decrease of the interion distances (cf. Fig. 4.26) and thus an increased CFS. In order to obtain a measure of the optical conductivity, the absorbance A can be calculated as $A = \log_{10}[1/T(E)]$, and from a linear extrapolation of the onset of total absorption (i.e., the absorption edge) the size of the charge gap can be deduced. The pressure dependence of the gap thus obtained is shown in Fig. 4.24(c): Up to approx. 8 GPa a smooth reduction of the gap from the initial 2 eV is observed, followed by a step drop, reaching a (seeming) closure above $p_{c1} \approx 12 \text{ GPa}$. It must be noted, though, that this procedure only yields an estimate for the gap, based on the available frequency range. From another study with frequencies in the far-infrared range the “relaxed” conclusion was drawn that the gap is gradually filled with additional electronic states down to at least 25 meV [Kuntscher08].

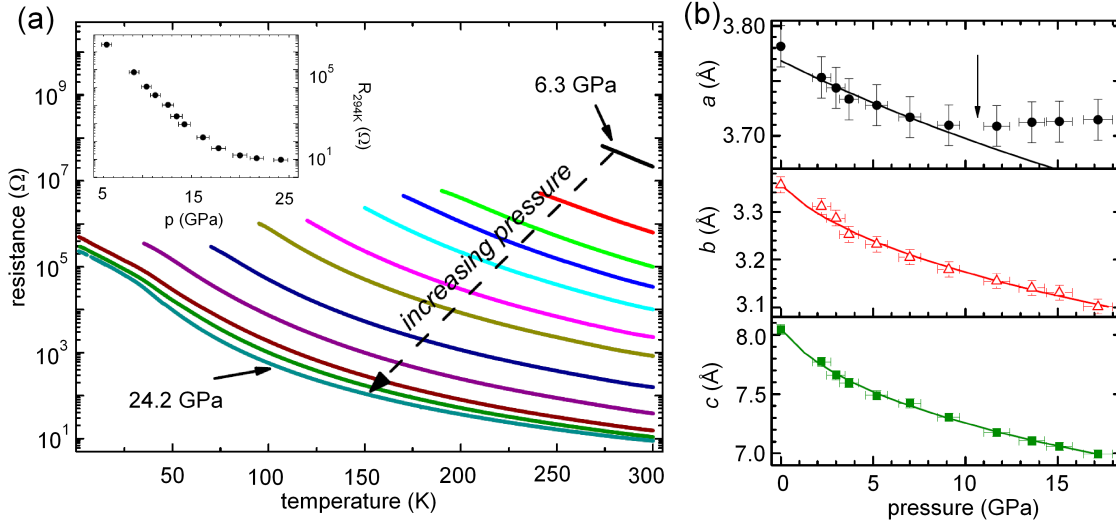


Figure 4.25: (a) Temperature dependence of the electrical resistance of TiOCl for various pressures from 6.3 GPa (top right, black curve) to 24.2 GPa (lower left, blue curve) on a logarithmic scale. The inset shows the pressure dependence of the electrical resistance at $T = 294$ K, corresponding to a vertical cut in the main panel. (b) Absolute magnitude of the lattice parameters a (top), b (center), and c (bottom) of TiOCl at $T = 300$ K up to pressures above the charge gap closing in IR experiments. The arrow in the topmost panel marks the anomalous change of the a axis parameter above 11 GPa (all data from [Forthaus08]).

These obvious changes in the electronic structure give evidence for the possible appearance of a metallic phase at high pressures, but conflicting results come from electrical transport measurements, which are shown in Fig. 4.25(a) [Forthaus08]. This data was recorded using a DAC filled with a 4:1 methanol-ethanol mixture submerged in a ⁴He cryostat. Although the pressure dependence of the electrical resistance at $T = 294$ K shows a huge reduction by six orders of magnitude (see inset of the figure) over a wide pressure range from 6.3 GPa up to 24.2 GPa, the electrical resistance always goes up with decreasing temperature, indicative of activated behavior as in a semiconductor or insulator. From an Arrhenius plot these authors estimated the activation energy, whose pressure dependence shows an abrupt change at roughly 13 GPa from -39 meV/GPa to -10 meV/GPa. Although this critical pressure is in good agreement with the supposed gap closure found above in infrared spectroscopy, the activation energy is $E_g(13 \text{ GPa}) \sim 0.3$ eV and decreases only to ca. 160 meV at the highest pressure investigated (24.2 GPa). This is obviously at variance with the above results of a gap closure in the far-infrared region.

A question naturally arising when aiming at a microscopic understanding of the observed changes is the influence of pressure on the crystal structure. To this end, we performed room-temperature XRD of TiOCl and TiOBr under pressure at beamline ID09A of the European Synchrotron Radiation Facility (ESRF) in Grenoble, France

[Kuntscher07, Kuntscher08, Ebad-Allah10]. For the measurements, monochromatic radiation with wavelength $\lambda = 0.4128 \text{ \AA}$ and Helium as hydrostatic pressure-transmitting medium were used. From subsequent LeBail fits¹ the lattice parameters can be determined as a function of pressure. A similar study has also been performed by Forthaus *et al.* [Forthaus08] at HASYLAB, the results of which are shown in Fig. 4.25(b). According to their study initially all lattice parameters smoothly decrease upon increasing the pressure. Above ca. 11 GPa, however, the a axis parameter abruptly changes its behavior [see arrow in top panel of Fig. 4.25(b)] and remains nearly constant, while the ones of the b and c axes continue to decrease up to the highest measured pressures of ~ 18 GPa. The authors ascribe this to the nearest-neighbor ion-ion distances (Ti–O along the a axis). Their result of $d(\text{Ti–O})_{11 \text{ GPa}} = 2.02 \text{ \AA}$ (not to be confused with the lattice parameter) is very close to the sum of the radii of the respective ions at ambient pressure, $d(\text{Ti–O})_{\text{ion}, 0 \text{ GPa}} = 2.05 \text{ \AA}$. Due to the largely increased energy cost for interpenetrating electron clouds it is expected that this represents a lower boundary for the distance between Ti and O ions. The anomalous behavior of the a axis parameter, however, is most probably an artifact of the authors' assumption that no structural phase transition occurs at high pressures, in contrast to another study by some of these authors [Blanco-Canosa09], our own results, and those from a DFT study in combination with molecular dynamics [Zhang08b].

Part of our own pressure-dependent XRD data taken over a wide pressure range is shown together with LeBail fits in Fig. 4.26(a). They clearly indicate that there is a symmetry lowering at high pressures. New peaks incompatible with the ambient-pressure (orthorhombic $Pm\bar{m}n$) crystal symmetry are found, and the refinements show that there is a mixture of $Pm\bar{m}n$ domains and domains of $P2_1/m$ symmetry above $p_{c1} \approx 15$ GPa, with another transition at $p_{c2} \approx 22$ GPa [Fausti07, Zhang08b, Ebad-Allah10]. Although this is the same dimerized, monoclinic space group as in the SP phase, one must note, however, that there are different unique axes and monoclinic angles in the two cases (b axis and $\beta \sim 99^\circ$ under pressure, c axis and $\gamma = 90.023^\circ$ for low temperatures). For the orthorhombic portion of the sample the behavior of the normalized lattice parameters is shown in Fig. 4.26(b). Qualitatively in line with the data of Forthaus *et al.* for pressures below approx. 10 GPa we find that the a axis parameter barely changes, in contrast especially to the c axis. This is expected because the wide van-der-Waals gaps along this direction allow for a relatively large compression.

In the monoclinic phase above p_{c1} , the unit cell is doubled along the b axis due to the dimerization, resulting in $a \times 2b \times c$, and two different Ti–Ti distances occur ($d_{\text{intra}} = 2.85 \text{ \AA}$ and $d_{\text{inter}} = 3.55 \text{ \AA}$). Their values can be explained in analogy to the discussion above. The intradimer distance is comparable to the close-contact distance in Ti metal at ambient conditions (2.896 \AA) and most likely represents a lower boundary. Thus, noting also that the relative change of the b lattice parameter upon pressure exertion ($\sim 20\%$)

¹A variant of the Rietveld method which uses peak intensities as independent parameters instead of extracting them from least-square fits of the respective structure factors $F(h, k, l)$.

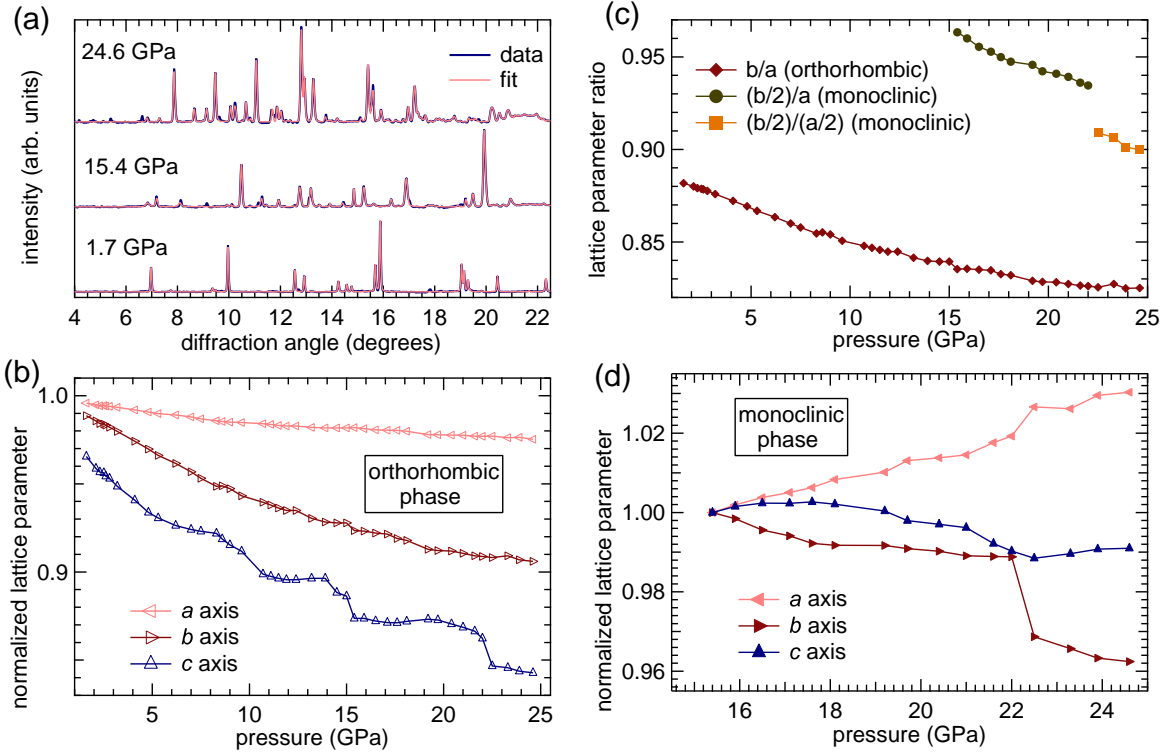


Figure 4.26: (a) XRD data of TiOCl at $T = 300$ K and corresponding LeBail fits at selected pressures in the three different phases. Above $p_{c1} \approx 15$ GPa a mixture of two phases ($Pm\bar{m}n$ and $P2_1/m$) has to be used for fitting. (b) Lattice parameters obtained from LeBail fits for the orthorhombic portion of the sample, normalized to their ambient-pressure value. (c) Various ratios between the b and a lattice parameters, also accounting for the unit-cell doubling above $p_{c1} \approx 15$ GPa and $p_{c2} \approx 22$ GPa. (d) Lattice parameters obtained from LeBail fits for the monoclinic high-pressure phases, normalized to their value at the orthorhombic-to-monoclinic transition ($p_{c1} \approx 15$ GPa).

is much larger than in the ambient-pressure SP phase ($\sim 5\%$), the electrons are expected to be delocalized in a molecular-orbit fashion within a dimer such that a widening of the bandwidth occurs. Accordingly, DOS calculations using LDA+ U [Blanco-Canosa09] and molecular dynamics methods combined with GGA+ U [Zhang08b] find that the influence of the (anisotropic) magnetic exchange interactions is significantly smaller than in the SP phase, and that the larger bandwidth drives both the structural changes as well as the closing of the charge gap. Thus, the authors of these studies interpret the high-pressure phase as a Peierls instead of a spin-Peierls phase.^{1,2} This non-trivial crossover from Mott insulator with SP ground state to more or less a band insulator with the usual Peierls distortion seems to be a unique feature of TiOCl, although other quasi-one-dimensional

¹In the sense that the *electronic* instead of the *magnetic* free energy is minimized.

²In a recent study at $T = 6$ K it was found that not only the undimerized room-temperature structure, but also the spin-Peierls phase can be driven into a Peierls-only state by pressure exertion, with dimerization along the a axis [Prodi10].

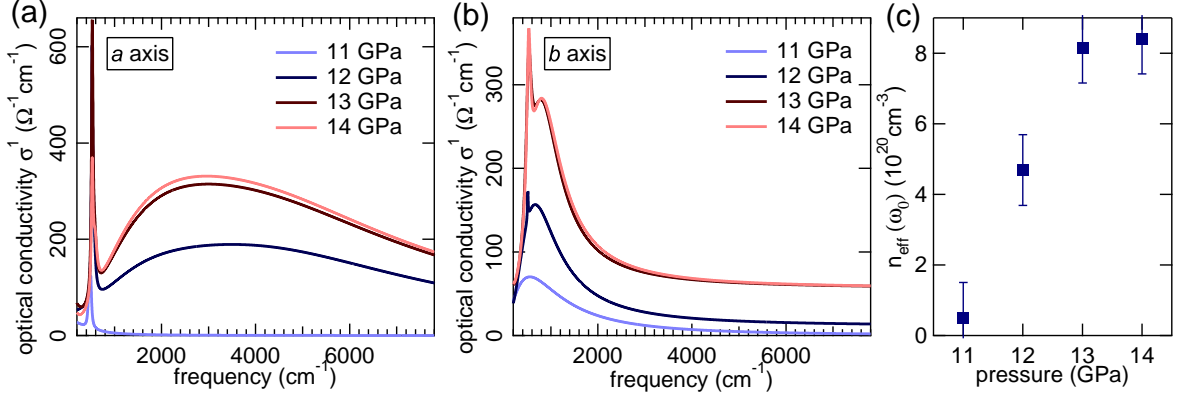


Figure 4.27: (a,b) Pressure-dependent optical conductivity of TiOBr at $T = 300 \text{ K}$ with light polarization along the (a) a and (b) b axis, respectively. (c) Effective charge-carrier density n_{eff} determined from the data in panels (a) and (b) using Eq. 4.8.

systems might display comparable changes.

These findings have certain implications for the dimensionality of TiOCl at elevated pressures. Figure 4.26(c) shows different pressure-dependent ratios of the lattice parameters b and a for the orthorhombic and monoclinic symmetry domains. In a simplistic view, these ratios can be taken as a measure of the anisotropy in the ab plane. One sees that the ratio $(b/2)/a$, which is the appropriate one for the doubled unit cell along b above p_{c1} , is much closer to one than b/a in the ambient-pressure phase. Looking at the normalized lattice parameters of the monoclinic domains shown in Fig. 4.26(d) this can be explained by the fact that while b continuously shrinks, the lattice is expanded along the a axis. For the orthorhombic phase, such a behavior of the a axis parameter is not observed [cf. Fig. 4.26(b)]. Thus, while the orthorhombic portion of the sample becomes more *one*-dimensional, the monoclinic portion has significantly more *two*-dimensional character, which becomes even stronger with increasing pressure [cf. Fig. 4.26(d)].

Above $p_{c2} \approx 22 \text{ GPa}$ the XRD pattern shows peaks which indicate a further unit-cell doubling along a , leading to a $2a \times 2b \times c$ superstructure. The corresponding ratio $(b/2)/(a/2)$ also has higher values than at ambient pressure, justifying the statement that the exertion of pressure drives TiOCl more two-dimensional. As a final remark on this issue, it shall be stated that although Zhang *et al.* already predicted a second critical pressure of $p = p_{c2} \approx 1.26p_{c1}$ their finding of an undimerized metallic state with $Pm\bar{m}n$ symmetry cannot be confirmed [Zhang08b]; instead, a mixture of both $Pm\bar{m}n$ and $P2_1/m$ is found in the whole pressure range studied.

The fact that the calculations in [Blanco-Canosa09] and [Zhang08b] yield a finite DOS at the chemical potential above p_{c1} and thus indicate an insulator-metal transition brings us back to our infrared results. Fitting the reflectance R with a Drude-Lorentz model and taking the diamond-sample interface into account by combination with the normal-

incidence Fresnel equation, R can be related to the complex dielectric function of the sample, ϵ_s :

$$R = \left| \frac{n_{dia} - \sqrt{\epsilon_s}}{n_{dia} + \sqrt{\epsilon_s}} \right|^2, \quad \epsilon_s = \epsilon_\infty + \frac{i\sigma}{\epsilon_0\omega} \quad . \quad (4.7)$$

ϵ_∞ is the background dielectric constant (assumed to be ≈ 3 in the following), n_{dia} is the refractive index of diamond, and σ the optical conductivity. From ϵ_s the real part of the latter, $\sigma_1(\omega)$, can be obtained, which in turn can be used to calculate the effective carrier density from the equation

$$n_{eff}(\omega_0) = \left(\frac{2m_0}{\pi e^2} \right) \int_0^{\omega_0} \sigma_1(\omega) d\omega \quad , \quad (4.8)$$

with m_0 being the free-electron mass. Setting a reasonably high cut-off frequency $\omega_0 = 8000 \text{ cm}^{-1}$ and using the high-pressure unit-cell volume of 93 \AA^3 (82 \AA^3) for TiOBr (TiOCl), the effective number of charge carriers per Ti ion, N_{eff} , can be calculated from spectra of the optical conductivity, as they are shown in Figs. 4.27(a) and (b) for TiOBr. The development of the carrier density n_{eff} obtained under these assumptions is shown in Fig. 4.27(c) for TiOBr. This can be translated into the estimated numbers $N_{eff}(\text{TiOBr}) = 0.03 \pm 0.01$ and $N_{eff}(\text{TiOCl}) = 0.05 \pm 0.01$ at $p = 14 \text{ GPa}$, which are comparable to half-metals or doped semiconductors. Thus, they are well below the values expected for a metal, and one can envisage several explanations for their magnitude. Firstly, the charge carriers might contribute only partly to the excitations in the investigated frequency range. Secondly, the low values could be related to an enhanced effective mass of the charge carriers, a phenomenon that is typical for strongly correlated systems, especially in the vicinity of a MIT [Merino08]. Additionally, it was shown in the studies by Merino *et al.* that above certain temperatures the Drude term in the optical response related to coherent quasiparticles can be suppressed on the metallic side of the transition. It can thus be speculated that the absence of such a contribution in our spectra is due to the elevated temperatures ($T = 300 \text{ K}$) at which the experiments were conducted.

Nevertheless, independent of what the microscopic origin for the small amount of charge carriers might be, these numbers could explain the discrepancies between the results from spectroscopical and electrical transport studies concerning the question of a pressure-induced MIT in TiOCl. Although an unambiguous identification of a metallic phase still remains an open issue, the sheer possibility of a MIT motivates studies of the doping-dependent behavior and the search for a filling-induced metallic phase, which will be presented in the next chapter. As a final remark, note that the only obviously incorrect conclusion from the admittedly somewhat confusing amount of data presented in this section is that of a missing structural phase transition by Forthaus *et al.* [Forthaus08].

The commonly accepted results can be summarized as follows:

- $p_{c1} < p < p_{c2}$:
 - Two symmetry domains: $Pmmn$ (“1D”; ambient-pressure phase) and $P2_1/m$ (“2D”, with $a \times 2b \times c$ unit cell)
 - Gap closure in infrared absorption/transmission
 - 1D metallic state inferred from finite DOS at E_F in LDA+ U and molecular dynamics plus GGA+ U
 - No metallic conductivity in transport measurements

- $p > p_{c2}$:
 - Two symmetry domains: $Pmmn$ and $P2_1/m$ (with $2a \times 2b \times c$ unit cell)
 - Gap closure in infrared absorption/transmission
 - 2D metallic state in molecular dynamics plus GGA+ U
 - No metallic conductivity in transport measurements

5 Doping a Mott Insulator

The second main topic under investigation in the course of this thesis has been the possibility of a bandfilling-induced Mott-insulator-to-metal transition in the oxyhalides. On the one hand, a thorough understanding of such transitions might help to understand, e.g., the nature of the superconducting state in cuprate high- T_C superconductors. On the other hand, as outlined in the previous section, there is evidence for a metallic state in TiOCl from optical experiments under high external pressure, which would imply a bandwidth-controlled metal-insulator transition. Recalling that other typical “ingredients” common to the above-mentioned and other quantum-critical systems are found as well, e.g., low spin, low dimensionality, and frustration, it is both fascinating and promising to explore the phase diagram of the oxyhalides also from the perspective of doping.

It will be shown in this chapter how and why TiOCl and VOCl manage to remain in an insulating state upon doping with alkali metal ions, although both intercalation and electron transfer are successfully achieved. Not surprisingly, impurity potentials of the dopants play a crucial role in the suppression of metallicity, as is evidenced by comparison of the experimental results to molecular dynamics calculations combined with results obtained within density functional theory. Another very important finding is that upon doping the oxyhalides show characteristic spectroscopic signatures inherent to strongly correlated systems, once again emphasizing their potential as prototypical multiorbital Mott-Hubbard systems.

5.1 Intercalation of Oxyhalides with Alkali Metal Atoms

The van-der-Waals gap in the layered crystal structure of the oxyhalides potentially offers the possibility to introduce atoms and ions, while at the same time minimizing effects on the original crystal lattice. Corresponding techniques are called “intercalation” and have long been applied successfully to many different systems, e.g., fullerenes deposited on noble metals [Tjeng97, Hoogenboom98], and thin films of organic molecules [Minakata93, Craciun09]. Materials that are structurally similar to the oxyhalides were shown to display superconductivity at temperatures up to $T_C = 25.5$ K upon Li intercalation [Yamanaka98]. In this case dopant atoms were placed within the van-der-Waals gaps of ready-grown crystals by means of electrochemical intercalation. Another possible method which is commonly applied to high- T_C superconductors is to incorporate dopants

already during crystal growth. However, these materials are different from TiOCl in a very important aspect: cuprates and pnictides are composed of CuO_2 and FeAs layers, respectively, which carry the superconducting electrons and alternate with layers of other constituents. Dopant ions are incorporated only into this latter kind of layers which do not participate in the superconducting transport. Thus, the impurity potential introduced by dopants seems to be sufficiently separated from the superconducting layers so it does not lead to, e.g., Anderson-like trapping of charge carriers. The detailed mechanisms, however, remain the major open issue concerning high- T_C superconductors. As was explained in Sec. 4.1.1 the crystal structure is somewhat different in TiOCl. Here, similar chemical doping could only be accomplished by replacement of the transition metal ion, namely Ti, by non-isovalent species like, e.g., Sc for hole and V for electron doping, which however places impurities directly into the electronically active parts of the crystal lattice. This has been tried in our group, but it turns out to be more delicate than for pure TiOCl to grow single crystals of the form $\text{Ti}_{1-x}\text{X}_x\text{OCl}$ ($X = \text{Sc}, \text{V}$) large enough for photoemission experiments. Although other groups showed early on that it is possible to obtain lightly hole-doped $\text{Ti}_{1-x}\text{Sc}_x\text{OCl}$ crystals ($x \approx 3 - 5\%$), the spin-Peierls transition and the precursor incommensurability break down already for very small x ($\lesssim 1\%$) [Seidel03, Clancy08]. This evidences the strong influence of the impurity potential, and it is very likely that the electronic properties of oxyhalides doped in this way are also largely altered from the prototypical Mott behavior found in pristine TiOCl. We tried to grow $\text{Ti}_{1-x}\text{V}_x\text{OCl}$ crystals with the standard chemical vapor transport technique by sealing both the precursor materials for TiOCl and VOCl in varying amounts in the same ampule. The larger single crystals obtained in this manner, however, were identified by XRD and ESCA as pure VOCl without Ti incorporation.

We thus resorted to intercalation doping using alkali metals, Na and K in particular. Elements from the first group of the periodic table are known to easily donate their single s electron to other ions. This has been used successfully for electron doping of, e.g., fullerenes [Hoogenboom98], or very recently for compensation of the self-doping in the cleaved, polar surface of the cuprate superconductor YBCO [Hossain08]. The main method used for the intercalation process which will be discussed in this section was *in vacuo* evaporation of the alkali metals from so-called “Alkali Metal Dispensers” (referred to as “getters” in the following) purchased from SAES Getters. With these getters, the alkali metal is released from an alkali metal chromate upon direct heating by currents up to approx. 7 A. There is a rather sharp threshold for evaporation which depends on the particular alkali metal (e.g., 6.0 ± 0.2 A for Na), and a constant evaporation rate is ensured for several hours of operation. Since this can be done in the same vacuum chamber as the photoemission measurements it is possible to easily survey both the core level and valence electronic structure between consecutive evaporation steps. One must note, though, that the reactive nature of alkali metals does not allow for the crystals to be removed from the vacuum after the doping process. As no *in situ* device for measuring (surface) transport properties was available, only results from PES could be used to distinguish metallic from insulating behavior. Since photoemission is highly

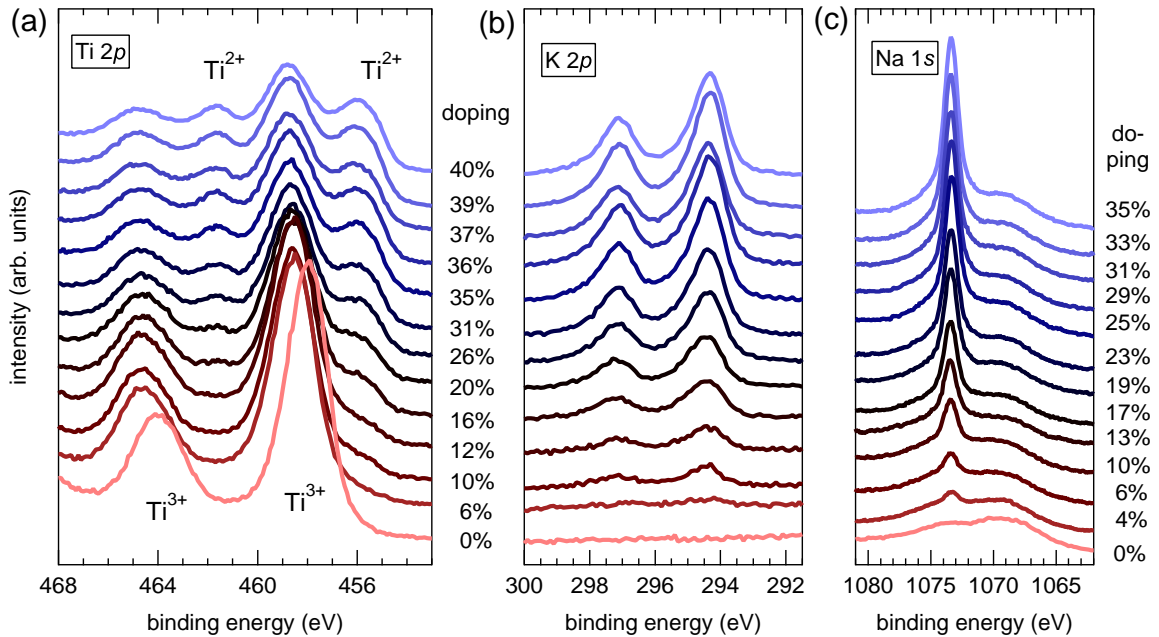


Figure 5.1: (a) Ti 2*p*, (b) K 2*p* and (c) Na 1*s* core levels of TiOCl as a function of doping [panels (a) and (b) from same series]. The spectrum at the bottom is from an undoped crystal, and the top spectrum corresponds to the highest amount of doping achieved in the two series. The 2*p* core levels in panels (a) and (b) appear as a doublet due to spin-orbit splitting. The single Na 1*s* core level in panel (c) rests on a Ti Auger peak.

surface sensitive, intercalated crystals can be expected to appear homogeneously doped within the probing depth of PES, while they certainly are not on a macroscopic scale. Although crystals were kept at elevated temperatures ($T \approx 470$ K) during spectrum acquisition and dosing, diffusion rates and also the amounts of dopants provided in these experiments appear to be far too low to allow for an uniform distribution within the entire crystal on time scales of a few hours or days on which the measurements were conducted. However, we will report on efforts towards bulk doping later in this section.

5.1.1 Core Level Studies - Chemical vs. Electronic Doping

Figure 5.1 shows core-level spectra from doping series with Na and K, namely Ti 2*p*, K 2*p* and Na 1*s*. First, we will concentrate on the Ti 2*p* spectra in panel (a). In the undoped case (bottom spectrum), a spin-orbit split doublet is observed, corresponding to the more intense $2p_{3/2}$ and the tighter bound (higher binding energy) $2p_{1/2}$ peaks, respectively. Already after negligibly small doping (i.e., between $x = 0$ and $x = 6$ %) a rigid shift of the whole spectrum towards higher binding energies is observed. The reason for this will be clear later from the discussion in Sec. 5.1.2. For the moment, we will concentrate on an equally prominent effect, namely the appearance and continuous

growth of a second doublet at slightly (~ 2.7 eV) smaller binding energy compared to the original doublet, obviously at the expense of the latter. One can see that there is a direct correlation between increasing Na/K content, as observed by the growing Na $1s$ / K $2p$ peak(s), and the new Ti $2p$ doublet (Ti spectra are from the same doping series as the K spectra). With this in mind, the behavior of Ti $2p$ can be explained as follows. In an ionic picture, undoped TiOCl has one electron at each Ti site, leaving it with formal valence $3+$. Once an electron is transferred to such a site from the alkali metal the valence at this Ti ion is reduced to $2+$, which is well-known to be reflected by a shift of the binding energy of the corresponding peaks observed in photoemission spectroscopy. Thus, the new doublet is straightforwardly assigned to doubly occupied Ti sites, whose number can only increase by reducing the number of singly occupied sites due to introduction of additional electrons. This allows for a direct determination of the actual electron doping x from the ratio of the area A under the Ti^{2+} peaks to the total area under all four peaks:

$$x = \frac{A(\text{Ti}^{2+})}{A(\text{Ti}^{3+}) + A(\text{Ti}^{2+})} \quad (5.1)$$

The areas are determined by fitting four peaks to the spectra after subtracting a suitable background as shown in Fig. 5.2, for which we used a Shirley background and Voigt profiles. As explained in Sec. 2.1 peaks in core-level photoemission represent a convolution of a lifetime-induced Lorentzian with a Gaussian profile given basically by the analyzer resolution, which results in Voigt profiles. Care was taken to keep the fitting parameters (individual peak position, amplitude, Gaussian and Lorentzian widths) in sensible ranges during the fits. Note that, unless stated otherwise, the doping x quoted throughout this thesis is the *electronic* and not a *chemical* doping, as it directly reflects the number of transferred electrons. The amount of dopant atoms, identifiable as chemical doping and termed x_{stoich} in the following, can easily be larger, since it is not *a priori* clear that every dopant actually donates its electron. In principle, x_{stoich} can be determined relative to the Ti content from an ESCA analysis (Eq. 2.24), but as mentioned earlier, this carries significant error bars.

Electronic doping of up to $x = 43 \pm 2\%$ ($x = 40 \pm 2\%$) could be reached for K (Na) by evaporation from getters, where the error was estimated from the variation of results when using different initial guesses for the fit parameters (especially peak widths). An example can be seen in Fig. 5.2(a), where two fit results to the same Ti $2p$ spectrum at high K doping are shown. The four constituting Voigt profiles are shown at the bottom. The fits turn out to be quite robust, allowing an accuracy of about $\pm 5\%$ with respect to the total x value. At lesser doping, this uncertainty is naturally slightly larger. Knowing of this reliability of the determined electronic doping, one must note that although the spectra used to determine these numbers have typically been measured within less than one hour after evaporation, time-dependent effects are possible. Figure 5.2(b) shows x determined from consecutive photoemission spectra (both XPS and UPS, where the latter have been scaled to mimic the x -vs.- $2x$ scaling identified in Sec. 5.1.2) over a period

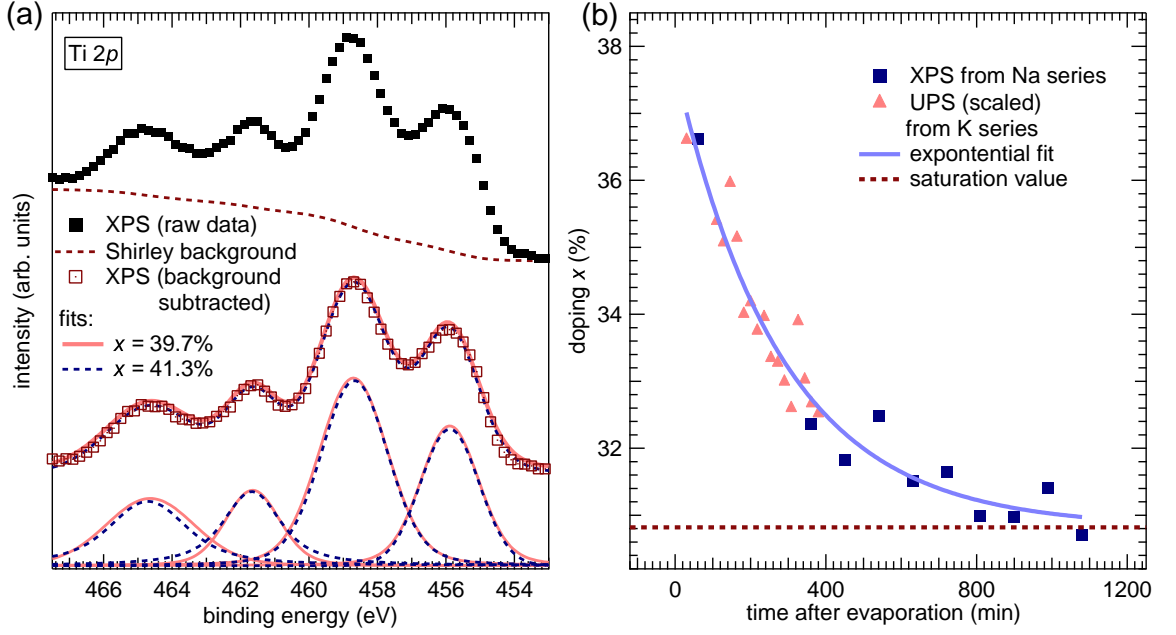


Figure 5.2: (a) Top: as-measured Ti 2p core levels after extensive K dosing (black full markers) and calculated Shirley background (brown dashed curve). Center: Ti 2p spectrum after background subtraction (brown empty markers), and fits obtained from slightly different initial parameters to illustrate the possible spread in the determination of the electronic doping (full red curve: $x = 39.7\%$; blue dashed curve: 41.3%). Bottom: Single Voigt peaks constituting the fits in the center. All spectra have been arbitrarily shifted vertically for clarity. (b) Time development of x after evaporation, as determined from different doping series and fits of both XPS and (scaled, cf. text and Sec. 5.1.2) UPS data. x seemingly drops from $x_0 = 37\%$ to $x_{sat} = 31\%$, as is evidenced by the saturation value obtained from an exponential fit to the data points.

of several hours. One observes an exponential decrease of the effective electron doping by up to 20% compared to the doping right after evaporation and before saturation is reached. Several mechanisms can be imagined to be responsible for this. For example, there is obvious re-desorption of alkali metal atoms away from the oxyhalide crystal, which could be seen on several occasions by monitoring the residual gas composition in the vacuum chamber with a quadrupole mass spectrometer. Additionally, it could also be possible that a concentration gradient leads to diffusion deeper into the bulk, which would further enhance such a decrease, once again because only information on the uppermost atomic layers is available from PES. Overall, due to such effects there appears to be an upper bound for the doping achievable using evaporation from getters, as can be seen from exponential fits of the behavior of x versus integral dosing time, as indicated for both K and Na doping in Figs. 5.3(a) and (b).

These panels also include results from an ESCA analysis to check if the amount of electrons donated per dopant atom is constant, by virtue of a comparison between the development of x and x_{stoich} upon increasing evaporation time. Please note that during

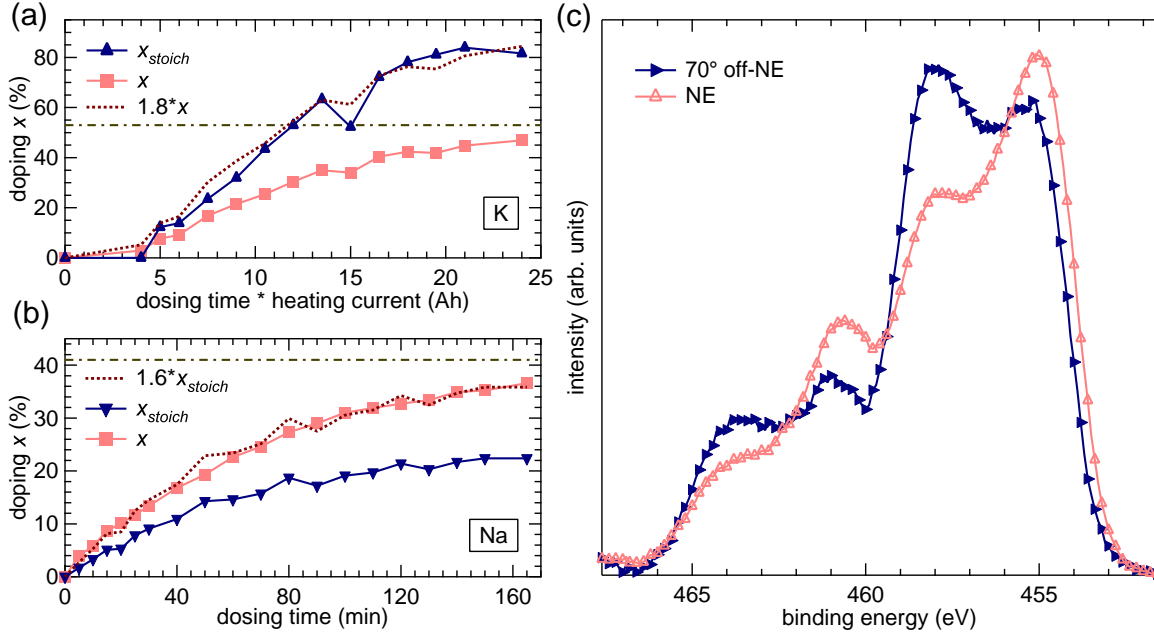


Figure 5.3: (a,b) Development of x and x_{stoich} as determined from Eqs. 5.1 and 2.24 upon increased dosing with (a) K and (b) Na. Due to changes in the heating current the former is plotted versus “heating current” times “dosing time” (in units of Ah). Also shown are curves multiplied by a common factor, indicating the correspondence between x and x_{stoich} . The dash-dotted line represents the saturation value obtained from exponential fits to the behavior of x . (c) Ti 2p core-level spectra (background removed), measured bulk- (NE) and surface- (70° off-NE) sensitive and obtained after extensive dosing with Na from an ampule.

the K series the heating current through the getters was not kept constant between different doping steps, which is why x and x_{stoich} values are plotted versus “heating current” times “dosing time” (in units of Ah). What can be learned from these graphs is that, apart from a unique multiplicative factor, the electronic and chemical doping behave in the exact same way, and neither seems to saturate independently from the other. This suggests that the most important error lies in the photoionization cross-sections used (from [Yeh85]) as mentioned in Sec. 2.1, and that the assumption of a constant number of transferred electrons per alkali metal ion is actually justified.

In order to possibly reach dopings higher than the ones reported above and also to achieve bulk doping, we tried to provide a significantly larger amount of Na by using a sealed ampule, containing several grams of Na, instead of getters.¹ This ampule was mounted such that it could be cracked *in situ* and heated to high enough temperatures to induce Na evaporation. The macroscopic amount of Na thus released upon heating was evidenced by a significantly stronger increase of pressure as compared to evaporation from getters. Motivated by the experience with getters it was taken care to keep the

¹One getter is specified by the manufacturer to contain 1.7 mg of Na.

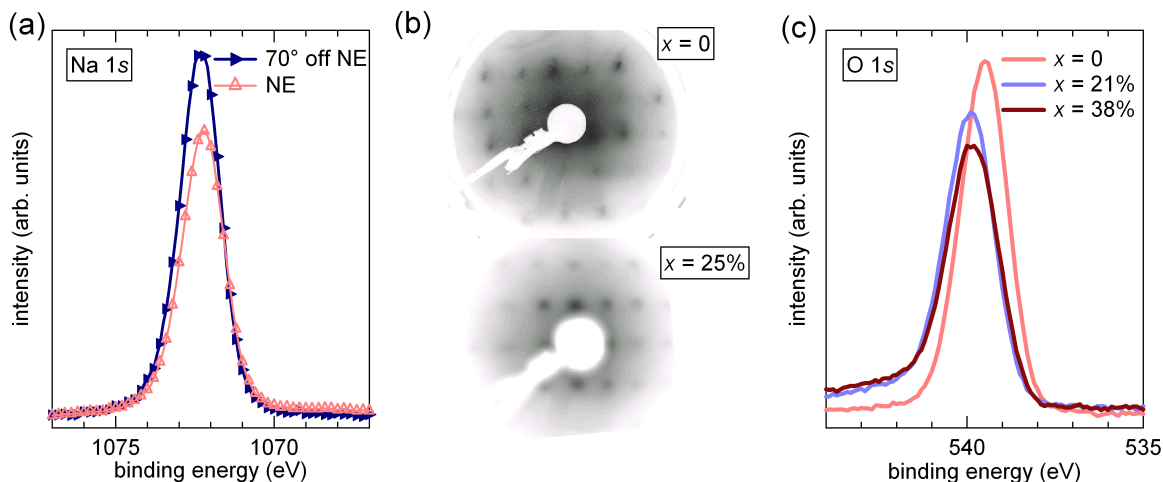


Figure 5.4: (a) Angle-dependent XPS of the Na 1s core level for doping of $x \approx 25\%$, measured at $\vartheta = 0^\circ$ (NE) and $\vartheta = 70^\circ$ (70° off-NE). (b) Room-temperature LEED patterns of TiOCl with (top) $x = 0$ and (bottom) $x = 25\%$, taken at a primary electron energy $E \approx 160$ eV. (c) O 1s core level measured at different Na dopings. An energy shift of ~ 0.5 eV between doped and undoped spectra can be observed as well as a slightly higher background due to a Na Auger peak lying below the O 1s peak, but no change in peak shape.

sample temperature in this case as high as possible. This was achieved by proximity to and thus radiative heating from a filament, which also heated the Na metal ampule.

Figure 5.3(c) shows Ti 2p spectra obtained after several hours¹ of Na evaporation from the ampule, measured 30 minutes after finishing evaporation and normalized to equal spectral weight after removing a Shirley background. The Ti²⁺ peak appears considerably higher than the Ti³⁺ peak, and an analysis yields $x = 60\%$ for bulk-sensitive (normal emission, i.e., $\vartheta = 0^\circ$; termed “NE” in the following) and $x = 50\%$ for surface-sensitive ($\vartheta = 70^\circ$; “off-NE”) spectra, i.e., well above the maximum doping achieved by evaporation from getters. Similar to dosing from getters, this amount reduces over a period of several hours and saturates at about $x = 50\%$ for NE. Measurements of the valence band spectrum (not shown) on crystals intercalated in this way showed little or no remaining features of Ti 3d weight, which might be due to a higher surface coverage by Na (UPS is more surface sensitive than XPS due to smaller electron kinetic energies, cf. Sec. 2.1), or to an increased influence of the large Na amounts on the crystal structure. However, it will be argued in the following that neither of these possible effects is of significance for the bulk (i.e., intrinsic) properties of electron-doped TiOCl.

Figure 5.4(a) compares spectra of the Na 1s peak for doping of $x \approx 25\%$, taken in NE and off-NE. They were normalized to an equal inelastic background a few electron volts away from the peak. As this background does not behave in the exact same way in the

¹Dosing from the ampule could not be performed in such a controlled fashion as from getters. Thus, a further specification of dosing times would not be meaningful.

two cases, this introduces an unavoidable uncertainty concerning the absolute values of Na content extracted from these spectra. The information depth as determined from Eqs. 2.18 and 2.19 is roughly 90 \AA (30 \AA) for $\vartheta = 0^\circ$ ($\vartheta = 70^\circ$) around the kinetic energy of Na $1s$ photoelectrons, i.e., also here the layers close to the surface contribute the largest portion to photoemission spectra. Despite the observed enhancement of the surface contribution to the spectral weight, the maximum of the off-NE spectrum is only moderately higher than the one from NE. This already suggests that there is no (thick) overlayer of Na atoms on the surface, in line with the observation that the surface diffraction pattern in low energy electron diffraction (LEED) is robust upon doping and does not show additional superstructure peaks, as can be seen in Fig. 5.4(b) for $x = 0$ and $x = 25\%$. Unless adsorbates adopt the structure of the substrate this is clear evidence that the coverage cannot significantly exceed the monolayer range, because LEED at typical energies (100–200 eV; 160 eV for the pictures shown) is about as surface-sensitive as photoemission spectroscopy. As an additional remark, the O $1s$ core level peak displayed in Fig. 5.4(c) gives evidence that only the Ti ions are directly affected by the doped electrons: it shows only a slight broadening and is sitting on a higher background upon doping, but neither does it change its shape nor do additional components emerge. This applies to other core levels from O and Cl as well (not shown).

Coming back to the saturation effects found from the data in Figs. 5.3(a) and (b), depth-profiling by angle-dependent XPS will be used to identify a possible additional driving force for this saturation. Namely, electrostatic potentials developing to avoid the so-called “polar catastrophe” which is well-known for polar heterojunction interfaces [Harrison78] and currently discussed in the context of oxide thin-film heterostructures [Nakagawa06] could induce a rearrangement of dopant ions. A sketch to illustrate the situation is shown in Fig. 5.5(a). One realizes that for a sequence of layers alternately carrying a charge equivalent of, for instance, “+” and “-” one elemental charge per formula unit, the electrostatic potential diverges when going away from the surface. This can be remedied by transferring half an electron (to be understood on average) from one layer to the one next to it, leaving a charge of $0.5e$ at the surface layer and $-0.5e$ at the far side of the specimen. The potential thus oscillates about a low finite value which circumvents the polar catastrophe and restores energetic stability of the crystal.

In doped TiOCl alternately charged layers develop since the buckled TiO double layers of the original lattice gain additional electrons (i.e., become negatively charged), while the dopants remain as positive ions between them. Assuming that a redistribution of positive charge is achieved by a diffusion of dopants along the crystallographic c axis (and implying that each alkali metal ion donates one electron) the effects should be observable by angle-dependent XPS. In this case, the amount of alkali metal lying on top should be only a fraction (in the ideal model exactly $1/2$) of the amount in each van-der-Waals gap. We will thus refer to the “fractional monolayer coverage” (FMC) in the following, which is the amount of alkali metal on the surface divided by the average amount deposited in the van-der-Waals gaps. In order to quantify possible differences,

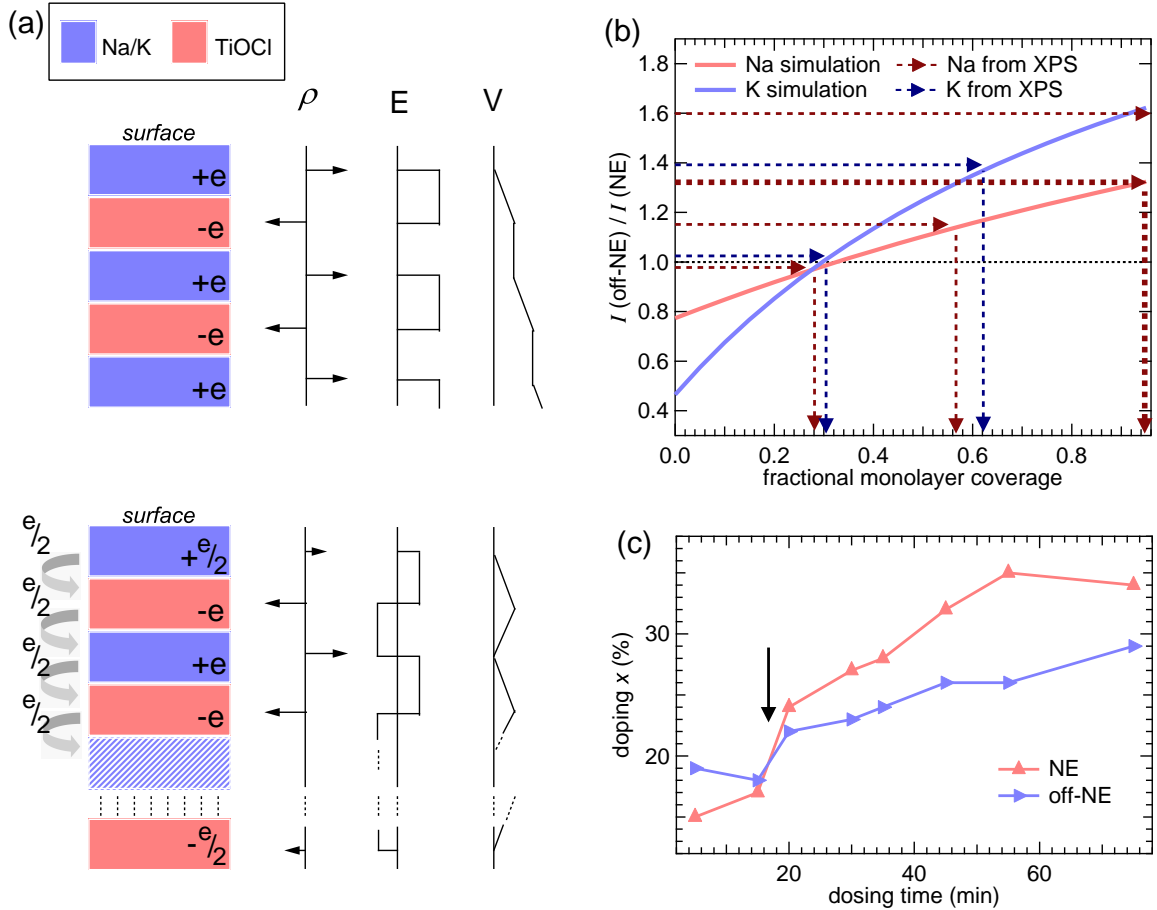


Figure 5.5: (a) Series of alternately charged layers in doped TiOCl, together with net charges ρ , electric field E and electric potential V . Without electronic reconstruction the latter diverges (top), while it oscillates about a low finite value if half the average charge of a layer is transferred away from the surface to the far side of the specimen (indicated at the bottom). (b) Calculated intensity ratios $I(\vartheta = 70^\circ)/I(\vartheta = 0^\circ)$ of the Na $1s$ and K $2p$ core levels for varying surface coverage (fractional monolayer coverage, in units of the average amount of alkali metal within the van-der-Waals gaps; see text for details). Results from several doping series are indicated by arrows. The thickest brown arrow corresponds to results from three different series of Na doping. (c) Doping x determined from Ti $2p$ spectra taken in NE and off-NE, plotted versus overall dosing time along a doping series with Na. The arrow marks the point where x observed in NE (the bulk doping) becomes larger than the one at large angles (the surface doping).

the vertical distribution of Na and K ions in a doped crystal was simulated using a model of discrete, point-like ions building the Na/K:TiOCl crystal. The idea was to calculate the intensity ratios of the different atomic species observed under $\vartheta = 70^\circ$ (off-NE) and $\vartheta = 0^\circ$ (NE) depending on the FMC of TiOCl by Na/K. The attenuation lengths λ_{AL} which were used instead of the IMFP because they are more exact were calculated using Eq. 2.20 [Cumpson97]: $\lambda_{AL}(\text{Na } 1s) = 27.3 \text{ \AA}$, $\lambda_{AL}(\text{K } 2p) = 12.2 \text{ \AA}$, and $\lambda_{AL}(\text{Ti } 2p) = 15.6 \text{ \AA}$.

Calculated intensity ratios representing the polar catastrophe model are shown in Fig. 5.5(b), together with those determined from measurements on various crystals with different dopings from a wide range of $20\% < x < 45\%$. From the limited amount of data points, no dependence on the actual value of x can be inferred, nor on the method of doping (from getters or from a Na ampule). Thus, these different cases are not distinguished in the figure. The thickest brown arrow corresponds to three different crystals doped by Na which yield almost the same values for the intensity ratio, while the other arrows represent one measurement each. Reading off the FMC from the abscissa, quite some spread is observed. Especially for Na dosing, this is partially due to the flat behavior of the intensity ratio obtained from the model calculation, which itself comes from the larger attenuation length compared to K. The data point at $I(\vartheta = 70^\circ)/I(\vartheta = 0^\circ) \approx 1.6$ stems from a measurement where the sample could not be heated while dosing from the ampule with Na. This extraordinarily high value is assumed to be due to the lower thermal mobility of dopants which leads to slower diffusion into the bulk and thus a relatively thick surface layer of Na, and should not be taken too seriously. In all other cases, the FMC appears as ≤ 1 , and especially for K doped crystals even close to the expectation within the polar catastrophe model, namely a FMC of 0.5.

As hinted at above, it was assumed in this discussion that $x = x_{stoich}$, which (on a quantitative level) has not been confirmed yet, remembering the results shown above in Fig. 5.3. In the discussion of this figure, the fact that $x_{stoich}^{\text{K}} > x$ while $x_{stoich}^{\text{Na}} < x$ was attributed to the photoionization cross-sections, which might be overestimated for one element while they are underestimated for the other. The differences between Na and K observed in the simulations of Fig. 5.5(b) might provide another possible facet in this respect. For $\text{FMC} \gtrsim 0.3$ the intensity ratio for Na is flatter than that of K, i.e., a Na overlayer contributes less to the total spectral weight than a K overlayer. As a consequence, the latter is more likely than Na to erroneously suggest a higher chemical doping than the actual electronic value ($x_{stoich} > x$), as it is observed in Fig. 5.3(a), but not for Na in Fig. 5.3(b). These findings thus give evidence that the assumption $x_{stoich} = x$ is actually fulfilled, despite the impression from the data in Fig. 5.3.

Finally, also the data shown in Fig. 5.5(c) corroborates the polar catastrophe model and gives further evidence on the importance of the overall time given to the system to equilibrate, as far as the observed surface coverage is concerned. The panel shows the electronic doping x determined during a series of several dosing steps from Na getters both in NE and off-NE. Note that each step allows the system roughly two hours to

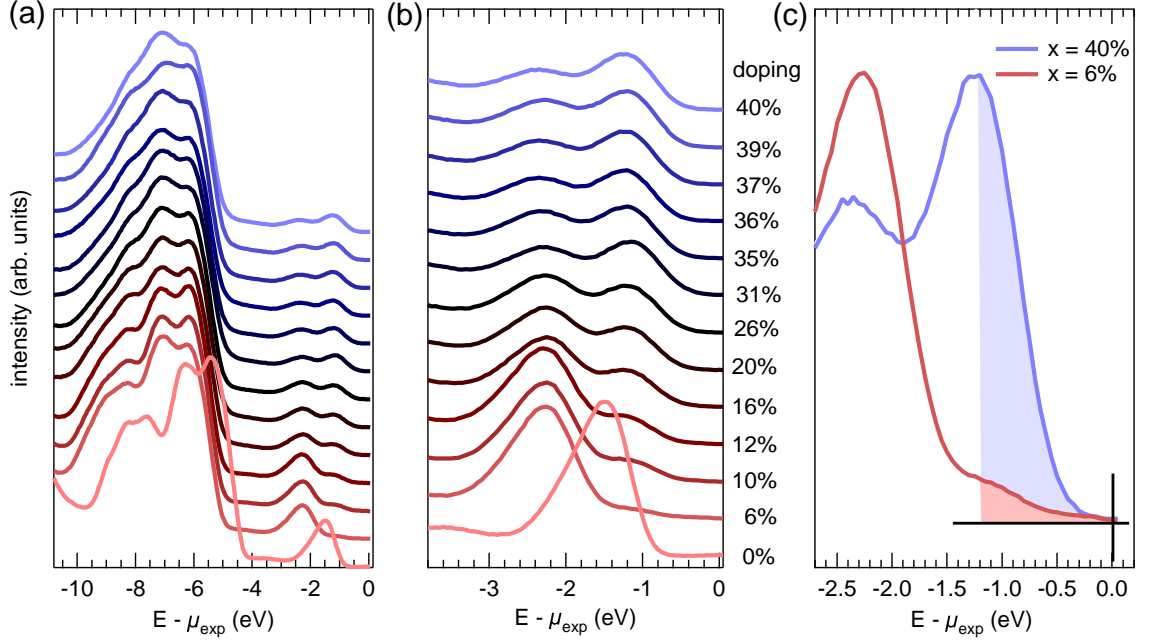


Figure 5.6: (a) Valence band and (b) Ti 3d spectral weight of TiOCl upon K doping, from the same series as the data in Figs. 5.1(a) and (b). x values given next to panel (b) apply also to panel (a). (c) Persistent soft-gap behavior, illustrated with spectra at small ($x = 6\%$) and large ($x = 40\%$) K doping.

get closer to an equilibrium distribution of charge (and thus, as we assumed, dopants), since this is the average time spent to perform different measurements after each step. The important result is that while the surface doping (off-NE) initially appears larger, already after a few dosing steps a relaxation is observed such that reproducibly a smaller doping is found than in the bulk (NE). This indicates that the systems wants to have less charge at the surface than in the bulk, which can be achieved if enough (overall) time is given to the dopants to diffuse into the bulk (or re-evaporate into the vacuum, which would have the same effect).

5.1.2 Low-Energy Electronic Structure - Alloying and Spectral Weight Transfer

As expected, major changes happen in the valence band as well. Figure 5.6 shows spectra from the same K doping series as in Figs. 5.1(a) and (b), and again one observes a jump of the spectrum to higher binding energies as well as a new peak, developing now between the original Ti 3d peak (the lower Hubbard band, LHB) and the chemical potential. The shape of the bands at higher binding energies of O and Cl character, however, is only slightly changed. As will be shown below, the intercalated ions induce a distortion of the lattice, which leads to a (local) change of the Ti 3d crystal-field splitting (CFS), and the

slight effects this has on the O/Cl-bands is what can be seen here. Concerning the main open question, namely, whether a transition from an insulator to a metal takes place upon doping, an answer can be given only partially from photoemission data alone. In the simple Hubbard model one would expect the development of a quasiparticle (QP) peak at the chemical potential, in photoemission observable with a Fermi-edge cut-off (cf. Fig. 3.2 and [Kajueter96, Bulla99]). However, as becomes clear from the blow-ups in Figs. 5.6(b) and (c), showing the region from the LHB to μ , there is a persistent gap in electron-doped TiOCl, i.e., a QP peak is completely absent and no spectral weight is found at the chemical potential for any doping investigated. The comparison in panel (c) between spectra with $x = 6\%$ and $x = 43\%$ also shows that although the gap at higher dopings softens, i.e., it becomes gradually filled, it never closes in the sense of allowing for finite weight at μ . This behavior is not found in the DFT calculations presented later in this section, but is reminiscent of so-called “soft Hubbard gaps” discussed recently in the context of disorder and short-range Coulomb interactions [Shinaoka09].

Overall, metallicity cannot be confirmed by the combination of photoemission data and the performed theoretical approaches, but it cannot be completely excluded, either. Several mechanisms are known that can lead to a suppression of the QP weight in spite of metallic behavior, all of which involve intricate coupling of the electronic structure to other bosonic excitations, like phonons or magnons. This effect, known, e.g., from photoemission on hydrogen molecules [Asbrink70] and cuprate high- T_C superconductors [Damascelli03], was mentioned already in Sec. 4.2.4 in the context of a loss of momentum information. Now, the important point is that it shifts spectral weight of the coherent QP peak to incoherent structures at higher binding energies. As will be shown below, however, the absence of the QP at the chemical potential in TiOCl has a different origin of actually single-particle nature, which, as it turns out, also suppresses metallic conductivity for all possible doping levels.

Before going into more detail on this issue the orbital character of the new peak shall be clarified. Since it is clear from the Ti core-level spectra that additional electrons reside at Ti ions, and Ti $3d$ is the lowest-energy partially filled shell, it appears natural to assign $3d$ character to this peak as well. In a Mott-Hubbard picture it would thus correspond to the upper Hubbard band (UHB). As in Sec. 4.2.1, ResPES was used to determine the orbital character and (by virtue of polarization changes) the symmetry of the valence band structures. Measurements were taken during the same beamtime as those on undoped crystals, i.e., all experimental parameters (excitation energies, resolution, etc.) are the same or close to the ones mentioned earlier. Results from TiOCl doped to $x = 31\%$ by K are presented in Figs. 5.7(a) and (d), with light polarized along the a and b axis, respectively.¹ Similar to the undoped case a resonant enhancement especially of the two low-energy features is observed, and the high-energy (O and Cl) bands are qualitatively unchanged and only slightly resonate. This gives proof that the new peak

¹The same shorthand-notation as in Sec. 4.2.1 will be used, i.e., the term “light polarization” will be omitted in the following.

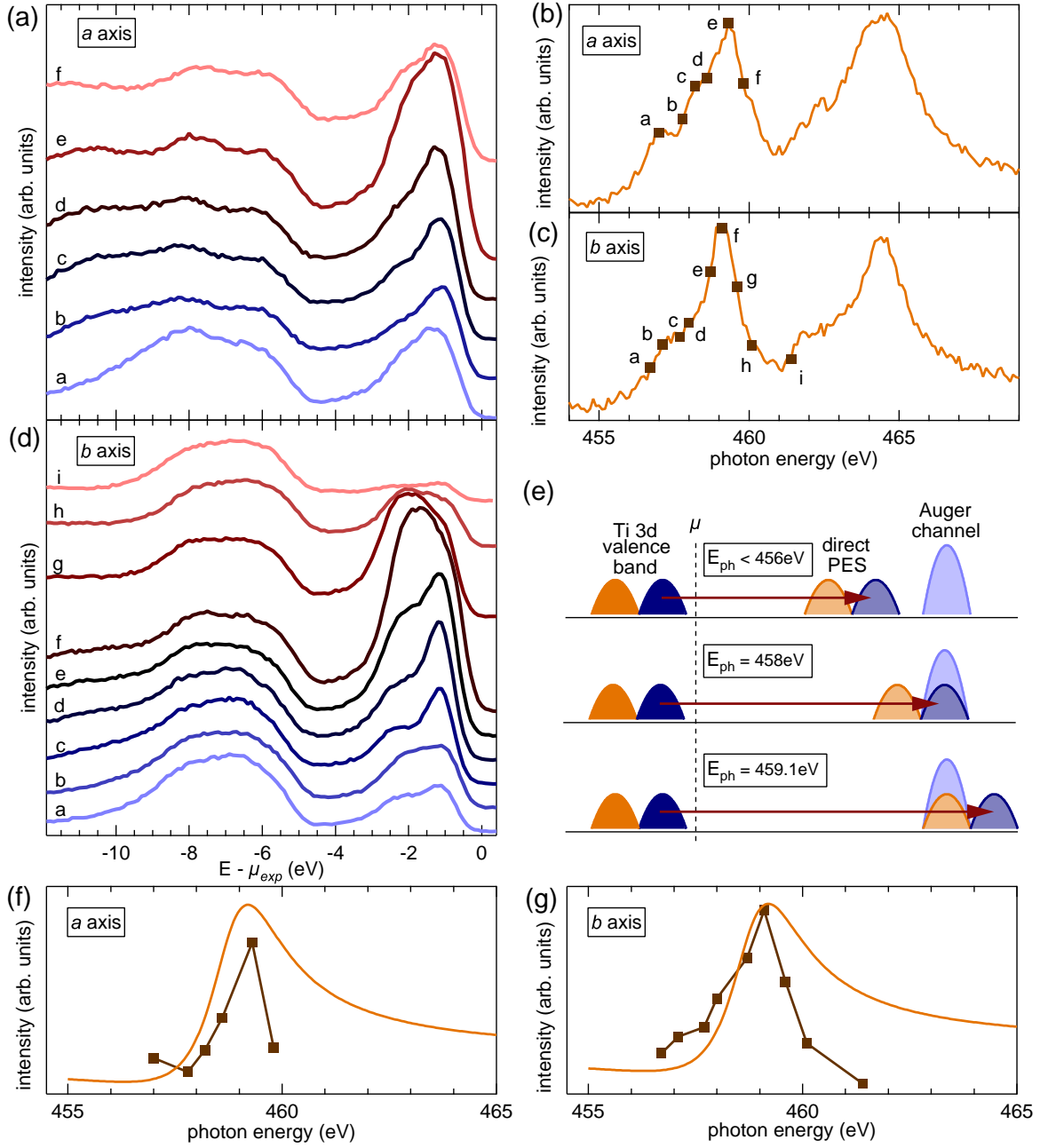


Figure 5.7: Ti L edge ResPES of the valence band of K -doped $TiOCl$ ($x = 31\%$) with light polarization along the (a) a and (d) b axis, respectively. Different photon energies are marked by letters according to those assigned in the corresponding absorption spectra shown in panels (b) and (c) along the respective axes. To account for increased sample charging for high resonant enhancement, all spectra have been shifted in energy such that the new peak is centered at 1.2 eV below μ_{exp} . All spectra were normalized to equal effective acquisition times. (e) Single-particle scheme of ResPES at certain photon energies. See text for details. (f,g) Total spectral weight of Ti $3d$ character in the range from 0 to -4 eV below μ_{exp} for different photon energies along (f) a and (g) b , as determined by integrating the peak area after background subtraction. Areas under the peaks were normalized for displaying purposes to give the closest match with the Fano curve obtained for $q = 2.5$.

has Ti 3d character, and that at most minor changes to the hybridization between Ti and O/Cl bands occur upon doping. Following the LHB and the new peak independently it seems that the latter is enhanced already at smaller photon energies. This can be understood from a very simplistic approach to ResPES which is sketched in Fig. 5.7(e). Due to the energetic separation between the LHB and the new peak of roughly 1 eV the latter can be assumed to traverse the absorption edge (at which the enhancement takes place, cf. Fig. 2.5) sufficiently early as to decouple the process into a sequence of two independent resonances. Unfortunately, it is not possible to fully decompose the spectra and obtain enhancement factors for each peak separately. Instead, Figs. 5.7(f) and (g) show the behavior of spectral weight (instead of the peak maximum) of both peaks in the energy range $-4\text{ eV} < E < 0\text{ eV}$ together with a Fano curve ($q = 2.5$). It must be noted that already in undoped TiOCl the 3d peak(s) appear significantly broadened for high enhancement (i.e., “on-resonance”), an effect well known in ResPES, which also affects the extracted spectral weight. This might make especially the weight of the spectra in the center of the resonance (i.e., those labeled “e” and “f” along a and b , respectively) appear too high, thus leading to an incorrect normalization factor, in particular concerning the high-photon-energy side of the Fano lineshape. Overall, the agreement with canonical resonance behavior is even worse than in the undoped case.

Off-resonant PolPES taken at $E_{ph} = 150\text{ eV}$ is shown in Fig. 5.8 for K doping of up to $x = 30\%$. Samples were mounted such that $d_{x^2-y^2}$ orbitals have non-zero matrix elements along b and are suppressed along a . The opposite is true for the next higher-lying orbital (d_{xz}). From an analysis of the valence band at $x = 30\%$ shown at the top of Fig. 5.8(a), a reduction of the overall Ti 3d spectral weight (LHB plus new peak) by a factor of only ~ 3.5 is observed when changing the polarization from b to a . This can be compared to ~ 10 in undoped TiOCl (cf. Fig. 4.8), and to ~ 6.7 at $x = 10\%$ [cf. bottom of Fig. 5.8(a)]. One also sees that the LHB is affected much stronger than the new peak. To understand this behavior, one must remember that the ground state of a d^2 configuration in the atomic limit $t \ll U$ (similar to what is encountered in doped TiOCl) has an energy of $U - 3J_H + \delta$ (cf. Tab. 4.3, with additional CFS of δ), i.e., the electrons form a triplet which involves two single-particle orbitals. The lowest singlet configuration would have an energy $U + 2J_H$ and is less favorable, recalling typical values of $U = 4.5\text{ eV}$, $J_H = 0.7\text{ eV}$, and δ of the order of some 100 meV (cf. Sec. 4.2.3). Thus, one would expect both $d_{x^2-y^2}$ and d_{xz} orbitals to be relevant in doped TiOCl. Another important consideration is that photoemission spectra reflect the final state of the process, which for doped TiOCl still can be characterized using the customary single-particle notation for the orbitals. This means that in addition to the different energy at which electrons from a doubly occupied site are detected compared to electrons from singly occupied sites, two different final states can result: one with the remaining electron in a $d_{x^2-y^2}$ orbital, and one with this electron in a d_{xz} orbital, where both possibilities have equal probability to occur.

The expected behavior upon polarization change in our geometry is sketched in Fig. 5.8(b). Along b (in our geometry horizontal polarization), the LHB (having only

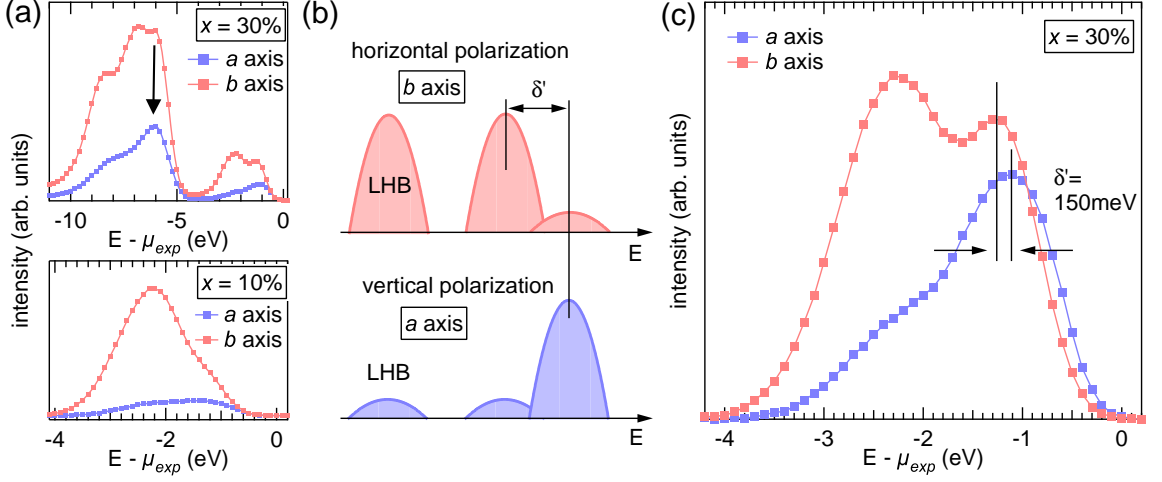


Figure 5.8: Polarization-dependent PES on TiOCl doped by K , taken in normal emission at an excitation energy of $h\nu = 150 \text{ eV}$. (a) Top: Full valence band at $x = 30\%$. Spectra have been normalized using the photocurrent induced in the crystal mirror of the beamline optics (“mirror current”). Bottom: $\text{Ti } 3d$ peak at $x = 10\%$ (background subtracted). (b) Illustration of the expected behavior of the components of the $\text{Ti } 3d$ spectral weight, assuming that the new peak upon doping involves two different final states (see text for details). (c) Data from panel (a) in the range around the $\text{Ti } 3d$ peak after background subtraction. Spectra were normalized to equal spectral weight of the new peak in both polarizations, as obtained from a simple fit of two Gaussian peaks to the spectrum. An independent component analysis (see text) yields $\delta' = 150 \text{ meV}$.

$d_{x^2-y^2}$ character) and the $d_{x^2-y^2}$ part of the new peak should contribute to the spectrum, while the final state with d_{xz} character should be suppressed. Changing to vertical polarization (i.e., along the a axis), only the latter should be visible. This is what is observed in the background-corrected spectra in Fig. 5.8(c). Also indicated is the energetic difference $\delta' = 150 \text{ meV}$ between the $d_{x^2-y^2}$ and the d_{xz} components, which was determined using a so-called “independent component analysis”. This analysis was necessary due to the incomplete cancellation of spectral weight upon switching the polarization. The idea is to construct the spectrum measured under one polarization (either horizontal, H_{exp} , or vertical, V_{exp}) from a sum of the intrinsic spectrum of this polarization (H_i, V_i) and a contribution of the spectrum of the other polarization, with the respective weights (δ, η) being unknown parameters:

$$\begin{aligned} H_{exp}(E) &= H_i(E) + \delta \cdot V_i(E) \\ V_{exp}(E) &= V_i(E) + \eta \cdot H_i(E) \end{aligned} \quad . \quad (5.2)$$

One then uses an iterative procedure with the measured spectra as starting points, until

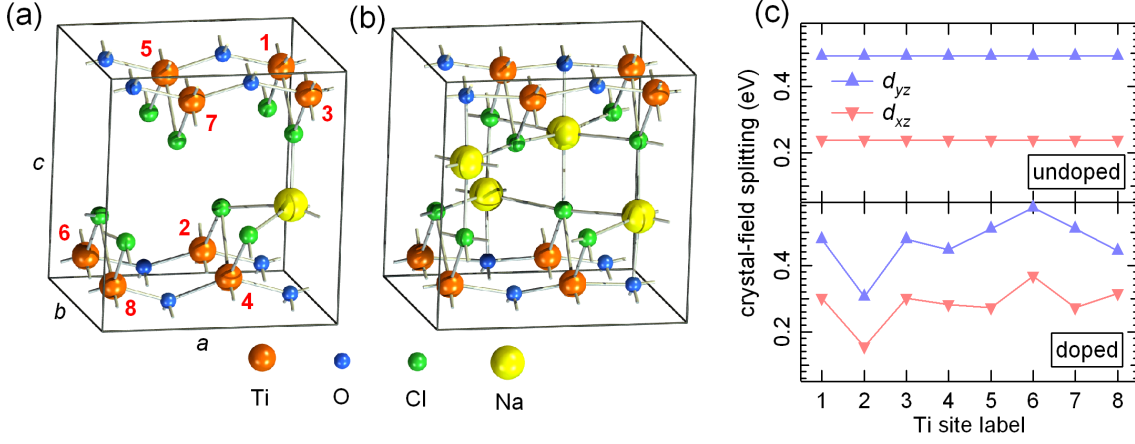


Figure 5.9: (a,b) Supercell used for the molecular dynamics calculations, and resulting ion arrangement for (a) $x = 12.5\%$ and (b) $x = 50\%$. This corresponds to twice the unit cell of the crystal lattice. The different Ti sites are marked by red numbers. (c) Crystal-field splitting of the d_{xz} and d_{yz} orbitals with respect to the $d_{x^2-y^2}$ orbital, obtained from GGA for $x = 0$ (δ ; top) and 12.5% (δ' ; bottom) at the different Ti sites marked in panel (a).

proper convergence is reached, for example:

$$\begin{aligned}
 V_i^0 &= V_{exp} \\
 H_i^0 &= H_{exp} \\
 H_i^1 &= H_{exp} + \delta \cdot V_i^0 \\
 V_i^1 &= V_{exp} + \eta \cdot H_i^1 \\
 H_i^2 &= H_{exp} + \delta \cdot V_i^1 \\
 &\vdots \\
 \text{if } H_i^{n+1} &= H_i^n \Rightarrow H_i^n \equiv H_i \Rightarrow V_i^{n+1} \equiv V_i \quad .
 \end{aligned} \tag{5.3}$$

δ and η are estimated from a comparison of the measured spectra to be in the range of $0.1 - 0.25$, and the results concerning maxima positions of the different components turn out to be rather insensitive to the exact choice.

In principle, the separation δ' reflects the CFS between the single-particle orbitals $d_{x^2-y^2}$ and d_{xz} . This finding shows that a single-band Hubbard model is not applicable to doped TiOCl, in contrast to the undoped system, as it was inferred from LDA+VCA calculations [Aichhorn09]. The reason why δ' is different from the value for the CFS given in Tab. 4.5 becomes clear from a combination of molecular dynamics calculations and DFT, which will be presented in the following.

Although DFT is well-suited to gain information about the equilibrium ground-state energy of a system it has two major shortcomings. Firstly, it is an effective single-particle approach and thus fails to account in the correct fashion for many observations inherent to strongly correlated electron systems. In combination with DMFT this can partially

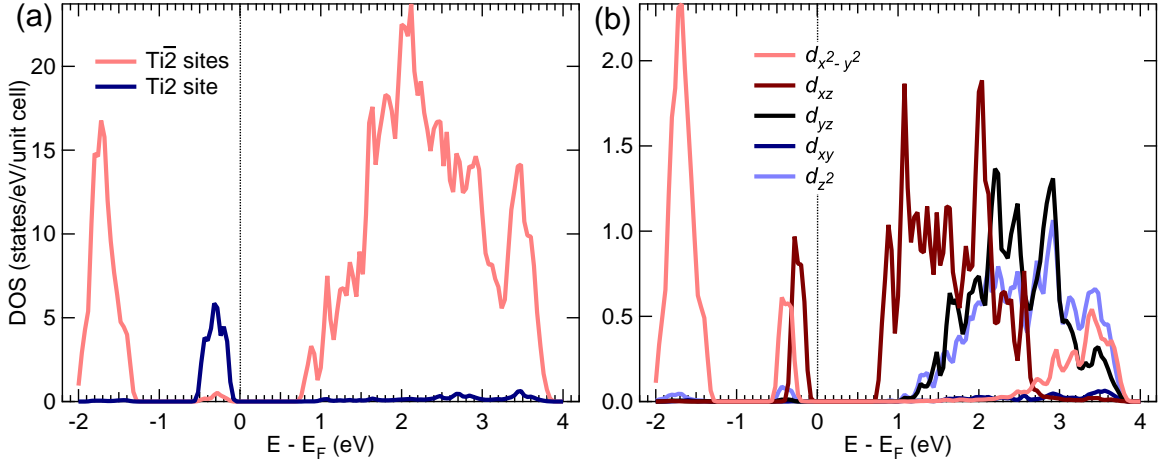


Figure 5.10: Ti 3d pDOS for Na doping of $x = 12.5\%$ as obtained from GGA+ U . (a) Contributions from the Ti2 site closest to the Na ion (blue) and all other sites in the supercell (Ti2; red). (b) Orbital-resolved Ti 3d pDOS. The peaks between approx. -0.5 eV and the Fermi energy constitute the Ti2 peak in panel (a).

be reconciled, cf. Sec. 3.3. Secondly, DFT is a static theory not suitable to track ion dynamics on their way to stable positions. This issue can be tackled by using dedicated *ab initio* molecular dynamics calculations, e.g., the so-called Car-Parinello projector augmented wave method [Car85, Parrinello80], and combining this with DFT [Blöchl94]. The group of R. Valentí applied this approach to TiOCl doped in various ways, with special focus on Na intercalation [Zhang10]. They used a 2×2 supercell, thus allowing for dopings to be calculated that are multiples of $1/8$ (e.g., $\text{Na}_{1/8}\text{TiOCl}$, $\text{Na}_{1/4}\text{TiOCl}$, etc.). The first important result concerns the relaxed positions of Na ions shown in Figs. 5.9(a) and (b). It is found that intercalated alkali metals do not remain in the van-der-Waals gaps but occupy a cage of 5 Cl and 1 O ions within the chlorine layers, as can be seen in the figure. Thus, they come rather close to the Ti ions within the TiO double layers, which in turn leads to a lowering of the CFS between $d_{x^2-y^2}$ and d_{xz} at the nearest Ti site (labelled “Ti2”) from $\delta = 250$ meV to roughly $\delta' = 150$ meV, in very good agreement with the above-mentioned peak separation observed upon polarization change. This is shown in Fig. 5.9(c) for a Na doping of 12.5% (one Na ion in a $2 \times 2 \times 1$ supercell, i.e., only one Ti2 site), but was observed for other doping levels as well.

Figure 5.10 shows the Ti 3d partial density of states (pDOS) obtained from GGA+ U for $x = 12.5\%$. It is inherent to the calculations that $x = x_{stoich}$, which are thus not distinguished in the following. Both the site-resolved DOS in panel (a) and the orbital-resolved DOS in panel (b) give important results from the electronic point of view. Firstly, no spectral weight is found at the chemical potential and a finite gap persists, meaning that the insulating state found in the experiment is consistently reproduced by the calculations. The Fermi energy E_F is taken as the valence band maximum in the

calculations. It is thus different from the position of μ_{exp} used as a reference for the experimental energy scale. Secondly, in contrast to the behavior seen in experiment [cf. Fig. 5.6(c)] the spectral weight shows a true gap for all values up to $x = 1$, i.e., the soft gap is not reproduced in the present GGA+ U . It might be possible, though, to account for this behavior by allowing for other (metastable) configurations in which the Na ions occupy different positions in the unit cell. To understand this, note that the sites Ti2 and Ti6 (cf. Fig. 5.9) are symmetrically almost equivalent in the unit cell considered for the calculations, so if one allows for different starting points of the Na ions different sites can end up as the Ti2 site, but then all other sites change their character accordingly. Nevertheless, the gap between occupied and unoccupied states must not be assumed to be correct, remembering the discussion of Fig. 4.9.

Integrating over the occupied part of the DOS, a transfer of one electron per Na ion to Ti is found, i.e., no charge is transferred to O or Cl. Fig. 5.10(a) shows that the peak close to the Fermi energy has contributions only from Ti2 sites, in contrast to all other valence band structures captured by these calculations, which consist solely of weight from the other (Ti $\bar{2}$) sites. A final observation derived from the data in Fig. 5.10(b) is that the additional electron acquires d_{xz} character instead of doubly occupying the LHB ($d_{x^2-y^2}$), in line with the results from PolPES and the accompanying discussion of the energetics made above.

In order to fully understand why TiOCl stays insulating upon electron doping, the impurity potential Δ introduced by the Na ions must be considered explicitly. First of all, due to this potential the lattice is slightly distorted, which induces the change of the CFS observed both in experiment in theory. Furthermore, a long-range (intersite) Coulomb repulsion between singly (Ti $^{3+}$) and doubly (Ti $^{2+}$) occupied sites is induced. Together, these effects lead to a localization of the doped electron at the Ti2 site and thus suppress metallic conductivity.

Figure 5.11(a) shows a schematic which illustrates how these considerations even allow for a quantitative understanding of the low-energy electronic structure of doped TiOCl. All peaks have been labeled with the respective single-particle excitation, such that, e.g., $d^2 \rightarrow d^1$ corresponds to electron removal from a doubly occupied site. In this scheme, μ in the undoped case lies centered between LHB (electron removal, $d^1 \rightarrow d^0$) and UHB (electron addition, $d^1 \rightarrow d^2$) which are separated by a gap of ~ 2 eV. In the doped case, μ lies in the center between UHB and the new highest occupied level, which shall be called the ‘‘alloy band’’ (AB). As implied in the figure there is a shift of the spectrum if the chemical potential is aligned at the same energy as before (which is done in experiment).¹ Experimentally, a shift of approx. 0.6 eV is observed, which was also reflected in the core-level spectra in Fig. 5.1. If the chemical potential would be pinned to the lower edge of the UHB upon doping, a jump by half the gap value, namely by 1 eV should have occurred. This discrepancy supports our picture given in Fig. 5.11(a).

¹More precisely, it is the chemical potential which jumps to a new position, not the spectrum. However, μ_{exp} can be set to zero energy, as it corresponds to the chemical potential of the analyzer.

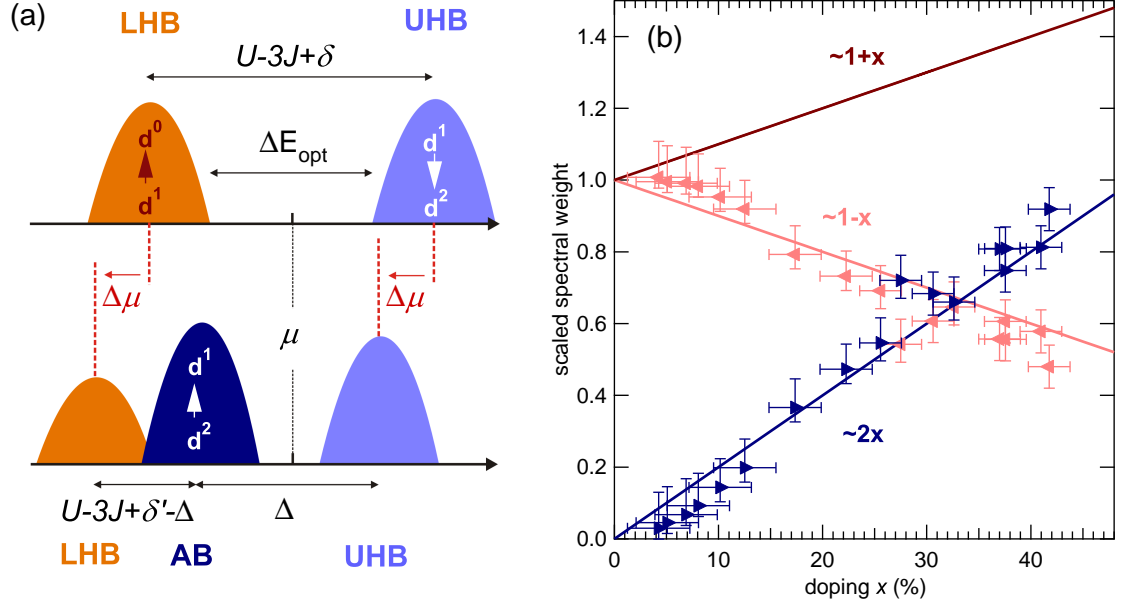


Figure 5.11: (a) Schematic of the Ti 3d spectral weight in the undoped (top) and doped (bottom) case. Peaks are labeled both in alloy Hubbard model terms (LHB, UHB, AB), and with the corresponding single-particle excitations (e.g., $d^2 \rightarrow d^1$). Red arrows indicate peak shifts upon doping, since μ remains at the same position (in absolute energies). (b) Scaled spectral weights of LHB and AB plotted versus x from fitting Ti 2p core levels (for details see text).

The separation between the LHB and the new peak is observed to be approx. 1 eV. In the atomic limit, this should correspond to $U - 3J + \delta' - \Delta$, and assuming for Δ a value in the range of 1.5–2.5 eV (depending on the choice of U and J) the spectral weight distribution can be fully reconciled. Such values for Δ appear reasonable, as the Coulomb energy which the positive Na ion induces at the Ti2 site is 1.6 eV in the relaxed crystal structure, assuming the same dielectric constant of 3 as in Sec. 4.2.5.

The introduction of the potential Δ directly motivates the naming of the $d^2 \rightarrow d^1$ peak as alloy band, since such a situation corresponds to the one of a so-called ionic or binary alloy Hubbard model [Byczuk04, Balzer05, Lombardo06, Paris07, Bouadim07]. Apart from hopping (t) and Coulomb repulsion (U) this model incorporates the additional (attractive) potential (Δ) on random or alternating sites of a bipartite lattice, which are called alloy sites. For certain combinations of these parameters as well as of the fraction ρ of alloy sites, and especially for certain bandfillings n , both band and Mott insulating phases can occur, while in all other cases either metallic or Anderson insulating behavior is observed. For example, for negligible hopping ($t \ll 1$) and $\rho < 1$, all alloy sites are singly occupied for $n = \rho$. The insulating state found in this case must thus be that of an alloy Mott insulator. Increasing n , metallicity occurs, and once $\Delta > U$, additional electrons will doubly occupy the alloy sites, leading to an alloy band

insulator at $n = 2 \cdot \rho$. Going up to $n = 1 + \rho$ one arrives at a situation where all alloy sites host two electrons and all other sites are singly occupied. Again, this yields an alloy Mott insulator. In any other case and specifically for any other bandfilling there should be finite spectral weight at the chemical potential, in seeming contrast to what is observed in TiOCl. However, this is naturally resolved by the fact that the Na ions themselves create the alloy sites. Thus, as was also shown by the results already reported, in the present case it is always $\rho = x$ and $n = 1 + x = 1 + \rho$, arriving at the important result that TiOCl is an alloy Mott insulator for any doping x . This is also independent from the fact that $\Delta < U$ in the present case, because the localization of electrons is governed by the slight change in CFS at the Ti2 sites, together with the long-range Coulomb interaction.

Apart from the single-particle alloy picture presented up to now, characteristic many-body effects are found in the valence band of the oxyhalides when quantifying the development of the spectral weight. This was done akin to the fits of Ti $2p$ core levels as presented in the previous section, although the involved peaks do not necessarily have Voigt character, because in angle-integrated measurements dispersive structures are broadened in a non-canonical fashion.

Taking x as determined from the core-level analysis, the overall Ti $3d$ spectral weight should scale as $1 + x$, because it was shown that all doped electrons reside in Ti orbitals. Normalizing the overall weight at different doping x accordingly and applying the respective normalization factors to the individual weights of LHB and AB, one obtains a behavior as the one shown in Fig. 5.11(b). It is seen that the LHB loses its weight proportional $1 - x$, while the AB grows with $2x$. This is exactly what one would expect in a local picture ($t = 0$), i.e., when no QP is present, for the LHB and UHB of a Mott insulator, and is known as “spectral-weight transfer” (SWT). It was examined theoretically by means of exact diagonalization by Eskes, Meinders and Sawatzky [Eskes91, Meinders93] and observed experimentally in x-ray absorption spectroscopy on cuprate superconductors [Chen91, Chen92, Hybertsen92, Peets09]. In the case of electron removal (i.e., photoemission) it can be understood as follows. Every double occupation due to a doped electron reduces the number of singly occupied sites and, accordingly, the weight of the LHB, by one. At the same time, the two-electron entity at the alloy site offers two possibilities for removing an electron from the AB, making its spectral weight grow with two times the number of alloy sites. The SWT thus occurs from the LHB to the AB, which takes over the role played by the UHB in a simple Mott-Hubbard picture. This is fundamentally different from an uncorrelated solid (e.g., semiconductor). There, the spectral weight of the valence band is completely unchanged, while new weight grows in the conduction band at a rate x .

The essence of the findings from photoemission is also reflected in electron energy-loss spectroscopy (EELS) data from Na doped TiOCl thin films cut from single crystals, performed by R. Kraus and M. Knupfer. With this method one measures the loss function $\text{Im} \left(-\frac{1}{\varepsilon(\mathbf{q}, \omega)} \right)$ at very high primary electron energies (172 keV), which has two advan-

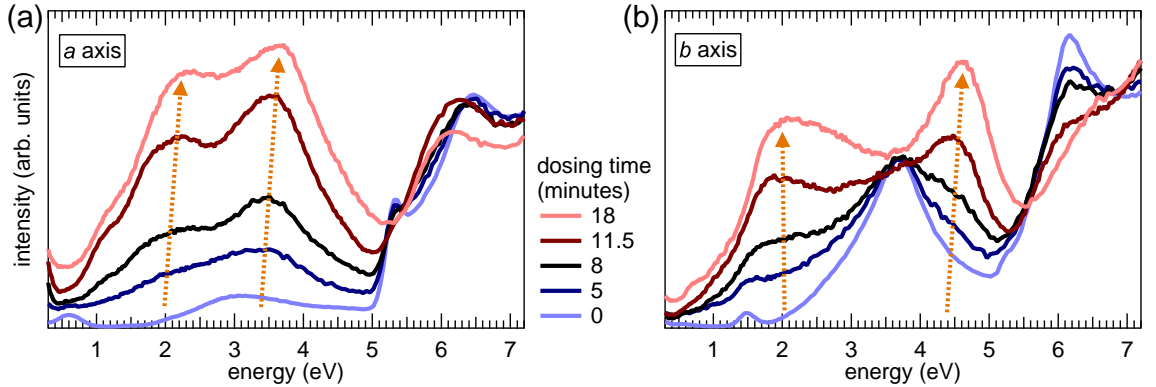


Figure 5.12: EELS of Na doped TiOCl after various dosing times, with momentum transfer along (a) a and (b) b . Spectra have been normalized to equal intensity at $E = 8$ eV. Arrows indicate the new features which correspond to excitations involving doubly occupied sites.

tages: the signal (at least with the thin samples investigated here) can be measured in transmission, and the significant electron momentum allows for \mathbf{q} -dependent measurements throughout the whole BZ of TiOCl. However, as no dispersion was observed for the Ti 3d derived structures in undoped crystals (cf. [Kraus10]) the \mathbf{q} -dependence is not quantified here but only used as to induce polarization-dependent changes. Since the sample thickness is only of the order of 100 nm one can safely assume that the samples are homogeneously doped, i.e., that the spectra reflect bulk properties. However, no experimental probe was available to quantify the electronic (or stoichiometric) doping in this EELS study, which is why only the dosing times are given. Figure 5.12 shows spectra at various dopings with momentum transfer both along a and b . One observes that upon doping those structures identified previously as crystal-field excitations (~ 0.6 eV and ~ 1.5 eV along a and b , respectively) and intersite excitations (Mott excitations for $E \gtrsim 2$ eV, and charge-transfer (CT) excitations above $E \gtrsim 5$ eV) from EELS on undoped crystals are becoming less discernible, and two new peaks emerge along both directions of momentum transfer. Just as the features of undoped TiOCl stem from electrons originating from the LHB, the new peaks can in direct analogy be assigned to additional excitations from the AB into the UHB (centered at approx. $E \approx 2$ eV) as well as new CT excitations [$E \approx 3.5$ eV (4.5 eV) along a (b)]. To a good approximation, the AB \rightarrow UHB and AB-CT peaks appear rigidly shifted by approx. 1.5 eV compared to the LHB \rightarrow UHB and LHB-CT excitations in the undoped case. This reflects the fact that the energies of intersite excitations starting from the AB are reduced by the impurity potential $\Delta \approx 1.5$ eV, which is effective only at doubly occupied sites. A straightforward assignment of features above the onset of CT excitations at approx. 5 eV is not possible because of the richness of bands at these energies already in undoped TiOCl. Nevertheless, recalling that the analysis is still rather preliminary, the presented spectra are in qualitative agreement with the alloy Hubbard model inferred from photoemission data.

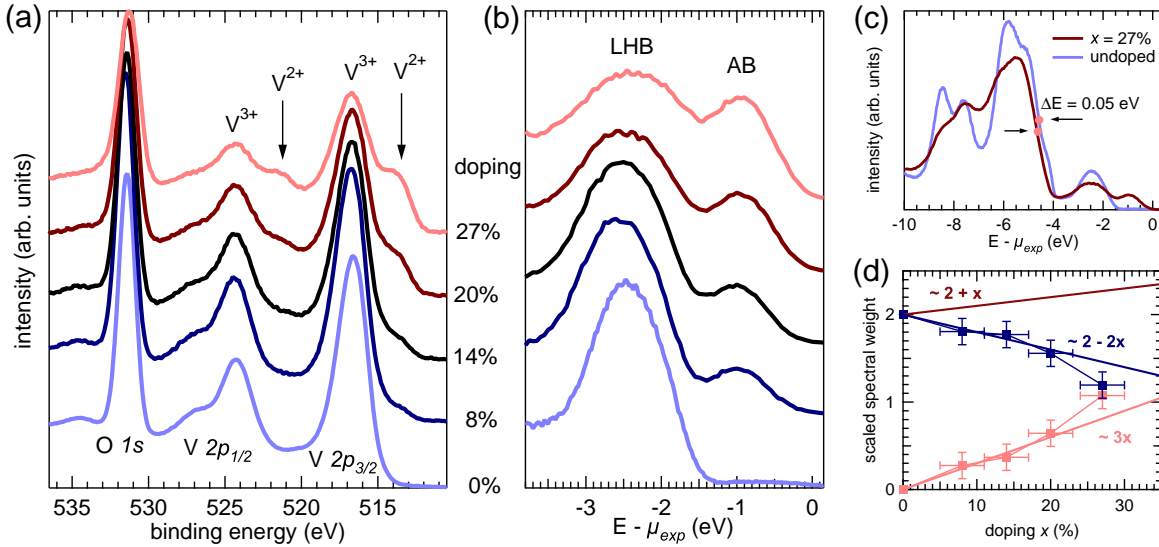


Figure 5.13: PES on VOCl for increased doping from $x = 0\%$ (bottom) to $x = 27\%$ (top). (a) XPS in the region of V 2p and O 1s core levels. (b) V 3d spectral weight close to the chemical potential. Doping is the same as indicated next to panel (a). (c) Full valence band at $x = 0\%$ and $x = 27\%$. Dots and arrows mark the half-maximum height of the O/Cl-dominated feature in the range $-7 < E - \mu_{exp} < -4$ eV, showing a difference of only approx. 50 meV. (d) Scaled spectral weights of LHB and AB plotted versus x from fitting V 2p core levels (see text for details).

Intercalation of VOCl

Before closing this section, some results from intercalation of VOCl shall be summarized. Figure 5.13 shows relevant core-level and valence-band spectra from a doping series with K. For several reasons a quantitative evaluation as it was done for TiOCl is more complicated in this case. From the core-level spectra in Fig. 5.13(a) it is seen that the V 2p doublet of VOCl has significant satellites on the high-binding-energy side which even overlap partially with the nearby O 1s core level at $E_{bind} \approx 531.5$ eV. Upon doping a second doublet (related to V²⁺) at smaller binding energies than the original one (V³⁺) emerges. Since 2p spectra of di- and trivalent vanadium consist of a number of multiplet peaks [Zimmermann99] obtaining x from Eq. 5.1 requires fitting with at least eight individual peaks [Scholz08], making the uncertainty in the value of x larger than for TiOCl. Furthermore, a rigid shift of the doped spectra like in the latter (cf. Figs. 5.1 and 5.6) is virtually absent ($\Delta E \lesssim 0.1$ eV). The same is observed in the valence spectra shown in Figs. 5.13(b) and (c). Although it might appear at a first glance that the onset of the O/Cl-dominated structures at $E - \mu_{exp} \approx -4$ eV is different between $x = 0$ and $x = 27\%$, this turns out not to be the case when looking at the energetic position of the initial slope at its half-maximum height [marked by dots in Fig. 5.13(c)]. The separation between the LHB and the UHB of VOCl has the same energy of $U - 3J + \delta'$ in a simple Hubbard model as in TiOCl, although it is given by a $d^2 \rightarrow d^3$ instead of

a $d^1 \rightarrow d^2$ excitation [Ole05]. While it can be assumed that alloy effects are at work in the same way due to the similar crystal structure, the absent jump of the chemical potential gives evidence that Coulombic parameters U , J and Δ are different such as to compensate the change of μ . Unfortunately, they are not known as good as in TiOCl, so that a quantitative agreement between model and experiment cannot be found.

Aiming at identification of an eventual SWT also in VOCl, the spectra in Fig. 5.13(b) must be analyzed. There, the original V $3d$ spectral weight appears broader than the Ti $3d$ peak in TiOCl, especially upon doping: its onset seemingly expands closer and closer towards μ_{exp} so that the new peak which is observed similar to doped TiOCl is sitting on this increasing background. Although no molecular dynamics calculations are available for VOCl, it is well justified to assume that the alloy Hubbard model with its localization effects and thus the terminology of LHB and AB are applicable here as well. Extracting their individual spectral weights, however, is exacerbated both due to the background just mentioned as well as their asymmetry, which is apparent from Fig. 5.13(b). This makes fitting by, e.g., Gaussian lineshapes less reliable, as these are intrinsically symmetric. Nevertheless, it appears natural to expect a SWT in VOCl as well, which however would be quantitatively different from the one in TiOCl, as becomes clear from the following considerations.

Suppose one has V sites which are occupied by two electrons each. Such sites constitute the LHB in undoped VOCl, and their spectral weight observed by PES shall be taken equivalent to 2. Now, adding x electrons (which in the atomic limit ($U \gg t$) localize at the V sites and lead to a total weight $2 + x$) reduces the LHB weight to $2 - 2x$, because for each now triply occupied site, two electrons are lost at the energetic position of the LHB. The new peak, on the other hand, gains weight at a rate of $3x$ because of the three electrons at a “doped site”. Figure 5.13(d) shows the spectral weight behavior obtained from the presented data, and the experimental values agree reasonably with the SWT expected in the fully localized limit just considered. Thus, within the remaining uncertainty, doped VOCl represents another compound in which correlation effects are wonderfully manifested by virtue of a spectral-weight transfer.

5.2 Efforts Towards Hole Doping

As we have seen, the electronic structure of n-doped TiOCl is governed by multi-band effects. Being a $3d^1$ system in its pristine form, it is tempting to investigate also the possibility of hole doping, thus possibly remaining in the single-band regime. In principle, this should be achievable by choosing acceptor instead of donor intercalants to be incorporated into the van-der-Waals gaps. Two different routes were investigated for this purpose [Go08]. The first was to expose TiOCl crystals to Br_2 or I_2 vapor for an extended period of time. Besides F and Cl (which are poisonous in vapor form) these are the elements with the highest electron affinity [Tro08]. Due to the low vapor pressure of these gases this has been done *ex situ*. A second way was *in situ* evaporation of the

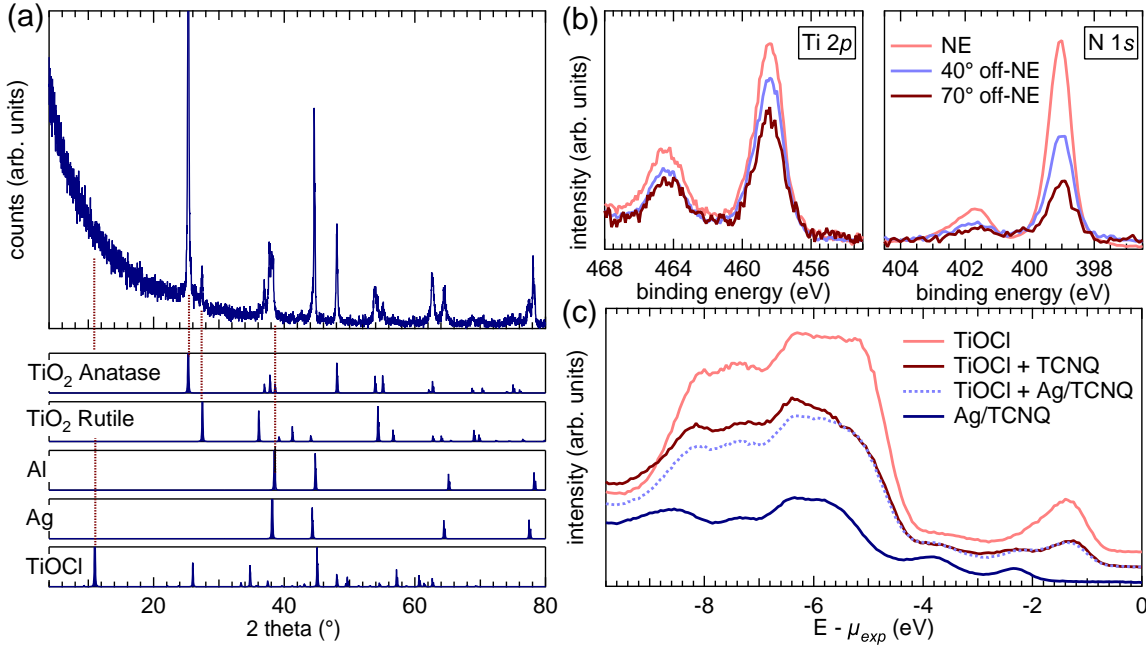


Figure 5.14: (a) Upper panel: X-ray diffraction (XRD) from halide-doped TiOCl. Lower panels: theoretical positions of XRD peaks of different substances. Obviously, TiOCl has been reduced to TiO₂ anatase and rutile. Admixtures of Ag and Al stem from the sample holder. Some characteristic reflexes (or the absence thereof, cf. expected peaks for TiOCl) have been highlighted for clarity. (b) Ti 2p (left) and N 1s (right) core levels measured with different detection angles (see legend in right panel). (c) Valence band region of pristine TiOCl (top), TiOCl after evaporation with TCNQ (center), and TCNQ on polycrystalline Ag foil (“Ag/TCNQ”; bottom). Also shown is a linear combination of the top and bottom spectra which closely resembles TCNQ on TiOCl (dotted curve; see text for details).

organic molecule TCNQ which is known for its high electron affinity, leading, e.g., to the formation of charge-transfer salts like TTF-TCNQ [Klots74].

Unfortunately, in none of the approaches investigated, indications for a successful hole doping of TiOCl were seen. Figure 5.14 summarizes the basic observations which can be made. The chemically very aggressive halide vapor destroys the TiOCl crystal structure by complete reduction, i.e., formation of TiO₂ in its different forms anatase and rutile. This is evident from the x-ray diffraction data shown in panel (a), obtained from crystals after several days at elevated temperatures ($\sim 400^\circ\text{C}$) in Br or I atmosphere. The fact that no more Cl signal was observed in core-level spectra of these crystals, while at the same time Ti and O core levels remained essentially unchanged (not shown), gives further support to this interpretation. Also, Br or I core levels appeared only as small admixtures, most likely reflecting a mere coverage (of monolayer thickness) of the resulting crystals instead of halide ions incorporated into the crystal lattice.

From angle-dependent XPS on TiOCl evaporated with TCNQ comes strong evidence that the molecules actually do intercalate into the van-der-Waals gaps. In Fig. 5.14(b)

the common trend towards smaller signal-to-noise ratios for both Ti $2p$ and N $1s$ core levels¹ at large angles from the surface normal indicates that there is no thick overlayer of TCNQ molecules. On the other hand, there is also no explanation why the N signal in NE is so much higher than in grazing incidence, as this would imply a higher content in the bulk than on the surface. Irrespective of these open questions, unfortunately do neither the core-level nor the valence-band spectra shown in panel (c) display any indication of successful charge transfer to the host lattice or even spectral weight at the chemical potential. Instead, from a comparison to TCNQ evaporated onto polycrystalline Ag foil (which was used as a reference substrate providing a well-known background) one finds that the observed structures are a superposition of the valence band of pristine TiOCl and the one of TCNQ on silver, given that one shifts the latter in energy by approx. ~ 0.85 eV. Since TCNQ molecules in (or on) TiOCl are likely to feel a different electronic potential from the one on silver (e.g., due to charge transfer from/to the substrate, mirror charges, etc.) such a shift is not unexpected. Also, this observation is not at variance with successful intercalation of TCNQ because the probing depth is significantly smaller in UPS compared to XPS, i.e., UPS probes essentially only the first TCNQ and the first TiOCl layer.

Even from the drastically summarized data presented here it can safely be stated that p-doping of TiOCl is not achievable using the above approaches, thus leaving the still fascinating possibility of obtaining hole-doped transition metal oxyhalides open for future research efforts.

¹N $1s$ is characteristic for TCNQ molecules.

6 Summary and Outlook

The goal of this thesis was to investigate the potential of transition metal (TM) oxyhalides of the form TiOX ($X = \text{Cl}, \text{Br}$) and VOCl as prototypical strongly correlated electron systems. This was done by evaluating their magnetic and electronic dimensionality and phase transitions. Major emphasis was laid on a possible bandfilling-controlled insulator-metal-transition induced by intercalation of appropriate dopants.

Due to their layered crystal structure with weakly bound sheets stacked along the c axis, electronic and magnetic interactions are confined to two dimensions. While monatomic chains along the b axis suggest a further reduction to one dimension (1D), one has to check to what degree such confinement actually takes place. From measurements of thermodynamic quantities and methods to determine the crystal structure and lattice parameters an unconventional transition into a low-temperature dimerized spin-Peierls (SP) state could be identified in TiOCl and TiOBr , which points at a one-dimensionality of these systems. VOCl , on the other hand, shows two-dimensional (2D) Néel order at low temperatures. The particular character of the SP transition involving an incommensurate intermediate phase, however, is induced by frustrated interchain interactions due to the quasi-triangular Ti sublattice on which the spins reside. Applying external pressures above approx. ~ 15 GPa at room temperature, a dramatic reduction of the charge gap is observed, which motivated investigations of bandfilling- in addition to bandwidth-related effects, hoping to find an insulator-metal-transition in TiOCl upon doping.

Photoemission spectroscopy (PES) in combination with band-structure and density-of-states calculations was used to identify the electronic ground state of the oxyhalides as being Mott insulators. While TiOCl and TiOBr are single-band systems, VOCl has two electrons in different orbitals and is thus intrinsically a multi-band system. As it was shown from angle-resolved photoemission spectroscopy (ARPES) this also affects the electronic dimensionality. Namely, while TiOCl has quasi-1D character along the b axis, this is less pronounced in TiOBr , and VOCl is clearly a 2D system due to significant orbital overlap also along the a axis. In this respect, several issues of a theoretical description of the oxyhalides have been addressed, like the importance of intersite and interchain fluctuations, the correct choice of the Coulomb parameters U and J , and state-of-the-art calculations to give a better account of the observed dispersions of the lower Hubbard band. This was necessary because the dispersion of TiOCl measured by ARPES could not be described by single-particle band-structure methods like $\text{LDA}(+U)$ and also did not display characteristic spectroscopic signatures of (purely) 1D systems, like spin-charge separation or a shadow band. Investigations of the unoccupied electronic

structure by x-ray absorption as well as low-energy excitations observed in resonant inelastic x-ray scattering (RIXS) provided further insight into hybridization, served as a benchmark for the values of U and J used in calculations, and helped pinpointing the actual crystal-field splitting in TiOCl. In addition, a feature lying at roughly 100 meV in RIXS could be identified as a two-spinon excitation, the first time that it was possible with this technique to observe such an excitation on a system that is not a cuprate superconductor.

Electron doping by intercalation of alkali metals into TiOCl yielded fascinating results. Using angle-dependent x-ray photoemission spectroscopy (XPS), successful charge transfer within the available probing depth was evidenced. XPS also allowed for a reliable quantitative determination of the electronic doping x . Furthermore, the resulting arrangement of the (charged) dopant ions was found to be in line with a polar catastrophe scenario, namely a redistribution of charge to avoid a divergence of the electrostatic potential which would occur in the limit of an infinite crystal. Although an immediate insulator-metal-transition was to be expected for an ideal single-band Mott-Hubbard system already at smallest doping, evidenced in PES by the appearance of a quasi-particle peak at the chemical potential, no indications for metallicity could be observed in $M_x\text{TiOCl}$ ($M = \text{Na}, \text{K}$) even for $x \geq 40\%$. Instead, it was found from molecular dynamics calculations in combination with density functional theory that alkali metal ions intercalated into the van-der-Waals gaps occupy distinct sites with respect to the host lattice. Their electrostatic (impurity) potential leads to a localization of the doped electrons at the TM site closest by, thus suppressing metallic conductivity. This situation can be termed “electrostatic alloying” in the sense that impurities incorporated into the host without changing its original lattice affect only the electronic structure. Extending the Mott-Hubbard description to that of an alloy Hubbard model, the energetic arrangement of lower and upper Hubbard bands as well as the newly appearing “alloy band” observed in PES can be fully reconciled. Besides this quite unique appearance of a self-trapped insulator not governed by effects like, e.g., Anderson localization, another fascinating result is that in the oxyhalides a so-called spectral-weight transfer can be observed in PES. This unique feature of strongly correlated electron systems, for which previously only evidence from x-ray absorption on cuprates was available, gives another prime justification to classify them as prototypical examples of this kind of systems.

Ongoing research is focussed mainly on TiOCl and its not yet fully resolved phase diagram. Knowing about the trapping potential of the dopants it is highly interesting to investigate the possibility of doping with earth alkali metal ions. While these also provide an impurity potential, the fact that they can donate two electrons each might render the second electron essentially unaffected by the rearrangement of the orbital energies and thus free to hop. Hole doping is in principle also of interest but seems to be a more delicate task, as can be seen from the results using halide vapor and organic molecules.

Bibliography

- [Aichhorn06] M. Aichhorn, E. Arrigoni, M. Potthoff, and W. Hanke. “Antiferromagnetic to superconducting phase transition in the hole- and electron-doped hubbard model at zero temperature”. *Physical Review B* **74**, 024508, 2006.
- [Aichhorn09] M. Aichhorn, T. Saha-Dasgupta, R. Valentí, S. Glawion, M. Sing, and R. Claessen. “Momentum-resolved single-particle spectral function for TiOCl from a combination of density functional and variational cluster calculations”. *Physical Review B* **80**, 115129, 2009.
- [Allen92] J. W. Allen. *Synchrotron Radiation Research: Advances in Surface and Interface Science*. Volume 1, Chapter 7, Plenum, 1992.
- [Ament09] L. J. P. Ament, G. Ghiringhelli, M. Moretti Sala, L. Braicovich, and J. van den Brink. “Theoretical Demonstration of How the Dispersion of Magnetic Excitations in Cuprate Compounds can be Determined Using Resonant Inelastic X-Ray Scattering”. *Physical Review Letters* **103**, 117003, 2009.
- [Andersen00] O. K. Andersen and T. Saha-Dasgupta. “Muffin-tin orbitals of arbitrary order”. *Physical Review B* **62**, R16219, 2000.
- [Anderson73] P. W. Anderson. “Resonating valence bonds: A new kind of insulator?”. *Materials Research Bulletin* **8**, 153, 1973.
- [Anderson87] P. W. Anderson. “The Resonating Valence Bond State in La_2CuO_4 and Superconductivity”. *Science* **235**, 1196, 1987.
- [Anisimov97] V. I. Anisimov, F. Aryasetiawan, and A. I. Lichtenstein. “First-principles calculations of the electronic structure and spectra of strongly correlated systems: the LDA+ U method”. *Journal of Physics: Condensed Matter* **9**, 767, 1997.
- [Asbrink70] L. Asbrink. “The Photoelectron Spectrum of H_2 ”. *Chemical Physics Letters* **7**, 549, 1970.
- [Ashcroft76] N. W. Ashcroft and N. D. Mermin. *Solid State Physics*. Thomson Learning Inc., 1976.

- [Balzer05] M. Balzer and M. Potthoff. “Disorder- and correlation-driven metal-insulator transitions”. *Physica B* **359**, 768, 2005.
- [Bednorz88] J. G. Bednorz and K. A. Müller. “Perovskite-type oxides – The new approach to high- T_c superconductivity”. *Reviews of Modern Physics* **60**, 585, 1988.
- [Benthien04] H. Benthien, F. Gebhard, and E. Jeckelmann. “Spectral Function of the One-Dimensional Hubbard Model away from Half Filling”. *Physical Review Letters* **92**, 256401, 2004.
- [Berglund64] C. N. Berglund and W. E. Spicer. “Photoemission studies of copper and silver”. *Physical Review* **136**, 1030, 1964.
- [Bethe31] H. A. Bethe. “Zur Theorie der Metalle: I. Eigenwerte und Eigenfunktionen der linearen Atomkette”. *Zeitschrift für Physik A* **71**, 205, 1931.
- [Beynon93] R. J. Beynon and J. A. Wilson. “TiOCl, TiOBr – are these RVB d^1 , $S = 1/2$ materials? The results of scandium substitution set in the context of other $S = 1/2$ systems of current interest for high-temperature superconductivity and the metal-insulator transition”. *Journal of Physics: Condensed Matter* **5**, 1983, 1993.
- [Blaha01] P. Blaha, K. Schwarz, and J. Luitz. “computer code WIEN2K”, 2001. URL <http://www.wien2k.at>.
- [Blanco-Canosa09] S. Blanco-Canosa, F. Rivadulla, A. Piñeiro, V. Pardo, D. Baldomir, D. I. Khomskii, M. M. Abd-Elmeguid, M. A. López-Quintela, and J. Rivas. “Enhanced Dimerization of TiOCl under Pressure: Spin-Peierls to Peierls Transition”. *Physical Review Letters* **102**, 056406, 2009.
- [Blöchl94] P. E. Blöchl. “Projector augmented-wave method”. *Physical Review B* **50**, 17953, 1994.
- [Bouadim07] K. Bouadim, N. Paris, F. Hébert, G. G. Batrouni, and R. T. Scalettar. “Metallic phase in the two-dimensional ionic Hubbard model”. *Physical Review B* **76**, 085112, 2007.
- [Bulla99] R. Bulla. “Zero Temperature Metal-Insulator Transition in the Infinite-Dimensional Hubbard Model”. *Physical Review Letters* **83**, 136, 1999.
- [Butler81] P. H. Butler. *Point Group Symmetry Applications: Methods and Tables*. Plenum Press New York, 1981.
- [Byczuk04] K. Byczuk, W. Hofstetter, and D. Vollhardt. “Mott-Hubbard metal-insulator transition at noninteger filling”. *Physical Review B* **69**, 045112, 2004.

-
- [Car85] R. Car and M. Parrinello. “Unified Approach for Molecular Dynamics and Density-Functional Theory”. *Physical Review Letters* **55**, 2471, 1985.
- [Chen91] C. T. Chen, F. Sette, Y. Ma, M. S. Hybertsen, E. B. Stechel, W. M. C. Foulkes, M. Schuller, S-W. Cheong, A. S. Cooper, L. W. Rupp, B. Batlogg, Y. L. Soo, Z. H. Ming, A. Krol, and Y. H. Kao. “Electronic states in $\text{La}_{2-x}\text{Sr}_x\text{CuO}_{4+\delta}$ probed by soft-x-ray absorption”. *Physical Review Letters* **66**, 104, 1991.
- [Chen92] C. T. Chen, L. H. Tjeng, J. Kwo, H. L. Kao, P. Rudolf, F. Sette, and R. M. Fleming. “Out-of-plane orbital characters of intrinsic and doped holes in $\text{La}_{2-x}\text{Sr}_x\text{CuO}_4$ ”. *Physical Review Letters* **68**, 2543, 1992.
- [Chioncel07] L. Chioncel, H. Allmaier, E. Arrigoni, A. Yamasaki, M. Daghofer, M. I. Katsnelson, and A. I. Lichtenstein. “Half-metallic ferromagnetism and spin polarization in CrO_2 ”. *Physical Review B* **75**, 140406, 2007.
- [Clancy07] J. P. Clancy, B. D. Gaulin, K. C. Rule, J. P. Castellan, and F. C. Chou. “Commensurate fluctuations in the pseudogap and incommensurate spin-Peierls phases of TiOCl ”. *Physical Review B* **75**, 100401(R), 2007.
- [Clancy08] J. P. Clancy, B. D. Gaulin, J. P. Castellan, K. C. Rule, and F. C. Chou. “Suppression of the commensurate spin-Peierls state in Sc-doped $\text{Ti}_{1-x}\text{Sc}_x\text{OCl}$ ($x = 0.0, 0.01, \text{ and } 0.03$)”. *Physical Review B* **78**, 014433, 2008.
- [Cowan81] R. D. Cowan. *The Theory of Atomic Structure and Spectra*. University of California Press Berkeley, 1981.
- [Craciun09] M. F. Craciun, G. Giovannetti, S. Rogge, G. Brocks, A. F. Morpurgo, and J. van den Brink. “Evidence for the formation of a Mott state in potassium-intercalated pentacene”. *Physical Review B* **79**, 125116, 2009.
- [Craco06] L. Craco, M. S. Land, and E. Müller-Hartmann. “Metallizing the Mott insulator TiOCl by electron doping”. *Journal of Physics: Condensed Matter* **18**, 10943, 2006.
- [Cumpson97] P. J. Cumpson and M. P. Seah. “Elastic Scattering Corrections in AES and XPS. II. Estimating Attenuation Lengths and Conditions Required for their Valid Use in Overlayer/Substrate Experiments”. *Surface and Interface Analysis* **25**, 430, 1997.
- [cxro10] “U.S. Department of Energy, Center for X-Ray Optics and Lawrence Berkeley National Laboratory”, 2010. URL <http://www-cxro.lbl.gov/>.
- [Daghofer08] M. Daghofer, A. Moreo, J. A. Riera, E. Arrigoni, D. J. Scalapino, and E. Dagotto. “Model for the Magnetic Order and Pairing Channels in Fe Pnictide Superconductors”. *Physical Review Letters* **101**, 237004, 2008.

- [Damascelli03] A. Damascelli, Z. Hussain, and Z.-X. Shen. “Angle-resolved photoemission studies of the cuprate superconductors”. *Reviews of Modern Physics* **75**, 473, 2003.
- [Damascelli04] A. Damascelli. “Probing the Electronic Structure of Complex Systems by ARPES”. *Physica Scripta* **T109**, 61, 2004.
- [de Boer37] J. H. de Boer and E. J. W. Verwey. “Semi-conductors with partially and with completely filled 3d-lattice bands”. *Proceedings of the Physical Society* **49**, 59, 1937.
- [de Groot89] F. M. F. de Groot, M. Grioni, J. C. Fuggle, J. Ghijsen, G. A. Sawatzky, and H. Petersen. “Oxygen 1s x-ray-absorption edges of transition-metal oxides”. *Physical Review B* **40**, 5715, 1989.
- [de Groot90a] F. M. F. de Groot, J. C. Fuggle, B. T. Thole, and G. A. Sawatzky. “2p x-ray absorption of 3d transition-metal compounds: An atomic multiplet description including the crystal field”. *Physical Review B* **42**, 5459, 1990.
- [de Groot90b] F. M. F. de Groot, J. C. Fuggle, B. T. Thole, and G. A. Sawatzky. “ $L_{2,3}$ x-ray-absorption edges of d^0 compounds: K^+ , Ca^{2+} , Sc^{3+} , and Ti^{4+} in O_h (octahedral) symmetry”. *Physical Review B* **41**, 928, 1990.
- [de Groot93] F. M. F. de Groot, J. Faber, J. J. M. Michiels, M. T. Czyzyk, M. Abbate, and J. C. Fuggle. “Oxygen 1s x-ray absorption of tetravalent titanium oxides: A comparison with single-particle calculations”. *Physical Review B* **48**, 2074, 1993.
- [de Groot08] F. M. F. de Groot and A. Kotani. *Core Level Spectroscopy of Solids*. Taylor & Francis, 2008.
- [des Cloizeaux62] J. des Cloizeaux and J. J. Pearson. “Spin-Wave Spectrum of the Antiferromagnetic Linear Chain”. *Physical Review* **128**, 2131, 1962.
- [Doniach70] S. Doniach and M. Sunjic. “Many-electron singularity in x-ray photoemission and x-ray line spectra from metals”. *Journal of Physics C: Solid State Physics* **3**, 285, 1970.
- [Duffy68] W. Duffy and K. P. Barr. “Theory of Alternating Antiferromagnetic Heisenberg Linear Chains”. *Physical Review* **165**, 647, 1968.
- [Ebad-Allah10] J. Ebad-Allah, A. Schönleber, S. van Smaalen, M. Hanfland, M. Klemm, S. Horn, S. Glawion, M. Sing, R. Claessen, and C. A. Kuntscher. “Two pressure-induced structural phase transitions in $TiOCl$ ”. *Physical Review B* **82**, 134117, 2010.

- [Einstein05] A. Einstein. “Über einen die Erzeugung und Verwandlung des Lichtes betreffenden heuristischen Gesichtspunkt”. *Annalen der Physik* **17**, 132, 1905.
- [Eskes91] H. Eskes, M. B. J. Meinders, and G. A. Sawatzky. “Anomalous transfer of spectral weight in doped strongly correlated systems”. *Physical Review Letters* **67**, 1035, 1991.
- [Fano61] U. Fano. “Effects of Configuration Interaction on Intensities and Phase Shifts”. *Physical Review* **124**, 1866, 1961.
- [Fausti07] D. Fausti, T. T. A. Lummen, C. Angelescu, R. Macovez, J. Luzon, R. Broer, P. Rudolf, P. H. M. van Loosdrecht, N. Tristan, B. Büchner, S. van Smaalen, A. Möller, G. Meyer, and T. Taetz. “Symmetry disquisition on the TiOX phase diagram (X = Br,Cl)”. *Physical Review B* **75**, 245114, 2007.
- [Fink94] J. Fink, N. Nücker, E. Pellegrin, H. Romberg, M. Alexander, and M. Knupfer. “Electron energy-loss and X-ray absorption spectroscopy of cuprate superconductors and related compounds”. *Journal of Electron Spectroscopy and Related Phenomena* **66**, 395, 1994.
- [Forthaus08] M. K. Forthaus, T. Taetz, A. Möller, and M. M. Abd-Elmeguid. “Effect of pressure on the electrical transport and structure of TiOCl”. *Physical Review B* **77**, 165121, 2008.
- [Fröhlich54] H. Fröhlich. “On the theory of superconductivity: the one-dimensional case”. *Proceedings of the Royal Society of London A* **223**, 296, 1954.
- [Fujii97] Y. Fujii, H. Nakao, T. Yosihama, M. Nishi, K. Nakajima, K. Kakurai, M. Isobe, Y. Ueda, and H. Sawa. “New inorganic spin-Peierls compound NaV_2O_5 evidenced by X-ray and neutron scattering”. *Journal of the Physical Society of Japan* **66**, 326, 1997.
- [Georges92] A. Georges and G. Kotliar. “Hubbard model in infinite dimensions”. *Physical Review B* **45**, 6479, 1992.
- [Georges96] A. Georges, G. Kotliar, W. Krauth, and M. J. Rozenberg. “Dynamical mean-field theory of strongly correlated fermion systems and the limit of infinite dimensions”. *Reviews of Modern Physics* **68**, 13, 1996.
- [Ghiringhelli06] G. Ghiringhelli, A. Piazzalunga, C. Dallera, G. Trezzi, L. Braicovich, T. Schmitt, V. N. Strocov, R. Betemps, L. Patthey, X. Wang, and M. Grioni. “SAXES, a high resolution spectrometer for resonant x-ray emission in the 400-1600 eV energy range”. *Review of Scientific Instruments* **77**, 113108, 2006.

- [Glawion09] S. Glawion, M. R. Scholz, Y.-Z. Zhang, R. Valentí, T. Saha-Dasgupta, M. Klemm, J. Hemberger, S. Horn, M. Sing, and R. Claessen. “Electronic structure of the two-dimensional Heisenberg antiferromagnet VOCl: A multi-orbital Mott insulator”. *Physical Review B* **80**, 155119, 2009.
- [Goß08] K. Goß. “Photoemissionsspektroskopie an dem prototypischen Mott-Isolator TiOCl - Interkalation vs. Dotierung mit Elektronenakzeptoren”. Diploma thesis, Universität Würzburg, 2008.
- [Gutzwiller63] M. C. Gutzwiller. “Effect of Correlation on the Ferromagnetism of Transition Metals”. *Physical Review Letters* **10**, 159, 1963.
- [Harrison78] W. A. Harrison, E. A. Kraut, J. R. Waldrop, and R. W. Grant. “Polar heterojunction interfaces”. *Physical Review B* **18**, 4402, 1978.
- [Hase93] M. Hase, I. Terasaki, and K. Uchinokura. “Observation of the spin-Peierls transition in linear Cu^{2+} (spin-1/2) chains in an inorganic compound CuGeO_3 ”. *Physical Review Letters* **70**, 3651, 1993.
- [Haverkort05] M. W. Haverkort. “Spin and orbital degrees of freedom in transition metal oxides and oxide thin films studied by soft x-ray absorption spectroscopy”. arXiv:cond-mat/0505214v1, 2005.
- [Haverkort10] M. W. Haverkort. “Theory of Resonant Inelastic X-Ray Scattering by Collective Magnetic Excitations”. *Physical Review Letters* **105**, 167404, 2010.
- [Hemberger05] J. Hemberger, M. Hoinkis, M. Klemm, M. Sing, R. Claessen, S. Horn, and A. Loidl. “Heat capacity of the quantum magnet TiOCl”. *Physical Review B* **72**, 012420, 2005.
- [Henke93] B. L. Henke, E. M. Gullikson, and J. C. Davis. “X-ray interactions: photoabsorption, scattering, transmission, and reflection at $E=50\text{-}30000$ eV, $Z=1\text{-}92$ ”. *Atomic Data and Nuclear Data Tables* **54**, 181, 1993.
- [Hertz87] H. R. Hertz. “Über den Einfluss des ultravioletten Lichtes auf die elektrische Entladung”. *Annalen der Physik und Chemie* **31**, 983, 1887.
- [Hohenberg64] P. Hohenberg and W. Kohn. “Inhomogeneous Electron Gas”. *Physical Review* **136**, B864, 1964.
- [Hoinkis05] M. Hoinkis, M. Sing, J. Schäfer, M. Klemm, S. Horn, H. Benthien, E. Jeckelmann, T. Saha-Dasgupta, L. Pisani, R. Valentí, and R. Claessen. “Electronic structure of the spin-1/2 quantum magnet TiOCl”. *Physical Review B* **72**, 125127, 2005.

-
- [Hoinkis06] M. Hoinkis. “Phase Transitions in Low-Dimensional Transition Metal Compounds”. PhD thesis, Universität Augsburg, 2006.
- [Hoinkis07] M. Hoinkis, M. Sing, S. Glawion, L. Pisani, R. Valentí, S. van Smaalen, M. Klemm, S. Horn, and R. Claessen. “One-dimensional versus two-dimensional correlation effects in the oxyhalides TiOCl and TiOBr”. *Physical Review B* **75**, 245124, 2007.
- [Hoogenboom98] B. W. Hoogenboom, R. Hesper, L. H. Tjeng, and G. A. Sawatzky. “Charge transfer and doping-dependent hybridization of C-60 on noble metals”. *Physical Review B* **57**, 11939, 1998.
- [Hossain08] M. A. Hossain, J. D. F. Mottershead, D. Fournier, A. Bostwick, J. L. McChesney, E. Rotenberg, R. Liang, W. N. Hardy, G. A. Sawatzky, I. S. Elfimov, D. A. Bonn, and A. Damascelli. “In situ doping control of the surface of high-temperature superconductors”. *Nature Physics* **4**, 527, 2008.
- [Hubbard63] J. Hubbard. “Electron correlations in narrow energy bands”. *Proceedings of the Royal Society of London Series A* **276**, 238, 1963.
- [Hüfner99] S. Hüfner, R. Claessen, F. Reinert, T. Straub, V. N. Strocov, and P. Steiner. “Photoemission spectroscopy in metals: band structure-Fermi surface-spectral function”. *Journal of Electron Spectroscopy and Related Phenomena* **100**, 191, 1999.
- [Hybertsen92] M. S. Hybertsen, E. B. Stechel, W. M. C. Foulkes, and M. Schlüter. “Model for low-energy electronic states probed by x-ray absorption in high- T_c cuprates”. *Physical Review B* **45**, 10032, 1992.
- [Imada98] M. Imada, A. Fujimori, and Y. Tokura. “Metal-insulator transitions”. *Reviews of Modern Physics* **70**, 1039, 1998.
- [Imai03] T. Imai and F. C. Chou. “Novel Spin-Gap Behavior in Layered $S = \frac{1}{2}$ Quantum Spin System TiOCl”. cond-mat/0301425, 2003.
- [Jeckelmann02] E. Jeckelmann. “Dynamical density-matrix renormalization-group method”. *Physical Review B* **66**, 045114, 2002.
- [Kajueter96] H. Kajueter, G. Kotliar, and G. Moeller. “Doped Mott insulator: Results from mean-field theory”. *Physical Review B* **53**, 16214, 1996.
- [Kanamori63] J. Kanamori. “Electron Correlation and Ferromagnetism of Transition Metals”. *Progress of Theoretical Physics* **30**, 275, 1963.

- [Karbach97] M. Karbach, G. Müller, A. H. Bougourzi, A. Fledderjohann, and K.-H. Mütter. “Two-spinon dynamic structure factor of the one-dimensional $s = 1/2$ Heisenberg antiferromagnet”. *Physical Review B* **55**, 12510, 1997.
- [Kettle07] S. F. A. Kettle. *Symmetry and Structure - Readable Group Theory for Chemists*. Wiley, 2007.
- [Kivelson87] S. Kivelson. “Nature of the pairing in a resonating-valence-bond superconductor”. *Physical Review B* **36**, R7237, 1987.
- [Klots74] C. E. Klots, R. N. Compton, and V. F. Raaen. “Electronic and ionic properties of molecular TTF and TCNQ”. *The Journal of Chemical Physics* **60**, 1177, 1974.
- [Kohn65] W. Kohn and L. J. Sham. “Self-Consistent Equations Including Exchange and Correlation Effects”. *Physical Review* **140**, A1133, 1965.
- [Komarek09] A. C. Komarek, T. Taetz, M. T. Fernández-Díaz, D. M. Trots, A. Möller, and M. Braden. “Strong magnetoelastic coupling in VOCl: Neutron and synchrotron powder x-ray diffraction study”. *Physical Review B* **79**, 104425, 2009.
- [Koningsberger88] D. C. Koningsberger and R. Prins, editors. *X-Ray Absorption*. John Wiley & Sons, 1988.
- [Koralek06] J. D. Koralek, J. F. Douglas, N. C. Plumb, Z. Sun, A. V. Fedorov, M. M. Murnane, H. C. Kapteyn, S. T. Cundiff, Y. Aiura, K. Oka, H. Eisaki, and D. S. Dessau. “Laser Based Angle-Resolved Photoemission, the Sudden Approximation, and Quasiparticle-Like Spectral Peaks in $Bi_2Sr_2CaCu_2O_{8+\delta}$ ”. *Physical Review Letters* **96**, 017005, 2006.
- [Kotani01] A. Kotani and S. Shin. “Resonant inelastic x-ray scattering spectra for electrons in solids”. *Reviews of Modern Physics* **73**, 203, 2001.
- [Kotani05] A. Kotani. “Resonant inelastic X-ray scattering in d and f electron systems”. *The European Physical Journal B* **47**, 3, 2005.
- [Kotliar04] G. Kotliar and D. Vollhardt. “Strongly Correlated Materials: Insights From Dynamical Mean-Field Theory”. *Physics Today* **57**, 53, 2004.
- [Kramers25] H. A. Kramers and W. Heisenberg. “Über die Streuung von Strahlung durch Atome”. *Zeitschrift für Physik* **31**, 681, 1925.
- [Kraus10] R. Kraus, B. Büchner, M. Knupfer, S. Glawion, M. Sing, and R. Claessen. “Anisotropic crystal field, Mott gap, and interband excitations in TiOCl: An electron energy-loss study”. *Physical Review B* **81**, 125133, 2010.

-
- [Krimmel06] A. Krimmel, J. Stremper, B. Bohnenbuck, B. Keimer, M. Hoinkis, M. Klemm, S. Horn, A. Loidl, M. Sing, R. Claessen, and M.v. Zimmermann. “Incommensurate structure of the spin-Peierls compound TiOCl in zero and finite magnetic fields”. *Physical Review B* **73**, 172413, 2006.
- [Kuntscher06] C. A. Kuntscher, S. Frank, A. Pashkin, M. Hoinkis, M. Klemm, M. Sing, S. Horn, and R. Claessen. “Possible pressure-induced insulator-to-metal transition in low-dimensional TiOCl”. *Physical Review B* **74**, 184402, 2006.
- [Kuntscher07] C. A. Kuntscher, S. Frank, A. Pashkin, H. Hoffmann, A. Schönleber, S. van Smaalen, M. Hanfland, S. Glawion, M. Klemm, M. Sing, S. Horn, and R. Claessen. “Pressure-induced metallization and structural phase transition of the Mott-Hubbard insulator TiOBr”. *Physical Review B* **76**, 241101(R), 2007.
- [Kuntscher08] C. A. Kuntscher, A. Pashkin, H. Hoffmann, S. Frank, M. Klemm, S. Horn, A. Schönleber, S. van Smaalen, M. Hanfland, S. Glawion, M. Sing, and R. Claessen. “Mott-Hubbard gap closure and structural phase transition in the oxyhalides TiOBr and TiOCl under pressure”. *Physical Review B* **78**, 035106, 2008.
- [Langreth83] D. C. Langreth and M. J. Mehl. “Beyond the local-density approximation in calculations of ground-state electronic properties”. *Physical Review B* **28**, 1809, 1983.
- [Lee05] J. S. Lee, M. W. Kim, and T. W. Noh. “Optical excitations of transition-metal oxides under the orbital multiplicity effects”. *New Journal of Physics* **7**, 147, 2005.
- [Lemmens04] P. Lemmens, K. Y. Choi, G. Caimi, L. Degiorgi, N. N. Kovaleva, A. Seidel, and F. C. Chou. “Giant phonon softening in the pseudogap phase of the quantum spin system TiOCl”. *Physical Review B* **70**, 134429, 2004.
- [Lemmens05] P. Lemmens, K. Y. Choi, R. Valentí, T. Saha-Dasgupta, E. Abel, Y. S. Lee, and F. C. Chou. “Spin gap formation in the quantum spin systems TiOX, X=Cl and Br”. *New Journal of Physics* **7**, 74, 2005.
- [Lieb62] E. Lieb and D. Mattis. “Ordering Energy Levels of Interacting Spin Systems”. *Journal of Mathematical Physics* **3**, 749, 1962.
- [Loa99] I. Loa, U. Schwarz, M. Hanfland, R. K. Kremer, and K. Syassen. “Crystal Structure and Optical Spectroscopy of NaV₂O₅ under Pressure”. *Physica Status Solidi (b)* **215**, 709, 1999.
- [Lombardo06] P. Lombardo, R. Hayn, and G. I. Japaridze. “Insulator-metal-insulator transition and selective spectral-weight transfer in a disordered strongly correlated system”. *Physical Review B* **74**, 085116, 2006.

- [Macovez07] R. Macovez, J. Luzon, J. Schiessling, A. Sadoc, L. Kjeldgaard, S. van Smaalen, D. Fausti, P. H. M. van Loosdrecht, R. Broer, and P. Rudolf. “Hybridization, superexchange, and competing magnetoelastic interactions in TiOBr”. *Physical Review B* **76**, 205111, 2007.
- [Maekawa04] S. Maekawa, T. Tohyama, S. E. Barnes, S. Ishihara, W. Koshibae, and G. Khaliullin. *Physics of Transition Metal Oxides*. Springer, 2004.
- [Mao86] H. K. Mao, J. Xu, and P. M. Bell. “Calibration of the ruby pressure gauge to 800 kbar under quasi-hydrostatic conditions”. *Journal of Geophysical Research* **91**, 4673, 1986.
- [Maule88] C. H. Maule, J. N. Tothill, P. Strange, and J. A. Wilson. “An optical investigation into the $3d^1$ and $3d^2$ transition metal halides and oxyhalides, compounds near to delocalisation”. *Journal of Physics C: Solid State Physics* **21**, 2153, 1988.
- [Max09] J.-J. Max and C. Chapados. “Isotope effects in liquid water by infrared spectroscopy”. *Journal of Chemical Physics* **131**, 184505, 2009.
- [Meinders93] M. B. J. Meinders, H. Eskes, and G. A. Sawatzky. “Spectral-weight transfer: Breakdown of low-energy-scale sum rules in correlated systems”. *Physical Review B* **48**, 3916, 1993.
- [Merino08] J. Merino, M. Dumm, N. Drichko, M. Dressel, and R. H. McKenzie. “Quasiparticles at the Verge of Localization near the Mott Metal-Insulator Transition in a Two-Dimensional Material”. *Physical Review Letters* **100**, 086404, 2008.
- [Mermin66] N. D. Mermin and H. Wagner. “Absence of Ferromagnetism or Antiferromagnetism in One- or Two-Dimensional Isotropic Heisenberg Models”. *Physical Review Letters* **17**, 1133, 1966.
- [Metzner89] W. Metzner and D. Vollhardt. “Correlated Lattice Fermions in $d = \infty$ Dimensions”. *Physical Review Letters* **62**, 324, 1989.
- [Miller96] T. Miller, W. E. McMahon, and T.-C. Chiang. “Interference between bulk and surface photoemission transition in Ag(111)”. *Physical Review Letters* **77**, 1167, 1996.
- [Minakata93] T. Minakata, M. Ozaki, and H. Imai. “Conducting thin films of pentacene doped with alkaline metals”. *Journal of Applied Physics* **74**, 1079, 1993.
- [Mott37] N. F. Mott and R. E. Peierls. “Discussion of the paper by de Boer and Verwey”. *Proceedings of the Physical Society* **49**, 72, 1937.

-
- [Mott49] N. F. Mott. “The Basis of the Electron Theory of Metals, with Special Reference to the Transition Metals”. *Proceedings of the Physical Society* **62**, 416, 1949.
- [Mott56] N. F. Mott. “On the transition to metallic conduction in semiconductors”. *Canadian Journal of Physics* **34**, 1356, 1956.
- [Müller81] G. Müller, H. Thomas, H. Beck, and J. C. Bonner. “Quantum spin dynamics of the antiferromagnetic linear chain in zero and nonzero magnetic field”. *Physical Review B* **24**, 1429, 1981.
- [Nakagawa06] N. Nakagawa, H. Y. Hwang, and D. A. Muller. “Why some interfaces cannot be sharp”. *Nature Materials* **5**, 204, 2006.
- [NIST10] “National Institute of Science and Technology, Physical Reference Data”, 2010. URL <http://www.nist.gov/physlab/data/>.
- [Okada93] K. Okada, T. Uozumi, and A. Kotani. “Charge-Transfer Satellites in Ti 2p XAS and XPS of Ti Compounds”. *Japanese Journal of Applied Physics* **32**, 113, 1993.
- [Oleś05] A. M. Oleś, G. Khaliullin, P. Horsch, and L. F. Feiner. “Fingerprints of spin-orbital physics in cubic Mott insulators: Magnetic exchange interactions and optical spectral weights”. *Physical Review B* **72**, 214431, 2005.
- [Paris07] N. Paris, A. Baldwin, and R. T. Scalettar. “Mott and band-insulator transitions in the binary-alloy Hubbard model: Exact diagonalization and determinant quantum Monte Carlo simulations”. *Physical Review B* **75**, 165113, 2007.
- [Parrinello80] M. Parrinello and A. Rahman. “Crystal Structure and Pair Potentials: A Molecular-Dynamics Study”. *Physical Review Letters* **45**, 1196, 1980.
- [Peets09] D. C. Peets, D. G. Hawthorn, K. M. Shen, Y.-J. Kim, D. S. Ellis, H. Zhang, S. Komiya, Y. Ando, G. A. Sawatzky, R. Liang, D. A. Bonn, and W. N. Hardy. “X-Ray Absorption Spectra Reveal the Inapplicability of the Single-Band Hubbard Model to Overdoped Cuprate Superconductors”. *Physical Review Letters* **103**, 087402, 2009.
- [Perdew81] J. P. Perdew and A. Zunger. “Self-interaction correction to density-functional approximations for many-electron systems”. *Physical Review B* **23**, 5048, 1981.
- [Perfetti01] L. Perfetti, H. Berger, A. Reggiani, L. Degiorgi, H. Höchst, J. Voit, G. Margaritondo, and M. Grioni. “Spectroscopic Indications of Polaronic Carriers in

- the Quasi-One-Dimensional Conductor $(\text{TaSe}_4)_2\text{I}^+$. *Physical Review Letters* **87**, 216404, 2001.
- [Pisani05] L. Pisani and R. Valentí. “Ab initio phonon calculations for the layered compound TiOCl ”. *Physical Review B* **71**, 180409, 2005.
- [Potthoff03a] M. Potthoff. “Self-energy-functional approach to systems of correlated electrons”. *European Physical Journal B* **32**, 429, 2003.
- [Potthoff03b] M. Potthoff, M. Aichhorn, and C. Dahnken. “Variational Cluster Approach to Correlated Electron Systems in Low Dimensions”. *Physical Review Letters* **91**, 206402, 2003.
- [Prodi10] A. Prodi, J. S. Helton, Y. Feng, and Y. S. Lee. “Pressure-induced spin-Peierls to incommensurate charge-density-wave transition in the ground state of TiOCl ”. *Physical Review B* **81**, 201103(R), 2010.
- [Racah42] G. Racah. “Theory of Complex Spectra. I”. *Physical Review* **61**, 186, 1942.
- [Reinert05] F. Reinert and S. Hüfner. “Photoemission spectroscopy – from early days to recent applications”. *New Journal of Physics* **7**, 97, 2005.
- [Rückamp05a] R. Rückamp, J. Baier, M. Kriener, M. W. Haverkort, T. Lorenz, G. S. Uhrig, L. Jongen, A. Möller, G. Meyer, and M. Grüninger. “Zero-Field Incommensurate Spin-Peierls Phase with Interchain Frustration in TiOCl ”. *Physical Review Letters* **95**, 097203, 2005.
- [Rückamp05b] R. Rückamp, E. Benckiser, M. W. Haverkort, H. Roth, T. Lorenz, A. Freimuth, L. Jongen, A. Möller, G. Meyer, P. Reutler, B. Büchner, A. Revcolevschi, S.-W. Cheong, C. Sekar, G. Krabbes, and M. Grüninger. “Optical study of orbital excitations in transition-metal oxides”. *New Journal of Physics* **7**, 144, 2005.
- [Ruffieux00] P. Ruffieux, P. Schwaller, O. Gröning, L. Schlapbach, P. Gröning, Q. C. Herd, D. Funnemann, and J. Westermann. “Experimental determination of the transmission factor for the Omicron EA125 electron analyzer”. *Review of Scientific Instruments* **71**, 3634, 2000.
- [Saha-Dasgupta04] T. Saha-Dasgupta, R. Valentí, H. Rosner, and C. Gros. “ TiOCl , an orbital-ordered system?”. *Europhysics Letters* **67**, 63, 2004.
- [Saha-Dasgupta05] T. Saha-Dasgupta, A. Lichtenstein, and R. Valentí. “Correlation effects on the electronic structure of TiOCl : A NMTO+DMFT study”. *Physical Review B* **71**, 153108, 2005.

-
- [Saha-Dasgupta07] T. Saha-Dasgupta, A. Lichtenstein, M. Hoinkis, S. Glawion, M. Sing, R. Claessen, and R. Valentí. “Cluster dynamical mean-field calculations for TiOCl”. *New Journal of Physics* **9**, 380, 2007.
- [Schäfer58] H. Schäfer, F. Wartenpfehl, and E. Weise. “Titan(III)-oxychlorid”. *Zeitschrift für Anorganische und Allgemeine Chemie* **295**, 268, 1958.
- [Schlappa10] J. Schlappa. private communication, 2010.
- [Scholz08] M. R. Scholz. “Photoemissionsspektroskopie an niederdimensionalen korrelierten Elektronensystemen”. Diploma thesis, Universität Würzburg, 2008.
- [Schönleber06] A. Schönleber, S. van Smaalen, and L. Palatinus. “Structure of the incommensurate phase of the quantum magnet TiOCl”. *Physical Review B* **73**, 214410, 2006.
- [Schönleber08] A. Schönleber, G. Shcheka, and S. van Smaalen. “Normal-to-incommensurate phase transition in the spin-Peierls compound TiOCl: An x-ray diffraction study”. *Physical Review B* **77**, 094117, 2008.
- [Schönleber09] A. Schönleber, J. Angelkort, S. van Smaalen, L. Palatinus, A. Senyshyn, and W. Morgenroth. “Phase transition, crystal structure, and magnetic order in VOCl”. *Physical Review B* **80**, 064426, 2009.
- [Schrupp05] D. Schrupp, M. Sing, M. Tsunekawa, H. Fujiwara, S. Kasai, A. Sekiyama, S. Suga, T. Muro, V.A.M. Brabers, and R. Claessen. “High-energy photoemission on Fe₃O₄: Small polaron physics and the Verwey transition”. *Europhysics Letters* **70**, 789, 2005.
- [Seah79] M. P. Seah and W. A. Dench. “Quantitative Electron Spectroscopy of Surfaces: A Standard Data Base for Electron Inelastic Mean Free Paths in Solids”. *Surface and Interface Analysis* **1**, 2, 1979.
- [Seidel03] A. Seidel, C. A. Marianetti, F. C. Chou, G. Ceder, and P. A. Lee. “S=1/2 chains and spin-Peierls transition in TiOCl”. *Physical Review B* **67**, 020405(R), 2003.
- [Sénéchal04] D. Sénéchal and A.-M. S. Tremblay. “Hot Spots and Pseudogaps for Hole- and Electron-Doped High-Temperature Superconductors”. *Physical Review Letters* **92**, 126401, 2004.
- [Shaz05] M. Shaz, S. van Smaalen, L. Palatinus, M. Hoinkis, M. Klemm, S. Horn, and R. Claessen. “Spin-Peierls transition in TiOCl”. *Physical Review B* **71**, 100405(R), 2005.

- [Shinaoka09] H. Shinaoka and M. Imada. “Soft Hubbard Gaps in Disordered Itinerant Models with Short-Range Interaction”. *Physical Review Letters* **102**, 016404, 2009.
- [Shirley72] D. A. Shirley. “High-resolution x-ray photoemission spectrum of the valence bands of gold”. *Physical Review B* **5**, 4709, 1972.
- [Siegbahn82] K. Siegbahn. “Electron spectroscopy for atoms, molecules and condensed matter”. *Science* **217**, 111, 1982.
- [Sugano70] S. Sugano, Y. Tanabe, and H. Kamimura. *Multiplets of Transition Metal Ions in Crystals*. Academic Press New York, 1970.
- [Tjeng97] L. H. Tjeng, R. Hesper, A. C. L. Heessels, A. Heeres, H. T. Jonkman, and G. A. Sawatzky. “Development of the electronic structure in a K-doped C-60 monolayer on a Ag(111) surface”. *Solid State Communications* **103**, 31, 1997.
- [Tro08] N. J. Tro. *Chemistry: A Molecular Approach*. Pearson Prentice Hall, 2008.
- [Trzhaskovskaya01] M. B. Trzhaskovskaya, V. I. Nefedov, and V. G. Yarzhemsky. “Photoelectron angular distribution parameters for elements $Z=1$ to $Z=54$ in the photoelectron energy range 100-5000 eV”. *Atomic Data and Nuclear Data Tables* **77**, 97, 2001.
- [van Smaalen05] S. van Smaalen, L. Palatinus, and A. Schönleber. “Incommensurate interactions and nonconventional spin-Peierls transition in TiOBr”. *Physical Review B* **72**, 020105(R), 2005.
- [Vénien79] J. P. Vénien, P. Palvadeau, D. Schleich, and J. Rouxel. “Vanadium (III) oxychloride : Magnetic, optical and electrical properties; lithium and molecular intercalations”. *Materials Research Bulletin* **14**, 891, 1979.
- [von Schnering72] H. G. von Schnering, M. Collin, and M. Hassheider. “TiOBr; Darstellung, Eigenschaften und Struktur”. *Zeitschrift für Anorganische und Allgemeine Chemie* **387**, 137, 1972.
- [White92] S. R. White. “Density matrix formulation for quantum renormalization groups”. *Physical Review Letters* **69**, 2863, 1992.
- [Wicks09] R. C. Wicks and N. J. C. Ingle. “Characterizing the detection system nonlinearity, internal inelastic background, and transmission function of an electron spectrometer for use in x-ray photoelectron spectroscopy”. *Review of Scientific Instruments* **80**, 053108, 2009.

-
- [Wiedenmann83] A. Wiedenmann, J. P. Vénien, P. Palvadeau, and J. Rossat-Mignod. “Magnetic ordering of the quasi-two-dimensional system VOCl”. *Journal of Physics C: Solid State Physics* **16**, 5339, 1983.
- [Yamanaka98] S. Yamanaka, K.-I. Hotehama, and H. Kawaji. “Superconductivity at 25.5 K in the electron-doped layered hafnium nitride”. *Nature* **392**, 580, 1998.
- [Yeh85] J. J. Yeh and I. Lindau. “Atomic subshell photoionization cross sections and asymmetry parameters: $1 \leq Z \leq 103$ ”. *Atomic Data and Nuclear Data Tables* **32**, 1, 1985.
- [Zaanen85] J. Zaanen, G. A. Sawatzky, and J. W. Allen. “Band Gaps and Electronic Structure of Transition-Metal Compounds”. *Physical Review Letters* **55**, 418, 1985.
- [Zhang08a] Y.-Z. Zhang, H. O. Jeschke, and R. Valentí. “Microscopic model for transitions from Mott to spin-Peierls insulator in TiOCl”. *Physical Review B* **78**, 205104, 2008.
- [Zhang08b] Y.-Z. Zhang, H. O. Jeschke, and R. Valentí. “Two Pressure-Induced Transitions in TiOCl: Mott Insulator to Anisotropic Metal”. *Physical Review Letters* **101**, 136406, 2008.
- [Zhang10] Y.-Z. Zhang, K. Foyevtsova, H. O. Jeschke, M. U. Schmidt, and R. Valentí. “Can the Mott Insulator TiOCl be Metallized by Doping? A First-Principles Study”. *Physical Review Letters* **104**, 146402, 2010.
- [Zimmermann99] R. Zimmermann, P. Steiner, R. Claessen, F. Reinert, S. Hüfner, P. Blaha, and P. Dufek. “Electronic structure of 3d-transition-metal oxides: on-site Coulomb repulsion versus covalency”. *Journal of Physics: Condensed Matter* **11**, 1657, 1999.

List of Own Publications

(in chronological order)

- **S. Glawion**, M. Sing, M. Hoinkis, C. A. Kuntscher, and R. Claessen. “Unusual Spin-Peierls Physics in the Layered Quantum Magnet TiOCl”. *AIP Conference Proceedings* **918**, 2007.
- M. Hoinkis, M. Sing, **S. Glawion**, L. Pisani, R. Valentí, S. van Smaalen, M. Klemm, S. Horn, and R. Claessen. “One-dimensional versus two-dimensional correlation effects in the oxyhalides TiOCl and TiOBr”. *Physical Review B* **75**, 245124, 2007.
- M. Sing, J. Meyer, M. Hoinkis, **S. Glawion**, P. Blaha, G. Gavrila, C. S. Jacobsen, and R. Claessen. “Structural vs electronic origin of renormalized band widths in TTF-TCNQ: An angular dependent NEXAFS study”. *Physical Review B* **76**, 245119, 2007.
- C. A. Kuntscher, S. Frank, A. Pashkin, H. Hoffmann, A. Schönleber, S. van Smaalen, M. Hanfland, **S. Glawion**, M. Klemm, M. Sing, S. Horn, and R. Claessen. “Pressure-induced metallization and structural phase transition of the Mott-Hubbard insulator TiOBr”. *Physical Review B* **76**, 241101(R), 2007.
- T. Saha-Dasgupta, A. Lichtenstein, M. Hoinkis, **S. Glawion**, M. Sing, R. Claessen, and R. Valentí. “Cluster dynamical mean-field calculations for TiOCl”. *New Journal of Physics* **9**, 380, 2007.
- C. A. Kuntscher, A. Pashkin, H. Hoffmann, S. Frank, M. Klemm, S. Horn, A. Schönleber, S. van Smaalen, M. Hanfland, **S. Glawion**, M. Sing, and R. Claessen. “Mott-Hubbard gap closure and structural phase transition in the oxyhalides TiOBr and TiOCl under pressure”. *Physical Review B* **78**, 035106, 2008.
- **S. Glawion**, M. Sing, and R. Claessen. “Ti oxohalides: A playground for electron correlation physics”. *Physica B - Condensed Matter* **404**, 530, 2009.
- C. A. Kuntscher, J. Ebad-Allah, A. Pashkin, S. Frank, M. Klemm, S. Horn, A. Schönleber, S. van Smaalen, M. Hanfland, **S. Glawion**, M. Sing, and R. Claessen. “Filling of the Mott-Hubbard gap in the oxyhalides TiOCl and TiOBr induced by external pressure”. *High Pressure Research* **29**, 509, 2009.

- M. Aichhorn, T. Saha-Dasgupta, R. Valentí, **S. Glawion**, M. Sing, and R. Claessen. “Momentum-resolved single-particle spectral function for TiOCl from a combination of density functional and variational cluster calculations”. *Physical Review B* **80**, 115129, 2009.
- **S. Glawion**, M. R. Scholz, Y.-Z. Zhang, R. Valentí, T. Saha-Dasgupta, M. Klemm, J. Hemberger, S. Horn, M. Sing, and R. Claessen. “Electronic structure of the two-dimensional Heisenberg antiferromagnet VOCl: A multiorbital Mott insulator”. *Physical Review B* **80**, 155119, 2009.
- M. Sing, **S. Glawion**, M. Schlachter, M. R. Scholz, K. Goss, J. Heidler, G. Berner, and R. Claessen. “Photoemission of a doped Mott insulator: spectral weight transfer and qualitative Mott-Hubbard description”. arXiv:0905.1381v2, 2009 (submitted for publication).
- R. Kraus, B. Büchner, M. Knupfer, **S. Glawion**, M. Sing, and R. Claessen. “Anisotropic crystal field, Mott gap, and interband excitations in TiOCl: An electron energy-loss study”. *Physical Review B* **81**, 125133, 2010.
- N. Hlubek, M. Sing, **S. Glawion**, R. Claessen, S. van Smaalen, P. H. M. van Loosdrecht, B. Büchner, and C. Hess. “Heat conductivity of the spin-Peierls compounds TiOCl and TiOBr”. *Physical Review B* **81**, 144428, 2010.
- J. Ebad-Allah, A. Schönleber, S. van Smaalen, M. Hanfland, M. Klemm, S. Horn, **S. Glawion**, M. Sing, R. Claessen, and C. A. Kuntscher. “Two pressure-induced structural phase transitions in TiOCl”. *Physical Review B* **82**, 134117, 2010.
- G. Berner, **S. Glawion**, J. Walde, H. Hollmark, L. C. Duda, S. Thiel, C. Richter, J. Mannhart, M. Sing, and R. Claessen. “Resonant Inelastic X-ray Scattering on LaAlO₃-SrTiO₃ Oxide Heterostructures”. accepted for publication in *Physical Review B (Rapid)*, 2010.
- **S. Glawion**, J. Heidler, M. W. Haverkort, L. C. Duda, T. Schmitt, V. N. Strocov, M. Sing, and R. Claessen. “Two-Spinon and Orbital Excitations of the Spin-Peierls System TiOCl”. submitted for publication (2010).

Acknowledgment

To *Prof. Ralph Claessen* I am thankful for making the bold decision of hiring me as his first PhD student in Würzburg, thus introducing me to the fascinating field of strongly correlated electron systems, while at the same time allowing me the chance to participate in the first steps of the then re-established research group “Experimentelle Physik 4”, and for his scientific guidance and expertise on the way towards writing this thesis.

Invaluable and undeniably the most direct impact both on the results presented in this thesis and on my development as a scientist was made by *Dr. Michael Sing*. I am utmost indebted to him for being a never-ending well of physical insights, patiently and thoroughly sharing his understanding with me, proof-reading this thesis, and above all, for being not just a mere colleague but also a good friend while sharing our office over the last years.

Both in preparation of experiments, data acquisition, and data analysis, a huge contribution to my work was made by the great diploma students I had the pleasure to work with during my time: *Götz Berner*, *Matthias Schlachter*, *Karin Goss*, *Markus Scholz*, and *Jakoba Heidler*. Each of them were highly motivated and reliable co-workers who shared a refreshing verve on all (or, let’s say, most) aspects of experimental physics with me. To *Karin Goss* I am especially thankful for her valuable first-stage proof-reading of this thesis. I also thank my predecessor *Dr. Markus Hoinkis* for his work on the oxyhalides and helpful tips to get me started on the topic.

All crystals investigated in the course of this thesis were grown by *Thomas Demarczyk* who did a great job in this manner. Additionally, I thank *Franz Schwabenländer* for characterizing crystals using Laue and x-ray diffraction.

Coming to the numerous external collaborators involved in our work on the oxyhalides I would foremost like to thank *Prof. Roser Valentí*, on the hand for co-reporting on this thesis, and on the other hand for many DFT-based calculations and those involving DMFT and molecular dynamics, together with her colleagues *Dr. Tanusri Saha-Dasgupta*, *Dr. Harald Jeschke*, and *Dr. Yu-Zhong Zhang*. In this line, I also thank *Dr. Markus Aichhorn* for his calculations using LDA+VCA. *Dr. Maurits Haverkort* is acknowledged for his multiplet and spinon theory-based calculations for RIXS and XAS as well as very useful discussions.

On the experimental side, I thank *Prof. Christine Kuntscher* for giving me the opportunity to participate in a beamtime at the ESRF to perform pressure-dependent optical and x-ray diffraction experiments, and her former student *Dr. Simone Frank* as well as *Prof. Sander van Smaalen* who also participated in these experiments and performed the data analysis. Acquisition and analysis of the high-energy EELS data by *Robert Kraus*

and *Dr. Martin Knupfer* as well as of high-resolution EELS by *Patrick Bayersdorfer* is also gratefully acknowledged. To *Dr. Matthias Klemm* and *Dr. Joachim Hemberger* I am thankful for SQUID and specific heat measurements, respectively.

Furthermore, I thank the staff of the ADDRESS beamline at SLS, foremost *Dr. Thorsten Schmitt* and *Dr. Vladimir Strocov*, along with *Prof. Laurent C. Duda*, for valuable support during our RIXS beamtimes as well as scientific discussions. For support during XAS and ResPES beamtimes I thank *Dr. Gianina Gavrilă* and *Mike Sperling* from BESSY.

Not only for creating a wonderfully familial atmosphere I thank our secretary *Monika Seifer*, and my *Oxide* and (*unbelievable*) *Nanoteam* colleagues (former and present) not mentioned specifically by name.

Finally, I thank *Dorit Eisenacher* for many efforts to comfort me, and her along with my family and many close yet unnamed friends for moral support (not only) in the final stage of my PhD work.

Curriculum Vitae

Personal Data

Sebastian Karl-Heinz Glawion
born 06.12.1980 in Groß-Umstadt
german

Education

09/1991 – 07/2000 07/2000	FRIEDRICH-DESSAUER-GYMNASIUM ASCHAFFENBURG Abitur
10/2001 – 08/2004 08/2003	UNIVERSITÄT WÜRZBURG Vordiplom
08/2004 – 05/2005 07/2005	STATE UNIVERSITY OF NEW YORK AT BUFFALO, USA M. S. in physics, Advisor: Prof. H. Luo
since 08/2005	UNIVERSITÄT WÜRZBURG PhD in physics, Advisor: Prof. R. Claessen

Work Experience

09/2000 – 07/2001	Alternative service, LEBENSILFE E.V., Aschaffenburg
since 08/2005	Research assistant at the Chair of Experimental Physics 4, UNIVERSITÄT WÜRZBURG

Eidesstattliche Erklärung

Hiermit versichere ich an Eides statt, dass ich die vorliegende Dissertation eigenständig angefertigt habe und keine anderen als die angegebenen Quellen und Hilfsmittel benutzt habe.

Würzburg, den 13. August 2010

Sebastian Glawion

Erklärung

Hiermit erkläre ich, dass ich die vorliegende Dissertation nicht in gleicher oder anderer Form bereits in einem anderen Fach vorgelegt habe.

Würzburg, den 13. August 2010

Sebastian Glawion